Structural Studies of Human GABA-A Receptors

Simonas Masiulis

Medical Sciences Doctoral Training Centre

Kellogg College

University of Oxford

A thesis submitted in fulfilment of the requirements for the degree of *Doctor of Philosophy* at the University of Oxford

Trinity Term 2017

Structural studies of human GABA-A receptors

Simonas Masiulis, Kellogg College, University of Oxford

DPhil, Medical Sciences Doctoral Training Centre

Trinity Term 2017

Abstract

Type-A γ-amino-butyric acid receptors ($GABA_ARs$) are pentameric ligand-gated ion channels (pLGICs), which mediate the majority of fast inhibitory neurotransmission in the animal central nervous system. Their dysfunction is related to numerous conditions including epilepsy, insomnia, anxiety, panic disorders, depression and schizophrenia. $GABA_ARs$ are therefore major targets of clinically important drugs, including benzodiazepines and the intravenous general anaesthetics etomidate and propofol, as well as endogenous modulators, for example neurosteroids. Despite recent progress in structural biology of pLGICs, $GABA_AR$ structures remain notoriously elusive. Structural information available at the beginning of this project was limited to the benzamidine-bound homopentameric $GABA_AR$-β3, in a desensitised conformation. A large number of fundamental questions, including the molecular architecture of physiological, heteromeric $GABA_ARs$, their signalling mechanisms, the binding and action modes of their numerous ligands, remained to be answered.

During this *DPhil* project, I employed structural biology techniques (X-ray crystallography and single particle cryo-electron microscopy) to further the molecular understanding of human $GABA_ARs$. I used subunit-specific llama nanobodies to aid crystallization of homomeric $GABA_A$-β3 receptors, which led to a 3.16 Å structure in complex with the general anaesthetic etomidate. This structure elucidates the binding mode of the etomidate, the basis for its subunit selectivity and illustrates conformational changes it triggers. I then used cryo-electron microscopy to determine the first structure of a heteromeric $GABA_AR$, the human α1β3γ2, bound to an activating llama nanobody at a medium (5.2 Å) resolution. The numerous other insights obtained range from unambiguously establishing the subunit arrangement and stoichiometry, to proposing a mechanism for receptor assembly and discovering an unexpected role played by N-linked glycans in this process.

The work described here opens multiple avenues for future research. Immediate opportunities include high resolution structural characterization of heteromeric $GABA_ARs$, via cryo-electron microscopy, further development of nanobodies as novel, high affinity and subunit specific tools to modulate GABA-ergic signalling, and structural characterization of numerous small-molecule modulators, of clinical and physiological relevance, bound to human $GABA_ARs$.

DECLARATION OF WORK

All the described work herein is my own, except that detailed immediately below:

Chapter 3. Llama nanobodies as $GABA_AR$ crystallization chaperones:

- Dr Paul Miller produced human α1β3 $GABA_AR$ used for llama immunisation and subsequent nanobody clone selection by phage display/ELISA assays.
- Nanobodies were produced by Dr Els Pardon as part of the collaboration with Prof Jan Steyaert's laboratory.
- Nanobody cloning into pHLsec-Nt-mV vector was performed by Dr Paul Miller's summer student Jana Gajewski.
- Some of the $GABA_AR$-β3 homopentamer used for initial crystallization trials with nanobodies was produced by Dr Paul Miller.
- Crystal mounting, dehydration and X-ray data collection was completed by/or with help of Prof Radu Aricescu and Dr Jonathan Elegheert.
- X-ray crystallographic data processing was performed with guidance of Prof Radu Aricescu.

Chapter 4. Intravenous anaesthetic etomidate binding site in $GABA_ARs$ revealed by X-ray crystallography:

- Dr Paul Miller identified $GABA_AR$-β3 K297T mutation to be more thermostable and more likely to crystallize while using DDTM detergent.
- Dr Paul Miller performed electrophysiology experiments on $GABA_AR$-β3 K297T mutant
- Propofol bromide was received from Prof Nick Franks's laboratory.
- Crystal soaking, X-ray data collection and processing was completed with help of Prof Radu Aricescu.

Chapter 5. Analysing $GABA_A$ receptors with cryo-electron microscopy:

- Cryo-electron microscopy and data analysis of $GABA_AR$-β3 homopentamer in complex with nanobody Nb25 was carried out with guidance of Prof Juha Huiskonen

Chapter 6. Cryo-EM structure of a heteromeric human GABA$_A$-α1β3γ2 receptor:

- Dr Paul Miller has developed and produced the human α1β3γ2 GABA$_A$ receptor construct (intracellular loops were truncated to increase the stability), which was used for cryo-EM structural analysis in this chapter (termed α1β3γ2$_{EM}$).
- Dr Paul Miller performed the electrophysiology experiments and data analysis for α1β3γ2$_{EM}$ GABA$_A$ construct.
- Cryo-electron microscopy and data analysis were performed with help of Prof Juha Huiskonen and Dr Abhay Kotecha.
- Molecular dynamics experiments were carried out in collaboration with Prof Mark Sansom and Prof Stephen Tucker.

Chapter 7. Alternative GABA$_A$R solubilisation methods:

- The stable cell line producing human full-length α1β3γ2 GABA$_A$ receptor was received from Prof Keith Miller laboratory as part of a collaboration.

Table of Contents

List of Figures

List of Tables

List of Non-Standard Abbreviations

5-HT3	5-hydroxytryptamine receptor 3
Å	Ångström
ADP	adenosine diphosphate
BRIL	apocytochrome b(562)RIL
BZ	benzodiazepine
CC	cross correlation
CDR	complementarity determining region
CHAPS	3-[(3-cholamidopropyl)dimethylammonio]-1-propanesulfonate
CHS	cholesteryl hemisuccinate
CNS	central nervous system
CPU	core processing unit
cryo-EM	cryo-electron microscopy
CTF	contrast transfer function
DDM	n-dodecyl β-D-maltopyranoside
DDTM	n-dodecyl β-D-thiomaltopyranoside
DMNG	decyl maltose neopentyl glycol
DNA	deoxyribonucleic acid
DTT	dithiothreitol
E. coli	*Escherichia coli*
ECD	extracellular domain
EDTA	ethylenediaminetetraacetic acid
ELIC	pentameric-ligand gated ion channel from *Erwinia chrysanthemi*
EM	electron microscopy
ER	endoplasmic reticulum
FSC	Fourier shell correlation
FSEC	fluorescence-detection size exclusion chromatography

GABA	gamma-aminobutyric acid
$GABA_AR$s	gamma-aminobutyric acid receptors A
GLIC	pentameric-ligand gated ion channel from *Gloeobacter violaceus*
GluCl	glutamate-gated chloride channel
GlyR	glycine receptor
GPU	graphics processing unit
HEK293	human embryonic kidney (cells) 293
ICD	intracellular domain
KCC2	chloride potassium symporter 5
kDa	kilo Dalton
MR	molecular replacement
mRNA	messenger ribonucleic acid
mV	mono-Venus
nAChR	nicotinic acetylcholine receptor
NCS	non-crystallographic symmetry
NTA	nitrilotriacetic acid
OD_{600}	optical density at 600 nm
PAM	positive allosteric modulation
PEG	polyethylene glycol
PEG-MME	polyethylene glycol-monomethyl ether
pLGIC	pentameric ligand gated ion channel
POPC	phosphatidylcholine
PTX	picrotoxin
RMSD	root mean square deviation
SCK	single cycle kinetics
SDS-PAGE	sodium dodecyl sulfate polyacrylamide gel-electrophoresis
SEC	size exclusion chromatography
SGD	stochastic gradient descent

SOC	super optimal broth with catabolite repression
SPR	surface plasmon resonance
TAE	Tris-acetate-EDTA
TEM	transmission electron microscopy
THDOC	tetrahydrodeoxycorticosterone
THP	tetrahydroprogesterone
TLS	translation/libration/screw
TM	transmembrane
TMD	transmembrane domain
V_H	variable domain, heavy chain
V_L	variable domain, light chain
ZAC	zinc-activated cation channels

Introduction

The work in this thesis is concerned with the structural and functional understanding of human $GABA_A$ receptors. $GABA_A$ receptors are proteins, whose activity is crucial for fast inhibitory signalling in the adult central nervous system (CNS). $GABA_A$Rs are integral membrane proteins located in neurons, both in synapses and extrasynaptically. Gamma-aminobutyric acid (GABA) acts as a ligand to these receptors and upon its binding $GABA_A$Rs undergo a conformational change leading to transmembrane pore opening. This allows anion passage across the neuronal membrane prompting membrane hyperpolarization and inhibition of action potentials. Defects in $GABA_A$R signalling cause excessive neuronal signalling, which is implicated in a wide range of human disease like epilepsy, anxiety, insomnia and depression. Structurally, $GABA_A$Rs belong to pentameric ligand-gated ion channel (pLGIC) family and there are several genes encoding for the different subunits that make up the receptor. The large subunit variety allows $GABA_A$Rs to assemble into multiple functionally and pharmacologically distinct units. Specific subunit interfaces contain binding pockets for natural ligands and modulation sites for clinically relevant medications like anxiolytics and anaesthetics. The binding modes of small drug molecules and heteromeric $GABA_A$ receptor architecture is the main focus of this work. In order to address these questions, I employed a range of structural biology techniques. In the following sections I will provide a brief introduction to $GABA_A$R biology and mode of action. I will describe what is known about the gating cycle of the receptor, what are predicted small molecule binding sites and their modulation mechanisms. Finally, I will finish this section by addressing the unknowns in the field and will provide the aims of this work.

1.1. GABA as a neurotransmitter

Neurotransmitter GABA is one of the most abundant neurotransmitters in the brain (Curtis and Crawford, 1969; Hebb, 1970). GABA is a metabolic product of glutamate, an amino acid which also acts as a major excitatory neurotransmitter in the CNS. GABA binding to $GABA_A$Rs leads to channel pore opening, which allows Cl^- anion passage across the neuronal membranes. During the CNS development, $GABA_A$ receptor activation leads to membrane depolarisation, since the developing neurons do not express K+/Cl- co-transporter (KCC2) to extrude intracellular Cl^- (Kaila et al., 1999).

Due to this reversed potential, $GABA_AR$s mediate the excitatory signalling in the developing brain (Kirmse et al., 2017). However, in adult neurons KCC2 is expressed and the intracellular Cl^- concentration is maintained at low levels. $GABA_AR$ activation by GABA, leads to receptor pore opening and Cl^- anions rush into the neurons hyperpolarizing the membrane potential. This leads to inhibition of neuronal signalling, as a much stronger stimulus is required to depolarise the membrane and initiate an action potential. The balance between the inhibitory activity mediated by $GABA_AR$s and the excitatory signalling shapes a properly functioning CNS (Petroff, 2002).

1.2. Pentameric ligand gated ion channels

The pentameric ligand-gated ion channel (pLGIC) superfamily is one of the major fast neurotransmitter-gated signalling components in the central and peripheral nervous systems (CNS and PNS). Neurotransmitter binding to pLGICs causes them to open a pore across the cell membrane for cation and anion flow. Members of the excitatory cation-selective pLGICs include nicotinic acetylcholine receptors (nAChR) (Dani, 2015), type 3 5-hydroxytryptamine receptors (5-HT3/serotonin) (Lummis, 2012) and zinc-activated cation channels (ZAC) (Davies et al., 2003). The inhibitory anion-selective pLGICs are type-A γ-aminobutyric acid receptors ($GABA_AR$) (Sigel and Steinmann, 2012) and glycine receptors (GlyR) (Lynch, 2004). All these ion channels possess a loop containing a characteristic cysteine disulphide bond and are therefore referred to as Cys-loop receptors. In addition to Cys-loop receptors, the pLGIC superfamily contains members in prokaryotes which do not possess the characteristic cysteine residues in the aforementioned loop. Notable examples would be GLIC from *Gloeobacter violaceus* (Bocquet et al., 2007) and ELIC from *Erwinia chrysanthemi* (Hilf and Dutzler, 2008).

$GABA_AR$s are the main subject of study in this thesis. Although pLGICs share a common basic architecture, their biological functions and mechanisms of action are very diverse. Even in a single $GABA_A$ receptor family there are multiple subunits which can assemble into heteropentamers with very distinct pharmacological profiles and cellular localization patterns. Therefore, although some general principles of action can be inferred from other pLGICs, the exact molecular details of how GABA$_A$Rs work can only be understood by analysing their structure and function directly.

1.3. GABA$_A$ receptor subunit variation

GABA$_A$ receptors form pentamers, which can be assembled from multiple subunit types. To date, 19 subunit sequences were characterised that belong to GABA$_A$Rs in mammalian genomes (Olsen and Sieghart, 2008; Sigel and Steinmann, 2012). These subunits are distributed across 8 main groups: α1-6, β1-3, γ1-3, ρ1-3, δ, ε, π and θ (Fig. 1.1a). GABA$_A$Rs are produced in the endoplasmic reticulum (ER), where they assemble into pentameric channels. Although the number of possible GABA$_A$R subunit combinations could be quite large, they are limited just to certain types of assemblies. The allowed combinations are based on different subunit complementarity and affinity to each other (Luscher et al., 2011). Most of the GABA$_A$Rs found in the CNS are composed of two α, two β and one γ (or δ/ε/π/θ) subunits (Fig. 1.1b) with a predicted β-α-β-α-γ subunit arrangement (as viewed counter-clock wise from the extracellular space) (Fig. 1.1c) (Olsen and Sieghart, 2008). The most prevalent type of GABA$_A$Rs was found to be α1β2γ2 heteromers (60%) followed by α2β3γ2 (15-20%) and α3βnγ2 (10-15%) types (Möhler, 2006; Möhler et al., 2002). There is an added layer of complexity, where two different α subunits can assemble to form an αβγ heteromer (Benke et al., 2004) or where a subunit encoding messenger ribonucleic acid (mRNA) is spliced into different variants (Whiting et al., 1990). Improperly folded receptor subunits are marked for degradation and do not reach the cell membrane (Luscher et al., 2011).

1.4. GABA$_A$R localization

GABA$_A$Rs are widespread in the CNS, however their individual subunits show specificity to particular brain regions or cellular location, which determines their function in neural circuits. Overall, GABAergic inhibitory activity in the CNS is defined by phasic and tonic inhibition (Brickley and Mody, 2012; Nusser and Mody, 2002). Synaptic GABA$_A$Rs have low affinity for GABA and respond to high concentrations of the neurotransmitter released in the synapses. Activation of such GABA$_A$Rs mediate the fast inhibitory postsynaptic potentials (phasic inhibition). Synaptic GABA$_A$Rs tend to composed of α(1/2/3), β(2/3) and γ(2/3) subunits. In particular, the γ2 subunit seems to be essential for GABA$_A$R heteromer localisation in synapses (Essrich et al., 1998). Overall, receptors of this type are widely distributed across the CNS. In contrast, GABA$_A$Rs with high affinity for GABA mediate constant tonic inhibition and are located extrasynaptically. GABA$_A$R heteromers contributing to tonic inhibition tend to contain α(4/5/6) and δ subunits. In particular, the heteromeric GABA$_A$Rs containing δ subunits are highly sensitive to GABA and show reduced rates of desensitisation, therefore they are the prime mediators of the tonic inhibition in the CNS (Brickley and Mody, 2012). In addition, such receptors tend to have distinct cellular localisation patterns, for example, α4βδ receptors are located in the forebrain, whereas α6βδ receptors are found in the cerebellar granule cells (Luscher et al., 2011).

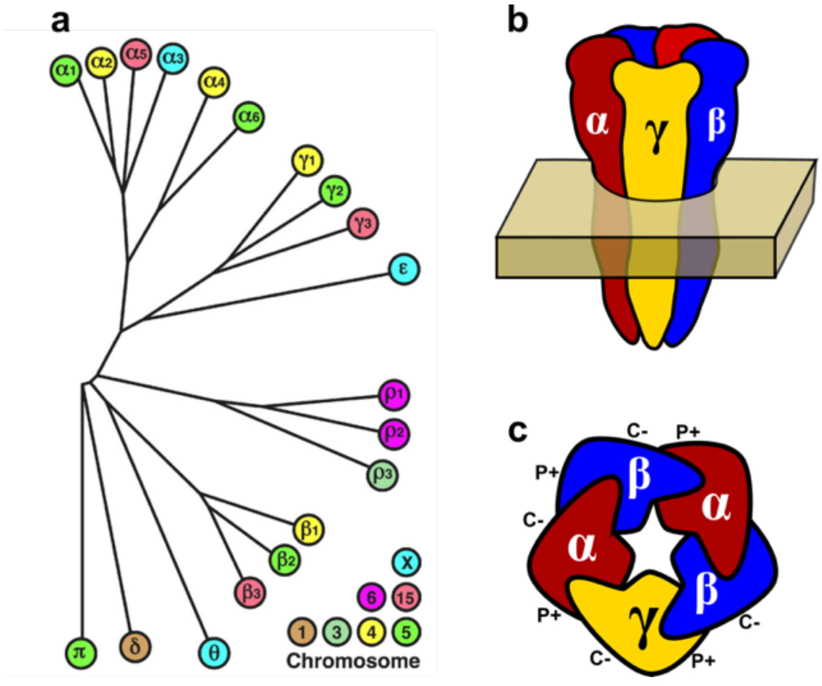

Figure 0.1 GABA$_A$R subunit diversity.

a, Phylogenetic tree for the 19 GABA$_A$ receptor genes (panel adapted from Sigel and Steinmann, J. Biol. Chem., 2012). **b,c,** Schematic representation of a heteropentameric GABA$_A$-αβγ receptor viewed from a side **(b)** and from the top **(c)**. Heteromeric GABA$_A$Rs are expected to adopt β-α-β-α-γ subunit order. Principal (P+) and complementary (C-) subunit faces are marked.

1.4.1. GABA$_A$ receptor architecture

To date, the only GABA$_A$R structure available is of human β3 homopentamer in a desensitised state (Miller and Aricescu, 2014). The crystal structure of the β3 homomer revealed that GABA$_A$Rs adopt a characteristic pLGIC architecture defined by a radial pentameric subunit assembly along the central ion channel pore, which forms a barrel-like overall structure (Fig. 1.2ab). pLGIC subunits are composed of an extracellular domain (ECD), transmembrane domain (TMD) and intracellular domain (ICD) (Fig. 1.2b). The ECDs are large N-terminal domains with a twisted β-sandwich structure composed of 10 β-strands (Fig. 1.2bc). Loops joining β-strands at the ECD have important functional roles in ligand binding and signal transduction to the TMD. For example, the sensor loop-C caps the orthosteric agonist GABA and allosteric modulator benzodiazepine binding sites at the β(P+)-α(C-) and α(P+)-γ(C-) interfaces, respectively. The β6-β7 loop, or the Cys-loop (named after the characteristic disulphide bridge in the loop) (Fig. 1.2c), is located at the bottom of the ECD, where it interacts directly with the TMD to transmit conformational changes to the pore. In addition, GABA$_A$R ECDs contain multiple N-linked glycosylation sites, and some of them might have stabilising structural roles related to agonist binding (Lo et al., 2010; Miller and Aricescu, 2014).

The TMD of GABA$_A$ receptors is composed of four transmembrane α-helices (termed M1-M4). The M2 α-helices are positioned towards the centre of the channel where they form a pore across the membrane (Fig. 1.2cd). The M2 helix amino acid make-up is similar across all Cys-loop receptors, where hydrophobic residues at the middle of the helix form a channel gate, whereas charged residues constitute an ion selectivity filter (Miller and Smart, 2010). The M2 helix is supported by the M1 and M3 α-helices from both sides and create a wall which separates the M2 from the lipids. Between the M1 and M3 α-helices from neighbouring subunits, there are small pockets accessible from the lipid bilayer. These are thought to be involved in modulation by small hydrophobic molecules like anaesthetics (Forman and Miller, 2011). The M4 helix is positioned at the outermost part of the TMD which is also thought to modulate the receptor function through interactions with lipids (Barrantes, 2015).

Finally, $GABA_AR$ ICDs are formed by loops between the M3-M4 transmembrane α-helices and range between 85-255 residues in length (Karlin and Akabas, 1995) (Fig. 1.2b). Overall, these loops are the least conserved domains and huge variations in sequence length are observed across different pLGICs (Tasneem et al., 2005). For example, *Gloeobacter violaceus* GLIC contains only 7 amino acid M3-M4 linker loop (Bocquet et al., 2007). The ICDs were shown to be not essential for ion channel gating function (Jansen et al., 2008). The ICDs are thought to act as platforms for interactions with intracellular proteins, regulatory phosphorylation and $GABA_AR$ synaptic trafficking (Boué-Grabot et al., 2003; Dumoulin et al., 2000). In addition, full-length nAChR (Unwin and Fujiyoshi, 2012) and mouse $5\text{-}HT_3$ receptor (Hassaine et al., 2014) structures show that ICDs contain α-helical fragments that interact with each other at the base of the pore. Such interactions might have an effect on the structural stability of the protein. However, due to a lack of structural information, it is not clear whether $GABA_ARs$ also have similar α-helical fragments or if their ICDs are completely disordered.

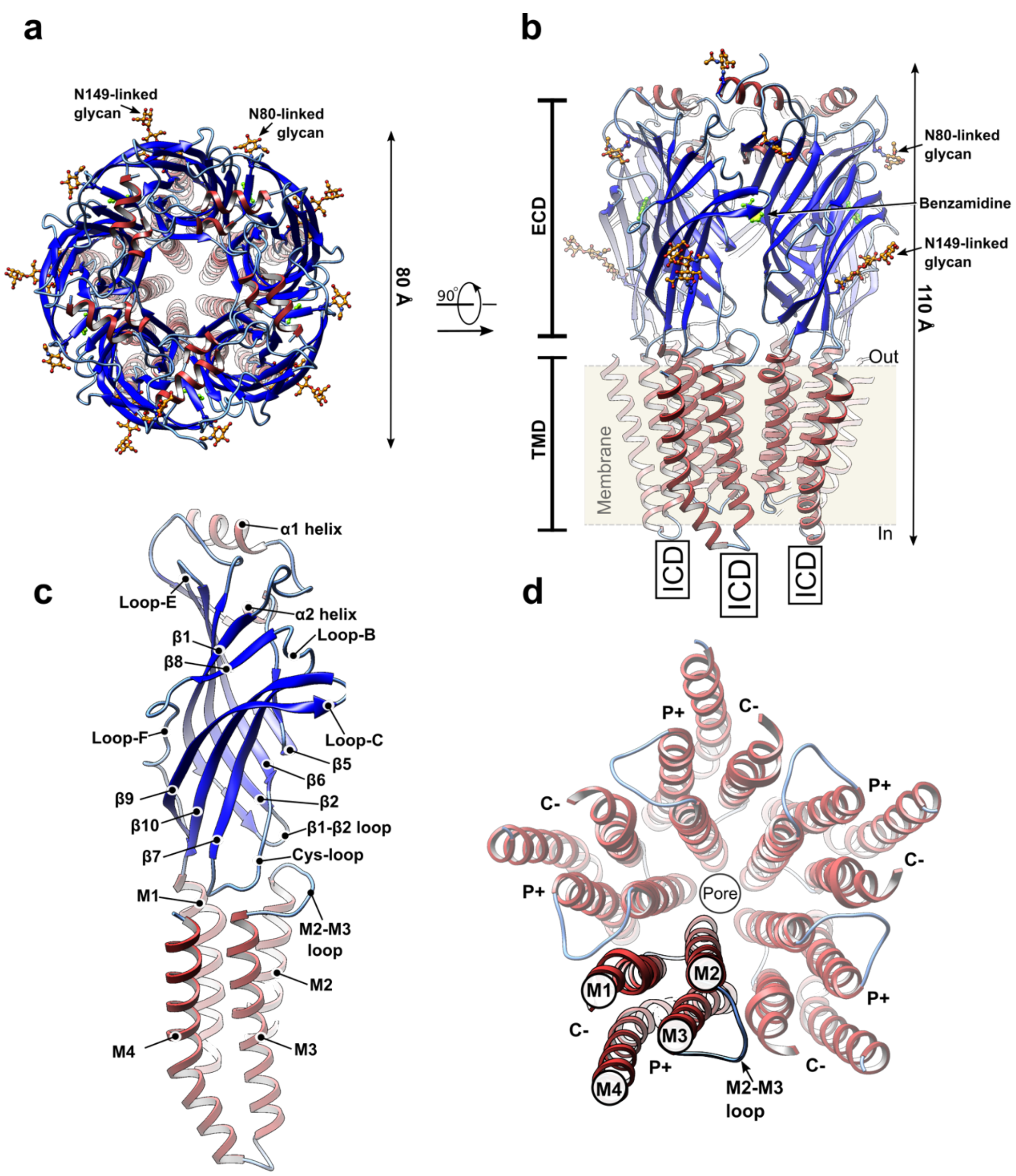

Figure 0.2 Architecture of GABA$_A$ receptors.

a,b, GABA$_A$R-β3 homomer (PDB 4COF) viewed from the extracellular space (**a)** and parallel to the membrane **(b)**. β-sheets are coloured in blue, α-α-helices in dark red, N-linked glycans in orange, agonist benzamidine in green. Note, M3-M4 loops (intracellular domains) were truncated for this protein to assist crystallisation. The ICD positions relative to the protein are marked with black boxes. **c,** Close-up of a single β3 subunit; view is parallel to the membrane. α-helix and β-strand numbering is shown. **d,** Close-up of the transmembrane domain revealing how the M1-M4 α-helical bundles form a pore across the membrane. Principal (P+) and complementary (C-) faces of the TMD are shown.

1.4.2. Agonist binding and channel gating

The neurotransmitter GABA binds to heteromeric GABA$_A$Rs at the β(P+)-α(C-) interface, underneath the loop-C of the β subunit. Using structural information from other pLGIC structures, it is possible to estimate what conformational changes might occur during GABA binding and how it opens the channel. One of the most complete studies regarding the pLGIC gating was performed for a zebrafish glycine receptor (GlyR) using cryo-EM (Du et al., 2015). This receptor was captured in three distinct conformations which, based on pore shape and estimated conductivity, corresponded to closed, open and partially desensitized states. These structures agree well with pore conformations observed in various other homomeric pLGIC structures solved to date (Althoff et al., 2014; Bocquet et al., 2009; Corringer et al., 2010; Hassaine et al., 2014; Miller and Aricescu, 2014; Ulens et al., 2014). I will use the GlyR structures to summarise below how agonist binding to homomeric pLGICs leads to pore opening and to subsequent desensitisation.

The GlyR neurotransmitter, glycine, binds to a pocket underneath the loop-C and causes it to adopt a "closed" conformation. Loop-C closure around the agonist induces flexure of the β-sheets, which leads to twisting of the ECD as a rigid body around the pore axis and tilting towards the centre of the channel (Fig. 1.3a). The ECD motion impacts on the TMD through the Cys-loop and the β1-β2 loop interactions with the M2-M3 loop of the transmembrane domain (Fig. 1.3a). This causes the transmembrane α-helical bundles to rotate outwards, counter-clockwise, as a rigid body, which leads to pore enlargement (Fig 1.3b). Hydrophobic residue side chains in the middle of the M2 (Leu227, 9′) move away from the centre of the channel and enabled the ion flow through the pore (Fig. 1.3d). During desensitisation, while agonist and allosteric modulator ivermectin were still bound, GlyR TMD α-helical bundles move as rigid bodies clockwise towards the centre of the channel (Fig. 1.3c). Pro266 at the bottom of the M2 α-helices (-2′) caused constriction of the pore almost fully closing it (5 Å radius) to Cl^- anion passage (Fig. 1.3d). A very similar pore configuration was observed for the desensitised GABA$_A$R-β3 homomer in complex with agonist benzamidine (Miller and Aricescu, 2014). When agonist dissociates from the pocket, the glycine receptor should return to the closed/resting state configuration.

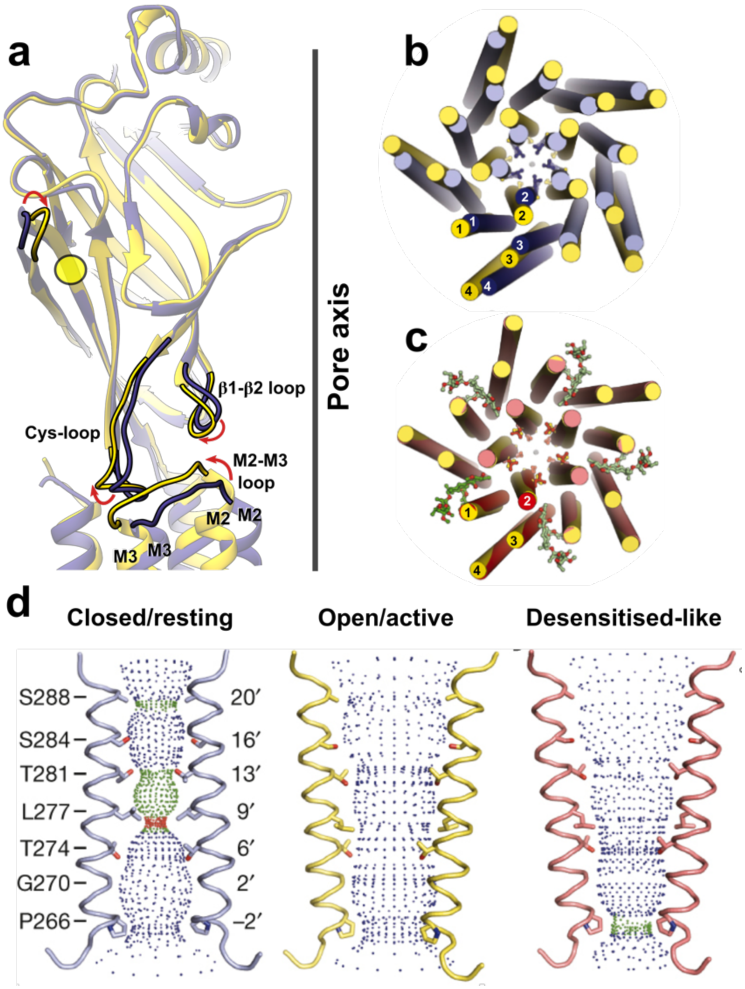

Figure 0.3 pLGIC gating mechanism

a, Superposition of closed state (PDB 3JAD, blue colour) and open state (PDB 3JAE, yellow) GlyR receptor structures determined by cryo-EM (Du et al., 2015). Bound agonist is represented as a yellow circle. Motions of loops involved in the ECD-TMD interface are highlighted with red arrows. **b,** Comparison between closed and open state GlyR TMDs. Agonist binding causes the TM α-helical bundle of each subunit to rotate outward in an anti-clockwise manner. This motion pulls hydrophobic side chains of Leu227 away from the pore axis, which enlarges the pore size and allows ion flow. **c,** Comparison between the open state and desensitised-like (coloured in red) structures. TMDs rotate so that the hydrophobic side chains of Pro266 come closer and constrict the pore. Ivermectin bound at the TMD interface is coloured in green. **d,** Shape of GlyR ion permeation pathway in different GlyR conformational states. Opposing M2 α-helices and pore lining amino acids are shown for closed/resting (blue), open (yellow) and desensitised-like (red) states. Blue, green and red spheres define pore radii of >3.3 Å, 1.8 – 3.3Å and <1.8 Å, respectively. Panels **(b-d)** were reproduced from Du et al., Nature, 2015, with the permission from Elsevier.

Most of the pLGIC structures solved to date are truncated homomers with five identical TMDs moving in unison when five binding sites interact with a ligand. Since the most common $GABA_A$ receptors are heteromers with distinct subunit interfaces, they are unlikely to follow exactly the same pattern of conformational changes discussed above. At the moment, the only gating study of a heteromeric full-length pLGIC was performed on nicotinic acetylcholine receptors (nAChRs) isolated from *Torpedo marmorata* electric organ (Unwin and Fujiyoshi, 2012). Closed-resting and agonist-bound nAChR states were imaged using electron microscopy. The comparison of the two states revealed that relatively small and asymmetric structural changes mediate the opening of the pore (Fig. 1.4). Acetyl choline binding to pockets at the α(P+)-γ(C-) and α(P+)-δ(C-) ECD interfaces resulted in β subunit TMD displacement (Fig. 1.4a) and flexure of the α subunit α-helices (Fig. 1.4b). The overall effect was pore dilation by 1Å. If this mechanism directly translates to the $GABA_AR$ heteromers, it would entail that the γ subunit is displaced and α M2 α-helices flex, however it remains to be seen if this might be the case.

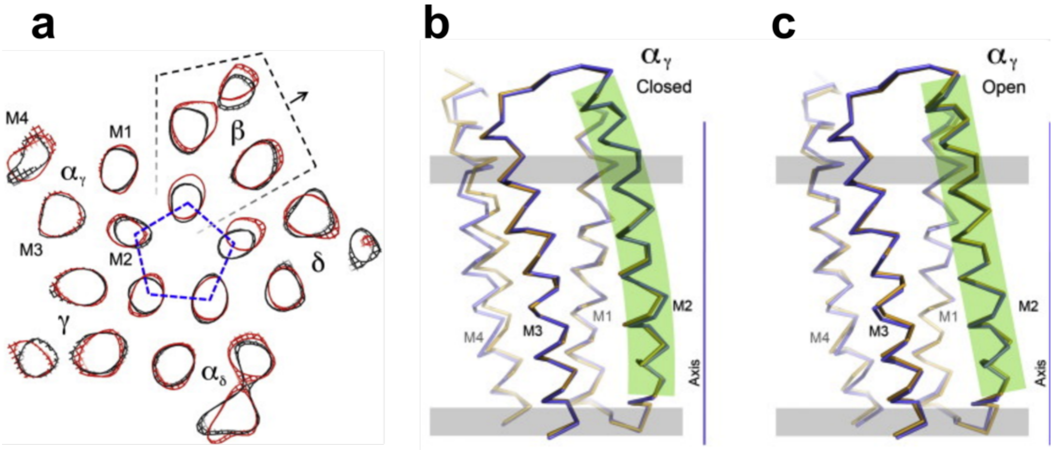

Figure 0.4 Conformational changes during heteromeric nAChR gating.

a, TMD cross-section showing β subunit displacement when open state (red) conformation is compared to closed state (black) conformation. **b,c,** α subunit M2 helix trajectory when channel is in closed-resting state **(b)** and in open state **(c)**. M2 helix is highlighted in green. Panels **(a-c)** were reproduced from Unwin and Fujiyoshi, J. Mol. Biol., 2012.

1.5. Pharmacology of GABAA Receptors

Malfunction of $GABA_A$ receptor signalling is implicated in various illnesses affecting the CNS such as anxiety and mood disorders, insomnia, schizophrenia and epilepsy (Möhler, 2006; Möhler et al., 2002; Smart and Paoletti, 2012). Various pharmacological agents targeting $GABA_A$Rs are used clinically to treat or ameliorate the symptoms of these disorders. Understanding how these drugs bind and modulate $GABA_A$R function at the atomic level could help to produce safer and more efficient therapeutic reagents.

1.5.1. Benzodiazepines

Benzodiazepines (BZs), such a diazepam or alprazolam, are positive allosteric modulators (PAMs) of $GABA_A$ receptors, which are widely administered as anxiolytics, anticonvulsants and sedatives-hypnotics. Benzodiazepines exert their function through enhancing the apparent $GABA_A$R affinity towards GABA (Rudolph and Knoflach, 2011). The benzodiazepine binding pocket is situated between the α and γ subunit ECDs, however this site is restricted to α1/2/3/5-subunit containing αβγ heteromers, due to substitution of a crucial histidine (e.g., α1His102) with arginine residues in α4/6 subunits (Minier and Sigel, 2004). $GABA_A$R α1 subunits seem to contribute to sedative actions of BZs, whereas the anxiolytic activity is mediated by α2-containing $GABA_A$Rs (Löw et al., 2000; Möhler et al., 2002). Tonic inhibition-mediating receptors, which contain δ subunits are insensitive to benzodiazepine action, since δ replaces γ subunits in these heteromers (Cope et al., 2005; Nusser and Mody, 2002). Better understanding of the benzodiazepine binding site would assist the design of new and more specific drugs with potentially less side effects like addiction and impairment of cognition (Richter et al., 2012; Uzun et al., 2010).

1.5.2. General anaesthetics

Most general anaesthetics, such as isoflurane, propofol and etomidate, act specifically on $GABA_A$ receptors to induce hypnosis, immobility and amnesia (Franks, 2008). Anaesthetics function as allosteric co-agonists where, at low concentrations, they increase the efficiency with which GABA activates

$GABA_A$Rs and, at higher concentrations, they can activate $GABA_A$Rs directly (Forman and Miller, 2011; Rüsch et al., 2004; Topf et al., 2003). It seems that most general anaesthetics modulate $GABA_A$R pore conformation by targeting a site which is proximal to the M2 15′ residue (Miller and Smart, 2010). In β3/2 subunits, 15′ residue is βMet256, which was shown to be crucial for activity of intravenous anaesthetics like propofol and etomidate (Jurd et al., 2002; Stewart et al., 2014). In heteromeric αβ and αβγ $GABA_A$Rs, numerous photolabelling experiments with photoreactive etomidate/propofol analogues and cysteine-substitution studies identified residues located nearby the M2 15′ site: βMet227, βVal290, βHis267, αMet236, αI239 (Bali and Akabas, 2004; Chiara et al., 2012; Li et al., 2010; Stewart et al., 2011, 2013a; Yip et al., 2013). There is evidence that inhaled anaesthetics, such as isoflurane, exert their activity through the equivalent 15′ sites in $GABA_A$R α subunits (αSer270) (Jenkins et al., 2001; Mihic et al., 1997; Nishikawa et al., 2002; Topf et al., 2003). This specific residue is situated in the M2 helix and faces a small pocket accessible from the membrane environment (Miller and Aricescu, 2014). It is therefore at an ideal position to transduce conformational changes to the pore upon small hydrophobic molecule binding. A better understanding on how general anaesthetics bind to this site and potentiate $GABA_A$Rs might contribute to development of new and safer drugs, reducing the complexity of anaesthesia maintenance (Vlassakov and Kissin, 2016).

1.5.3. Neurosteroids

Neurosteroids are endogenous allosteric modulators of $GABA_A$ receptors (Belelli and Lambert, 2005). Neurosteroids such as tetrahydroprogesterone (THP) and tetrahydrodeoxycorticosterone (THDOC) are metabolite products of the ovarian hormone progesterone and adrenal stress hormone deoxycorticosterone. They enhance $GABA_A$R activation by GABA at low concentrations and, at high concentrations, they cause direct activation (Hosie et al., 2006, 2009). Fluctuations in neurosteroid levels during the menstrual cycle affect neuronal excitability through enhancing GABAergic signalling, which can raise anxiety and elevate seizure frequency in women with catamenial epilepsy (Maguire et al., 2005). In addition, THP inhibitory modulation of α4βδ-containing $GABA_A$Rs increases level of anxiety during puberty (Shen et al., 2007). The neurosteroid binding mode in chimaeric pLGIC receptors with α1 and α5 $GABA_A$R TMDs has recently been determined by X-ray crystallography (Laverty et al., 2017; Miller et al., 2017). These structures revealed that neurosteroids bind at the lower portion of the transmembrane domain, in an external pocket between the M4 and M1 α-helices. Neurosteroid binding slightly deforms the interface between two subunits, which leads to pore enlargement (Forman and Miller, 2011). Neurosteroid-based pharmaceuticals have a potential to be used in clinical practice, for example the anticonvulsant ganaxalone is being developed to treat catamenial epilepsy as a THP replacement (Reddy and Estes, 2016; Reddy and Rogawski, 2009).

1.6. Aims of this work

Aims of this project were as follows:

- To generate a selection of llama nanobodies against α1 and β3 $GABA_AR$ subunits, and characterise their binding using biophysical techniques.
- To establish whether llama nanobodies can be used as crystallisation chaperones for homomeric $GABA_AR$-β3 receptors. If reproducible crystals diffracting to high resolution could be produced, crystal soaking experiments with drugs showing specificity to β3 subunits (general anaesthetics etomidate and propofol, as well as barbiturate pentobarbital) were to be performed.
- To test whether llama nanobodies can modulate $GABA_AR$ function.
- To establish whether llama nanobodies can be used as $GABA_AR$ subunit tags for reconstructing protein 3D volumes with cryo-electron microscopy.
- To obtain a 3D structure of a heteromeric human $GABA_A$ receptor.

2. Materials and methods

2.1. Molecular biology & cloning

2.1.1.Media and buffers

Luria-Broth (LB) and Terrific Broth (TB) media were prepared by dissolving commercially available powder (Thermo Fisher Scientific) in deionised water and autoclaved at 121 ºC. Buffers and solutions used in protein purification were filtered through 0.22 µm filter (Merck Milipore) to remove microbial contamination and undissolved salt particles.

2.1.2.Cloning and expression vectors

Table 1 Cloning and expression vectors

Plasmid	Notes
pMESy4	Phage display plasmid used for nanobody production in periplasm. Plasmid contains pelB secretion signal, ampicillin resistance marker, lac operon sequence. Protein expression is inducible with IPTG.
pET-45b	Bacterial expression for cytoplasmic protein expression. Plasmid contains ampicillin resistance marker, lac operator, T7 promoter. Protein expression is inducible with IPTG.
pHLsec	Mammalian expression vector for secreted proteins. It contains a chicken β-actin promoter, N-terminal protein secretion signal sequence, C-terminal His6 tag, rabbit beta-globin polyA signal and ampicillin resistance marker. Expression is non-inducible. Both secreted and membrane proteins can be produced using this plasmid.

2.1.3. Preparation of plasmid DNA

For DNA plasmid preparation, bacterial cells were transformed with the DNA of interest and transferred to 10 mL of LB medium for overnight growth at 37ºC. Cell cultures were collected by centrifugation (10 min, 1200xg) and plasmid DNA samples were extracted using commercial Qiagen QIAprep® Miprep kit according to manufacturer’s instructions. Alkaline lysis and DNA binding to silica (Boom et al., 1990) forms the basis for DNA purification in this commercial kit.

2.1.4.DNA digestion with restriction endonucleases

Digestion was performed by digesting 3-5 μg of vector/insert DNA with by 5 units of a particular restriction enzyme in a reaction mixture with a total volume of 10 μL. After 1-2 hours of incubation at 37°C, the reaction was stopped by adding 2 μL of TriTrack DNA loading dye (Thermo Fisher Scientific) and was either stored at -20ºC for future or used for gel extraction immediately.

2.1.5.DNA extraction from agarose gels

Agarose gels were prepared by dissolving 1% (w/v) of agarose powder in warm Tris-acetate-EDTA (TAE) buffer. Before gel solidification, SYBR® Safe DNA gel stain (Thermo Fisher Scientific) was supplemented in order to visualise the DNA bands. After running the DNA samples on 1% agarose gels, bands of interest were identified by illuminating with Safe Imager^{TM} (Thermo Fisher Scientific) at ~470 nm and cut out from the gel using and a clean scalpel. DNA from the resulting gel cubes were extracted using QIAquick® Gel Extraction kit (Qiagen) according to manufacturer’s instructions.

2.1.6.DNA fragment ligation

Insert and vector fragments extracted from agarose gels were joined by NEB Quick DNA ligase. Typically, 250 ng of vector DNA was mixed with 5-fold molar excess of the insert DNA and ligated using the QuikLigase (NEB) kit as recommended by the manufacturer. After the ligation, 5 μL of the reaction mix was used to transform DH5α™ Library Efficiency (Thermo Fisher Scientific) cells by heat shock.

2.1.7. Bacterial transformation by heat shock

Prior to use, bacterial cells were taken out of the -80 ºC freezer and gently thawed on ice. Aliquots of 3-5 μL containing 50-300 ng DNA were added to 30 μL of cells, gently swirled and incubated on ice for 30 min. Then competent cells were subjected to heat shock at 42 ºC for 45 s using a hot water bath. Tubes with bacterial cells were then returned to ice for 2 min, before adding 100 uL of SOC (Super Optimal with Catabolite repression) medium (Thermo Fisher Scientific). To allow bacterial cells to express antibiotic resistance genes, before plating on LB-agar plates with appropriate antibiotics, cells were incubated at 37 ºC for at least one hour with constant shaking (180 rpm).

2.2. Mammalian cell culture methods

2.2.1.Media and cultivation of HEK293 cells

Mammalian cells in adherent monolayer format were grown at 37 ºC in 175 cm^2 Corning® (Sigma) in an incubator providing ambient CO_2 levels of 5 %. Dulbecco's Modified Eagle Medium (DMEM, Sigma) supplemented with 1 % L-glutamine (Sigma), 1 % of non-essential amino acids (NEAA, Sigma) and 10 % of foetal calf serum (FCS, Thermo Fisher Scientific) was the primary medium for culturing HEK293T/S cells later to be used for transient transfection. For adherent monolayers of a full-length $GABA_AR$ α1β3γ2 stable cell line, DMEM F12 medium (Thermo Fischer Scientific) supplemented with 10 % FCS was used instead.

Mammalian cells in suspension cultures were grown in previously used (but sterile) DMEM medium bottles, shaken at 130 rpm rate (25 mm throw) with ambient CO2 levels of 8 % at 37 ºC in a Multitron (INFORS-HT) shaker. FreeStyle™ (Thermo Fisher Scientific) and Protein Expression Medium (PEM, Thermo Fisher Scientific) supplemented with 1 % L-glutamine, 1 % NEAA and 1 % of FCS were the main media used for suspension cell cultivation. Suspension cell densities were kept between 1-2×10^{-6} cells/mL.

2.2.2.Large scale transient transfection of suspension cells

GABA$_A$R homopentamers and heteromers were produced by transient transfection of HEK293S GnTI$^-$ suspension cell cultures. Freshly grown cells from 1L cultures (1.5×10^{-6} cells/mL) were pelleted by spinning down at 200xg for 5 min and then resuspended in 150 mL FreeStyle® medium (Thermo Fisher Scientific) supplemented with 3 mg PEI Max (Polysciences) and 1 mg of total plasmid DNA. For heteromer production, α:β=2:1 and α:β:γ=2:1:1 plasmid DNA ratios were used for preparing DNA mixes. After incubating cells with the transfection mix for 4-6 h, the cell volume was returned to 1 L by adding PEM medium containing 4 mM valproic acid and 5 mM sodium butyrate. Typically, cells were harvested 48 h post-transfection, frozen in liquid N2 and placed in -80 ºC freezer for long-term storage.

2.3. Protein purification and analysis methods

2.3.1.SDS-PAGE

Protein sample composition and purity was analysed by separating proteins based on their size via denaturing sodium dodecyl sulfate polyacrylamide gel-electrophoresis (SDS-PAGE). Protein samples were denatured using 2× Protein Gel Loading Buffer (PGLB, 100 mM Tris-HCl pH 6.8, 4% SDS, 20% (v/v) glycerol, 25% (v/v) β-mercaptoethanol, 0.05% bromophenol blue) for 5 min at 95ºC. The denatured samples were then loaded onto NuPAGE® Bis-Tris precast 4-12% polyacrylamide gels (Thermo Fisher Scientific) soaked with NuPAGE® MES SDS running buffer (Thermo Fisher Scientific) and separated by electrophoresis using in a XCell SureLock^{TM} electrophoresis system (Thermo Fisher Scientific) until the dye front ran out of the gel. The Precision Plus^{TM} Duo Color (Bio-Rad) protein standards were ran together with analysed samples for size reference. The protein was visualized by staining the gels with SimplyBlue^{TM} SafeStain (Life Technologies) and images of stained gels were recorded using Chemi-Doc (Bio-Rad) imager.

2.3.2. Western blotting

Western blotting was performed in order to identify individual protein bands in the SDS-PAGE gels. First, protein samples were separated by size on the SDS-PAGE gel before being transferred onto a polyvinylidene fluoride (PVDF) membrane (Amersham Biosciences) using an XCell II^{TM} Blot (Thermo Fisher Scientific) at 100 V for 75 min at 4ºC. Unspecific antibody binding to the membrane was prevented by blocking the membrane with 2.5% bovine serum albumin (BSA) solution in PBS + 0.1 % Tween 20 (PBST) for 1 h at room temperature or at 4ºC overnight. The membrane was then incubated with a primary antibody for 1h at room temperature followed by 3 x 5 min washes with PBST. Then the secondary antibody was added and incubated for 1h at room temperature followed by 3 x 5 min washes with PBST. Western blot was revealed by applying Amersham ECL western blot detection reagent (GE Healthcare) reagent and imaging with Chemi- Doc imager (Bio-Rad). The antibodies and dilution factors used in this work are summarized in table 2.

Table 2 Antibodies used in Western blot detection

Antibody target	**Antibody**	**Concentration**
His-tag	Mouse Penta-His antibody (Qiagen) Rabbit anti-mouse IgG HRP-linked antibody	1:5000 1:5000
Biotin / Streptavidin binding peptide (SBP)	HRP-streptavidin	1:10000
1D4 tag	Mouse Rho anti-1D4 antibody (University of British Columbia) Rabbit anti-mouse IgG HRP-linked antibody	1:10000 1:5000

2.4. Fluorescence-detection size-exclusion chromatography (FSEC)

Protein samples for FSEC were cleared by centrifugation (29,000xg, 15 min) and loaded onto a Superdex 200 or a Superose 6 3.2/30 column (GE Healthcare) equilibrated in a suitable gel filtration buffer and attached to a high-throughput liquid chromatography unit (Shimadzu) with automated liquid injection system, fluorescence detector and fractionator. Specific signals obtained from monoVenus (Ex/Em of 515/528 nm) or intrinsic Trp fluorescence (Ex/Em of 295/350 nm) allowed to screen multiple samples at low concentration. If needed, protein samples were collected into 100 uL fractions and further analysed using negative stain electron microscopy.

2.4.1.Llama nanobody purification

To produce nanobodies in bacteria, WK6su$^-$cells were transformed with ~150 ng of expression plasmid pMESy4 with the appropriate nanobody sequences and selected on LB-agar plates containing 2% glucose and ampicillin (100 µg/mL). A pre-culture was prepared by adding 3-4 colonies of transformed cells into 0.5 L Terrific broth (TB) cultures supplemented with 0.1 % (w/v) glucose, 2 mM $MgCl_2$ and 100 µg/mL ampicillin. Cultures were grown at 37 °C until an OD_{600} = 0.7 and then protein expression was induced with 1 mM IPTG. After the induction, cells were grown at 28 °C overnight and harvested by centrifugation (35 min at 5,000xg). The bacterial cell outer wall was broken using an osmotic shock buffer containing 0.2 M Tris pH 8.0, 0.5 mM EDTA, and 0.5 M sucrose to release nanobodies from the periplasm. Nickel affinity chromatography was used to capture nanobodies through their C-terminal 6xHis tag (binding buffer: 50 mM Hepes pH 7.2, 1 M NaCl, 10 mM imidazole; elution buffer: 50 mM Hepes pH 7.2, 0.2 M NaCl, 0.5 M imidazole), followed by size exclusion chromatography on a Superdex 75 16/600 column (GE Healthcare) equilibrated in 10 mM Hepes pH 7.2, 150 mM NaCl. Nanobodies were concentrated to 5-10 mg/mL, snap-frozen in liquid nitrogen and stored in -80 °C for future experiments.

2.4.2. Monomeric griffithsin production

The monomeric griffithsin construct used in this study was based on the 1GS-S construct described previously (Moulaei et al., 2010). A synthetic monomeric griffithsin 1GS-S construct with an N-terminal 10xHis tag followed by a TEV cleavage sequence was ordered from Eurofins Scientific. It was cloned into pET-45b vector. The protein was expressed using *E. coli* BL21 Star^{TM} (DE3) cells (Thermo Fisher Scientific). Bacterial cells were grown in TB (Thermo Fisher Scientific) supplemented with ampicillin (100 µg/mL) at 37 ºC until the O.D. reached ~0.8, then protein expression was induced with 1 mM IPTG. After 5 h of expression, cells were collected by centrifugation at 5,000xg for 25 min. The cell pellet of 1 L was resuspended in 30 mL of lysis buffer (50 mM Hepes pH 7.6, 500 mM NaCl, 10 mM imidazole) complemented with lysozyme (Sigma), cOmplete^{TM} EDTA-free protease inhibitors (Sigma) and lysed by sonication. Lysates were cleared by centrifugation at 30,000xg for 30 min at 4 ºC and the resulting supernatant was applied to Ni-NTA agarose (Thermo Fisher Scientific) in batch mode. It was left to rotate end-over-end for 1 h at room temperature. After protein binding, the IMAC resin was manually packed in a chromatography column and attached onto an Äkta FPLC system for purification. First, non-specific bound proteins were flushed off using Ni-A buffer (50 mM Hepes pH 7.6, 500 mM NaCl, 10 mM imidazole) and then washed with Ni-B buffer (50 mM Hepes pH 7.6, 150 mM NaCl, 400 mM imidazole) by increasing imidazole concentrations step-wise (30 mM, 50 mM). The eluted protein was dialysed overnight against size exclusion buffer (25 mM Hepes pH 7.6, 150 mM NaCl) supplemented with recombinant home-made TEV protease. TEV protease and uncleaved protein were removed with reverse binding to the Ni-NTA beads. Flow-through containing cleaved saposin-A was concentrated and injected onto a Superdex 200 Increase 10/300 GL column (GE Healthcare) using an Äkta FPLC system. After elution, peak fractions were pooled together, concentrated to 1.2 mg/mL, flash-frozen in liquid nitrogen and stored in -80 ºC for future use.

2.4.3. Large scale purification of GABA$_A$R-β3 homopentamer in detergent

All stages of GABA$_A$R-β3 (β$_{cryst}$ construct, refer to Chapter 2) purification were carried out on ice or at 4 ºC. Typically, 4 L of HEK293S GnTI$^-$ cells expressing GABA$_A$R-β3 homopentamer were lysed in 120 mL lysis buffer (40 mM Hepes pH 6.6, 300 mM NaCl, 1.5 % (w/v) decyl maltose neopentyl glycol

(DMNG, Anatrace) 0.15 % (w/v) cholesterol hemisuccinate (CHS, Anatrace) supplemented with 1 % mammalian protease inhibitors (Sigma) by rotating for 2 h. After detergent-mediated cell lysis, cellular debris was removed by centrifugation at 9,000xg for 15 min. Supernatant was collected and DMNG concentration was decreased to 1 % by adding dilution buffer (40 mM Hepes pH 6.6, 300 mM NaCl). After dilution, 4.0 mL of CNBr-activated sepharose beads (GE Healthcare) pre-coated with 25 mg Rho-1D4 antibody (termed 1D4 beads) was added and left to incubate for 2-3 h by end-to-end rotation. Later, beads were collected in a gravity flow column (Bio-Rad, inside diameter 2 cm). 1D4 beads were washed with 200 mL wash buffer WB1 (40 mM Hepes pH 6.6, 300 mM NaCl, 0.1 % (w/v) DMNG, 0.01 % (w/v) CHS), followed by 50 mL of wash buffer WB2 (40 mM Hepes pH 6.6, 300 mM NaCl, 0.007 % (w/v) DMNG, 0.0007 % (w/v) CHS). The protein was then eluted overnight using WB2 buffer supplemented with 500 μM 1D4 (TETSQVAPA) peptide. Eluted protein was applied onto the Superose 6 Increase™ 10/300 (GE Healthcare) size exclusion chromatography column equilibrated in 10 mM Hepes pH 7.2, 150 mM NaCl, 0.007 % (w/v) DMNG, 0.0007 % (w/v) CHS. The peak fractions were pooled together and the protein was mixed with selected purified nanobodies (10-fold molar excess) and concentrated to ~3.5 mg/mL using Vivaspin (Sartorius) centrifugal concentrators (100 kDa cut-off). The concentrated protein samples were treated with endoglycosidase F1(Chang et al., 2007) for 1 h at room temperature to reduce the heterogeneity arising from N-glycosylation. The protein was then immediately used for setting up vapour-diffusion crystallisation trays cryo-EM grid making or flash-frozen in liquid nitrogen for future use.

2.4.4. Large scale purification of GABA$_A$R-β3$_{K279T}$ homopentamer in detergent

GABA$_A$R-β3$_{K279T}$ homopentamer was produced in the same way as the β3$_{cryst}$ construct (see above), however CHS was not used and n-dodecyl 1-thio-β-maltoside (DDTM, Anatrace) was used instead of DMNG at all steps throughout the purification.

2.4.5. GABA$_A$R-β3 homopentamer reconstitution in amphipols

100 mg/mL amphipol A8-35 (Anatrace) stocks were prepared in deionised water, aliquoted and stored at -20 °C for future use. All reconstitution and purification steps were performed on ice or at 4 °C. GABA$_A$R-β3 homomer from 2 L of transient cell culture was extracted in DMNG as described in the Material and Methods section 7.4.3. Fractions from size exclusion chromatography containing monodisperse detergent-solubilised GABA$_A$R-β3 were pulled together and concentrated to 400 μL using using Vivaspin (Sartorius) centrifugal concentrators (100 kDa cut-off). Amphipol A8-35 was added to the concentrated protein at 1:8 (protein/A8-35, w/w) ratio and incubated for 2 h with constant agitation. This step allowed the amphipol to intermix with the detergent molecules. Then 40 mg of Bio-Beads (Bio-Rad) were added to the solution in order to remove detergents. After an over-night incubation, Bio-Beads were removed by applying the sample through a disposable column (0.5cm inner diameter) fitted with a filter (Bio-Rad). Aggregates in the flow-through were removed by centrifuging the sample for 15 min at 29,000xg. 10-fold molar excess of Nb25 was added and incubated for 30 min. Sample was then injected onto a Superose 6 Increase^{TM} 10/300 (GE Healthcare) size exclusion chromatography column equilibrated in 10 mM Hepes pH 7.2, 150 mM NaCl. Sample fractions with mAU$_{280}$=100 were approximately at 0.1 mg/mL concentration and were used directly for preparing cryo-EM grids.

2.4.6. GABA$_A$R-α1β3γ2$_{EM}$ construct design

Protein sequences used in this construct design: human GABA$_A$R-α1 (mature polypeptide numbering 1-416, QPSL…TPHQ; Uniprot P14867), human GABA$_A$R-β3 (mature polypeptide numbering 1-447, QSVN…YYVN; Uniprot P28472), human GABA$_A$R-γ2 (mature polypeptide numbering 1-427, QKSD…YLYL; Uniprot P18507). The α1 subunit intracellular M3-M4 loop amino acids 313-391 (RGYA…NSVS) were substituted by the SQPARAA sequence. Four residues located in the β3 ECD were replaced by β2 subunit residues (Gly171Asp, Lys173Asn, Glu179Thr, Arg180Lys), and the β3 intracellular M3-M4 loop amino acids 308-423 (GRGP…TDVN) were substituted by a modified SQPARAA sequence containing the soluble apocytochrome b(562)RIL (BRIL) (Chun et al., 2012), amino acids 23-130, ADLE…QKYL, Uniprot P0ABE7) to give an M3-M4 loop of sequence SQPAGT-BRIL-TGRAA. The γ2 intracellular M3-M4 loop amino acids 323-400 (NRKP…IRIA) were substituted by the SQPARAA sequence, and a C-terminal GTGGT linker followed by a 1D4 purification tag (TETSQVAPA).

2.4.7.Large scale purification of GABA$_A$R-α1β3γ2$_{EM}$

All purification steps were carried out on ice or at 4 °C. Cell pellets from 20 L of transiently transfected cells were solubilised in 600 ml buffer containing 20 mM HEPES pH 7.2, 300 mM NaCl, 1mM GABA, 1.5 % (w/v) DDTM (Anatrace), 1 % (v/v) mammalian protease inhibitor cocktail (Sigma) for 2 h at 4 °C. Supernatant was cleared by centrifugation (10,000xg, 15 min). The supernatant was diluted 2-fold in a buffer containing 20 mM HEPES pH 7.2, 300 mM NaCl and incubated for 2 h with 10 mL 1D4 beads. Samples were washed slowly by gravity flow over 1 hour at 4 °C with 200 mL buffer containing 20 mM HEPES pH 7.2, 300 mM NaCl, 1mM GABA, 0.1 % (w/v) DDTM (approximately 40 x CMC of 0.0026 %), 0.01 % (w/v) porcine brain polar lipid extract (Avanti; chloroform was evaporated under argon and the 100 mg lipid film was dissolved in 10 mL 10 % (w/v) DDTM (1000 mg) in water and stored at -80 C until needed). Protein bound to 1D4 beads was washed by slowly with 200 mL buffer containing 20 mM HEPES pH 7.2, 300 mM NaCl, 1mM GABA, 0.01 % (w/v) DDTM (approximately 4 x CMC), 0.001 % (w/v) porcine brain polar lipid extract for another 1 h. α1β3γ2 was eluted overnight in 15 mL buffer containing 15 mM HEPES pH 7.2, 225 mM NaCl, 750 µM GABA, 0.0075 % (w/v) DDTM (approximately 3 x CMC), 0.00075 % (w/v) porcine brain polar lipid extract, 500 µM 1D4 peptide (Genscript). The eluate was centrifuged (30,000xg for 15 min) and the supernatant was concentrated by centrifugation to 1-2 mL at 1-5 mg/mL using 100-kDa cut-off membranes (Millipore). The concentrated sample was centrifuged (30,000xg for 15 min) and the supernatant was aliquoted in 0.5-1.5 mg protein per 0.7 mL aliquots and either snap-frozen for storage at -80 °C or gel filtrated as appropriate. A single aliquot was loaded onto a Superose 6 10/300 Increase^{TM} size exclusion column (GE Healthcare) equilibrated in 10 mM HEPES pH 7.2, 150 mM NaCl, 1 mM GABA, 0.007 % (w/v)

DDTM. The eluted fractions were pooled and Nb38 was added at 4-fold molar excess and the complex was concentrated by centrifugal ultrafiltration to 2.5 mg/ml, using 100 kDa cut-off membranes (Millipore).

2.4.8. GABA$_A$R-α1β3γ2-FL purification

The full-length GABA$_A$R-α1β3γ2 receptor cells (HEK293S GnTI$^-$) were obtained from Professor Keith W. Miller laboratory (Dostalova et al., 2014a). Cells were grown to $\sim 1.5\times10^{-6}$ cell/mL density and induced with 3 μg/mL doxycycline for 18-28 h. At the induction stage, kifunensine was added to the medium at a final concentration of 0.8 mg/L to inhibit α-mannosidase-I activity and to enrich the oligomannose-9 (Man9) population as the main N-linked glycans for griffithsin binding (Chang et al., 2007). After expression, cells were pelleted by centrifugation (1,400xg, 7 min), flash-frozen and stored at -80 ºC until needed for purification. All stages of purification were carried out at 4 ºC. For a typical large scale purification, 1.6 L of cells were lysed in 50 mL lysis buffer (50 mM Hepes pH 7.8, 300 mM NaCl, 5 % (v/v) glycerol, 1.2 % (w/v) DDTM) supplemented with 1 % (v/v) mammalian protease inhibitors (Sigma) for 1.5 h. The lysate was cleared by centrifugation at 9,000xg at 4 ºC for 15 min. The supernatant was diluted with buffer containing 50 mM Hepes pH 7.8, 5 % (v/v) glycerol, 300 mM NaCl to decrease the DDTM concentration to 0.8 %. The protein was captured with 1.5 mL of 1D4 beads during 3 h incubation period. Afterwards, beads were washed with 200 mL wash buffer WB1 (50 mM Hepes pH 7.8, 300 mM NaCl, 5 % (v/v) glycerol, 0.1 % (w/v) DDTM) and 50 mL of wash buffer WB2 (50 mM Hepes pH 7.8, 300 mM NaCl, 5 % (v/v) glycerol, 0.01 % (w/v) DDTM). All washes were performed in batch mode using 15 mL falcon tubes (500xg centrifugation for 1 min). After washing, 1 mL of WB2 buffer supplemented with 800 μM 1D4 peptide was added to the beads for protein elution. In addition to the elution buffer, 60 μL of amphipol A8-35 (100 mg/mL) and 20 μL of bovine brain lipids (Sigma, 25 mg/mL, dissolved in 1% DDTM) were also added to the beads. Amphipols and lipids were allowed to intermix with the detergent belt around the protein for 2 h. Then 30 mg of Bio-Beads (Bio-Rad) were added for detergent removal overnight. The next day, the eluate was collected and cleared by centrifugation (29,000xg, 15 min). If necessary, Nb30 was added at 10-fold molar excess and incubated for 30 min before applying the sample onto a size exclusion chromatography column. Free amphipol and lipid molecules were removed by running a sample on a Superose 6 Increase^{TM} 10/300 column (GE Healthcare) equilibrated with 10 mM Hepes pH 7.8, 60 mM NaCl. The peak fractions containing were used directly to prepare negative stain and cryo-EM grids. Left-over protein was flash-frozen and kept in -80 ºC.

2.4.9.Small scale purification using Lipodiqs®

Pre-hydrolysed Lipodisq® Styrene-Maleic Acid Anhydride Copolymer 3:1 (Sigma) was dissolved in deionised water to prepare 6% (w/v) stock solution which was aliquoted and stored at -20 ºC for future use. All GABA$_A$R-β3 SMALP purification steps were performed on ice or at 4 ºC. Two samples containing 100 µL of cell pellet expressing GABA$_A$R-β3 were each resuspended in 500 µL of Resuspension Buffer (RB) buffer (50 mM Hepes pH 7.2, 400 mM NaCl, 1% (v/v) of mammalian protease inhibitors (Sigma), 10 U/mL of Benzonase® (Merck)). Cells were then lysed by adding 500 µL of 6 % (w/v) Lipodisq® solution to each sample and vigorously extruding the lysate through a 18G needle 10 times using a 5 mL syringe. The lysate was then incubated for 2 h with constant end-over-end agitation until nucleic acid digestion was complete and solution was clear and runny. Cellular debris were cleared by high speed centrifugation at 29,000xg for 1 h. The supernatant was carefully removed with 1 mL pipette and each sample was incubated with 20 µL of 1D4 beads for 3-4 h. After protein binding, beads were collected by centrifuging for 1 min at 300xg and supernatant was discarded. Then each tube with beads was resuspended with 1 mL RB buffer and centrifuged at 250xg for 30 s to discard the supernatant with unspecific contaminants. This washing step was repeated three more times. After washing, beads were combined into one tube and protein was eluted with 50 µL of Elution Buffer (50 mM Hepes pH 7.2, 150 mM NaCl, 500 µM 1D4 peptide) by gently shaking overnight. The eluate was then used directly to prepare negative stain or cryo-EM grids.

2.5. Biophysical protein interaction methods

2.5.1. Surface plasmon resonance – single cycle kinetics

SPR measurements were performed on a Biacore T200 (GE Healthcare) device at 25 °C temperature. All reagents and consumables for SPR work were purchased from GE Healthcare. The carboxyl groups on CM5 chip flow channels were activated with a 10 min injection of a 1:1 mixture of 0.1 mM N-hydroxysuccinimide (NHS) and 80 mM 1-ethyl-3-dimethylaminopropyl-carbodiimide (CDC). Streptavidin (Sigma-Aldrich) was covalently bound by a 5-minute injection until an immobilization level of 5000 RU was reached. Free activated carboxyl groups were quenched with a 10-minute injection of 1 M ethanolamine-HCl. The working flow-cell was functionalized by injecting biotinylated β3, α1β3 and α1β3γ2 $GABA_A$ receptors until 350-375 RU were reached, whereas the reference cell containing streptavidin was left unmodified. Running buffer contained 10 mM HEPES pH 7.5, 150 mM NaCl, 0.007% DMNG:CHS (5:1, w/w). To test the effect of GABA for Nb38 binding to α1β3γ2 $GABA_AR$, 1 mM GABA was supplemented to the running buffer. Measurements were performed by injecting nanobodies at concentrations ranging from 2.5 to 40 nM (2-fold increment serial dilutions) during a single cycle. For reliable SCK data fitting, the final dissociation phase was set to 15 minutes. Biacore T200 evaluation software was used to analyse all the SCK data. A 1:1 binding model was used to fit the experimental results.

2.6. X-ray crystallography methods

2.6.1. Crystallization and cryo-protection

$GABA_AR$ and nanobody complexes were crystallized using MemGold and MemGold2 screens (Molecular Dimensions) in SWISSCI 3-lens plates (Hampton Research) at 6 °C using sitting drop vapour diffusion method (Walter et al., 2005). Plates were prepared by mixing 100 nL of protein solution with the reservoir solution in ratios of 1:1, 2:1 and 1:2 with a Cartesian Technologies robotics system (Genomic Solutions). Reservoirs contain 30 µL of mother liquor. Crystal optimization was carried out by optimizing the pH and precipitant ratio of the particular condition of interest and by applying

MemAdvantage (Molecular Dimensions) additive screen (1:10 dilution to the reservoir). Before flash-freezing in liquid nitrogen, crystals were cryo-protected by adding a small volume of reservoir solution supplemented with either 20% PEG 400 or 30% ethylene glycol.

2.6.2. Crystal Soaking

For soaking experiments, the reservoir solution was supplemented with general anaesthetics (etomidate, iodo-etomidate, propofol and 4-bromo-propofol) to the total concentration of 1-10 μM. Then the reservoir solution containing anaesthetics was mixed with 30% ethylene glycol for cryo-protection. A small volume (0.3-0.5 μL) of this solution was added onto the droplet with crystals. Crystals were left soaking with etomidate for 0.5-4h with constant monitoring to ensure crystal morphology has not deteriorated. After incubation with drugs, crystals were collected and frozen in liquid nitrogen.

2.6.3. Data collection and processing

Diffraction images were collected at the Diamond Light Source synchrotron (DLS, UK) beamlines I02 and I24. Diffraction pattern indexing, integration and scaling was performed using HKL2000 (Otwinowski and Minor, 1997a). For the $\beta3\text{-Nb}25_{\text{ETM}}$ dataset, data merging was performed using AIMLESS (Evans and Murshudov, 2013). The $\beta3\text{-Nb}25_{\text{cryst}}$ structure was solved by molecular replacement, where the 3 Å $\text{GABA}_{\text{A}}\text{R-}\beta3$ structure (Miller and Aricescu, 2014) (PDB 4COF) and 1.1 Å gelsolin nanobody (Van den Abbeele et al., 2010) (PDB 2X1P) were used as search templates in Phaser (McCoy et al., 2007a). For the $\beta3_{\text{K279T}}\text{-Nb}25_{\text{Apo}}$ and $\beta3_{\text{K279T}}\text{-Nb}25_{\text{ETM}}$ structures, molecular replacement was performed using the 3.55 Å $\beta3\text{-Nb}25_{\text{cryst}}$ model. The initial structure refinement was performed with REFMAC (Murshudov et al., 2011), where rigid-body refinement was followed by jelly body refinement using secondary structure and non-crystallographic symmetry (NCS) restraints. Later the model was refined by iterative runs of BUSTER-TNT (Smart et al., 2012) and PHENIX (Adams et al., 2010) programs alternating with manual model building in COOT (Emsley and Cowtan, 2004). Refinement parameters included optimised target weight, NCS and secondary structure restraints. The

3.0 Å GABA$_A$R-β3 structure (PDB 4COF) was used as a high resolution reference model. Model quality at each iteration was evaluated using the MolProbity online server (Chen et al., 2010).

2.7. Cryo-electron microscopy (cryo-EM) methods

2.7.1. Sample preparation

Cryo-EM grids were glow discharged with Expanded Plasma Cleaner (Harrick Plasma) using the high tension setting before applying GABA$_A$R samples and plunge-freezing in liquid ethane with the VitroBot Mark IV (FEI) device. All samples, their composition and grid preparation parameters are summarized in table 3.

2.7.2. Graphene oxide grid preparation procedure

Graphene oxide grids were prepared based on the protocol described before (Bokori-Brown et al., 2016). Briefly, graphene oxide dispersion in water (Sigma) was diluted in deionised water 10-fold to reach 0.2 mg/mL concentration. Large aggregated graphene oxide sheets were cleared from the solution by a brief centrifugation run (300xg for 30s). Supernatant was carefully transferred to a fresh tube and was used for grid making. First, Quantifoil R1.2/1.3 (gold, 300 mesh) holey carbon grids were glow discharged using Expanded Plasma Cleaner (Harrick Plasma) at high tension setting for 1 min. Then 3 µL of graphene oxide solution was deposited onto a grid for 1 min. Excess of graphene oxide was blotted away with Whatman No1 filter paper and the grid side graphene oxide was washed once with 20 µL of deionised water. Grids were left for 10 min to dry in air at room temperature and were ready for use without any further treatment. Grids could be stored up to two months without any decrease in quality.

Table 3 Cryo-EM grid preparation parameters

$GABA_A$R Sample	Grid Type	Sample concentration (mg/mL)	Sample Volume (μL)	Glow Discharging (s)	Temperature (ºC)	Humidity (%)	Blotting Force	Blotting Time (s)
β3-Nb25 in DMNG	C-Flat™ R2/1, 300 Cu mesh	3.5	3.0	15	25	80-100	-25	2.0
$\alpha 1\beta 3\gamma 2_{EM}$ in DMNG ± DTT	C-Flat™ R2/1, 200 Cu mesh	2.8	3.5	12	25	80-100	-25	3.0
$\alpha 1\beta 3\gamma 2_{EM}$ in DDTM + pig brain lipids	C-Flat™ R2/1, 200 Cu mesh	3.2	3.5	12	25	80-100	-25	3.0-3.5
$\alpha 1\beta 3\gamma 2_{EM}$ in DDTM + porcine brain lipids + picrotoxin	C-Flat™ R2/1, 200 Cu mesh	4.2	3.5	12	25	80-100	-25	3.0-3.5
$\alpha 1\beta 3\gamma 2_{EM}$ in DDTM + pig brain lipids + picrotoxin	UltraAuFoil™ R1.2/1.3, 200 mesh	2.4	3.5	60	25	80-100	-15	7.5
FL-α1β3γ2 in A8-35 amphipols + bovine brain lipids	QUANTIFOIL® R1.2/1.3, 300 Gold mesh	0.1	3.5	15	14.5	95-100	-15	5.0-5.5
FL-α1β3γ2 in A8-35 amphipols + bovine brain lipids	Graphene oxide home-made grids	0.1	3.5	N/A	14.5	95-100	-15	8.0-12

2.7.3. Negative stain data collection and processing

Negative stain electron microscopy was used to evaluate protein sample quality and suitability for cryo-EM grid preparation. Continuous carbon grids (Cu 300 mesh, Agar Scientific) were glow discharged with Expanded Plasma Cleaner (Harrick Plasma) at high tension setting for 30 s and 4 μL of protein sample were applied. After 1 min incubation, protein samples were blotted away with a Whatman #1 filter paper and grids were washed twice in 50 μL ddH_2O before placing the grids onto a drop of 25 μL of 0.75 % (w/v) Uranyl formate (sample side down). After 30-40 s of staining, the excess of stain was blotted away with a Whatman #1 filter paper and grids were left to dry at room temperature for 5-10 min. Negative stain grids were imaged using a Tecnai T12 microscope (FEI company) operated at 120 kV and at a nominal magnification of 59,000× using an Eagle^{TM} 4k CCD camera (FEI), corresponding to a pixel size of 1.8 Å at the specimen plane. Reference-free 2D classification was used to average single particles and estimate the shape of a protein better. First, particles were picked in a semi-automated fashion using EMAN2 "swarm" feature and later 2D classified using Relion 1.4.

2.7.4. Cryo-EM data collection

All cryo-EM data were collected using a Tecnai F30 Polara (FEI Company, OPIC). Data collection parameters for different samples are summarized in table 4.

Table 4 Cryo-EM data collection parameters

	β3-Nb25$_{EM}$ in DMNG	α1β3γ2$_{EM}$ in DDTM + porcine brain lipids
Microscope	FEI TF30 Polara	FEI TF30 Polara
Detector	Gatan K2-Summit	Gatan K2-Summit
Voltage (kV)	300	300
Imaging mode	Counting	Counting
Slit (eV)	20	20
Other specs	GIF-Quantum energy filter	GIF-Quantum energy filter
Magnification	37,037	37,037
Pix size (Å)	1.35	1.35
Total Dose (e−/Å^2)	46	38
Exposure time (s)	10	14.1
Dose rate 1 (e−/Å^2/s)	4.60	2.70
Dose rate 2 (e−/pix/s)	8.38	4.91
Number of frames	25	47
Frame length (s)	0.4	0.3
Focusing range (µm)	-2.5 to -4.0	-2 to -3.5
Time used to collect data	48 hours	417 hours
Movies collected	1,016	8,587

2.7.5. GABA$_A$R-β3-Nb25 homopentamer data processing and model building

Movie frames 2-25 of the β3-Nb25$_{EM}$ data were motion-corrected using MotionCor2 (Zheng et al., 2017) using frame sub-division into 25 patches for the optimal local alignment. Frame 11 was used as a reference and electron dose-weighting scheme was applied to remove high resolution noise from frames with large cumulative electron dose. The aligned and dose-weighted (DW) micrographs were used for picking 3,000 particles by semi-automated algorithm in EMAN2 (Tang et al., 2007). These particles were 2D-classified using Relion (Scheres, 2012a) and the selected 2D classes were used for automated particle picking with Gautomatch (K. Zhang, MRC-LMB). False-positives or missing particles were manually removed from the auto-picked dataset to yield a total of 73,800 particles. Local CTF parameters were determined for each particle using Gctf v0.1.06 (Zhang, 2016). Spherical aberration (Cs) for Polara is 2.0, resolution range for CTF search was 4-80 Å, boxsize for CTF calculation was 512 pixels. The β3-Nb25$_{EM}$ dataset was processed using cryoSPARC software (Punjani et al., 2017) to generate the final 3D EM map. Particles were subjected to *ab initio* 3D classification where data was split between two models using C1 symmetry. Most of the particles were retained in a class which had the expected barrel-like shape of a Cys-loop receptor with five nanobodies bound to its ECD. The other class accumulated particles which could not align well. Particles belonging to the good *ab initio* class were selected for further 3D classification (multi-refinement protocol) to classify and refine the selected data into 5 classes using C5 symmetry. Three best classes from this 3D classification were then combined and the resulting 46,627 particles were subjected to *ab initio* classification into two classes again. This time only a small fraction of badly aligning particles was removed. The final 3D refinement was performed on 46,389 particles, which led to a refined structure at 3.94 Å. CryoSPARC automatically determined the optimal soft mask applied on the two half-maps before the Fourier shell coefficient (FSC) calculation as well as the B-factor used for map sharpening. Resolution estimation in cryoSPARC was based on the FSC criteria of 0.143.

2.7.6. GABA$_A$R-β3-Nb25 homopentamer model building

To build a model in the final map, the co-ordinates of 3 Å GABA$_A$R-β3 pentamer (PDB 4COF) and the nanobody Nb25 from the 3.25 Å crystal structure of β3$_{K279T}$-Nb25$_{Apo}$ were fitted into the electron density as rigid bodies using UCSF Chimera. The model was subjected to coordinate refinement with Rosetta (DiMaio et al., 2009) using Relax protocol. The refinement in Rosetta improved the model fitting in the map and reduced atom clash score. The model was further improved by adjusting co-ordinates manually with COOT and correcting the rotamers to match the higher resolution crystal structures. The final step of refinement was performed using *phenix.real_space_refine*. 4 macro cycles of global minimization refinement followed by 1 macro cycle of adp refinement were performed. Model was restrained by starting coordinate, secondary structure and Conformation-Dependent Libraries (cdl) restraints; geometry restraint files for N-linked glycans were also provided. N-linked glycan bond and angle restraint (.cif) files were generated using PRODRG server (Schüttelkopf and van Aalten, 2004). Model quality at each step of refinement were evaluated using Molprobity (Davis et al., 2007) and wwPDB validation server (Berman et al., 2003). For model validation, the final model coordinates were randomly displaced by 0.5 Å and then this model was refined against one of the half-maps produced by cryoSPARC. FSC curves were then calculated between the refined model and half-map used for refinement ('work') and between the second half-map, not used for refinement, ('free'). No significant separation between FSC$_{work}$ and FSC$_{free}$ curves indicates, indicating the model was not over-refined (Amunts et al., 2014).

2.7.7. GABA$_A$R-α1β3γ2 heteromer data processing and model building

A total of 8,548 movies were motion-corrected at micrograph level with UCSF MotionCorr (Li et al., 2013) and CTFFIND4 was used to estimate the contrast function parameters. Data processing was performed using RELION software package (Scheres, 2012b). First, ~5000 particles were picked using EMAN2 (Tang et al., 2007) and used as references for RELION automated particle picking. False-positives were manually removed leading to a dataset of 525,124 particles. Reference-free 2D classification was done and classes with GABA$_A$R features were selected (436,320 particles). An initial

3D model was generated from the β3$_{cryst}$ GABA$_A$R crystal structure (PDB ID: 4COF) and low-pass filtered to 40 Å resolution. Particles were grouped into a single 3D class with C5 symmetry, which was further 3D-classified using C1 symmetry by only allowing rotation around the symmetry axis. The best class showing features of two BRILs and two nanobodies was selected and used as a new initial reference model. Particles selected from 2D classes were 3D-classified into 10 classes using C1 symmetry. The best 3D volumes (186,786 particles) were used for particle 'polishing' step, where particle motion and radiation damage for particles from each movie frame was estimated. Refinement of the 'shiny' particles resulted in a 5.65 Å map. Movie motion correction with MotionCor2 (Zheng et al., 2016) using 25 patches and dose-weighting scheme improved the resolution of the refined map to 5.25 Å. These particles were further 3D-classified into 10 volumes. The best 9 classes were combined to yield a final map of 5.17 Å consisting of 165,621 particles. Map post-processed in RELION applies a soft mask on the half-maps along with correction for modulation transfer function of the K2 detector and sharpened using automatic B-factor estimation. Resolution was based on the FSC criteria of 0.143.

2.7.8. GABA$_A$R-α1β3γ2$_{EM}$ heteromer model building

The initial model for α1β3γ2$_{EM}$ GABA$_A$R was prepared with MODELLER (Eswar et al., 2006) using GABA$_A$R-β3 crystal structure as a starting reference (PDB 4COF). A related nanobody Nb25 (from 3.25 Å β3$_{K279T}$-Nb25$_{Apo}$ structure), was used as a template to produce the Nb38 model by manually mutating mismatching residues in COOT (Emsley and Cowtan, 2004). Nanobodies, α1β3γ2 GABA$_A$R ECDs and TMDs were docked into the 5.17 Å density map as rigid bodies using UCSF Chimera (Pettersen et al., 2004). The model was minimized with PHENIX (Adams et al., 2010) and Cα fitting was improved with Rosetta Relax protocol using the minimized starting model as a reference (DiMaio et al., 2009). Rotamers were manually adjusted to be the same as in GABA$_A$R-β3 crystal structure (PDB 4COF) and β3$_{ECD}$α5$_{TMD}$ chimera (PDB 5O8F), where possible. Then N-linked glycan moieties from 3.15 Å β3$_{ECD}$α5$_{TMD}$ chimera were docked into the model. The resulting model was further optimised by manual correction in COOT and iterative refinement in real space with *phenix_real_space_refine*. Reference model, secondary structure, Conformation-Dependent Libraries (cdl) restraints and geometry restraint files for N-linked glycan sugar moieties were used in this refinement. The stereochemistry of the final model was evaluated using MolProbity (Davis et al., 2007). The model was checked against over-refinement using half-maps and FSC function as in section 2.7.6.

3. Llama nanobodies as GABA$_A$R crystallization chaperones

3.1. Background

Several bottlenecks need to be overcome for the structural characterization of human GABA$_A$ receptors and their complexes with modulatory drugs or interacting proteins. In X-ray crystallography, the major hindrance is the difficulty of obtaining diffraction quality crystals. Production of well-diffracting membrane protein crystals is challenging because these proteins are extracted from native lipid bilayers and kept as soluble protein-detergent complexes. The detergent belt provides an environment with different physical properties than those found in the membranes, because of the dynamic exchange between free detergent monomers in solution and the detergent molecules in the belt around the protein (Bordag and Keller, 2010). Solubilisation in detergent often leads to decreased membrane protein stability and aggregation (Neale et al., 2013; Seddon et al., 2004). Therefore, a range of detergents and lipid additives needs to be tested to find the most thermostable protein-detergent complexes before crystallization trials can begin (Anandan and Vrielink, 2016; Hattori et al., 2012). Once the right detergent is identified, highly concentrated membrane proteins are subjected to crystallisation by the most commonly used vapour diffusion method (Delmar et al., 2015) or techniques exploiting lipidic phases (Deniaud et al., 2010). General physical laws governing protein assembly into ordered three-dimensional crystals are quite well understood but exact mother liquor formulations leading to well-diffracting crystals require exhaustive screening (McPherson and Gavira, 2014; Skarina et al., 2014). There have been efforts to analyse the available crystallographic data and create crystallization matrices specifically for membrane proteins (Parker and Newstead, 2012a, 2016). However, even well-tailored crystallization matrices might not help to overcome problems with membrane protein crystal packing, which are caused by the dynamic nature of the detergent/lipid environment and lack of extensive hydrophilic surfaces needed to form strong and stable crystal contacts. In some cases, even if a protein possesses large hydrophilic domains, crystallisation might not work due to the structural heterogeneity of N-linked glycans (Aricescu and Owens, 2013). The ECDs of human GABA$_A$Rs are quite sizeable and they have multiple glycosylation sites across various subunits (see Appendix 10.3). Post-purification deglycosylation fails to remove them completely as seen in the GABA$_A$R-β3 homopentamer structure.

(Miller and Aricescu, 2014). Taken together, these issues might explain the difficulties in crystallizing homomeric human $\mathrm{GABA_A}$Rs as opposed to bacterial Cys-loop receptors.

In order to increase the available hydrophilic surface at the ECD level and to provide a stable scaffold for crystal packing, antibody fragments can be employed as crystallization chaperones. A good example of such crystallization chaperones in the Cys-loop receptor field would be the glutamate-gated chloride (GluCl) (Althoff et al., 2014; Hibbs and Gouaux, 2011) and serotonin receptor (5-HT3) (Hassaine et al., 2014) structures where ECD-bound Fab fragments and camelid nanobodies, respectively, helped to crystallise these proteins. In both cases, antibody fragments extended away from the ECD and, by contacting the neighbouring receptor molecules, formed bridge-like structures so that the disordered detergent belt did not hinder crystal packing and a well-organised system was achieved (Fig. 2.1). In the case of the serotonin receptor, bridging nanobodies enabled protein packing even though it has a heavily glycosylated ECD (Fig. 2.1b). In contrast, the $\mathrm{GABA_A}$R-β3 homopentamer developed in our laboratory could be crystallised without the help of antibody fragments (Miller and Aricescu, 2014). However, this type of crystal was not reproducible and further investigation of $\mathrm{GABA_A}$R pharmacology by co-crystallisation or soaking with small modulator molecules could not be performed. It seems that lateral crystal packing of this protein could be improved by crystallization chaperones as in the case of GluCl and 5-$\mathrm{HT_3}$ receptors (Fig. 2.1c).

To conclude, development of antibody fragments targeting human $\mathrm{GABA_A}$ receptors would significantly increase the chances of structurally analysing these highly pharmacologically important channels by X-ray crystallography. The most effective and versatile antibody fragments for such work would be llama nanobodies, described in more detail in the section below.

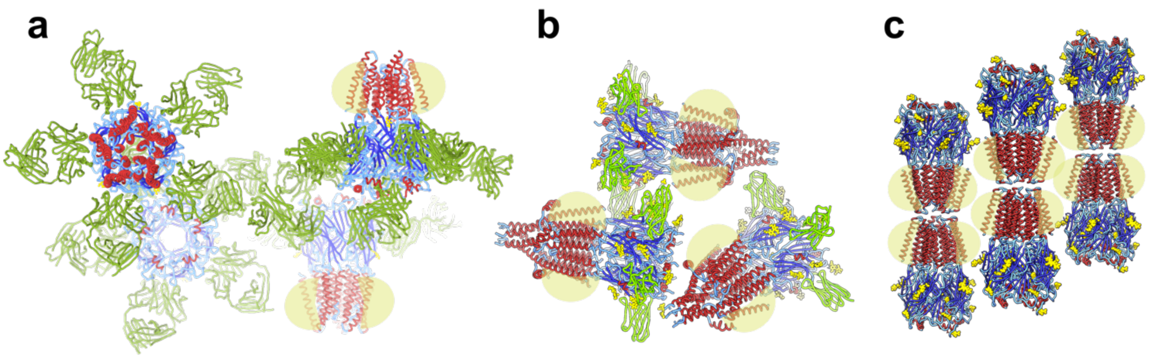

Figure 3.1 Crystal packing of Cys-loop receptors.

a,b, Crystal packing modes of nematode GluCl-Fab (PDB 3RHW) **(a)** and mouse serotonin (5-HT$_3$) receptor-nanobody (PDB 4PIR) **(b)** complexes. **c,** GABA$_A$R-β3 (PDB 4COF) crystal packing mode. α-helices are coloured in dark red, beta strands in dark blue, loops in light blue, Fab fragments and nanobodies in green and the detergent micelle was outlined in yellow green.

3.2. Llama nanobodies

Antibodies are immunoglobulin (Ig) fold superfamily members involved in antigen recognition as part of the vertebrate immune response. A conventional antibody has two identical light chains (~25 kDa) and two identical heavy chains (~50 kDa), which associate through covalent and non-covalent bonds to form a Y-shaped functional unit (Fig. 2.2a) (Schroeder et al., 2010). The light chain is made of 2 Ig fold domains, whereas the heavy chain is composed of 4-5 of Ig fold domains depending on the antibody type. The N-terminal Ig fold domains of light and heavy chains have hypervariable loops and together they form an antigen binding surface (designated V$_L$ and V$_H$, repectively), whereas the rest of the Ig domains are conserved and form the antibody scaffold (denoted as constant heavy or light chain domains, C$_H$ or C$_L$, respectively) (Fig. 2.2a). Interestingly, camelids (llamas, alpacas, guanaco, camel, dromedary) and cartilaginous fish (shark, chimera, ray) possess an additional class of antibodies which are only formed from two heavy chains (Flajnik et al., 2011) (Fig. 2.2b). Each of the heavy chains have a single Ig-fold domain with hypervariable loops capable of antigen binding (designated V$_H$H). Llamas possess two heavy chain-only antibody isotypes, Ig2 and Ig3, both differing in the length of the linker between V$_H$Hs and the constant domains of the heavy chain (Fig. 2.2b) (Muyldermans, 2013). V$_H$Hs can be cloned and expressed in high yields as small (~15 kDa) and soluble single domain fragments retaining the antigen binding capacity of the original heavy chain-only antibodies (Pardon et al., 2014). Due to their small size and ability to bind antigens, V_HHs were termed nanobodies. They have the typical beta sheet sandwich shape of immunoglobulins with three complementarity determining regions (CDR1-3) responsible for binding to antigens (Fig. 2.2c). CDR3 is the largest of the three loops and it normally mediates the majority of interactions between the nanobody and the antigen. As conventional antibodies evolved into heavy chain-only antibodies, four hydrophobic residues, positioned at the interface between the light and heavy chains, mutated into polar residues, improving the solubility of the V_HHs (Muyldermans, 2013; Vu et al., 1997).

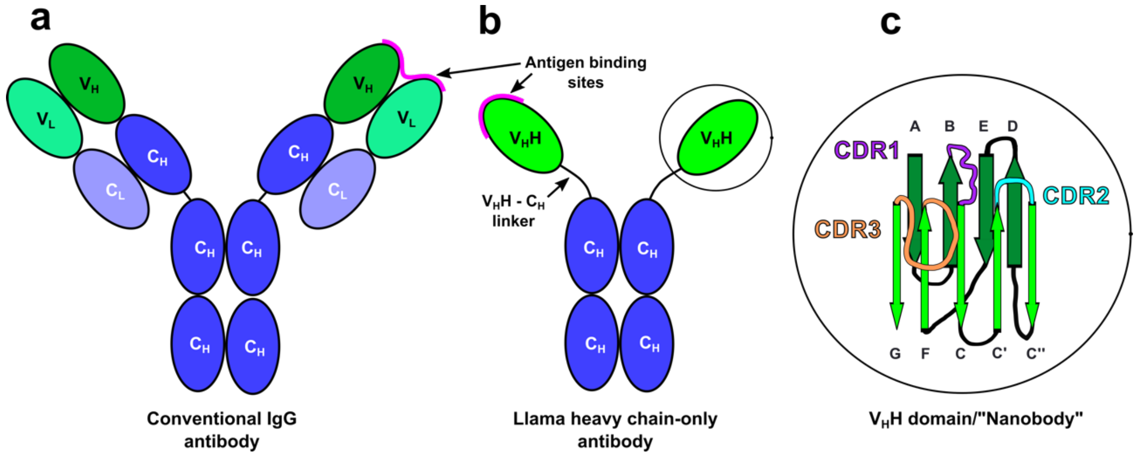

Figure 3.2 Conventional and llama heavy chain-only antibody types.

a, Schematic representation of a conventional IgG antibody. Constant light and heavy chain domains are denoted as C_L and C_H, respectively. Variable light and heavy chain domains are named V_L and V_H, respectively. **b,** Schematic representation of llama heavy chain-only antibodies. Variable heavy chain domain is denoted as V_HH to distinguish it from conventional antibody V_H. Conventional antibodies possess concave binding clefts in contrast to convex antigen binding surfaces in the llama V_HHs. **c,** A structure of a llama V_HH or a nanobody. It is comprised of 9 β-strands (A-G) joined by loops, three of which are variable and can recognise foreign antigens (CDR1-3).

Many nanobody qualities make them excellent crystallization chaperones (Traenkle et al., 2016). They tolerate variable pH values, are thermostable and extremely soluble, thus unlikely to crystallise on their own. Due to the long variable loops, nanobodies can target cryptic antigen sites, which normally are not accessible to flat paratopes of conventional antibodies. Nanobodies are capable of recognizing and stabilizing specific conformational states of a target protein. For example, conformation-specific nanobodies were used to capture the active state structure of the β2 adreno receptor (Rasmussen et al., 2011; Ring et al., 2013) and the semi-closed state of mouse 5-HT$_3$ receptor (Hassaine et al., 2014) by X-ray crystallography. Due to their high affinity and conformational specificity, nanobodies can be used for multiple therapeutic applications such as drug delivery systems targeting malignant cells, acting as immune system modulators or anti-microbial agents (Van Bockstaele et al., 2009; Detalle et al., 2015; Hassanzadeh-Ghassabeh et al., 2013; Rissiek et al., 2014). Importantly, nanobodies can to cross the blood-brain barrier (Abulrob et al., 2005; Li et al., 2012), which might allow targeting proteins in the CNS, such as GABA$_A$Rs.

The robust properties and multipurpose nature of nanobodies would make them a valuable tool in GABA$_A$R research. In this chapter I will focus on our efforts to use llama nanobodies as crystallization chaperones for human GABA$_A$ receptors.

3.3. Expression and purification of llama nanobodies

To facilitate GABA$_A$R structural studies, we raised llama nanobodies against human GABA$_A$ receptor α1 and β3 subunits in collaboration with Prof. Jan Steyeart (Vrije University of Brussels, Belgium). The nanobody production pipeline employed in this laboratory was described before (Pardon et al., 2014). Briefly, a single llama ("Pipette") was immunized with ~100 μg of detergent-solubilized GABA$_A$-α1β3 receptor over a period of several weeks. Peripheral blood samples were extracted from the llama and V$_H$H fragment cDNA library was produced. Antigen-specific nanobodies were selected by phage display and ELISA panning assays, using the detergent-solubilized GABA$_A$-α1β3 receptor as the binding target. In total, 18 nanobody cDNA sequences were identified to code for nanobodies showing binding to the detergent-solubilized GABA$_A$-α1β3 receptor. These sequences can be classified into 16 families based on the CDR3 amino acid similarity and, thus, the likely ability of binding to the same epitope. Nanobody sequence alignments and family table is in the Appendix section 10.1 and 10.2. Nanobodies were expressed in bacterial cells using methods as described in Materials and Methods. Briefly, after nanobody expression into bacterial periplasm, the outer bacterial cell membrane was broken using high concentration sucrose buffer. Cellular debris were spun down by centrifugation and nanobodies were affinity-purified through a C-terminal 6xHis tag, followed by a size exclusion chromatography on a Superdex 75 16/600 column. Nanobodies eluted in homogeneous, monodisperse peak and had no other contaminants (Fig. 2.3)

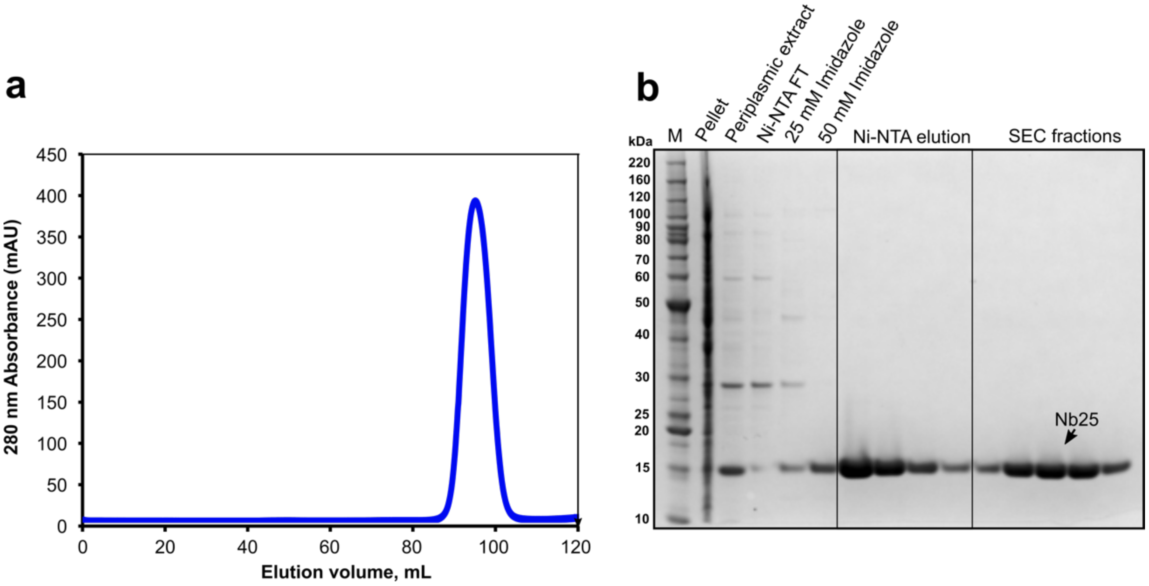

Figure 3.3 Llama nanobody purification.

a, Size exclusion chromatogram (Superdex 75 16/600) of a representative nanobody Nb25. **b,** SDS-PAGE gel with samples from different purification stages of a representative nanobody Nb25.

3.4. Nanobody selectivity and binding characteristics

The capacity of nanobodies to bind to human GABA$_A$ receptors was initially screened using fluorescence size exclusion chromatography (FSEC). Nanobody genes were cut from the original pMES4y vector and transferred to the pHLsec-Nt-mV vector, which introduced a monoVenus (mV) fluorescence tag (Nagai et al., 2002) on the N-terminal end of the nanobodies. mV-tagged nanobodies were then expressed in HEK293T cells and secreted into the growth medium using a small scale 6-well plate format. GABA$_A$-β3 homopentamer and α1β3 heteromer receptors with truncated ICDs were purified in detergent as described in Materials and Methods. Small amounts of these samples were mixed with media containing mV-nanobodies. After 1 h incubation, the GABA$_A$R and mV-nanobody mixtures were tested by FSEC for complex formation. Samples were loaded on Superdex-200 3.2/300 size exclusion column and fluorescence signal for mV-nanobodies was recorded. The initial screening revealed that most nanobodies bound to GABA$_A$-β3 homopentamer receptor and migrated together during size exclusion experiments (Fig. 2.4a). The apparent strength of this binding seemed to vary between nanobodies (Fig. 2.4a). In addition, the screen revealed that there were two nanobodies (Nb30 and Nb38) which showed no binding to β3 homopentamers but only to α1β3 heteromers, indicating that they are α1 subunit-specific (Fig. 2.4b). In order to obtain more detailed nanobody binding characteristics, surface plasmon resonance (SPR) single cycle kinetics (SCK) was used (Ring et al., 2013). Single cycle kinetics methodology was chosen over the equilibrium steady state analysis, since nanobodies tend to have very high binding affinities and slow dissociation rates. Otherwise, harsh chip regeneration conditions needed for multiple analyte concentration injections would inactivate surface-immobilized GABA$_A$Rs. Biotinylated versions of β3 homopentamer and heteromeric α1β3 and α1β3y2 receptors were purified in detergent and immobilized on an SPR chip through streptavidin capture as described in Materials and Methods. Five different concentrations for each selected nanobody were injected sequentially over the chip to perform the single cycle kinetics measurements (Fig. 2.4c,d). Affinity and kinetic data for tested nanobodies is shown in table 5. Nanobody binding affinities were in the range of 240 pM to 30 nM. Based on the SPR results, the highest affinity binders were selected for crystallization trials of the GABA$_A$-β3 homopentamers.

Table 5 Characterization of selected nanobody binding to GABAA receptors by SPR single cycle kinetics

GABA$_A$R-α1β3 (α1-specific)

Nanobody	K_D(M)	Dissoc. half-life (min)	k_{on} (1/Ms)	k_{off}(1/s)	Rmax (RU)	Chi^2 (RU^2)
Nb38	1.1E-09	4.2	2.5E+06	2.8E-03	54.3	0.4
GABA$_A$R-β3 (β3-specific)						
Nb25	8.5E-10	16.0	8.5E+05	7.2E-04	160.5	2.2
Nb27	3.5E-09	2.4	1.4E+06	4.9E-03	228.3	6.8
Nb29	3.8E-10	89.6	3.4E+05	1.3E-04	174.3	5.7
Nb32	3.7E-09	4.8	6.6E+05	2.4E-03	160.1	5.3
Nb37	3.1E-08	2.7	1.4E+05	4.2E-03	164.6	1.4
Nb41	1.7E-09	14.5	4.7E+05	8.0E-04	172.7	6.5
Nb42	3.1E-09	59.5	6.3E+04	1.9E-04	112.0	0.5

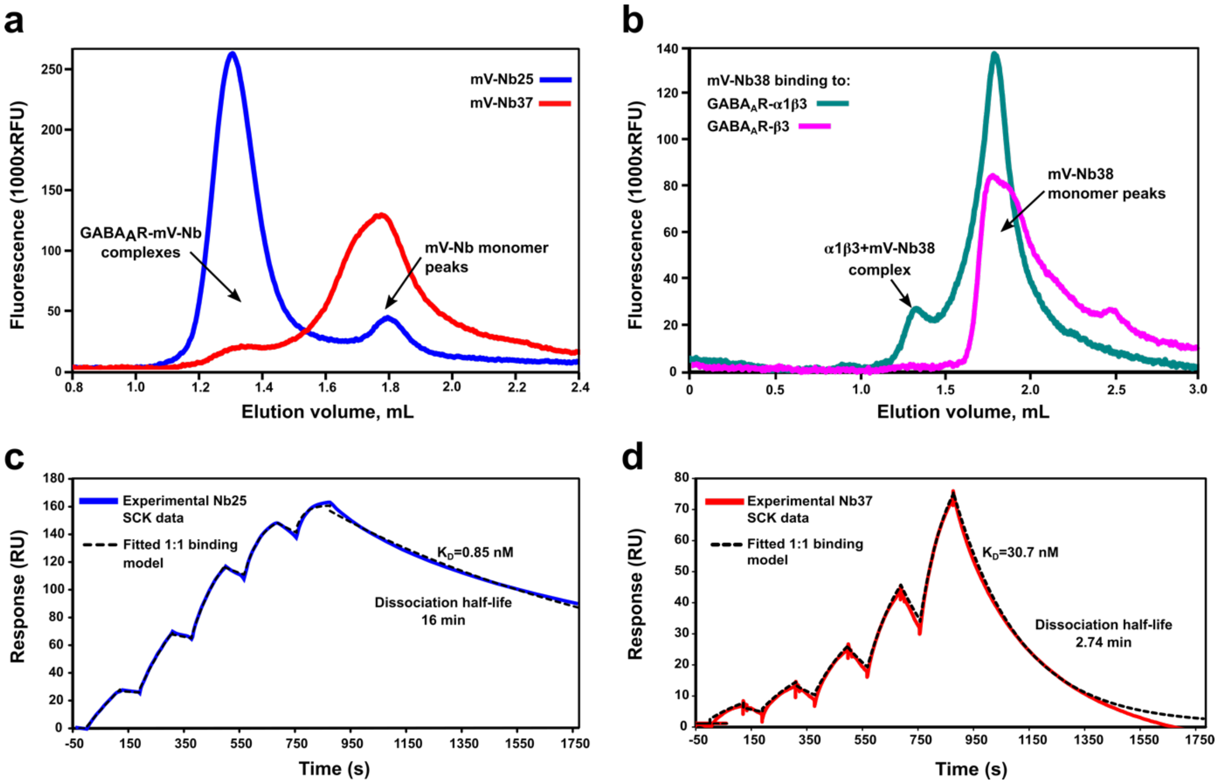

Figure 3.4 Biophysical characterisation of nanobody binding to human GABA$_{A}$ receptors.

a, Representative FSEC fluorescence traces of a monoVenus-tagged nanobody binding to GABA$_{A}$R-β3 homopentamer with high (mV-Nb25, blue trace) and low (mV-Nb37, red trace) affinities. **b,** FSEC fluorescence traces for a nanobody Nb38, which binds preferentially to GABA$_{A}$R-α1β3 over GABA$_{A}$R-β3, indicating it is an α1 subunit-specific nanobody. **c-d,** Surface plasmon resonance single-cycle kinetics sensograms of nanobodies binding to an immobilised GABA$_{A}$R-β3 homopentamer with high (Nb25) **(c)** and low affinities (Nb37) **(d)**.

3.5. GABA$_{A}$R-β3 purification and sample preparation for crystallization

For crystallisation trials I employed a GABA$_{A}$R-β3 construct, which was described before (Miller and Aricescu, 2014). This construct is a codon optimised version of the full-length human GABA$_{A}$R-β3 subunit sequence (GenBank accession No M82919), where the intracellular loop connecting M3 and M4 α-helices (Gly308-Asn421) was replaced by an SQPARAA linker (Jansen et al., 2008). For purification purposes, the construct contains a C-terminal TETSQVAPA sequence recognised by 1D4 monoclonal antibody (Molday and MacKenzie, 1983). The product of the construct is a functional

GABA$_A$R-β3 homopentamer, which responds to modulation by histamine and propofol (Miller and Aricescu, 2014).

To produce sufficiently large amounts of GABA$_A$R-β3 homopentamer for crystallisation, HEK293S GnTI$^-$ cells growing in suspension were transiently transfected with pHLsec-GABA$_A$R-β3 (Aricescu et al., 2006; Miller and Aricescu, 2014). 48 h post-transfection, HEK293S cells were collected and directly lysed with detergent. To increase the GABA$_A$R-β3 yield for more throughput crystallisation trials, I screened for the optimal pH value during the protein extraction step using small scale batch purification and FSEC. I found that lowering the extraction buffer pH from 7.2 to 6.6 yields ~15% more protein (Fig. 2.5a). Detergent-solubilised protein was then captured via the C-terminal 1D4 tag using affinity purification, which was followed by the size exclusion chromatography polishing step (Superdex-200 10/300, GE Healthcare) using 10 mM Hepes pH 7.2, 150 mM NaCl gel filtration buffer. GABA$_A$R-β3 eluted in a largely monodisperse peak (Fig. 2.5b). Peak fractions were pooled and 10-fold molar excess of a particular nanobody was added. After 30 min incubation protein was concentrated to 3.5-4.0 mg/mL using centrifugal concentrators. The concentrators had a 100 kDa molecular weight cut-off, therefore most of the unbound nanobodies passed through the filter with a small excess present in the final volume. This ensured that some free nanobody would always be present in the solution to occupy all the binding sites. Due to the high nanobody solubility, it is unlikely that such free nanobodies would crystallize on their own. The concentrated sample was deglycosylated and used for crystallization trials (Fig 2.5c).

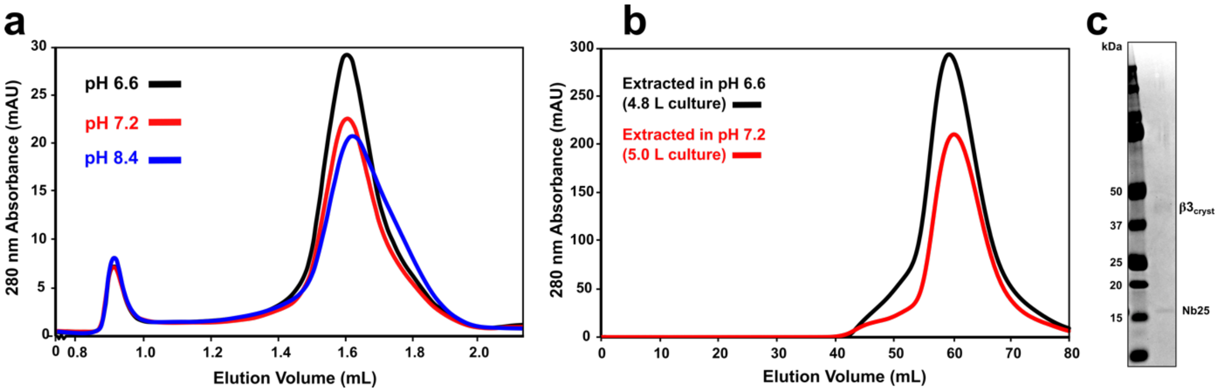

Figure 3.5 Optimizing GABA$_A$R-β3 homopentamer purification.

a, Size exclusion chromatograms of small scale GABA$_A$R-β3 homopentamer samples extracted at different pH values. **b,** Size exclusion chromatograms of large scale GABA$_A$R-β3 homopentamer purification samples extracted at optimal pH 6.6 and previously used pH 7.2. **c,** GABA$_A$R-β3 and representative nanobody (Nb25) sample for crystallization trials analysed on the SDS-PAGE gel.

3.6. Initial crystallization trials and optimization

Initial crystallization trials were performed for GABA$_A$R-β3 homopentamer in complex with Nb25, Nb29, Nb41 & Nb42 nanobodies. MemGold and MemGold II crystallisation screens (Newstead et al., 2008; Parker and Newstead, 2012b, 2016) were used to set up vapour diffusion crystal plates at room temperature or at 6 °C. In 5-30 days, multiple crystals appeared in various conditions for all tested samples. Crystals were harvested and their diffraction was tested at the Diamond Light Source synchrotron, UK. All crystals diffracted to at least 10 Å, while the best diffracting crystals were from samples were nanobody Nb25 was used (~5.0 Å). As the most promising sample, the GABA$_A$R-β3-Nb25 complex was chosen for further crystallisation screening. Optimal precipitant concentration and pH range was tested together with small molecule additive screens for membrane proteins (Parker and Newstead, 2012b).

3.7. Crystal structure of GABA$_A$R-β3-Nb25

3.7.1. Crystallization, structure solution and refinement

The optimized GABA$_A$R-β3-Nb25 crystals were grown in 100 mM Hepes pH 7.6, 200 mM choline chloride, 16 % PEG 2000 MME and 20 μM picrotoxin (channel blocker) at room temperature. Crystals were soaked in cryo-protection solution (mother liquor with 10% PEG-400) and dehydrated using an ambient humidity-controlling device (Sanchez-Weatherby et al., 2009) at 5% decreasing humidity steps (from 100% to 75%). Crystals were then flash-frozen in liquid nitrogen. Diffraction data were collected at 100K at beamline IO2 at the Diamond Light Source, United Kingdom. Data for one crystal, which was dehydrated to 85%, was processed using the HKL2000 package (Otwinowski and Minor, 1997b) to 3.55 Å resolution. The structure was solved by molecular replacement (MR) using PHASER (McCoy et al., 2007b) where GABA$_A$R-β3 homopentamer (PDB 4COF) and gelsolin nanobody (PDB 2X1P) served as search models. The structure was refined via iterative rounds of autorefinement with BUSTER (Smart et al., 2012), atomic position, B-factor and TLS refinement with PHENIX (Adams et al., 2010) and manual building using COOT (Emsley and Cowtan, 2004). The 3 Å GABA$_A$R-β3 homopentamer structure was used as a reference during the refinement to restrain the model towards a more stereochemically correct solution. Crystallographic data collection and model refinement statistics are summarized in table 6.

3.7.2. GABA$_A$R-β3-Nb25 crystal structure

The X-ray structure revealed that one GABA$_A$-β3 receptor was bound to five Nb25 nanobodies which were extending outwards from the ECD (Fig. 2.6a,b). As anticipated, nanobody binding enhanced the lateral crystal packing by bridging the gap between GABA$_A$-β3 receptor ECDs (Fig. 2.6c). The electron density map showed well-defined densities for α-α-helices, β-sheets and N-linked glycans (Fig. 2.6d). The density of the channel blocker, picrotoxin, could not be observed in the channel pore.

Table 6 Crystallographic data collection and structure refinement statistics.

	β3-Nb25$_{cryst}$
Data collection	
Space group	P 1 21 1
Cell dimensions	
a, b, c (Å)	140.40, 152.85, 169.73
α, β, γ (°)	90.00, 92.12, 90.00
Wavelength (Å)	1.072
Resolution (Å)	49.82 - 3.542 (3.67 - 3.54)
R-meas	0.31 (>1)
R-pim	0.13 (0.45)
I/σI	5.87 (1.62)
CC$_{1/2}$	0.99 (0.36)
Completeness (%)	99.70 (99.30)
Refinement	
Resolution (Å)	49.82 - 3.54 (3.67 - 3.54)
No. reflections	74157 (2028)
R_{work}	0.25 (0.31)
R_{free}	0.28 (0.34)
No. atoms	37136
Protein	36606
N-linked glycans	530
B-factors (Å^2)	47.92
Protein main/side chains	47.77
N-linked glycans	58.27
R.m.s deviations	
Bond lengths (Å)	0.003
Bond angles (°)	0.62
Ramachandran plot quality	
Favoured (%)	97.51
Allowed (%)	2,49
Outliers (%)	0.00
Molprobity score (percentile*)	1.47

*Across all resolution structures (N=1784)

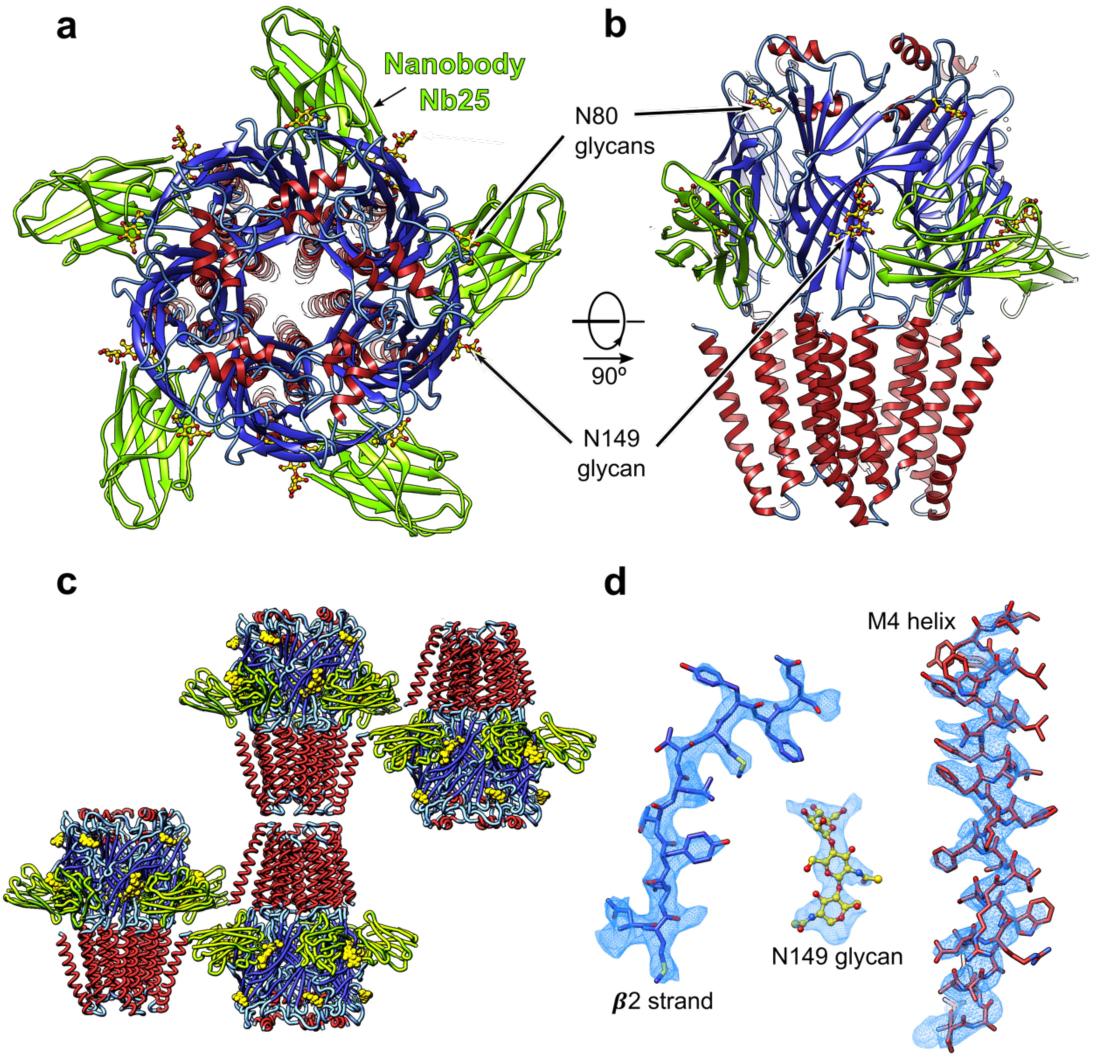

Figure 3.6 Crystal structure of GABA$_A$R-β3 homopentamer in complex with nanobody Nb25. a,b, GABA$_A$R-β3-Nb25 viewed from the extracellular space **(a)** and parallel to the membrane **(b)**. **c,** GABA$_A$R-β3-Nb25 crystal packing mode (P1 21 1 space group). Nanobodies are coloured in green, α-helices in red, beta sheets in dark blue, loops in light blue and N-linked glycans in yellow. **d,** Atomic model and SigmaA-weighted 2Fo-Fc electron density map (contoured at 1.3 rmsd) for the β2 strand, N149 glycan and M4 helix.

All three Nb25 CDR loops (Fig. 2.7a) contribute to nanobody binding to the interface which is situated between two β3 subunits (Fig. 2.7b). At each of the binding sites, a nanobody buries an average surface of 1100 Å which is roughly split in half between the principal and complementary faces. Nanobody binding also caps the lateral tunnels between the two subunits (Fig. 2.7c). The longest CDR3 loop forms most of the interactions by probing an agonist binding cleft below the loop C and reaching out to both principal and complementary faces (Fig. 2.7b,d). Two smaller nanobody loops also make a range of important contacts. CDR1 interacts with the N-linked glycan at Asn149 on the principal β3 face and with the β6-β7 loop, whereas CDR2 makes contacts with the β8'-β9 loop (Loop F) on the complementary subunit face (Fig. 2.7b).

3.7.3. Nanobody Nb25 impact on GABA$_A$R conformation and function

To evaluate the structural consequences of Nb25 binding to GABA$_A$R-β3, the GABA$_A$R-β3-Nb25 structure (termed as β3-Nb25$_{cryst}$) was compared to the previously determined desensitized GABA$_A$R-β3 structure in complex with an agonist (termed β3$_{cryst}$, PDB 4COF). β3$_{cryst}$ and β3-Nb25$_{cryst}$ subunits adopt a similar, activated conformation (RMSD in the 0.20-0.32 Å range between different chains, over 204 equivalent Cα positions) with the agonist-binding loop-C in a closed state (Fig. 2.8b). In addition, the β3-Nb25$_{cryst}$ channel pore outline highly resembles the pore configuration in β3$_{cryst}$ where the bottom gate at Ala248 is fully closed (Fig 2.8b). Therefore, β3-Nb25$_{cryst}$ represents the same desensitised state as in the previously published structure. Initial electrophysiology experiments were performed to test whether Nb25 can act as a modulator against the GABA$_A$R-β3 homopentamer but there was no indication of nanobody effect on channel function. In our laboratory, more detailed studies were carried out using homomeric Cys-loop receptor chimera containing subunits made of GABA$_A$R-β3 ECDs and GABA$_A$R-α5 TMDs (Miller et al., 2017). High concentrations of Nb25 alone did not cause any response when whole-cell patch clamping experiments were performed on cells expressing chimera ion channels (functional proteins, respond to histidine modulation). It also did not affect the maximal potentiation of the chimera by histamine and pregnanolone (Fig. 2.8c).

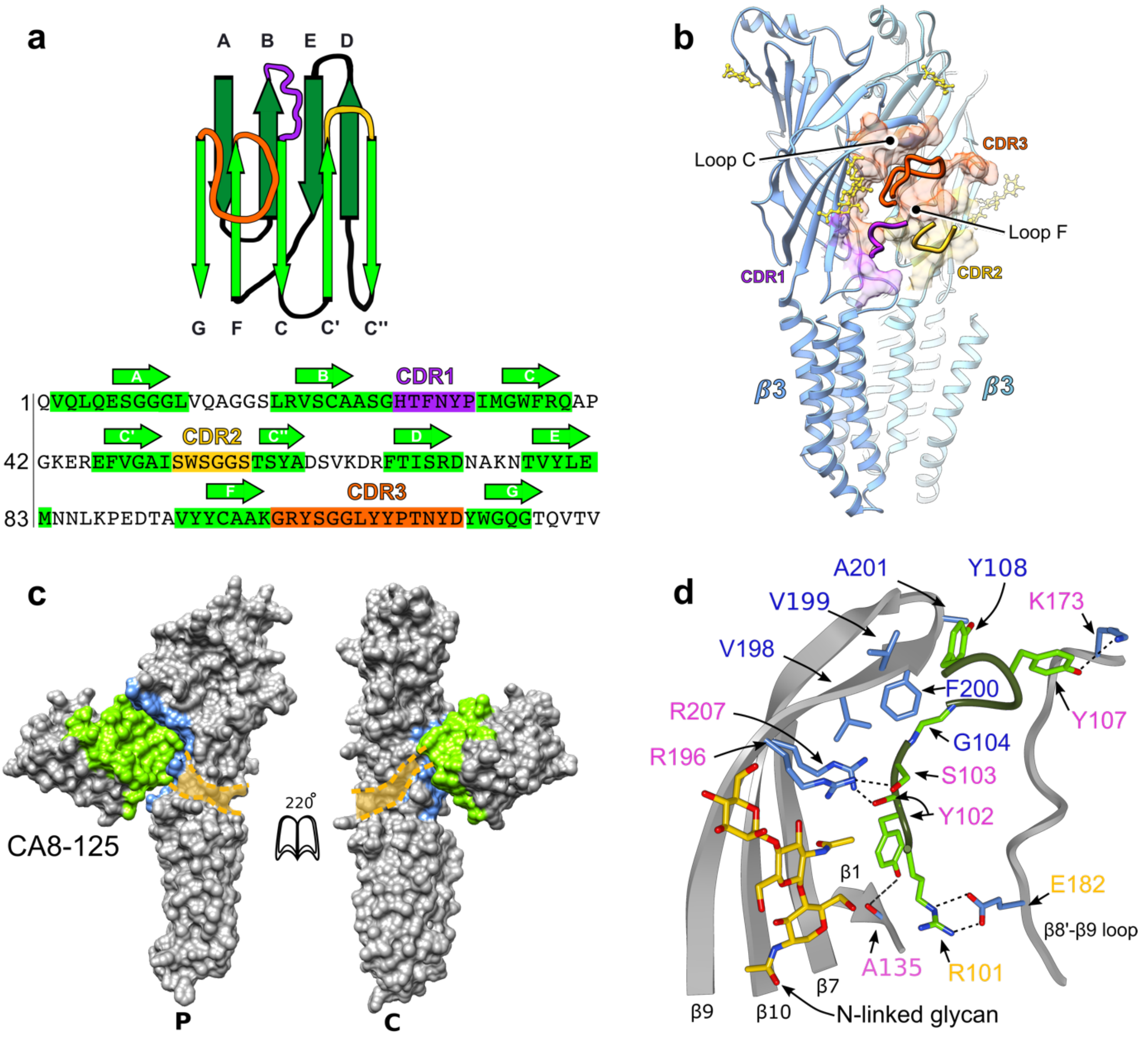

Figure 3.7 Nanobody Nb25 binding mode to GABA$_A$R-β3 homopentamer.

a, Schematic representation and sequence information for nanobody Nb25. **b,** CDR loops determine Nb25 binding to GABA$_A$-β3 receptor. CDR1 is coloured in purple, CDR2 in gold and CDR3 in orange. GABA$_A$R-β3 surface interacting with the nanobody CDR loops is shown and coloured accordingly. **c,** 'Open book' view of the inter-subunit interfaces (subunits were rotated 220º outwards around their longitudinal axis). Molecular surfaces involved in GABA$_A$R-β3 and nanobody interaction are coloured light blue and green, respectively. The outline of an inter-subunit side-tunnel is marked in orange. **d,** Detailed view of the CDR3 loop interaction interface with GABA$_A$R-β3. Nanobody residues are coloured in green and residues from GABA$_A$R-β3 are coloured in light blue. Cartoon for GABA$_A$R-β3 is shown in grey and dark green for nanobody CDR3 loop. Labels for residues involved in putative hydrophobic interactions are coloured blue, putative hydrogen bonding – pink and in putative salt bridges – orange.

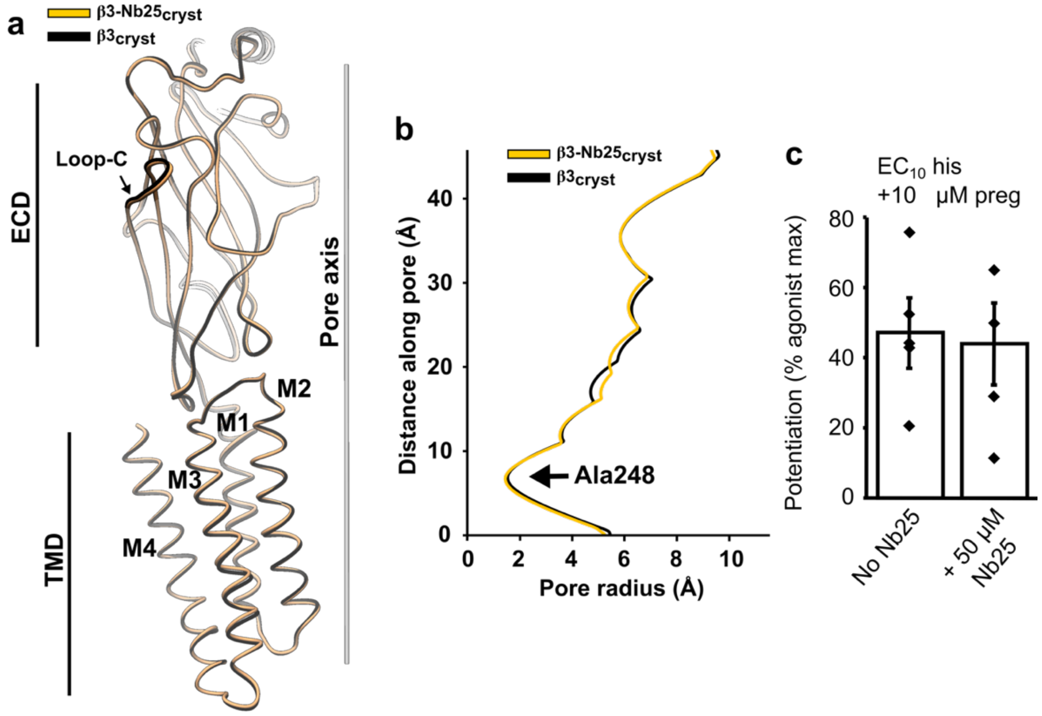

Figure 3.8 Structural and functional consequences of Nb25 binding to GABA$_A$R-β3 homopentamer.

a, Subunit alignment of β3$_{cryst}$ and β3-Nb25$_{cryst}$ structures. Subunits were aligned using SHP software (Stuart et al., 1979). **b,** Pore diameter of β3$_{cryst}$ and β3-Nb25$_{cryst}$ structures along the channel pore axis. The solvent accessible path was calculated with HOLE (Smart et al., 1993) plugin in Coot. **c,** Graph showing that the potentiation amount of EC$_{10}$ histamine (his) by 10 μM pregnanolone (preg) does not change after application of 50 μM Nb25. Five experiments were carried out, each from different cells, and the error bar represents the standard error. Figure adapted from Miller et al., Nat. Struct. Biol., 2017.

3.8. Conclusions

GABA$_A$ receptors represent a large group of ubiquitous ion channels in the human CNS important for inhibitory signalling. Currently, only limited structural information is available on their mechanism of action and modulation with small drug molecules. In order to study this protein by X-ray crystallography, detergent-purified GABA$_A$ receptors need to form well-diffracting crystals. To overcome this roadblock, I tested whether llama nanobodies can be used as crystallization chaperones. Firstly, I identified nanobodies binding to α1 and β3 subunits with low nanomolar affinities. I used high-affinity nanobodies for crystallisation trials and showed that nanobodies can significantly increase chances of $GABA_AR$ crystallisation. In particular, nanobody Nb25 appears to be a successful crystallization chaperone enhancing crystal growth for $GABA_AR$-β3 hompentamer. This nanobody recognises discontinuous amino acid sequences at the interface between β3 subunits, contacting the principal and complementary faces with a high degree of specificity. Such binding mode helps to bridge β3 ECDs during crystallisation and prevents the disordered detergent belt from contributing to crystal packing. Based on the functional experiments it seems that Nb25 binding to β3 ECDs is neutral towards the conformational state of the receptor. It was an unexpected finding, because in the X-ray crystal structure, the protein was in an activated-desensitised conformation even though there was no agonist in the crystallisation buffer. Since Nb25 interacts closely with the agonist binding loop-C, it was falsely suspected to act as an agonist. The activated state observed in β3-$Nb25_{cryst}$ without the presence of an agonist could be explained by the fact that this β3 homopentamers are leaky and can be spontaneously activate in the cells (Miller and Aricescu, 2014). Therefore, these channels could achieve a thermodynamically stable desensitised state in crystals without an agonist. However, a nanobody which does not modulate the receptor function is advantageous as a functionally-neutral crystallisation chaperone for $GABA_AR$ soaking or co-crystallisation experiments. Any conformational changes observed during drug molecule binding should not be difficult to interpret as nanobody contribution to channel conformation should be negligible. In addition, it seems this binding mode is quite common as there are three nanobodies (Nb25, Nb26, Nb27) with very similar sequence and high occurrence rate (Appendix 10.2). Nevertheless, the other nanobodies have distinct CDR loops and they might present a different binding mode which could be modulatory. For example, nanobodies binding to mouse 5-HT_3 receptor also targeted the same loop-C epitope. By wedging their CDR3 loop behind the loop-C of the serotonin receptor, they act as antagonists (Hassaine et al., 2014). In future, all nanobodies raised against $GABA_AR$-α1β3 should be subjected to a thorough investigation by electrophysiology to detect such modulatory properties. However, for now, nanobodies allow production of $GABA_AR$-β3 crystals needed to unlock small drug molecule binding sites and mechanisms of action.

4. Intravenous anaesthetic etomidate binding site in GABA$_A$R revealed by X-ray crystallography

4.1. Introduction

General anaesthetics are administered to thousands of patients worldwide to induce unconsciousness, immobility and amnesia during surgical procedures. Anaesthetics are potent drug molecules exhibiting high toxicity and low safety margins. However, in recent decades, refined application practises led to a marked decrease in anaesthetics-dependent mortality rates (Vlassakov and Kissin, 2016). Depending on their chemical nature, anaesthetics can be administered either in gas form or intravenously. The advantages of the intravenous anaesthesia include rapid induction of unconsciousness and immobility using a single-bolus injection. Small hydrophobic intravenous anaesthetics such as etomidate, propofol and thiopental (Fig. 3.1) rapidly diffuse in blood and reach the CNS where they primarily act on GABA$_A$ receptors (Kopp Lugli et al., 2009).

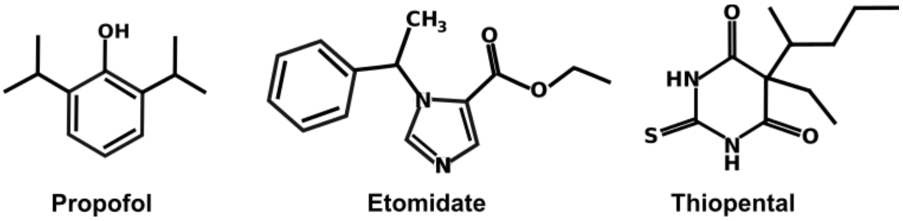

Figure 4.1 General intravenous anaesthetics.

Several examples of commonly used general intravenous anaesthetics and their chemical structures.

Anaesthetics potentiate GABA$_A$R function by lowering the GABA concentration threshold at which GABA$_A$Rs are activated (Forman and Miller, 2011). In addition, anaesthetics can be GABA$_A$ receptor subtype-specific. For example, most intravenous anaesthetics act on β-subunit containing GABA$_A$Rs (Franks, 2008). However, their binding sites, subunit specificity determinants and exact mechanisms of action are not fully known. The lack of understanding of their function prevents the development of novel, safer anaesthetics. Any improvement in anaesthetic safety would be highly beneficial as it would reduce the procedural complexity for anaesthetised state control in patients or reduce undesirable side-effects. For example, etomidate is a small lipid-soluble compound used for inducing general anaesthesia and sedation. It shows a good hemodynamic safety and minimal respiratory depression, which would make it an ideal anaesthetic for critically ill patients (Forman, 2011). However, etomidate causes adrenal cortical inhibition and its use has been discouraged. Structural characterisation of GABA$_A$Rs bound to anaesthetic molecules like etomidate would allow us to understand how structural-chemical properties confer their function and might contribute to safer drug design.

In this chapter I will describe my efforts to characterise the general intravenous anaesthetic binding sites in GABA$_A$Rs containing β3 subunits using X-ray crystallography.

4.2. GABA$_A$R-β3 K279T mutation

Recent work performed in our laboratory, by Paul Miller, led to the observation that the GABA$_A$R-β3 K279T mutation significantly enhances the β3 homopentamer thermostability in dodecyl 1-thio-β-maltoside (DDTM) detergent (Fig. 3.2a). It was noticed that the α5 TMD region was responsible for increased thermostability of the β3$_{ECD}$-α5$_{TMD}$ chimera when compared to the β3$_{cryst}$ homopentamer. Subsequent tests with progressively smaller regions of the α5 TMD sequence identified that the increased thermostability is linked to the α5 M2-M3 loop. Then β3 M2-M3 loop residues were replaced by the divergent α5 residues, one at a time, until receptor thermostability became similar to the β3$_{ECD}$-α5$_{TMD}$ chimera. Since the M2-M3 loop is critical for signal transduction from ECD to TMD, electrophysiology experiments were performed to investigate its effects on the β3$_{K279T}$ channel activity. Preliminary electrophysiology experiments performed by Paul Miller showed that β3$_{K279T}$ channels retain the ability to bind to the etomidate and propofol (Fig. 3.2b-e). However, the β3$_{K279T}$ channels are more spontaneously active than the β3 homomers and general anaesthetic binding results in their closure. The reason for such behaviour is not clear, but it is likely that anaesthetics drive the receptors to the desensitised state as they are at an elevated open state in the membranes already. Interestingly, the β3$_{ECD}$α5$_{TMD}$ chimeras are also spontaneously active (Fig 3.2f). However, introduction of the inverse mutation (T287K) to the M2-M3 loop of the chimeras decreased their spontaneous gating and allowed to measure the pregnanolone potentiation of submaximal histamine doses (Fig. 3.2g) (Miller et al., 2017). These results indicated that Lys279 residue is involved in $GABA_A$ receptor gating and its mutation has unexpected functional consequences. Owing to the increased $\beta 3_{K279T}$ mutant stability in detergent, it was more amenable to crystallisation and I used this protein to understand the structural impact of the K279T mutation and to explore general intravenous anaesthetic binding sites.

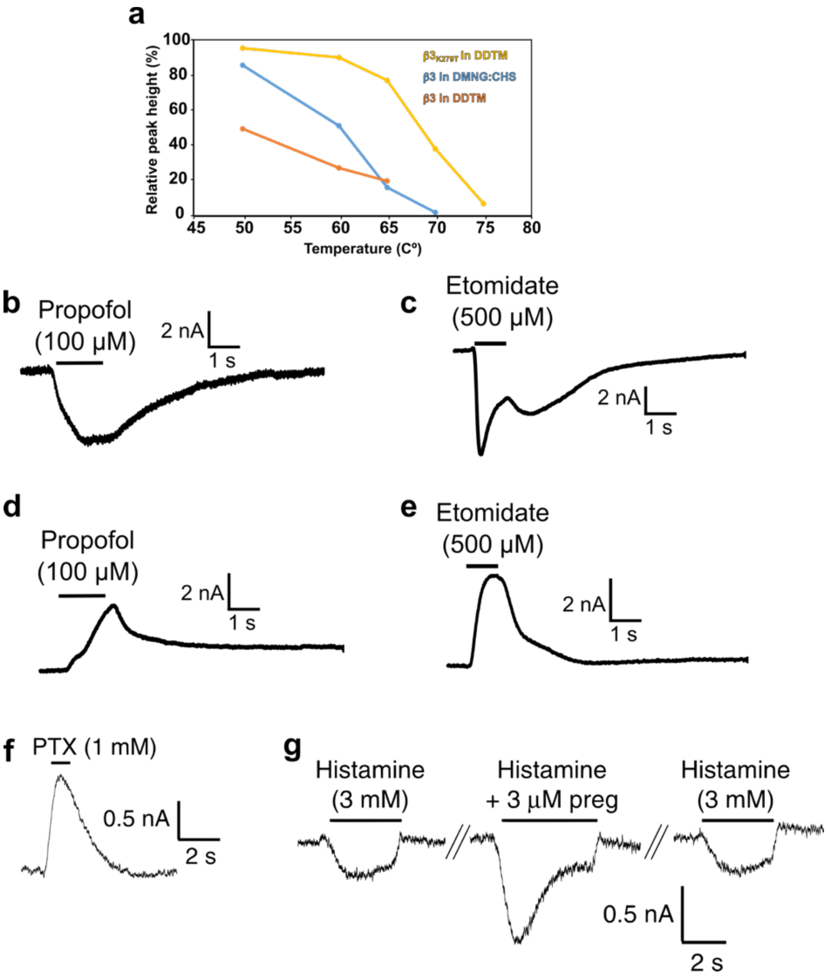

Figure 4.2 β3 K279T mutation functional effects.

a, $GABA_AR$-β3 and $\beta 3_{K279T}$ thermostability in different detergents as estimated with FSEC. $\beta 3_{K279T}$ in DDTM demonstrates superior thermostability up to 65 °C. **b-e,** HEK-293T whole-cell patch-clamp recording of propofol **(b)** and etomidate **(b)** activating inward currents in β3 transfected cells, whereas in $\beta 3_{K279T}$ transfected cells, propofol **(d)** and etomidate **(e)** contribute to blocking of spontaneous inward current leaks. **f,** $GABA_AR$ channel blocker picrotoxin blocks spontaneous inward current leaks in HEK-293T cell transfected with the $\beta 3_{ECD}\alpha 5_{TMD}$ chimera. **g,** HEK-293T whole-cell patch-clamp histamine responses (EC10) from HEK cells transfected with the T287K mutation-containing $\beta 3_{ECD}\alpha 5_{TMD}$ chimeras, before and after co-application with 3 μM pregnanolone (preg). Experimental data in panels **a-e** was kindly provided by Paul Miller. Panels **(f)** and **(g)** were adapted from Miller et al., Nat. Struct. Biol., 2017.

4.3. GABA$_A$R-β3$_{K279T}$-NB25 crystallisation and crystal soaking

GABA$_A$-β3$_{K279T}$ receptor construct was produced using the same protocol employed for the β3 homopentamer (Chapter 3). However, it was solubilised in DDTM and 5 mM histamine, an agonist for β3 homopentamers (Saras et al., 2008), was present throughout all purification steps to promote open/desensitised states of the receptor to which anaesthetics should bind more easily. GABA$_A$R-β3K$_{279T}$ was mixed with Nb25, concentrated to 3.5 mg/mL and subjected to crystallisation trials as described in Materials and Methods. Crystals grew in several different conditions in 1-14 days. Subsequently, crystals were cryo-protected with 30% ethylene glycol and snap-frozen in liquid nitrogen. Crystal diffraction was tested at the Diamond Light Source synchrotron, UK. The best diffracting crystals formed in MemGold D11 condition (0.2 M sodium acetate pH 6.8, 8.8 % PEG6000) (Fig. 3.3). These crystals grew rapidly (in 24-36 h) and often resulted in multiple small fragments if plates were cooled to 6 °C too quickly. Larger crystals were obtained by allowing fewer nucleation points to form at room temperature for half a day before placing the plates into the cold room imager. The same well-diffracting crystals could not be reproduced in a home-made or new commercially acquired batch of MemGold D11 condition, therefore all crystallisation tests were limited to the ~12 mL original precipitant stock. Nonetheless, enough crystals were produced for soaking experiments. After crystals stopped growing, small volumes (~0.2µl) of reservoir condition supplemented with 30% ethylene glycol and 1-10 µM general anaesthetics were added to the drops. Etomidate, iodo-etomidate, propofol and 4-bromo-propofol were tested for crystal soaking. Crystal morphology was monitored constantly for 0.5-4 h. Soaks with etomidate generally did not cause visible crystal cracks, however, the other drugs did induce fissures in crystals after the incubation for several hours. The cracks in crystals were accompanied by loss of diffraction.

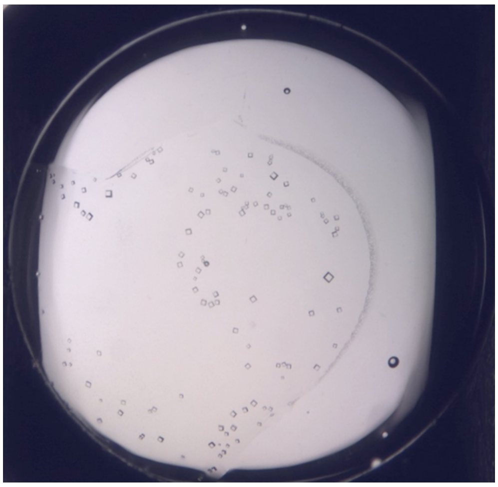

Figure 4.3 Crystals of GABA$_A$R-β3K$_{279T}$-Nb25.

Representative appearance of crystals grown in MemGold D11 reservoir condition

4.4. Data collection and refinement

Control apo-state and soaked crystals were flash-frozen in liquid nitrogen. Diffraction data were collected at beamline I03, Diamond Light Source, United Kingdom. Crystals soaked with iodo-etomidate, propofol and 4-bromo-propofol diffracted to medium resolution range (4-8 Å). The best X-ray diffraction data for control apo-structure was autoprocessed with XIA2 (Winter et al., 2013) to 3.25 Å. The best diffraction data for the etomidate bound structure was indexed, integrated, scaled and merged to 3.45 Å with the HKL2000 package (Otwinowski and Minor, 1997a). Both structures were solved by using the GABA$_A$R-β3-Nb25$_{cryst}$ structure for molecular replacement in PHASER (McCoy et al., 2007b). Models were improved via iterative rounds of refinement in Refmac (Murshudov et al., 2011), Phenix (Adams et al., 2010) and manual building using COOT (Emsley and Cowtan, 2004). Automated X-ray and atomic displacement parameter (ADP) weight optimization and torsion angle noncrystallographic symmetry (NCS) restraints were used during the refinement. The etomidate coordinates and geometry restraints were generated using the Grade Web Server (http://grade.globalphasing.org). Crystallographic data collection and model refinement statistics are summarized in table 7.

Table 7 Crystallographic data collection and structure refinement statistics.

	$\beta3_{K279T}$-Nb25$_{Apo}$	$\beta3_{K279T}$-Nb25$_{ETM}$
Data collection		
Space group	P 41 21 2	P 41 21 2
Cell dimensions		
a, b, c (Å)	111.86 111.86 718.08	112.99 112.99 741.56
α, β, γ (°)	90.00, 90.00, 90.00	90.00, 90.00, 90.00
Wavelength (Å)	0.976	0.976
Resolution (Å)	94.94 - 3.25 (3.37 - 3.25)	49.85 - 3.16 (3.42 - 3.16)
R-meas	0.20 (2.03)	0.36 (4.90)
R-pim	0.07 (0.75)	0.07 (0.64)
I/σI	7.94 (1.07)	10.00 (1.70)
CC$_{1/2}$	0.99 (0.32)	0.99 (0.60)
Completeness (%)	99.80 (99.34)	95.10 (76.90)
Refinement		
Resolution (Å)	94.94 - 3.25 (3.37 - 3.25)	49.85 - 3.16 (3.42 - 3.16)
No. reflections	73629 (7196)	48709 (263)
R_{work}	0.22 (0.34)	0.212 (0.30)
R_{free}	0.25 (0.38)	0.25 (0.31)
No. atoms	18905	18732
Protein	18415	18377
N-linked glycans	490	265
Etomidate	-	90
B-factors (Å^2)	112.6	69.33
Protein main/side chains	111.46	69.38
N-linked glycans	155.31	66.00
Etomidate	-	71.88
R.m.s deviations		
Bond lengths (Å)	0.004	0.003
Bond angles (°)	0.71	0.98
Ramachandran plot quality		
Favoured (%)	97.48	95.93
Allowed (%)	2.47	3.58
Outliers (%)	0.04	0.49
Molprobity score (percentile*)	1.46	1.83

*Across all resolution structures (N=1784)

4.5. Apo-state structure

The apo-state structure of GABA$_A$R-β3$_{K279T}$-Nb25 was solved to 3.25 Å resolution. Overall, this structure highly resembles the β3-Nb25$_{cryst}$ structure (RMSD in the 0.45-0.51 Å range between different subunit chains, over 333 equivalent Cα positions) (Fig. 3.4a). However, the K279T mutation induced structural changes in the area surrounding the M2-M3 loop (Fig. 3.4b-d). In β3-Nb25$_{cryst}$ and β3$_{cryst}$ structures, the Lys279 residue constrains the Arg269 side chain (C-terminus of the M2 helix) so that it does not form contacts with the M2-M3 loop (Fig. 3.4b). In contrast, introduction of the smaller Thr279 residue in β3$_{K279T}$-Nb25$_{Apo}$ allows the Arg269 side chain to reach up, form a putative hydrogen bond network with the M2-M3 loop, and the N-terminus of the M3 helix (Fig. 3.4c). In addition, the Arg269 residue cannot form hydrogen bonds anymore with the Asn224 residue on the M1 helix of a neighbouring subunit (Fig. 3.4b,c). This hydrogen bonding pattern results in a more compact arrangement between M2, M3 helixes and the M2-M3 loop (Fig. 3.4d). For example, Cα of Asp282 in the M3 and P273 in the M2-M3 loop are pulled closer to each other by average of 0.5 Å when compared to the β3-Nb25$_{cryst}$ structure (Fig. 3.4d). Overall, the K279T mutation allows the Arg269 side chain to act as an anchoring point for the M2, M3 helixes and the M2-M3 loop. This should cause the whole segment to be more rigid and stable. It also likely means that conformational changes at the ECD level should be more efficiently transferred to the TMD through the stabilised M2-M3 loop. Analysis of GABA$_A$R α,β and γ sequences reveals that the β3 Arg269 and Asp282 residues are highly conserved residues across different human subunits (Fig. 3.4e). In contrast, Lys279 is only conserved among the β subunits, while all other subunits contain a threonine at the equivalent position (Fig. 3.4e). This means that most subunits have the stabilised M2-M3 configuration, whereas β subunits will have a more flexible M2-M3 loop.

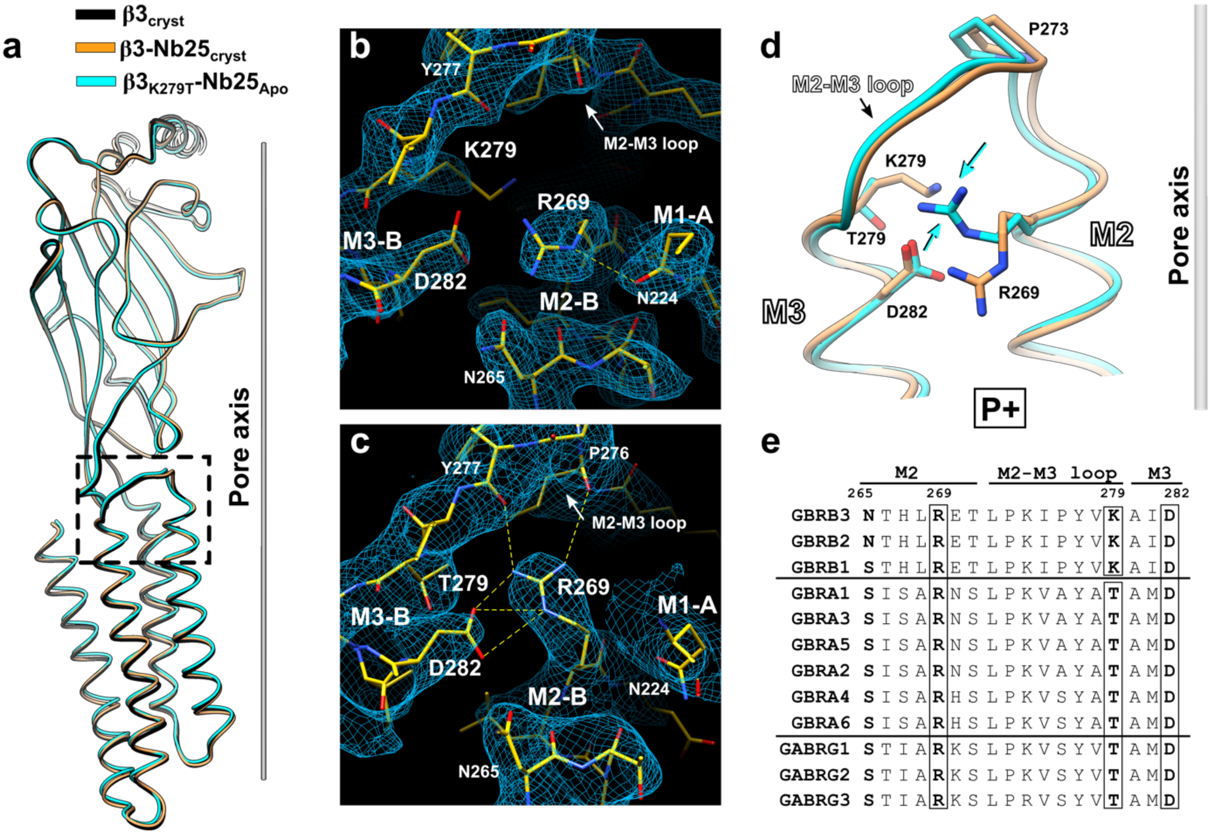

Figure 4.4 β3 subunit K279T mutation structural effects.

a, Alignment of whole subunits from $\beta3_{cryst}$, $\beta3$-Nb25$_{cryst}$ and $\beta3_{K279T}$-Nb25$_{Apo}$ structures. Area with small structural differences near the M2-M3 loop is boxed in black. **b,c,** SigmaA-weighted 2Fo-Fc (blue, contoured at 1.5 σ) electron density maps for $\beta3_{cryst}$ (PDB 4COF) **(b)** and $\beta3_{K279T}$-Nb25$_{Apo}$ **(c)** structures showing that the Arg269 side chain flips upwards when K279T mutation is introduced. $\beta3_{cryst}$ structure is shown since it is better resolved than and $\beta3$-Nb25$_{cryst}$ structure. Putative hydrogen bonds between the Arg269 side chain and the surrounding residues are shown in yellow dashed lines. Hydrogen bonds were calculated using UCSF Chimera. **d,** $\beta3$-Nb25$_{cryst}$ and $\beta3_{K279T}$-Nb25$_{Apo}$ TMD alignment reveals small conformational changes in the M2-M3 loop and in the M2 and M3 α-helices upon introduction of K279T mutation as viewed from the principal face. **e,** Multiple sequence alignment of GABA$_A$R α, β and γ subunits in the area close to the Lys279. Sequence numbering is based on the β3 subunit (mature isoform 1). The conservation of amino acids displayed in panel **c** is highlighted with bold font and black boxes. All alignments were performed using SHP software (Stuart et al., 1979).

Pore analysis of β3$_{cryst}$, β3-Nb25$_{cryst}$ and β3$_{K279T}$-Nb25$_{Apo}$ reveals that all constructs adopt a desensitised state pore conformation (Fig. 3.5a). However, the β3$_{K279T}$-Nb25$_{Apo}$ structure has a more inward looking pore outline at the level of the His267 residue. It seems that small conformational changes caused by the K279T mutation also affected the rotation of the His267 residue situated at the top of the M2 helix (Fig. 3.5b).

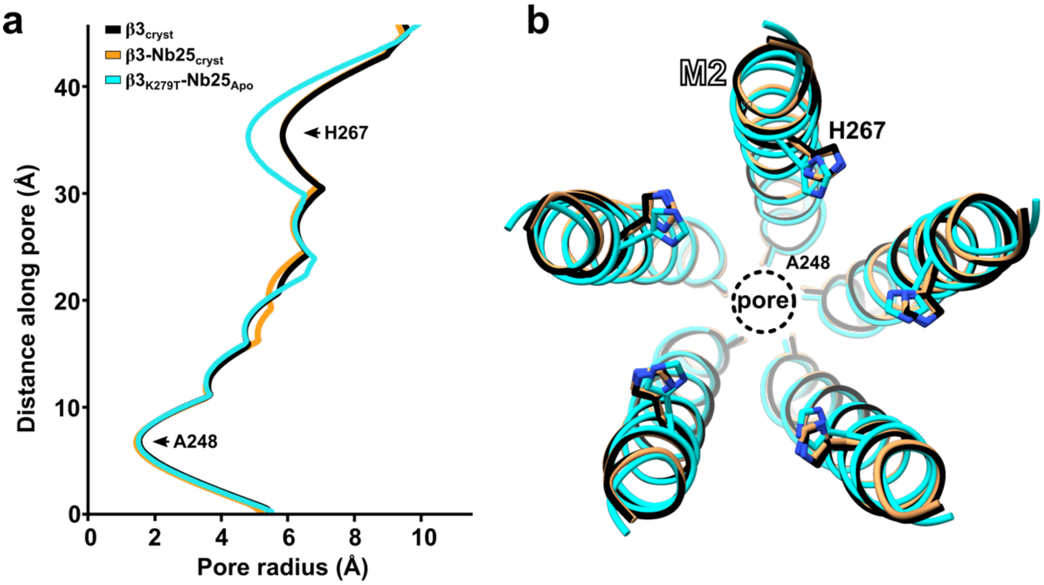

Figure 4.5 β3$_{K279T}$-Nb25$_{Apo}$ crystal structure is in a desensitized conformation.

a, Pore diameter analysis of β3$_{cryst}$ (PDB 4COF), β3-Nb25$_{cryst}$ and β3$_{K279T}$-Nb25$_{Apo}$ structures. Alanine 248 marks the desensitisation gate, His267 – the upper pore region. **b,** Position of M2 α-helices and His267 after globally aligning β3$_{cryst}$, β3-Nb25$_{cryst}$ and β3$_{K279T}$-Nb25$_{Apo}$ structures. Alignment was performed using the SHP software (Stuart et al., 1979).

To summarise, the β3$_{K279T}$-Nb25$_{Apo}$ structure is almost identical to other crystal structures of GABA$_A$-β3 receptors. However, this structure revealed small structural differences affecting the M2-M3 loop stability between β and the rest of GABA$_A$R subunits. These differences in M2-M3 loop stabilisation must have functional consequences in heteromeric GABA$_A$ receptor gating and must be investigated further. However, importantly for this study, it does not look like that these local changes should hinder the interpretation of anaesthetic-bound structures.

4.6. Etomidate-bound structure

The etomidate-bound structure of GABA$_A$R-$\beta3_{\mathrm{K279T}}$-Nb25 was solved to 3.16 Å resolution. This structure revealed that the binding site for etomidate is in the "upper" (close to extracellular) region of the TMD, between two adjacent subunits (Fig. 3.6a). In the $\beta3_{\mathrm{K279T}}$-Nb25$_{\mathrm{Apo}}$ F_o-F_c electron density map, no density was observed in this pocket (Fig. 3.6b). However, five large peaks were observed in the $\beta3_{\mathrm{K279T}}$-Nb25$_{\mathrm{ETM}}$ F_o-F_c electron density map (Fig. 3.6c). The etomidate model could only be refined in this density if the phenyl ring was positioned "upwards", i.e. pointing at the ECD (Fig. 3.6de).

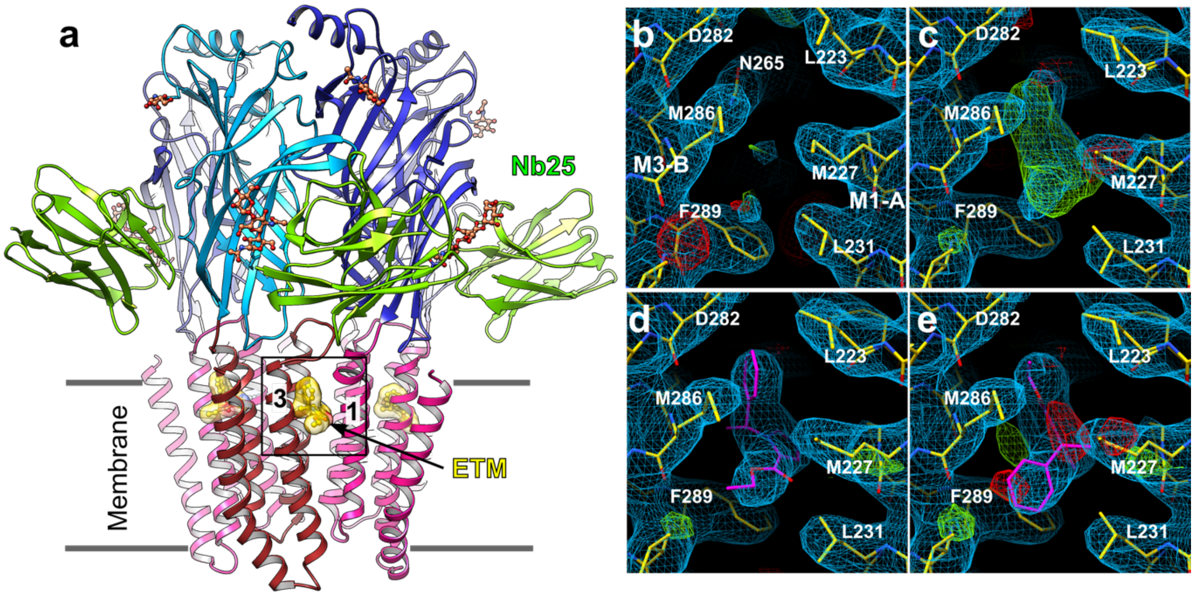

Figure 4.6 Etomidate-bound $\beta3_{\mathrm{K279T}}$-Nb25$_{\mathrm{ETM}}$ crystal structure.

a, $\beta3_{\mathrm{K279T}}$-Nb25$_{\mathrm{ETM}}$ viewed parallel to the membrane. Etomidate binding site between two β3 subunit transmembrane domains is boxed in black, **b-e,** Crystallographic quality control of the etomidate binding site. SigmaA-weighted 2F_o-F_c (blue, contoured at 1.3 σ) and F_o-F_c (red and green, contoured at -3 and +3 σ, respectively) electron density maps are shown for the etomidate binding site in the 3.25 Å $\beta3_{\mathrm{K279T}}$-Nb25$_{\mathrm{Apo}}$ structure after Phenix refinement **(b)**, 3.16 Å $\beta3_{\mathrm{K279T}}$-Nb25$_{\mathrm{ETM}}$ structure before placing etomidate and refinement **(c)**, $\beta3_{\mathrm{K279T}}$-Nb25$_{\mathrm{ETM}}$ electron density map after refinement in Phenix with etomidate phenyl group positioned upwards **(d)** and downwards **(e)**. Appearance of positive and negative peaks in the F_o-F_c maps around the etomidate model in **(e)** indicates that this pose is not correct, whereas in **(d)** it is well refined.

Closer inspection of the etomidate binding site in the β3$_{K279T}$ structure reveals that the pocket is sandwiched between the "upper" portion of the β3 M2 and M3 α-helices at the principal face and the M1 helix from the complementary face (Fig. 3.7a). The entrance to the pocket is lined with hydrophobic amino acids (Met286, V290 at the β3 principal face and Leu223, Met227, Leu231 at the β3 complementary face) (Fig. 3.7a). The side chains of Met227 and Met 286 residues close the middle section of the pocket around the etomidate. The ethyl group of the etomidate is situated just below the aforementioned methionines and protrudes towards the membrane (Fig. 3.7a). The phenyl ring of the etomidate is wedged in between the polar Asn265, Asp282 residues and the hydrophobic patch at the M3 helix lined by Met286 and Leu285 (Fig 3.7ab). The imidazole ring of the etomidate is likely to be involved in π-π interactions with the Phe289 side chain (Fig. 3.6b).

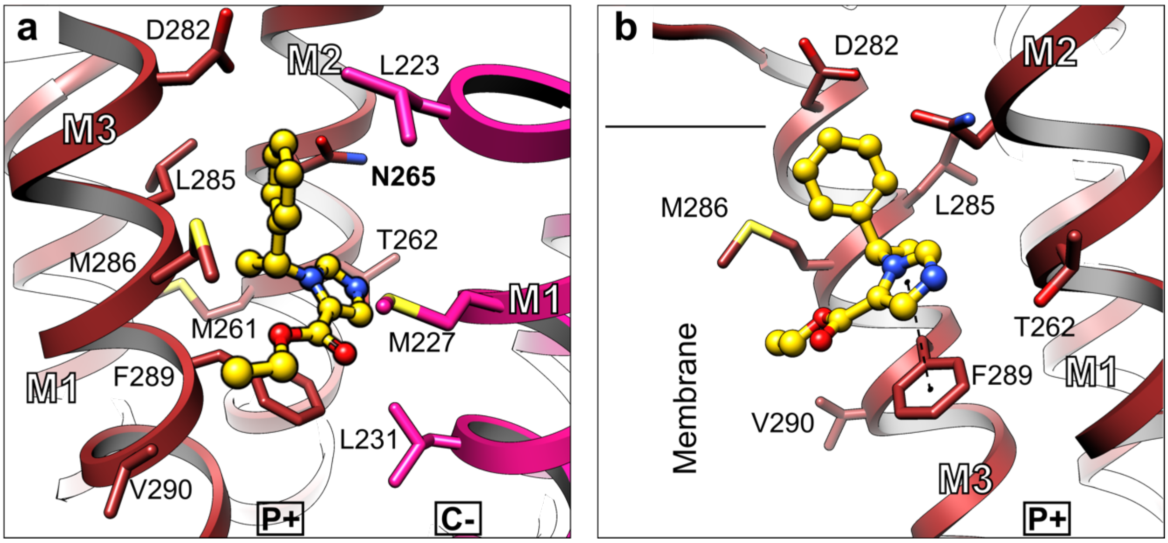

Figure 4.7 Etomidate binding site at β3-β3 TMD interface.

a, Etomidate (ball-and stick representation, carbon atoms in yellow, nitrogen in blue and oxygen in red) binding pocket viewed from lipid bilayer. Principal face (P+) β3 subunit is coloured in dark red, whereas the complementary face (C-) β3 subunit is coloured in pink. **b,** Etomidate binding pocket viewed from the complementary subunit perspective. The black dashed line indicates putative π-π interactions between etomidate imidazole ring and the Phe289 side chain at the principal face β3 subunit.

4.6.1.Previous photolabelling studies

The etomidate binding mode observed in the $\beta3_{K279T}$-$Nb25_{ETM}$ crystal structure is in close agreement with previous photolabelling studies (Chiara et al., 2012; Li et al., 2006) (Fig. 3.8). During these experiments, etomidate analogues with photoreactive moieties were used to label amino acids in close proximity to the etomidate binding pocket. Azi-etomidate and TBDzI-etomidate (Fig. 3.8a) were tested against full-length $GABA_A$-$\alpha1\beta3$ receptors produced in stable cell lines (Chiara et al., 2012) and native $\alpha\beta\gamma$ receptors extracted from bovine brain (Li et al., 2006), respectively. Both studies used quantifiable Edman degradation to detect the photolabelled residues. Azi-etomidate, which reacts to nucleophilic amino acid side chains, tagged significant amounts of Met236 in $\alpha1$ subunits and Met286 in $\beta3$ subunits (Li et al., 2006) (Fig. 3.8b). For TBDzI-etomidate, which can react to both aliphatic and nucleophilic side chains, major labelling peaks were observed for Met236 in $\alpha1$ and Met227, Met286, Val290 in $\beta3$ subunits (Chiara et al., 2012) (Fig. 3.8c). Since Met227 was labelled but no other residues in the $\alpha1$-M3 helix, these observations suggested that etomidate also binds to the $\beta3$-$\beta3$ interface. In addition, this compound labelled small amounts of Cys234 in $\alpha1$ and Cys288 in $\beta3$ (Fig 3.8d), however the aromatic diazirine is highly reactive towards cysteines and these peaks were deemed to be unspecific. The etomidate binding mode in $\beta3_{K279T}$-$Nb25_{ETM}$ structure explains well why these amino acids were labelled by the photoreactive etomidate analogs. Since the etomidate ester functional group is pointing away from the pocket and towards the lipid bilayer, it would position the photoreactive groups in close proximity to the labelled amino acids (Fig. 3.8d). In addition, when the etomidate phenyl ring was tagged with a photolabel, this compound did not modulate $GABA_A$Rs (Husain et al., 2010). It is clear now that such a compound cannot bind to this pocket due to steric hindrance, as the phenyl ring is situated in a closely confined space.

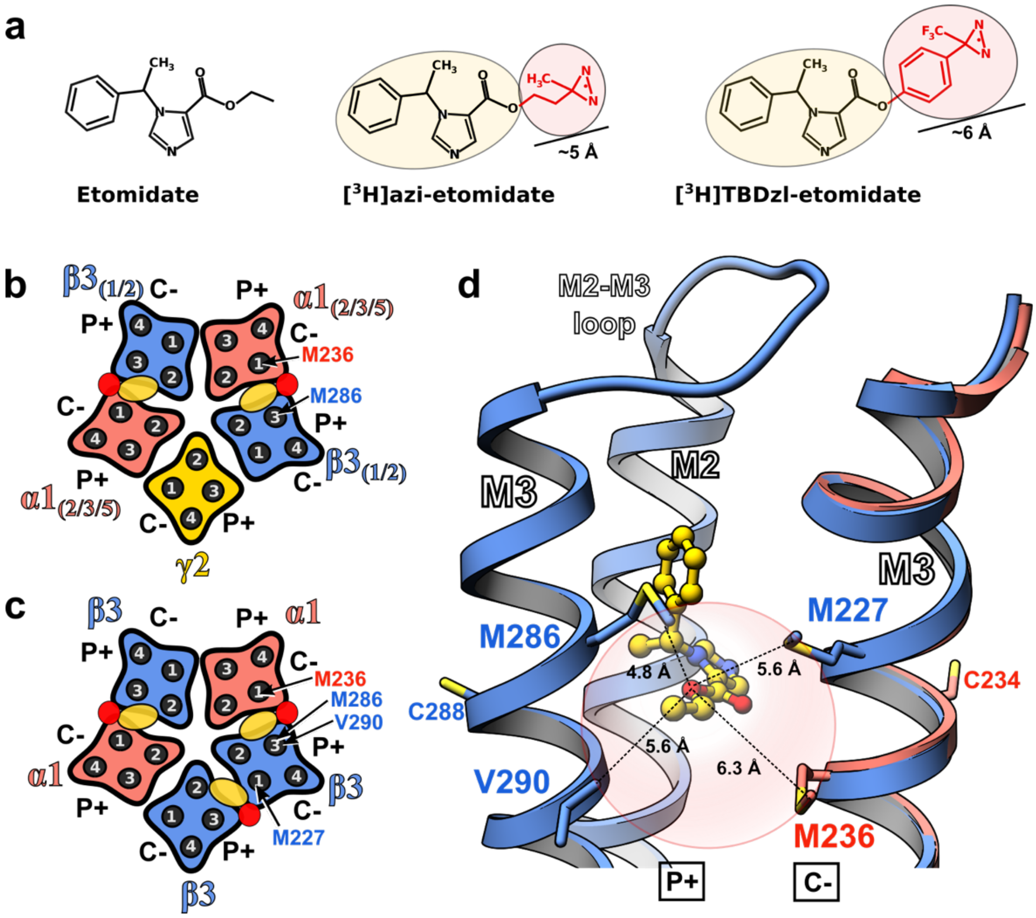

Figure 4.8 Comparison of etomidate photolabelling findings with the etomidate binding mode in $\beta3_{K279T}$-Nb25$_{ETM}$ structure.

a, Structures of etomidate and its functionally active photolabelling derivatives. Etomidate core is highlighted in light yellow, whereas the photoreactive label moieties attached through ester functional group are highlighted in light red. **b,c,** Schematic representation of α1β3 and αβγ GABA$_A$R heteromer TMDs showing azi-etomidate **(b)** and TBDzI-etomidate **(c)** binding sites and the labelled amino acids. GABA$_A$R β subunits are coloured in blue, α subunits in red and γ subunits in yellow. **d,** Photolabelled amino acid location in relation the $\beta3_{K279T}$-Nb25$_{ETM}$ etomidate binding pocket. Light red circle indicates the area accessible for photoreactive label moieties based on the etomidate position in the $\beta3_{K279T}$-Nb25$_{ETM}$ structure. Distances are shown between etomidate ester linkage to the terminal carbon atoms of the photolabelled amino acid side chains. α5 TMD (PDB 5O8F) was aligned to β3 TMD to depict the position where Met236 would be located on α1 subunit M3 helix.

4.6.2. Etomidate binding at heteromer interfaces

To understand the etomidate binding specificity in the heteromeric receptor context, I compared the amino acid sequences of α and β subunits and their corresponding surface profiles (Fig. 3.9a-d). Since β3(P+) face constitutes most of the pocket, these amino acids are highly likely to be the key determinants for etomidate potentiation (Fig. 3.9a). Firstly, it has been shown that only β2 and β3 subunit-containing $GABA_A$ receptors are modulated by etomidate (Hill-Venning et al., 1997). The only amino acid position which is different between β subunits at the etomidate binding pocket at the β-(P+) face is the M2-15′, where Asn265 is present in β2/3 subunits and Ser265 present in β1 subunit (Fig. 3.9e). Indeed, βAsn265 was shown to be the key residue in β subunits determining the sensitivity to the etomidate and propofol. For example, when Ser265 was replaced by asparagine in the β1 subunit, it enabled the resulting $GABA_AR$ heteromers to be modulated by both propofol and etomidate, whereas the N265S mutation in β3 subunits ablated such modulation (Cestari et al., 2000). In addition, the Asn265 mutations to amino acids with aliphatic side chains inhibit $GABA_AR$ modulation by the general anaesthetics. Electrophysiology studies revealed that the β2N265M mutation completely eliminated etomidate modulation (Desai et al., 2009; Siegwart et al., 2003), whereas the response of β3N265M mice to etomidate and propofol was severely compromised (Jurd et al., 2002). Similarly, the β2N265C mutation eliminated etomidate potentiation in α1β2γ2L receptors and high etomidate concentrations (300 mM) did not inhibit Cys265 modification by a water-soluble thiol modifier (Stewart et al., 2014). It seems that aliphatic side chains likely sterically block etomidate binding in the pocket, whereas smaller polar uncharged amino acids, like serine in β1, are not sufficient to initiate conformational changes needed for etomidate potentiation. Similarly to β1, all α and γ subunits contain a serine residue at this site and therefore they are not able respond to etomidate binding (Fig. 3.9b,e). All these results hint that size and chemical properties of the residue occupying M2-15′ are specifically linked to $GABA_AR$ gating upon general anaesthetic binding.

At the entrance to the etomidate binding pocket, α subunits have only small hydrophobic amino acids (αAla291 and αAla295), whereas β subunits possess larger Met286 and Val290 residues (Fig. 3.9a,b,e). It seems that the size of the hydrophobic amino acid at this site matters for etomidate modulation. For example, when β2Met286 was replaced by a smaller cysteine residue, etomidate potentiation of GABA-elicited currents was weakened 12-15-fold and the ability of etomidate to activate GABA$_A$R at high concentrations was abolished (Stewart et al., 2013b). However, if the amino acid at this site contains a bulky side chain, completely different results are obtained. βMet286 mutation to tryptophan (β2M286W) inhibited etomidate binding and induced spontaneous gating (Stewart et al., 2008). Based on the β3$_{K279T}$-Nb25$_{ETM}$ structure it clear that a tryptophan side chain would mimic the etomidate phenyl group and hence would have similar functional consequences for GABA$_A$R gating. Propofol modulation was similarly affected by variation of the amino acid side chain size at the βMet286 site (Krasowski et al., 2001). The β3$_{K279T}$-Nb25$_{ETM}$ structure suggests that β3Met286 constitutes a hydrophobic wall of necessary size against which the phenyl ring of the etomidate (or propofol) can rest and engage with the βAsn265 residue in order to modulate the activity of the channel. Equivalent residues in α and γ subunits are smaller, thus they cannot perform the same function. In contrast, complementary faces of α and β subunits have hydrophobic amino acids with similar size and properties, therefore they permit etomidate's binding to both β(P+)-α(C-) and β3(P+)-β3(C-) interfaces equally well (Fig. 3.9d).

Based on the surface property analysis of α and β at the etomidate binding site, it seems that etomidate could also access the equivalent pocket at the α(P+)-β(C-) interface, as there are no large amino acids which would obstruct its binding. However, this interface lacks important etomidate activity determinants, notably, βAsn265 and βMet286, therefore etomidate cannot modulate receptor function through this interface. In future, it would be interesting to perform molecular dynamics simulations of the etomidate bound at the β(P+)-α(C-), α(P+)-β(C-) and β3(P+)-β3(C-) interfaces to better understand the interplay between this general anaesthetic and the amino acids in these pockets.

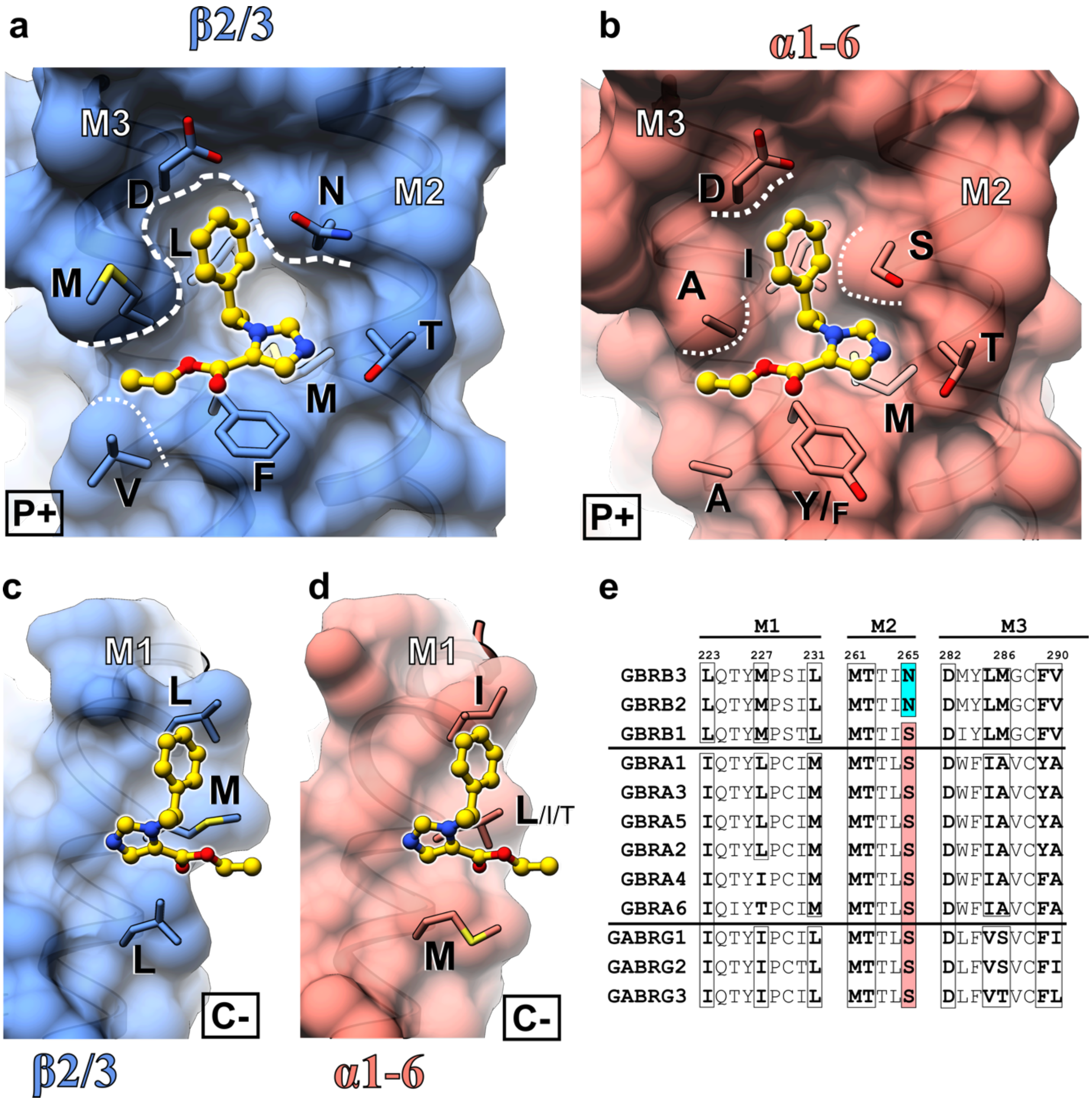

Figure 4.9 Amino acid conservation in the etomidate potentiation site.

a-d, Surface and cartoon representation of the β2/3 P+/C- and α1-6 P+/C- interfaces at the region of etomidate binding. For α α5 TMD from $\beta3_{ECD}\alpha5_{TMD}$ bound to pregnanolone (PDB 5OJM) was used to represent the α subunit interface. **e,** Multiple sequence alignment of M1, M2 and M3 motifs containing etomidate binding pocket residues. The critical Asn265 residue unique to β2 and β3 subunits is highlighted in cyan, whereas the equivalent serine residues present in α and γ subunits are coloured in salmon. Sequence numbering above the alignment is based on β3 subunit (mature isoform 1).

4.6.3. Etomidate binding impact on the β3-β3 interface

To understand what are the structural consequences of etomidate binding between two β3 TMDs are, I superimposed two neighbouring TMDs from the apo and etomidate-bound structures. Most notably, etomidate binding to the pocket between β3-β3 impacted on Asn265 and pushed it away (Cα displaced by 1.3 Å) (Fig. 3.10a). This happened in order to accommodate the phenyl ring of etomidate, which is wedged in tightly between the Asn265 and Met286 residues (Fig. 3.10b). In addition, the imidazole ring of etomidate displaced Thr262 (Cα displacement by 1.3 Å). The combined effect of etomidate impact to the Asn265 and Thr262 residues caused the "top" (C-terminal) portion of the M2 helix to flex along the residue positions 20′-10′ and rotate outwards relative to the pore axis (Fig. 3.10b,c). Such M2 straightening also affected the M2-M3 loop. Pro273, a residue which mediates the signalling between the ECD and the TMD, was pushed up and towards the pore axis (Cα displacement by 0.8 Å) (Fig. 3.10b). Arg269 maintained its side chain configuration and the stabilising hydrogen bonding to the M2-M3 loop as in the apo-structure (Fig. 3.10b). In addition to this, etomidate binding had an impact on the M1 helix at the complementary β3 face. Met 227 (Cα displaced by 0.6 Å) and Leu231 (Cα displaced by 0.9 Å) were displaced by the etomidate ester functional group which resulted in the whole M1 helix being pushed away from the β3-β3 interface (Fig. 3.10a,c). Interestingly, the Met286 and Val290 did not move significantly, implying that the M3 helix at the principal face acted as a support against which the etomidate molecule was pushing the M2 and M1 α-helices.

Overall, etomidate binding resulted in a significant rearrangement at the interface between the β3-β3 TMD. Most importantly, the Asn265 residue was shown to act as the key "sensor" amino acid involved in transferring the conformational change from the etomidate binding pocket to the pore lining M2 helix. This is in close agreement with various mutagenesis studies described in the previous section, which indicated the essential role of this residue in etomidate and propofol activity.

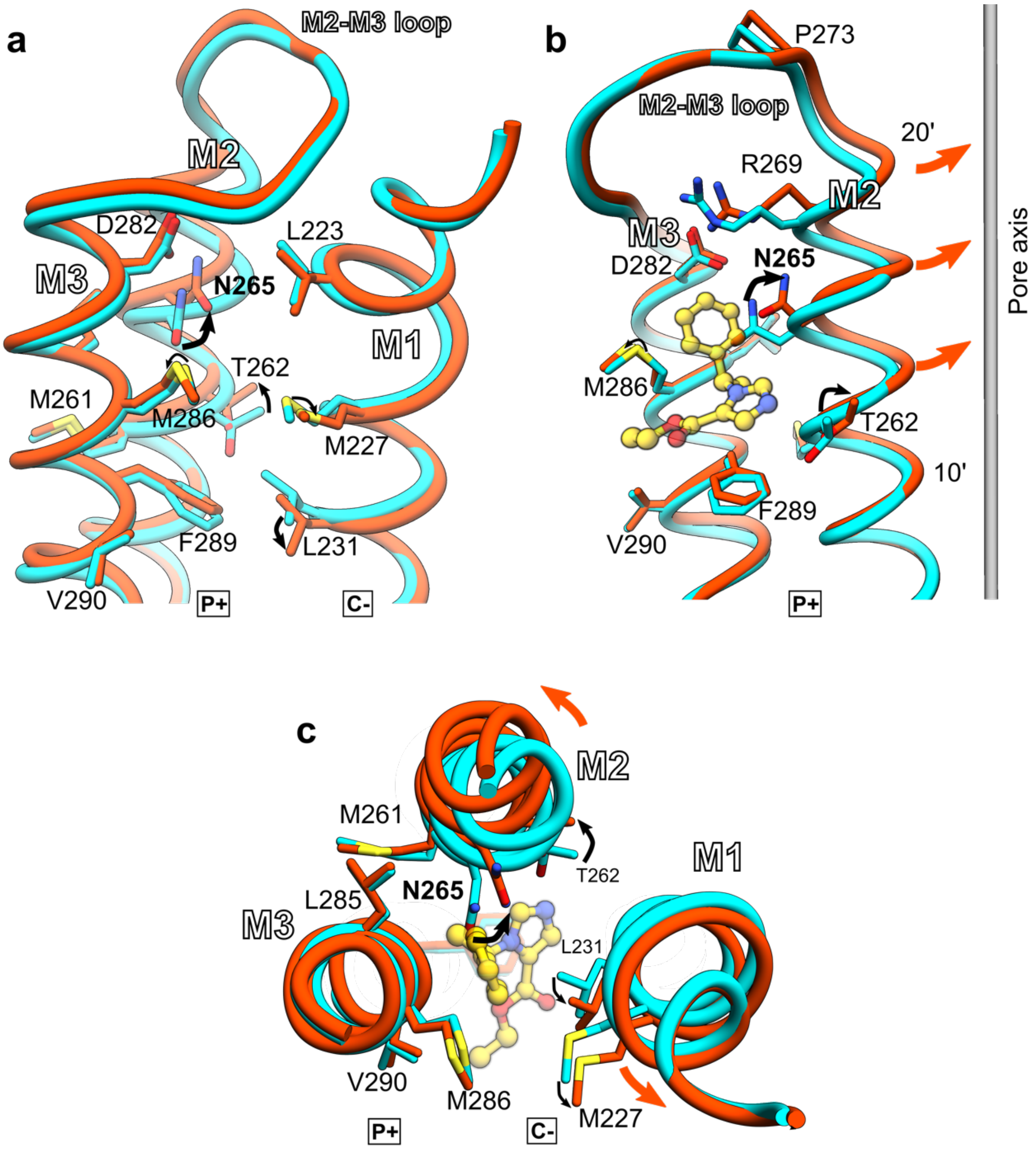

Figure 4.10 β3-β3 TMD interface remodelling upon etomidate binding.

a-c, Conformational changes in the etomidate binding pocket at the β3-β3 intersubunit interface as viewed from the membrane towards the interface **(a)**, from the perspective of the complementary face **(b)** and from the intracellular space **(c)**. To highlight the conformational changes, two neighbouring TMDs for β3$_{\mathrm{K279T}}$-Nb25$_{\mathrm{Apo}}$ (cyan) and β3$_{\mathrm{K279T}}$-Nb25$_{\mathrm{ETM}}$ (orange) were superimposed using SHP (Stuart et al., 1979). Etomidate is not shown in panel **(a)** in order not to obstruct the view of M2 helix. Amino acid motion is indicated with black arrows; motion of the whole helix is indicated with orange arrows.

4.6.4. Global structural consequences of etomidate binding to TMD

To examine the global impact on the $\beta3_{K279T}$ homopentamer structure caused by the etomidate binding, I compared the whole subunits of the apo- and etomidate-bound structures. Differences between individual subunits (RMSD in the 0.72-0.81 Å range between different subunit chains, over 333 equivalent Cα positions) because the ECD and TMD adopt different relative poses. It seems that etomidate binding at the β3-β3 inersubunit pocket had some long-range effects, which were transmitted to the ECD via the M2-M3 loop (Fig. 3.11a). The flexing of the M2 helix resulted in M2-M3 loop pushing against the ECD β1-β2 loop. The combined effect of this motion in the etomidate-bound structure led to the straightening of both the ECD and TMD when compared to the pore axis (Fig. 3.11b). Such relative ECD and TMD motions during allosteric modulation have been described for other pLGICs before, for example, for nAChR (Unwin and Fujiyoshi, 2012), GluCl (Althoff et al., 2014), GlyR (Du et al., 2015) and $\beta3_{ECD}\alpha5_{TMD}$ chimeras (Miller et al., 2017).

To inspect more closely the overall etomidate binding effect across five TMDs, I used the SHP software (Stuart et al., 1979) to align the transmembrane region (residues 217 – 447) of for $\beta3_{K279T}$-Nb25$_{Apo}$ and $\beta3_{K279T}$-Nb25$_{ETM}$ structures. Etomidate binding impacted on the M2 helix which in turn resulted in an overall anti-clockwise rotation of the TMDs (Fig. 3.12a). The pore diameter analysis indicates that the upper portion of the pore-lining M2 helix from $\beta3_{K279T}$-Nb25$_{ETM}$ structure is bent towards the pore axis, however the desensitisation gate at Ala248 is still shut (Fig. 3.12b). From thermostability experiments it was clear that the K279T mutation increases GABA$_A$R-β3 stability in the detergent. The apo-state structure revealed that the receptor was stabilised in the desensitised state. Therefore, it seems that etomidate binding was not enough to disrupt this desensitised receptor state, even though large conformational changes take place at the "top" of the TMD. Since the M2 helix is just flexing upon etomidate binding and not moving as a rigid body, it is not immediately obvious how exactly etomidate binding helps to open the channel.

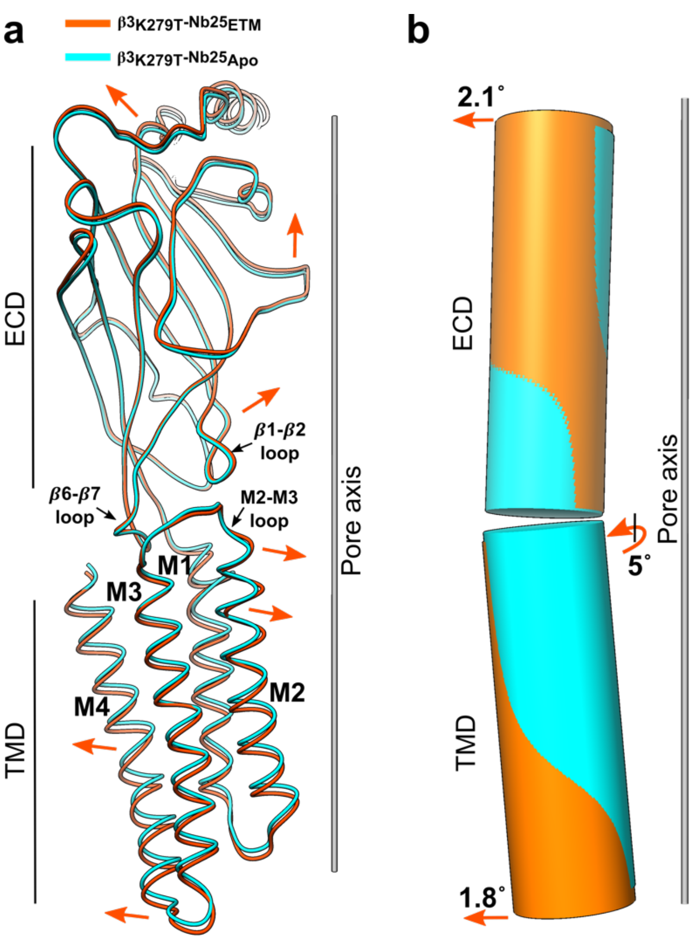

Figure 4.11Global GABA$_A$R-β3K279T conformational changes induced by etomidate.

a, Side view of globally aligned whole subunits (A chains) for β3$_{K279T}$-Nb25$_{Apo}$ (cyan) and β3$_{K279T}$-Nb25$_{ETM}$ (orange) structures. Orange arrows indicate motions occurring during small conformational changes across the ECD and TMD. **b,** Side view of apo and etomidate-bound state ECDs and TMDs represented as centre of mass vectors (using UCSF Chimera (Pettersen et al., 2004)). Upon the etomidate binding, the interface between the ECD and TMD acts as a pivot point along which ECD and TMD move relative to each other. The TMD tilts sideways by 5° and straightens up by 1.8°, whereas the ECD straightens by 2.1°. Structure alignment was performed using the SHP software (Stuart et al., 1979).

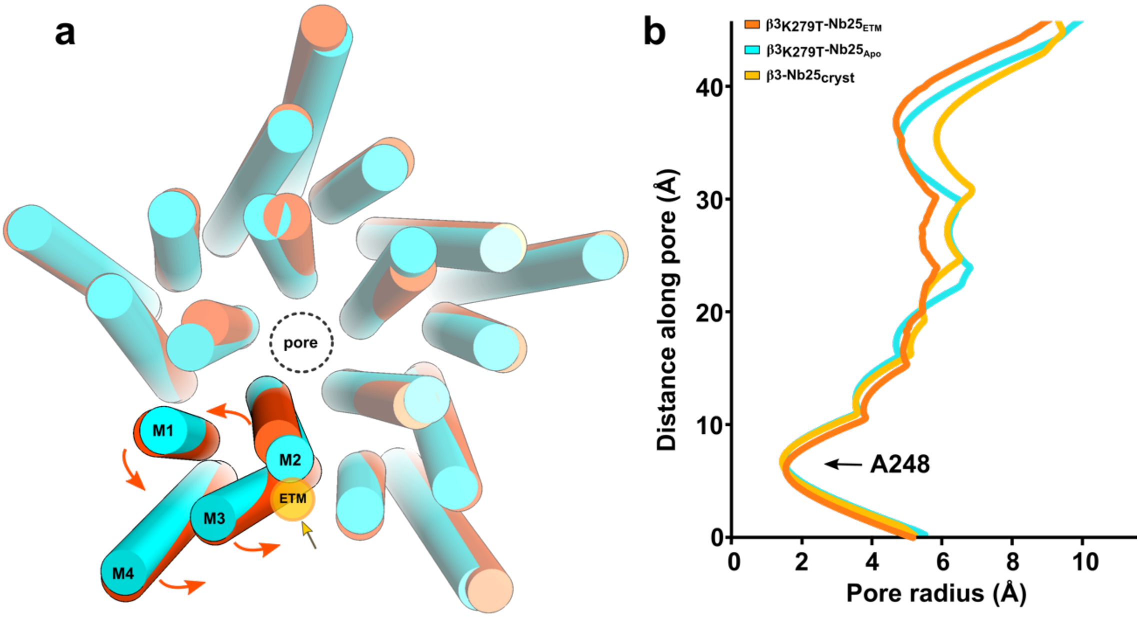

Figure 4.12 Etomidate-induced TMD conformational changes

a, Top view of globally aligned transmembrane domains of β3$_{K279T}$-Nb25$_{ETM}$ (orange) and β3$_{K279T}$-Nb25$_{Apo}$ (cyan) structures. TMD α-helices were depicted as rods using UCSF chimera (Pettersen et al., 2004). Orange arrows represent rotation motion direction upon etomidate (yellow circle) binding. **b,** Pore diameter analysis of β3-Nb25$_{cryst}$ and β3$_{K279T}$-Nb25$_{Apo}$ and β3$_{K279T}$-Nb25$_{ETM}$ structures. Desentisation gate at Ala248 is marked by an arrow.

4.6.5. Conclusions

General intravenous anaesthetics are important drugs targeting the central nervous system and used every day in clinical settings. However, anaesthetics are also very potent compounds which can cause death if the dose is not managed properly. Better structural understanding of how these drugs interact and modulate GABA$_A$Rs is necessary for rational drug design to improve their safety. In order to obtain higher resolution X-ray crystal structures of β3 homopentamer in complex with general anaesthetics, I used the β3$_{K279T}$ mutant which was more thermostable in detergent than the previous β3 construct. This mutant exhibited interesting physiological properties, where high proportions of the receptor were in an open state while in the membrane, however in detergent it was stabilised in the desensitised state. By comparing the GABA$_A$R-β3 and GABA$_A$R-β3$_{K279T}$ structures, I found out that actually it is the Arg269 residue which mediates this functional effect. By substituting the larger and positively charged Lys279 residue with a smaller threonine, Arg269 side chain is not sterically hindered to adopt a different conformation. Through multiple putative hydrogen bond interactions, this side chain position potentially rigidifies and strengthens the connection between the M2, M3 α-helices and the M2-M3 loop. This might be linked to a more efficient signal transduction from the ECD to the TMD. Since the Arg269 residue is highly conserved among human $GABA_AR$s and glycine receptors (Appendix section 10.3) it would be interesting to produce Arg269 mutants and characterise their functional behaviour by electrophysiology. In addition, α and γ subunits contain a threonine in the equivalent site to βLys279. This implies that these subunits should also show the tendency to adopt a conformation which leads to an open state, a behaviour seen in $\beta3_{ECD}\alpha5_{TMD}$ chimera and $\beta3_{K279T}$ homopentamers. Further analyses should clarify why M2-M3 loops in β subunits have different properties compared to α and γ subunits, and whether this is linked to agonist GABA binding specificity to β(P+) interface in heteromeric αβγ $GABA_A$ receptors. Further electrophysiology and structural biology experiments should be carried out to answer these questions.

The etomidate-bound structure of $GABA_AR$-$\beta3_{K279T}$ helped to better understand how general intravenous anaesthetics modulate $GABA_AR$ function. Etomidate potentiates $GABA_AR$ αβγ heteromers when it is bound to β(P+)α(C-) interface. The $\beta3_{K279T}$-$Nb25_{ETM}$ structure combined with previous mutagenesis studies helped to appreciate why β2/3 subunits confer such functional selectivity. I would single out two amino acids, βMet286 and βAsn265, as the major determinants for the etomidate activity. In $GABA_AR$s, both residues are conserved only in β2/3 subunits and they are intimately linked to etomidate binding (Fig. 3.13). Etomidate binding remodels the anaesthetic pocket by inserting its phenyl group between these amino acids and the resulting displacement of the asparagine residue transmits the conformational change to the M2 pore-lining helix. However, from these particular crystal structures it is still not clear how this particular conformational change is linked to increased open channel probability in heteromeric $GABA_AR$s. One can postulate that etomidate binding in this pocket will prevent $GABA_AR$-β3 subunit from adopting a desensitised conformation.

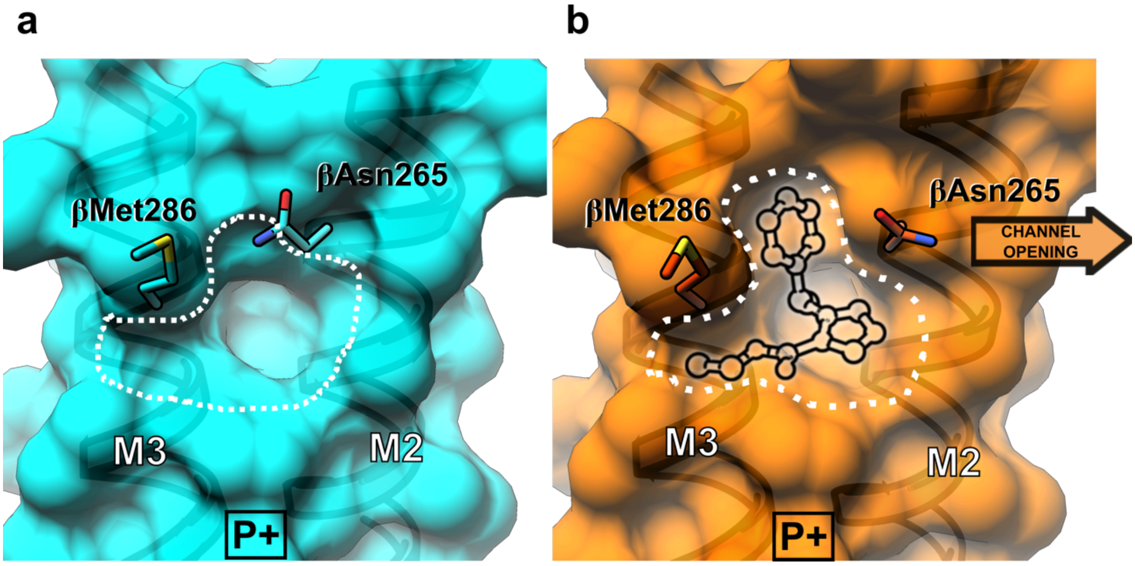

Figure 4.13 Anaesthetic pocket expansion induced by etomidate binding.

a,b, Anaesthetic pocket viewed from complementary subunit perspective in apo-state **(a)** and when etomidate is bound **(b)**. Pocket shape is demarcated in a white dotted line. Note, how βAsn265 and βMet286 are pushed apart from each other by the insertion of the etomidate phenyl ring leading to channel opening.

In addition, propofol, a potent and widely used intravenous general anaesthetic (McKeage and Perry, 2003), was shown to bind close to both βMet286 and βAsn265 residues based on cysteine substitution and photolabelling studies using *m*-azi-propofol (azi-P*m*) (Bali and Akabas, 2004; Stewart et al., 2013a, 2013b, 2014) (Fig. 3.14a) These findings suggested its binding pocket overlaps with the etomidate site. However, β3 homomer and α1β3 heteromer photolabelling with *o*-propofol diazirine (*o*-PD) identified a single βHis267 residue labelled and a different propofol binding site was proposed (Yip et al., 2013) (Fig. 3.14a). In the desensitised β3 X-ray crystal structures this residue faces the pore and there are several pockets which could accommodate binding of propofol (Franks, 2015). However, it was suggested that such βHis267 photolabelling can be explained by TMD rotation which prepositions the βHis267 to the etomidate pocket as indicated by homology modelling using GluCl open state structure (Stern and Forman, 2016). Indeed, the β3$_{\mathrm{K279T}}$-Nb25$_{\mathrm{ETM}}$ structure seems to corroborate this proposal since etomidate binding causes TMDs to rotate slightly and positions the His267 closer to the etomidate binding pocket (Fig. 3.14b). In addition, propofol possesses a phenyl ring which might demonstrate a similar binding mode to the etomidate phenyl group, explaining the photolabelling of the βM286 or αM236 residues.

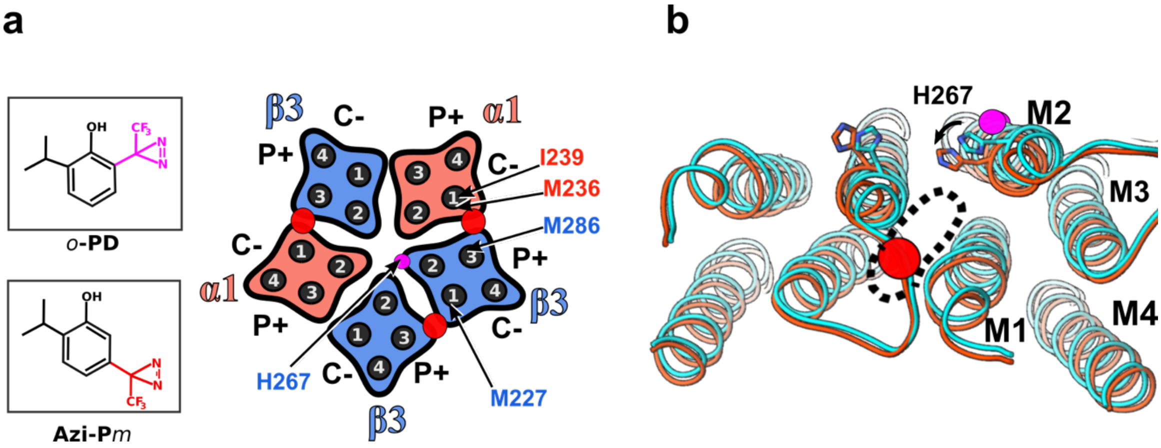

Figure 4.14 GABA$_A$R photolabelling with photoreactive analogs of propofol.

a, Schematic representation of a α1β3 GABA$_A$R heteromer with locations shown for amino acids labelled by *o*-propofol diazirine (*o*-PD, photoreactive group coloured in pink) and *m*-azi-propofol (azi-P*m*, photoreactive group coloured in red). Putative propofol binding pocket based on the *o*-PD result is marked as a pink circle, whereas the red circle shows the Azi-P*m* pholabelling site. **b,** Top view of superimposed β3$_{K279T}$-Nb25$_{ETM}$ (orange) and β3$_{K279T}$-Nb25$_{Apo}$ (cyan) TMDs shows His267 rotating towards the etomidate pocket.

To conclude, data presented in this chapter describe the first structural characterisation of a general anaesthetic bound to a GABA$_A$ receptor. This structure provides insights into how etomidate binding deforms the interface between the subunits and the conformation of the M2 pore-lining α-helices. Given that the etomidate binding site appears to be shared by other anaesthetics, these mechanisms will likely have a broader relevance. Future experiments will focus on obtaining diffraction quality crystals for the structural characterisation of propofol or pentobarbital binding modes.

5. Analysing GABA$_A$ receptors with cryo-electron microscopy

5.1. Introduction

Recent advances in cryo-electron microscopy is revolutionising structural biology. With the advent of the new direct electron detectors and image processing algorithms, cryo-EM single particle analysis now enables protein imaging at a speed and resolution which was not conceivable several years ago (Bai et al., 2015b; Callaway, 2015; Kühlbrandt, 2014). For membrane proteins, cryo-EM can routinely be used to determine structures at resolutions of 3.0-4.5 Å (Bai et al., 2015a; Du et al., 2015; Liao et al., 2013), and for soluble bacterial proteins resolution can achieved as high as 1.8 Å (Merk et al., 2016). There are major differences between single particle cryo-EM and X-ray or electron crystallography. In single particle cryo-EM, there is no need to form protein crystals, so it is a very attractive technique for membrane protein structural biology research, since these proteins are difficult to crystallise. Using this method, protein sample is simply deposited onto holey cryo-EM grids and rapidly frozen in liquid ethane at temperatures below -150 °C. As a result, protein particles are embedded into a thin layer (90-130 nm) of vitreous ice (Cho et al., 2013). In cryo-EM, proteins are frozen close to their native state because vitreous ice does not form a crystalline lattice, which would otherwise damage their secondary structure. In addition, cryoEM grids can be made using standard purification buffers without being subjected to extreme mother liquor conditions as in X-ray crystallography. Another advantage of cryo-EM is significantly lower amounts of protein required for grid preparation (micrograms of protein instead of milligrams). This is particularly important for transient multi-protein complexes obtainable from endogenous sources, or membrane proteins which are difficult to overexpress recombinantly in amounts sufficient for X-ray crystallography (Mesa et al., 2013). Cryo-EM can also provide means to analyse membrane proteins in more natural lipid bilayer systems through use of nano-scale lipid discs (Denisov and Sligar, 2017; Frauenfeld et al., 2016; Gao et al., 2016; Postis et al., 2015). In addition, methods are also available for capturing short-lived membrane protein conformational states through rapid spraying and mixing of protein sample with modulatory compounds, fractions of a second before freezing in liquid nitrogen (Berriman and Unwin, 1994; Unwin and Fujiyoshi, 2012). Most importantly, i*n situ* "particle purification" approach in cryo-EM can make near-atomic resolution structure determination possible for heterogeneous protein samples (Bai et al., 2015c), another feat which otherwise would not be feasible by using X-ray crystallography. Recently, single particle cryo-EM was used to investigate multiple pentameric glycine receptor conformations to provide insights into its gating cycle (Du et al., 2015), an important step forward in Cys-loop receptor research.

Cryo-EM single particle analysis also has its limitations. The major issue is the size of particles which can be aligned correctly to yield high resolution structures. Currently, imaging of particles with molecular mass lower than 200 kDa can be problematic due to low contrast and signal-to-noise ratio. In membrane protein samples, where detergents are used, this problem can be exacerbated due to the extra noise from the free detergent monomers and micelles. In future, when cryo-EM imaging using Volta phase plates is better established, it will be possible to perform 3D-reconstruction of particles with molecular mass down to ~50 kDa to near-atomic resolution routinely (Khoshouei et al., 2017). However, this technique is still not available in most laboratories doing cryo-EM research at the moment. Since $GABA_A$ receptors are around ~200 kDa, the small size problem can be mitigated through the use of llama nanobodies. Binding of camelid nanobodies to $GABA_A$Rs would increase particle size and contrast in cryo-EM micrographs, enabling to pick and align them easier. Most importantly, tagging a specific set of subunits with antibody fragments would allow to perform correct alignment and classification of heteromeric human $GABA_A$ receptor particles. Otherwise, the pseudo five-fold symmetric structure of this protein most likely would not provide enough low resolution features for correct particle alignment during the initial 3D reconstruction stage (averaging different subunits).

In this chapter I will describe our attempt to examine whether $GABA_A$R structural determination is possible using cryo-EM single particle analysis and whether llama nanobodies can be applied as subunit tags, setting the stage for the heteromeric $GABA_A$R structural studies.

5.2. Determining cryo-EM structure of GABA$_A$R-β3-Nb25 solubilised in detergent

5.2.1. Cryo-EM data collection and processing

The same detergent-solubilised GABA$_A$R-β3-Nb25 sample, which was used for X-ray crystallography (Chapter 2), was also utilised for cryo-EM grid preparation. Data were collected on a TF30 Polara (FEI Company) microscope operating at 300 kV and fitted with a K2 Summit direct electron detector (Gatan). The presence of the detergent affected sample surface tension properties, which caused uneven ice thickness across the grid holes and forced particles to move closer to the hole edge (Fig. 4.1a,b). This local crowding effect might also be the reason why there were large aggregates intermixed with single particles (Fig. 4.1b), even though grids were prepared directly after the size exclusion purification. However, such detergent-induced ice gradient across grid holes allowed data collection from areas with thin ice and minimal background. To maximise particle numbers, cryo-EM images were manually collected by exposing holes close to the edge of carbon substrate. In total, 1004 micrographs were collected in two 24 h sessions. Carbon support, as a high contrast material, increased the signal for contrast transfer function (CTF) calculation (Fig. 4.1c). However, CTF estimated for the whole micrograph might be biased by carbon signal, therefore local particle CTF estimation was performed using Gctf software (Zhang, 2016). Several thousands of particles were picked in semi-automatic fashion and were 2D-classified using Relion (Scheres, 2012a). 2D classes with representative particle views (Fig. 4.1d) were used as templates for automated particle picking with Gautomatch (Kai Zhang, MRC-LMB). A considerable amount of time was spent manually removing false-positives from carbon edges and aggregates to clean up the auto-picked dataset. In total, 73,800 particles were selected from 1003 micrographs and used for further processing

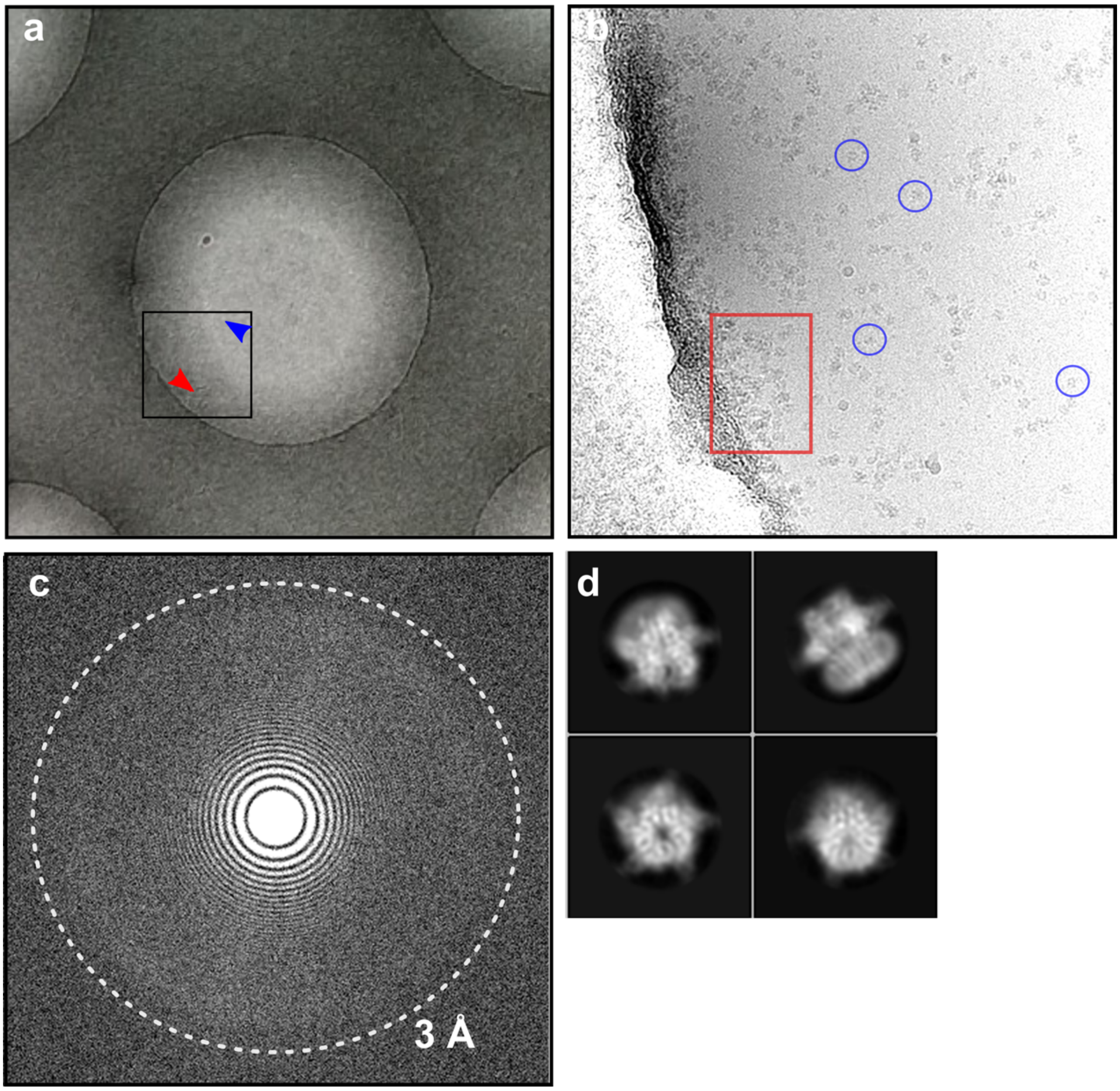

Figure 5.1 cryo-EM grids and particle distribution in ice.

a, A low magnification image of a cryo-EM grid showing uneven ice distribution in a hole. Red arrow points at a thicker ice area populated with larger numbers of particles, whereas the blue arrow indicates the thinner ice area with less or no particles. Black square represents an area where a cryo-EM micrograph would be taken from. **b,c,** A representative cryo-EM micrograph for GABA$_A$R-β3-Nb25 sample showing single particles suitable for picking (blue circles) and large protein aggregates (red rectangle) **(b)** and the Thon rings for this micrograph **(c)**. **d,** Representative 2D classes obtained from manual particle picking showing top and side views of GABA$_A$R-β3-Nb25 particles.

The advent of graphics processing unit (GPU)-accelerated computing and novel algorithms have significantly reduced data processing time (Kimanius et al., 2016; Punjani et al., 2017; Zhang, 2016). Previously, using central processing unit (CPU) clusters for computation, the 3D reconstruction of this dataset would have taken several weeks, whereas now the whole process can be completed in mere hours. To demonstrate the advances in the cryo-EM computation field, GABA$_A$R-β3-Nb25 data processing was performed using cryo-EM single particle *ab initio* reconstruction and classification (cryoSPARC) software (Punjani et al., 2017). CryoSPARC uses stochastic gradient descent (SGD) and branch-and-bound maximum likelihood optimization algorithms for *ab initio* model production and refinement. At each iteration, the SGD algorithm randomly initiates 3D structures from small subsets of particles and calculates the gradient of the approximate objective function. The objective function determines how well a 3D reconstruction explains the experimental particle images. SGD optimization scheme incrementally explores the space of possible 3D maps over many noisy steps. By approximate and quick objective function determination, SGD escapes the local optima and arrives towards the correct structure. The low resolution *ab-initio* structure is then used as an initial model for 3D refinement. During the cryo-EM refinement, the optimal orientation parameters are determined for each particle so that the 2D image is best aligned to the 3D density map. The optimal orientation will minimise the error between the observed 2D image and the 3D map projection. CryoSPARC 3D refinement employs the branch-and-bound algorithm to increase the calculation speed during the optimal pose selection. This algorithm uses computationally inexpensive methods to determine the lower bound on the error across the whole search space and then discards large sections which are unlikely to contain the optimum for the objective function, rather than checking every possible position for alignment. At every refinement iteration this procedure is repeated until only the optimal orientations remain. The gold-standard refinement procedure (Scheres and Chen, 2012) with FSC=0.143 criterion (Rosenthal and Henderson, 2003) and masking correction (Chen et al., 2013) is applied throughout the refinement.

GABA$_A$R-β3-Nb25 data processing was performed on a single GPU-machine equipped with a TitanX graphics card (12BG RAM, NVIDIA), a 1 TB NVMe solid state drive (Samsung) and two Xeon E5-2670 processors (8 Core, 2.60 GHz, Intel). From hardware price and energy consumption perspectives, this machine is a much more advantageous computing platform than large CPU clusters and is affordable to most small/medium labs using cryo-EM (Kimanius et al., 2016). The whole procedure from *ab initio* model generation to a refined map with cryoSPARC took only ~4 h and is described in detail in figure 4.2. Different to most commonly used cryo-EM processing pipelines (Cheng et al., 2015), this processing strategy did not use 2D classification step for removal of badly aligning particles before initiating the 3D classification. Performing several rounds of *ab initio* classification and multi-refinement protocols is enough to achieve a high resolution reconstruction (Fig. 4.2).

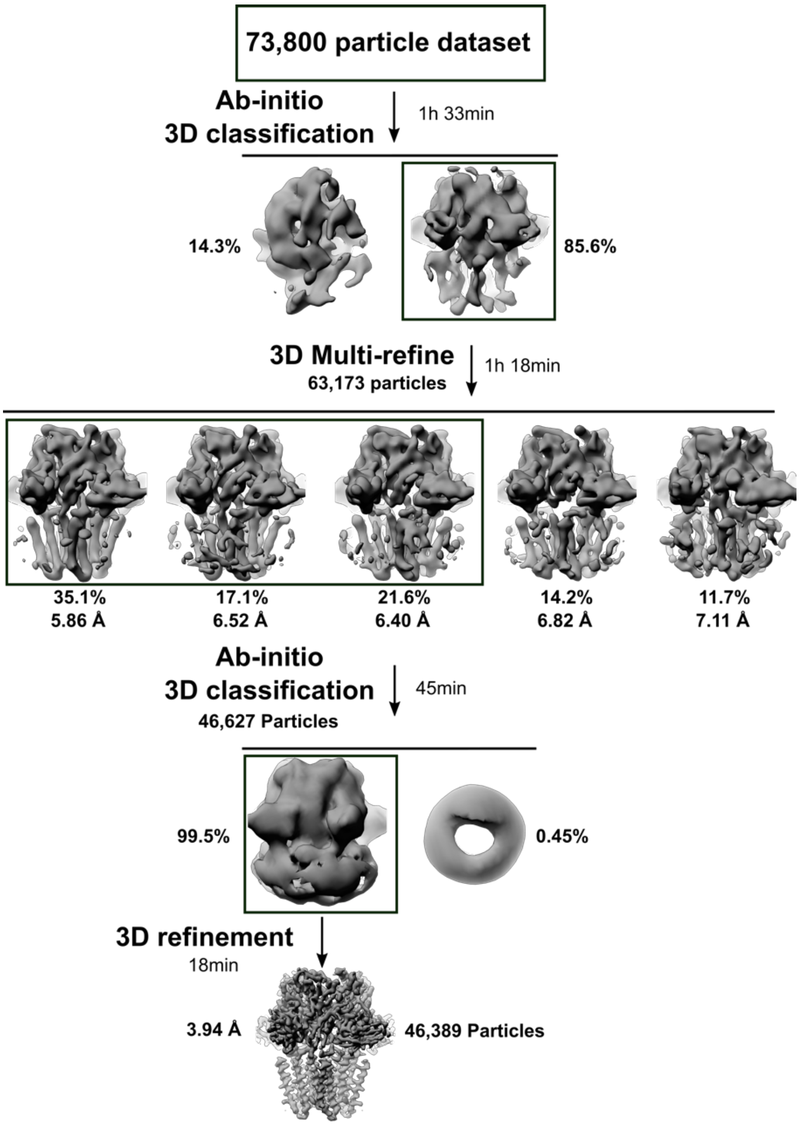

Figure 5.2 GABA$_A$R-β3-Nb25 cryo-EM data processing pipeline using cryoSPARC.

A dataset of 73,800 particles were subjected to *ab initio* 3D classification where data was split between two classes using C1 symmetry. 63,173 particles within the class with the expected protein shape were used for further processing. This class was also used as a starting model for the multi-refinement protocol, which classified and refined the selected data into 5 classes using C5 symmetry. Three best classes were then combined and the resulting 46,627 particles were subjected to *ab initio* classification into two classes again. This step led to removal of a small number of badly aligning particles and the final 3D refinement was performed on 46,389 particles, which led to a refined structure at 3.94 Å (C5 symmetry). This cryo-EM map was used for atomic model building and biological interpretation.

The final refinement produced a map with an overall 3.94 Å resolution based on the gold-standard FSC = 0.143 criterion (Fig 4.3a-c). Cryo-EM map was well ordered with characteristic Cys-loop receptor shape. Previous 2D classification results indicated that a large proportion of classes belong to top/bottom views. Using this particular processing pipeline, there preferred views were automatically discarded since particle angular spread was even throughout the sampling space (Fig. 4.3d). Local resolution analysis reveals that the core of the protein was the most stable and best resolved part, whereas the detergent micelle and nanobody edges were the most flexible regions with lowest resolution (Fig. 4.3e). Further 3D classification analysis using C1 symmetry showed no indication of GABA$_A$R-β3-Nb25 complex populations with less than five nanobodies.

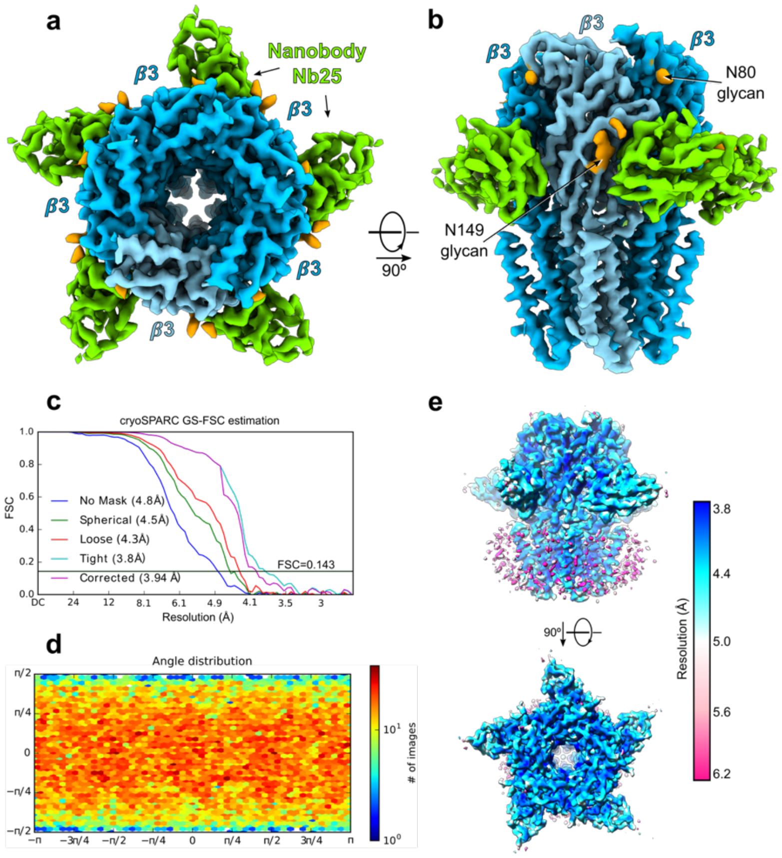

Figure 5.3 Cryo-EM map of GABA$_A$R-β3-Nb25 sample.

a,b, GABA$_A$R-β3-Nb25 cryo-EM map viewed from the extracellular space **(a)** and parallel to the membrane **(b).** Nanobodies are coloured in green, β3 subunits in blue and N-linked glycans in orange. **c,** Fourier shell correlation (FSC) curves for masked and unmasked cryo-EM maps used during the gold-standard 3D refinement. **d,** Angular distributions of particle projections. **e,** Filtered and sharpened cryo-EM map coloured according to local resolution estimation using ResMap (Kucukelbir et al., 2014).

5.2.2. Atomic model building based on the Cryo-EM data

The 3.94 Å map was of sufficient quality to attempt modelling of the GABA$_A$R-β3-Nb25 complex. α-α-helical turns and large side chains were clearly visible, beta strand side chains can be easily traced and the EM density for the N-linked glycan at Asn149 was better defined than in the GABA$_A$R-β3-Nb25 X-ray map (Fig. 4.4).

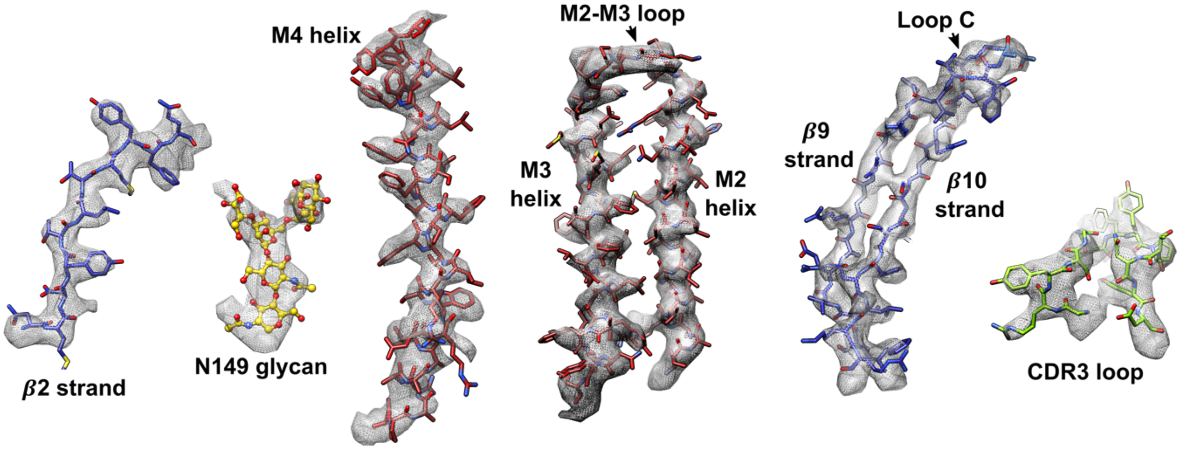

Figure 5.4 Cryo-EM map quality of the GABA$_A$R-β3-Nb25 complex.

Representative examples of various secondary structure elements within GABA$_A$R-Nb25 cryo-EM map with fitted model shown as sticks. Model of strands is coloured in blue, N-linked glycans in yellow, α-helices is coloured in dark red and nanobody loops in green.

For model building, the 3.0 Å GABA$_A$R-β3 X-ray crystal structure (PDB 4COF) and nanobody from the 3.25 Å β3-Nb25$_{APO}$ model were docked into the EM density map with UCSF Chimera (Pettersen et al., 2004) and refined using Rosetta Relax refinement (DiMaio et al., 2009) followed by manual adjustments with COOT (Emsley and Cowtan, 2004). Then multiple rounds of real space refinement with *phenix.real_space_refine* and manual correction with COOT were performed to increase the cross-correlation co-efficient (CC). At this resolution, extra care was taken to maintain a good model stereochemistry. The stereochemistry was evaluated using MolProbity online server (Chen et al., 2010). In addition, due to resolution limitations of the EM map, amino acid rotamers were manually adjusted to match to the 3 Å GABA$_A$R-β3 structure (PDB 4COF), as long as they did not contradict the EM map density. The final refined structure maintained the same general shape of a GABA$_A$ receptor bound to nanobodies as previously solved crystal structures (Fig. 4.5a) To avoid overfitting, the model was validated with accepted procedures (Fig. 4.5b) (Amunts et al., 2014; Brown et al., 2015). Final refinement statistics are shown in table 8.

Table 8 Statistics of cryo-EM data collection and 3D model refinement

	β3-125$_{EM}$
Data collection	
Microscope	FEI TF30 Polara
Voltage (kV)	300
Particles total	73,800
Particles final	46,389
Defocus range (μm)	-2.5 to -1.9
Exposure time (s)	10
Dose rate (e-pix^{-1} s^{-1})	10
Resolution (unmasked, Å)	4.8
Resolution (sharpened, Å)	3.9
Map Sharpening B-factor (Å^{2})	-220
Refinement	
Cross-correlation (volume)	0.8
Protein atoms	18,303
R.m.s deviations	
Bond length (Å)	0.1
Bond angles (°)	0.74
Clashscore, all atoms (percentile*)	3.71 (96th)
Rotamer Outliers (%)	0.0
Ramachandran statistics	
Favoured (%)	97.99
Allowed (%)	2.01
Outliers (%)	0.0
MolProbity score (percentile*)	1.16

* – across all resolution structures, N=1784

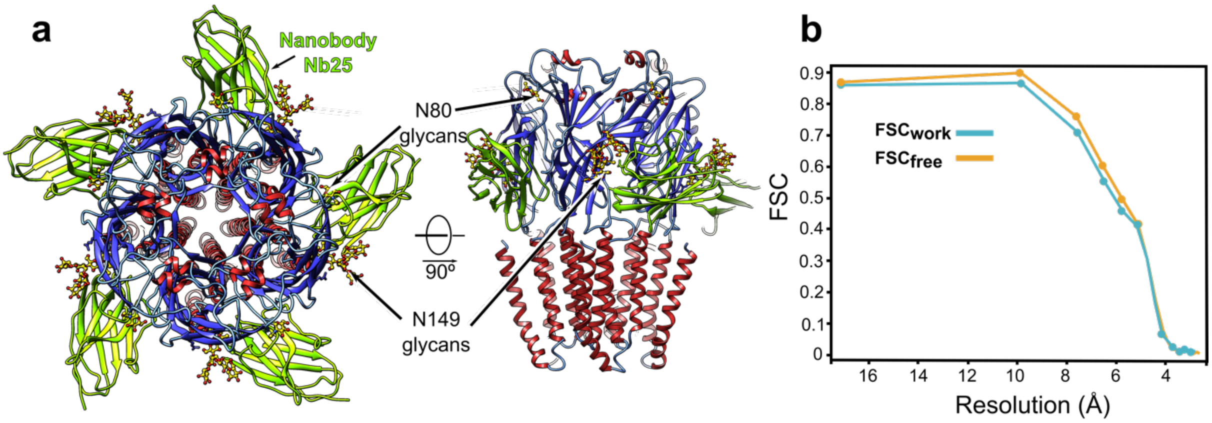

Figure 5.5 GABA$_A$R-β3-Nb25 atomic model built into the cryoEM map.

a, GABA$_A$R-β3-Nb25 model viewed from the extracellular space and parallel to the membrane **(b)**. **b,** For validation, the refined model atoms were semi-randomised (displaced by 0.5 Å RMSD) and refined against the half-map 1. By comparing this "unbiased" structure to the half-map 1, the FSC$_{work}$ (blue) curve was generated. Then FSC$_{free}$ (orange) curve was generated for the original refined model versus the half-map 2. Close agreement between the two curves indicates that there is no significant overfitting during the original model refinement.

5.3. Comparison of X-ray crystallography and cryo-EM structures

GABA$_A$R-β3-Nb cryo-EM model (termed β3-Nb25$_{EM}$) subunit conformation was compared with other available GABA$_A$R-β3-Nb25 homopentamer structures. β3$_{K279T}$-Nb25$_{ETM}$ and β3-Nb25$_{EM}$ are more similar to each other (RMSD in the 0.43-0.56 Å range between different chains, over 333 equivalent Cα positions) (Fig. 4.6a) than β3-Nb25$_{EM}$ and β3-Nb25$_{cryst}$ (RMSD in the 0.71-0.83 Å range between different chains, over 333 equivalent Cα positions) (Fig. 4.6b). Agonist binding loop-C is in the closed conformation in all the analysed GABA$_A$R structures which contrasts to glycine receptor open loop-C conformation (Du et al., 2015; Huang et al., 2015) (Fig. 4.6c). β3-Nb25$_{EM}$ pore outline is similar to other structures and the gate is shut at the Ala248 (Fig. 4.6d) meaning that the receptor is in the desensitised conformation. This finding shows that the desensitised conformation seen across all the analysed X-ray crystal structures is not induced by crystal packing. It further confirms the suspicion that detergent stabilises the desensitised state. A similar effect was observed in acetylcholine receptors where ~57% of receptors were in a desensitisation state when solubilised in CHAPS detergent, whereas in lipid bilayer it is just ~11% as determined by fluorescent agonist binding studies (Martinez et al., 2002).

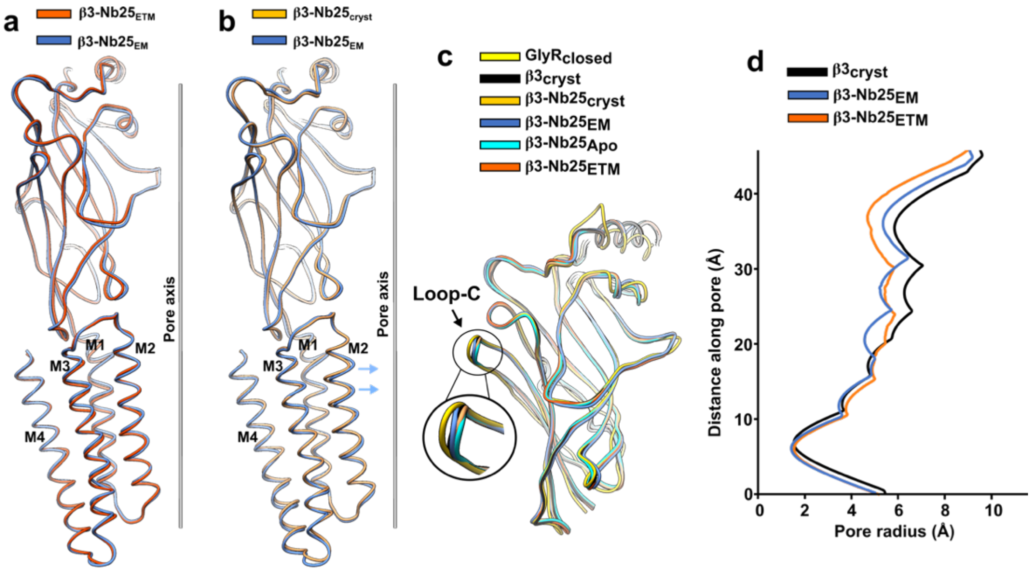

Figure 5.6 Comparison of β3-Nb25$_{EM}$ model with other available GABA$_A$R structures.

a, Subunit alignment between β3-Nb25$_{EM}$ and β3-Nb25$_{ETM}$ indicate that both structures have similar conformations. **b,** Comparison of β3-Nb25$_{EM}$ and β3-Nb25$_{cryst}$ models show that β3-Nb25$_{EM}$ M2 helix is kinked (blue arrows). **c,** Structural alignment between different available GABA$_A$R structure ECDs. Loop-C is zoomed in to show that all GABA$_A$R-β3 structures are in an activated state with loop-C in closed conformation. Glycine receptor in closed conformation (PDB 3JAD) was used to highlight and contrast the its open loop-C to GABA$_A$R counterparts. **d,** Pore radius along longitudinal axis of the channel for β3$_{cryst,}$ β3-Nb25$_{EM}$ and β3-Nb25$_{ETM}$ structures. β3-Nb25$_{EM}$ and β3-Nb25$_{ETM}$ pore outlines are quite similar to each other, although the channel is desensitised in all three cases. The solvent accessible path was calculated using HOLE. All structural alignment was performed using SHP.

β3$_{K279T}$-Nb25$_{ETM}$ and β3-Nb25$_{EM}$ transmembrane domains possess a kink at the top half of the M2 helix which is not seen in β3-Nb25$_{cryst}$ structure (Fig. 4.7a,b). In the β3-Nb25$_{EM}$ structure, this contributes to a more inward pore outline (Fig. 4.6d). The M2 helix kink seems to be related to a small EM density observed at the intravenous anaesthetic binding site between β3-β3 subunits (Fig. 4.7c). Since this density cannot be non-attributable to any of the neighbouring amino acids sidechains, it could be that the anaesthetic pocket is probed by a co-purified lipid head group, similarly to the POPC binding to GluCl channel (Althoff et al., 2014) (Fig. 4.7d). Or it could be part of detergent hydrophobic tails systematically interacting with this pocket. It is difficult to estimate what kind of molecule it is, since the rest of it could not be observed as it is not ordered. Lower local resolution in this area suggests the pocket is flexible and the interaction is dynamic (Fig. 4.7e). It is possible that this density was not observed in other GABA$_A$R-β3-Nb25 crystal structures because constraints and rigidity induced by crystal packing might make transient detergent/lipid interactions with this pocket unfavourable. It was shown that POPS lipid potentiates glutamate binding to GluCl channels, potentially through the same POPC binding site (Althoff et al., 2014). Therefore, it is likely that Cys-loop receptor agonist binding modulation by lipids (daCosta et al., 2013; Nothdurfter et al., 2013) might destabilise this interface and involve similar conformational changes which occur during the etomidate binding.

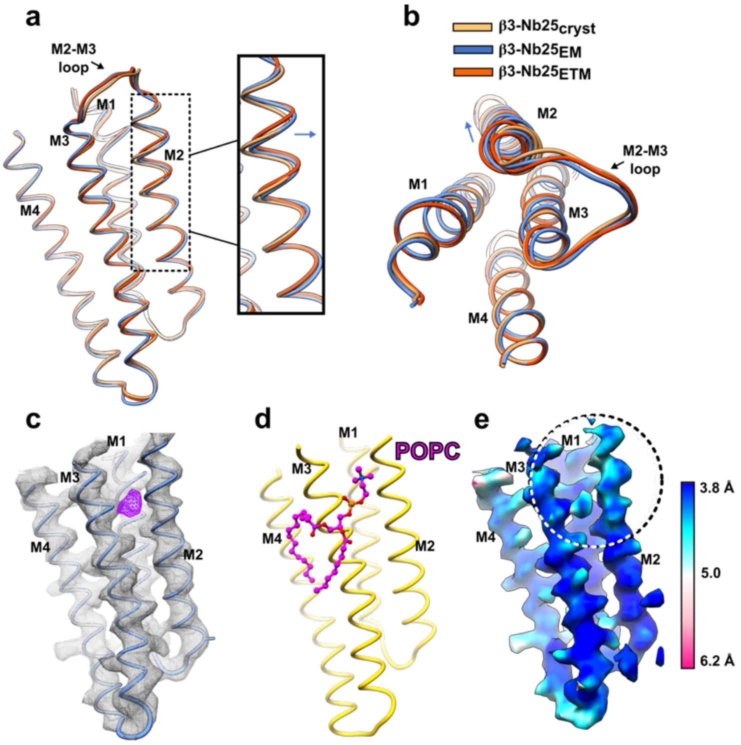

Figure 5.7 Unknown EM density in the etomidate binding pocket alters GABA$_A$R-β3 conformation during cryo-EM imaging.

a,b, Structural alignment of β3-Nb25$_{EM}$ (blue), β3-Nb25$_{ETM}$ (red orange) and β3-Nb25$_{cryst}$ (light orange) TMD regions reveal that both β3-Nb25$_{EM}$ and β3-Nb25$_{ETM}$ M2 α-helices are deformed and pushed towards to the channel pore in a similar fashion (blue arrow indicates the direction of the motion); **(a)** view from a side, **(b)** view from the top. **c,** Cryo-EM map of the TMD region with the outline of the β3-Nb25$_{EM}$ model in blue ribbon. The unknown density is coloured in purple. **d,** Equivalent side view of GluCl TMD region (yellow) bound to POPC (PDB 4TNW). POPC is coloured in purple and its head domain is positioned at the same pocket as the unknown density in the β3-Nb25$_{EM}$ map. **e,** Cryo-EM map of the β3-Nb25$_{EM}$ TMD domain coloured by local resolution estimation with Resmap. Area close to the unknown density (circle with dashed lines) has a lower local resolution estimation than the rest of the M2 and M3 α-helices, indicating higher degree of flexibility.

5.4. Conclusions

Cryo-electron microscopy is a powerful emerging technique for protein structure determination. It allows structural characterisation of membrane proteins, which are difficult to crystallise. Here, I tested whether cryo-electron microscopy can be applied for investigating GABA$_A$R structures using single particle analysis. Structural analysis of GABA$_A$R-β3 homomer was a key proof of principle experiment, because proteins of this size (~ 200kDa) are close to the current technological limits of single-particle cryo-EM. In addition, it was interesting to compare GABA$_A$R-β3 conformation adopted when protein was not in the crystal lattice but in solution. It seems that lack of crystal packing and contacts affect detergent belt plasticity and causes conformational changes in the TMD. This results in etomidate pocket being probed by either detergents or co-purified lipids. As a consequence, the protein adopts a slightly flexed M2 α-helical conformation similar to one observed in the β3-Nb25$_{ETM}$ crystal structure, which suggests potentiation activity. The physiological relevance of potential lipid interactions with this pocket must be studied further.

Since the β3-Nb25$_{EM}$ structure was in a desensitized state it can be assumed that such conformation is not induced by crystal packing but is always present in the solution when protein is solubilized in detergent. This raises questions about the physiological relevance of detergent-solubilized GABA$_A$R structures. To this date, all GABA$_A$R β3 or α5 homomer structures were desensitized (Miller and Aricescu, 2014) (Miller et al, 2017). It is possible that the desensitized conformation is artificially reinforced by the detergent as a low energy state and different conformations can be difficult to obtain. It would be interesting to visualize a different conformational state of GABA$_A$R-β3 homopentamer in the detergent. Since the open state might be short lived and difficult to capture, a closed GABA$_A$R-β3 homomer conformation could be imaged instead. α-bungarotoxin was shown to bind at the β3-β3 interface and it acts as an antagonist on homomeric GABA$_A$R-β3 receptors (McCann et al., 2006). It is likely that α-bungarotoxin binds to the β3 loop-C as observed in the nicotinic acetylcholine receptor α9 ECD-bungarotoxin structure (Zouridakis et al., 2014), stabilizing the β3 homomer closed state. Such an experiment would help to determine whether the GABA$_A$R-β3 homomer closed state is similar to the closed conformation of glycine receptor bound to strychnine (Du et al., 2015).

β3-Nb$_{EM}$ structure determination also confirmed the expectation that nanobodies can help to enhance particle contrast and work well as GABA$_A$R subunit tags. By making the use of the previously available X-ray crystal structures, the 3.94 Å cryo-EM β3-NB$_{EM}$ map was of sufficiently good quality to build a density well-describing and stereochemically correct atomic model. In the absence of prior structural information, *de novo* building of an atomic model from such a map would be more challenging and higher resolution maps (<3 Å) would be needed. Heteromer structure determination would require a significantly higher number of particles to match this resolution. It is to be expected that particle aggregation and low particle numbers in cryo-EM micrographs will make it difficult to obtain large particle numbers for the heteromer dataset. However, cryo-EM maps of GABA$_A$R heteromers with resolutions in range between 4-5 Å would still be very useful for analysing the subunit arrangement and gating cycle. To conclude, it was shown here that it is possible to use single particle cryo-EM for analysing GABA$_A$R homomer structures and that structural investigation of heteromeric GABA$_A$Rs should be feasible with the help of llama nanobodies.

6. Cryo-EM structure of a heteromeric human GABA$_A$-α1β3γ2 receptor

6.1. Introduction

The most common and physiologically relevant GABA$_A$Rs assemble into heteropentamers, which are composed of up to three different subunit types. It is believed, that the major classes of GABA$_A$Rs found in the brain consist of two α, two β and one γ subunits (Olsen and Sieghart, 2008). This modular design accounts for high variation in channel distribution and activity, which translates into a large pharmacological potential. GABA$_A$Rs are key targets for general intravenous anaesthetics like propofol and etomidate, anxiolytics such as benzodiazepines, endogenous neurosteroids and alcohol. To date, only homomeric GABA$_A$Rs could yield structural information explaining their architecture, defining drug binding sites and giving insights into the mechanism of action of this class of pLGICs (Laverty et al., 2017; Miller and Aricescu, 2014; Miller et al., 2017). Structural analysis of GABA$_A$R heteromers by X-ray crystallography was hampered by sample heterogeneity and poorly-diffracting crystals. However, recent developments in cryo-EM opened the possibility to study these proteins without the need of forming crystals. Therefore, we set out to determine the heteromeric GABA$_A$R structures by cryo-EM to characterize their architecture and to gain insights into their mechanisms of action.

6.2. GABA$_A$R α1β3γ2 heteromer construct

The GABA$_A$R-α1β3γ2 heteromer used in this work (α1β3γ2$_{EM}$ for short) has been designed and produced by Paul Miller. To achieve higher receptor yields, the intracellular loops connecting M3 and M4 α-helices in α1 and γ2 subunits were replaced with the SQPARAA linker (Jansen et al., 2008) as in the previously described β3 construct (Chapter 2). To allow unambiguous particle alignment during 3D reconstruction, the heteromeric receptor subunits were marked with a distinctive set of tags. β3 subunits were tagged with thermostabilised apocytochrome b(562)RIL (BRIL) domain (Chun et al., 2012), which was inserted into the SQPARAA linker

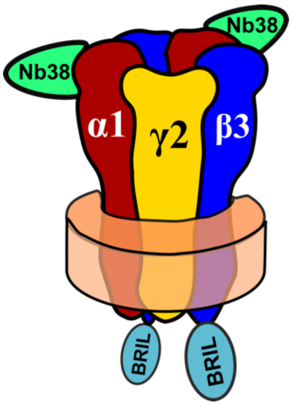

Figure 6.1 GABA$_A$R-α1β3γ2$_{EM}$ construct in complex with Nb38. Schematic representation of a GABA$_A$R-α1β3γ2$_{EM}$-Nb38 complex designed to be imaged by cryo-EM.

sequence (SQPAGT-BRIL-TGRAA) between the M3 and M4 α-helices. GABA$_A$R-α1 subunits were tagged with the nanobody Nb38, which was shown to bind to α1 subunits with high affinity and specificity (Chapter 2). Therefore, α1β3γ2$_{EM}$ heteromer particles had extra features added on both α1 and β3 subunits (Fig. 5.1) in order to allow particle alignment and subunit identification during cryo-EM 3D reconstruction. For purification, the C-terminus of the γ2 subunit was tagged with a 1D4 tag. This ensured that no β3 homomers or α1β3 heteromers will be co-purified with the α1β3γ2$_{EM}$ heteromer. Paul Miller produced and purified this protein, as described in Materials and Methods.

6.3. Nb38 is a positive modulator of GABAARs containing α1 subunit

We first checked whether Nb38 nanobody binding had any functional effects on the heteromeric GABA$_A$-α1β3γ2 receptors. I performed SPR-SCK experiments, which showed that the Nb38 binding affinity to detergent-solubilised α1β3γ2 heteromers was approximately 6.5-fold higher when 1 mM GABA was present in the buffer (Fig. 5.2a). This indicated that Nb38 favours the agonist-bound conformation of GABA$_A$R-α1β3γ2. Paul Miller performed whole cell patch-clamp recordings of HEK293S cells transfected with the α1β3γ2$_{EM}$ construct, which revealed that Nb38 strongly potentiates EC$_{10}$ GABA responses. For the α1β3γ2$_{EM}$ construct, EC$_{50}$ = 2.5 ± 0.2 μM, maximal potentiation = 480 ± 30 %, n = 7. For wild-type receptors, EC$_{50}$ = 1.5 ± 0.2 μM, maximal potentiation = 290 ± 20 %, n = 7 (Fig. 5.2c-e). Application of Nb38 alone at 10 μM exhibited a small amount of direct agonist activity on the electron cryo-microscopy construct, 3 ± 2 %, n = 4 of GABA I$_{max}$, and on wild-type receptors, 7 ± 2 %, n = 4 (Fig. 5.2e). Nb38 was shown to be α1-subunit selective, eliciting no potentiation on wild-type α2-α6β3γ2 receptors when applied up to 10 μM (Fig. 5.2f). These results indicate, that Nb38 behaves as an α1-specific GABA$_A$R positive allosteric modulator (PAM). Such nanobody might help to determine cryo-EM structures of the activated-state heteromeric receptor and can be useful as a novel pharmacological tool in GABA$_A$R research.

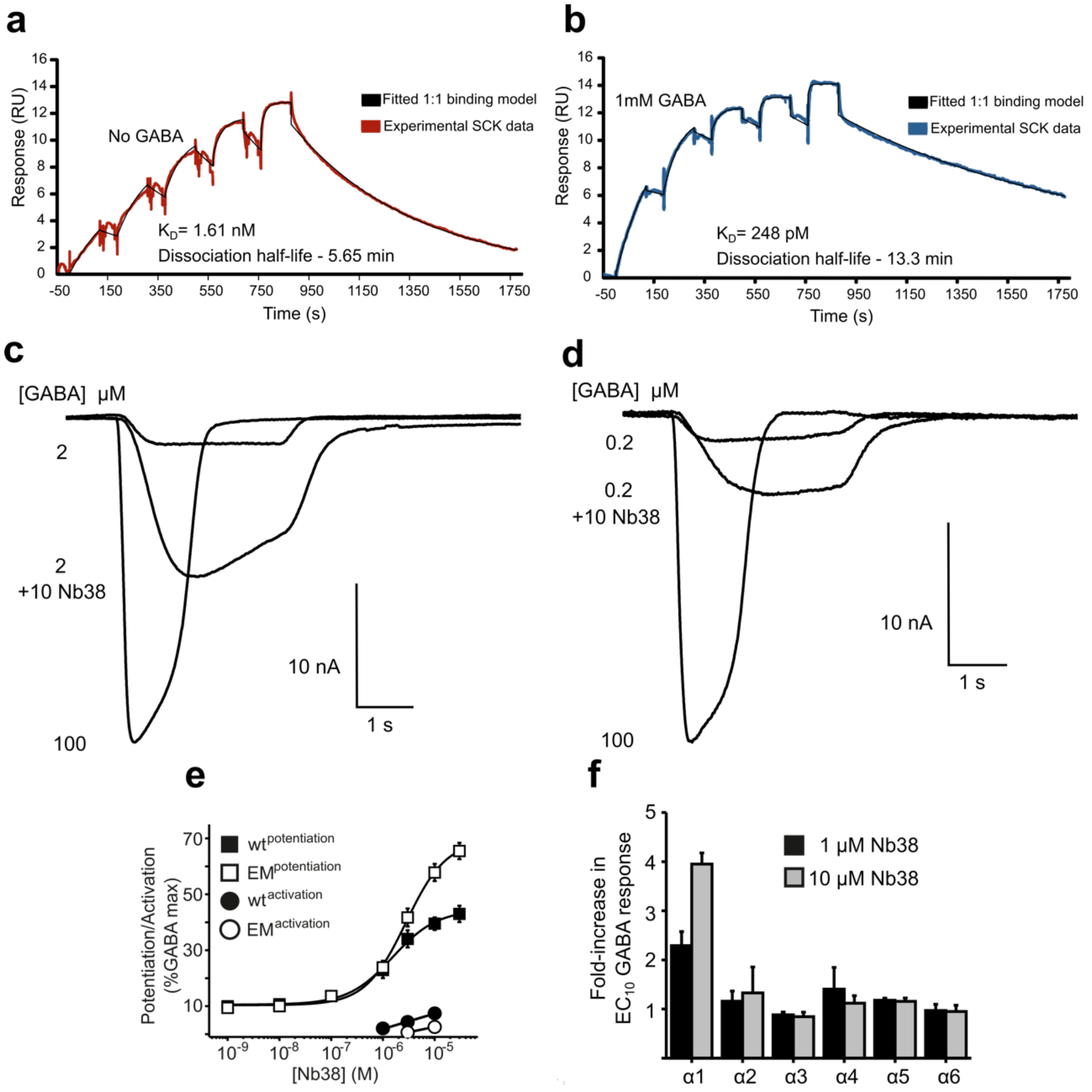

Figure 6.2 Nb38 is a positive allosteric modulator of GABA$_A$Rs.

a-b, Nanobody Nb38 binding to a heteromeric GABA$_A$-α1β3γ2 receptor analysed by surface plasmon resonance single-cycle kinetics (SPR-SCK) in the absence **(a)** and presence **(b)** of 1 mM GABA. **c-d,** Raw whole-cell patch-clamp EC$_{10}$ GABA responses, recorded from HEK293T cells transfected with α1β3γ2$_{EM}$ **(c)** or wild-type **(d)** constructs, with and without the co-application of 10 µM Nb38. **e,** Nb38 dose-response curves for potentiation/activation of GABA EC$_{10}$ responses in HEK293T cells expressing α1β3γ2$_{EM}$ or wild-type constructs. Each data point for potentiation represent mean ± s.e.m of n=7, and for activation – n=4. Each measurement was performed from different cells. **f,** Bar chart diagram showing fold-increase in GABA EC$_{5\text{-}15}$ responses when HEK cells were transfected with different types of full-length α subunits (together with β3 and γ2 subunits) and 1 µM and 10 µM of Nb38 were applied. Panels **(c-f)** were kindly provided by Paul Miller.

6.4. Initial α1β3γ2$_{EM}$ characterisation by cryo-EM

To enhance the Nb38 affinity and to increase chances of capturing the activated state of the receptor, 1 mM GABA was supplemented to the α1β3γ2$_{EM}$-Nb38 sample solubilised in decyl maltose neopentyl glycol (DMNG). Cryo-EM grids were prepared using the concentration of 2.8 mg/mL and the initial dataset was collected on a TF30 Polara (FEI) microscope using a K2 (Gatan) direct electron detector. Two types of grids were tested to check the particle numbers and reproducibility. The most commonly used holey carbon grids with copper mesh support (detailed information on grid preparation is specified in Materials and Reagents section) gave similar results as for the β3-Nb25 sample – aggregates with interdispersed single particles (Fig. 5.3a). The other type of grids tested was holey gold grids with gold mesh support. Gold specimen support was shown to significantly reduce the electron beam-induced motion during data collection, which helped to increase data quality (Russo and Passmore, 2014). Interestingly, particle aggregation was not prevalent anymore and protein spread was even across the images collected from these grids (Fig. 5.3b). In addition, beam-induced motion was reduced. However, only few holes in each grid square possessed the correct ice thickness, the most of them being empty or too dry. This was a major obstacle, which prevented high-throughput data collection from these grids. 2D classification of the α1β3γ2$_{EM}$-Nb38 specimen revealed particles in multiple orientations with clearly visible nanobodies and BRILs (Fig. 5.3c), meaning that particles have sufficient differences to be aligned and 3D reconstruction can be performed.

An initial dataset for α1β3γ2$_{EM}$-Nb38 DMNG-solubilised sample was collected using C-Flat^{TM} grids. After particle picking and 2D classification, 39,000 particles were used for 3D reconstruction with Relion (Scheres, 2012a). Gold-standard refinement yielded an 8 Å resolution map. GABA$_A$R subunits could be unambiguously assigned based on the molecular tags and their positions confirming the predicted β-α-β-α-γ stoichiometry (counter-clockwise, looking from the extracellular space) (Olsen and Sieghart, 2008). Two Nb38 molecules were bound at the sides of the α subunits and two BRILs could be seen in between M3 and M4 α-helices of β3 subunits (Fig. 5.4a-c). In addition, EM densities were observed for N-linked glycans at unique glycosylation sites in different subunits. However, an unusual transmembrane domain conformation was observed for this sample. The transmembrane domain of the γ2 subunit pushed through neighbouring α1 and β3 subunits towards the pore, completely blocking it (Fig. 5.4c). Interestingly, the γ2 subunit displaced the α1β3 subunit TMDs joined through β(P+)-α(C-) interface as two rigid modules. This suggests that the β(P+)-α(C-) TMD interfaces in the heteromeric GABA$_{\mathrm{A}}$ receptors are strong whereas, the β(P+)-α(C-), α1(P+)-γ2(C-) and γ2(P+)-β3(C-) TMD interfaces are weaker. Such large scale conformational rearrangements in the TMD region did not seem to be physiological, in comparison to all family members for which structures are available (Miller and Aricescu, 2014; Unwin and Fujiyoshi, 2012), and had to be minimised.

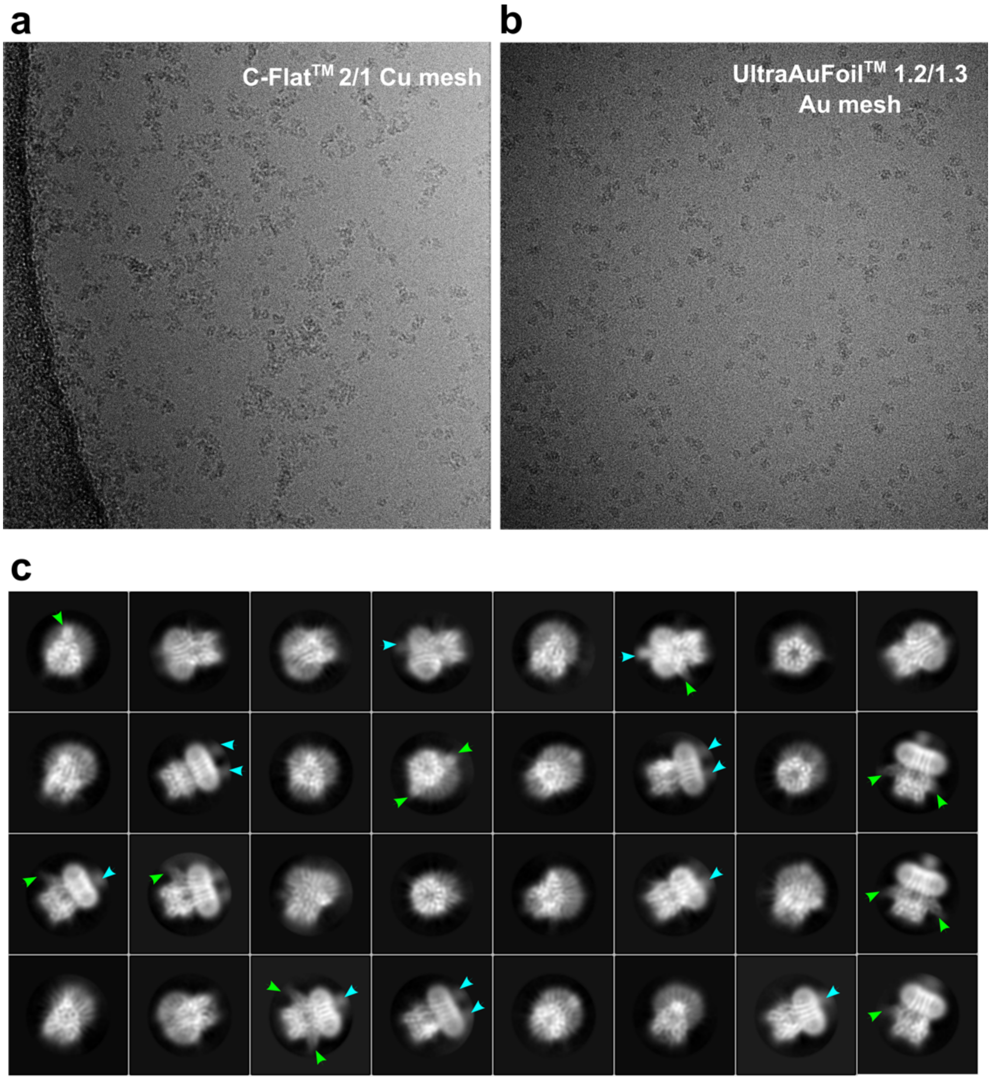

Figure 6.3 Cryo-EM data collection for GABA$_{\mathrm{A}}$R-α1β3γ2 sample.

a,b, Representative cryo-EM micrographs for the GABA$_{\mathrm{A}}$R-α1β3γ2 sample collected on carbon support C-Flat$^{\mathrm{TM}}$ **(a)** or gold support UltraAuFoil$^{\mathrm{TM}}$ **(b)** grids. **c,** Representative 2D classification results for a GABA$_{\mathrm{A}}$R-α1β3γ$_{\mathrm{EM}}$ sample. Green arrows indicate the presence of the nanobodies, whereas cyan arrows point at the BRIL tags.

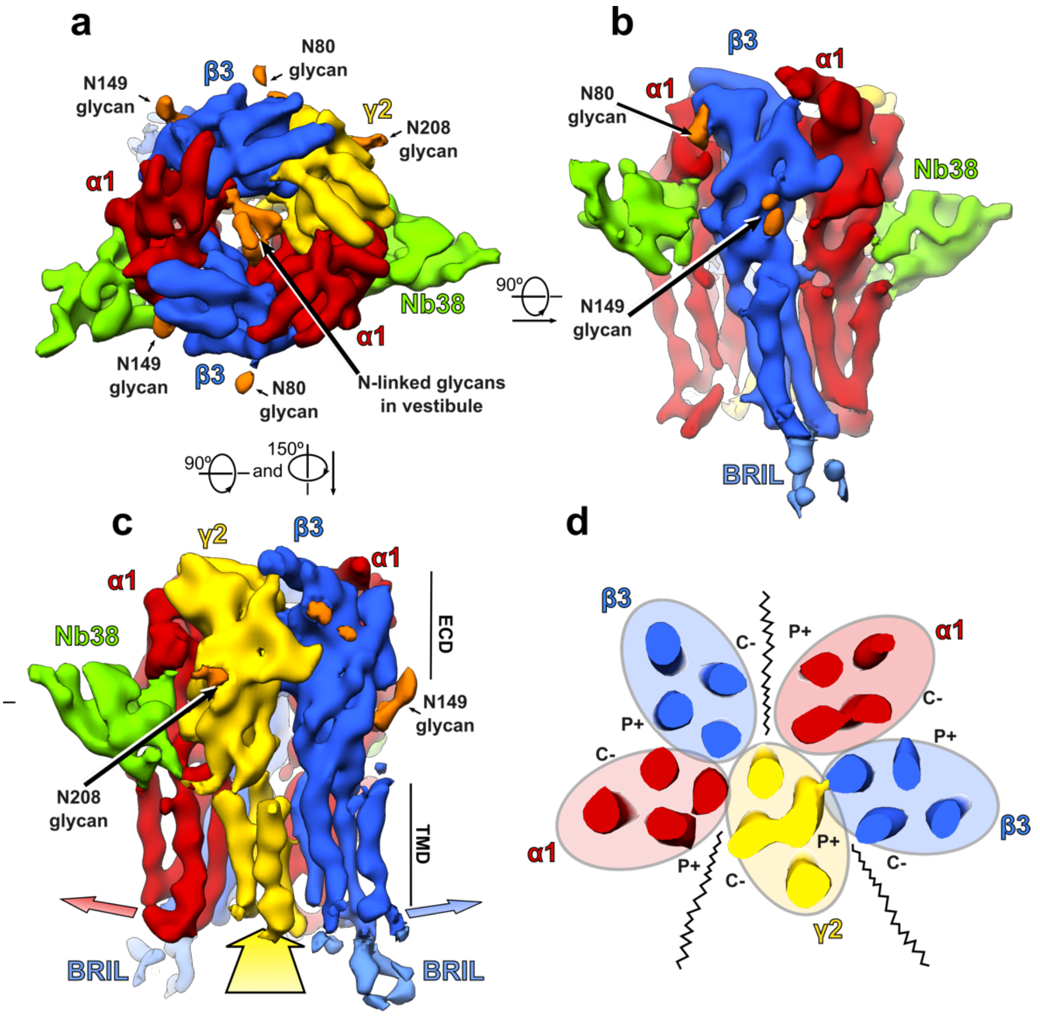

Figure 6.4 Cryo-EM map of a "collapsed" GABA$_A$R-α1β3γ2$_{EM}$ heteromer in DMNG.

a-c, "Collapsed" state α1β3γ2$_{EM}$ cryo-EM map viewed from the "top" (i.e. extracellular side) **(a)** and parallel to the membrane **(b-c)**. α subunits are coloured in red, β – in blue, γ – in yellow, nanobodies in green, BRILs – in light blue, N-linked glycans – in orange. Transmembrane domain of the γ subunit is destabilised by detergent and pushes neighbouring α and β subunit TMDs away (arrows indicate direction of their motion) **(c)**. **d,** Cross section of the transmembrane domains in the "collapsed" state α1β3γ2 heteromer. TMD interfaces which were destabilised by the detergent are highlighted by jagged lines.

6.5. Optimising the cryo-EM sample

To test what caused the "collapsed" γ2 TMD conformation and find ways to prevent or at least reduce it, smaller cryo-EM datasets were collected to test a range of purification conditions. Firstly, reducing reagent dithiothreitol (DTT) present in the original sample was suspected to have affected structurally important extracellular disulphide bridges, which could have compromised the structural integrity of the $GABA_AR$ subunits. Therefore, a small cryo-EM dataset was collected where DTT was not present in the protein purification buffer. Nevertheless, the structure generated from this dataset revealed that the pore was still "collapsed" (Fig. 5.5, panel 3), indicating that this state is not related to the DTT. It was then postulated that the "harsh" detergent environment and lack of structural lipids might destabilise the weaker interfaces between γ/β and γ/α TMDs. To test whether this might be the case, $\alpha1\beta3\gamma2_{EM}$ was extracted using a milder detergent, n-Dodecyl-β-D-thiomaltopyranoside (DDTM), and incubated with porcine brain lipid extract for 24 hrs. A small dataset (5,900 particles) of this sample was collected and processed to 10.12 Å. The results indicated that extraction in DDTM+lipids might be a less disruptive solubilisation strategy as it prevented the γ2 TMD from fully collapsing into the pore (Fig. 5.5, panel four).

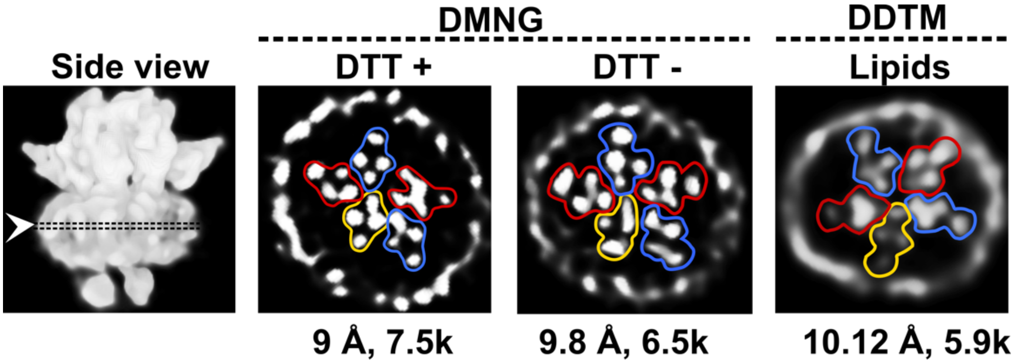

Figure 6.5 Stabilising $GABA_AR$-α1β3γ2 structure in detergent

Side view and cross-sections of $GABA_AR$-$\alpha1\beta3\gamma2_{EM}$ heteromer transmembrane domains in different solubilisation conditions. Total particle numbers and resolution are shown for each sample.

In an attempt to minimize the γ2 subunit TMD movement further, the channel pore blocker picrotoxin (PTX) was added to the sample and was left to incubate for 30 min before making cryo-EM grids. The PTX binding site is believed to bind at the lower region of the pore (Hibbs and Gouaux, 2011) and it was hoped that PTX binding will add extra stability to the channel pore. A larger dataset was collected to obtain a higher resolution structure, needed to confirm that this strategy will work. A total of 79,000 particles were used to generate a 7.83 Å map of the $\alpha1\beta3\gamma2_{EM}$ heteromer in DDTM+lipids+PTX (Fig. 5.6). The structure revealed that γ2 subunit TMD, although still moving with some degree, does not disrupt the pore anymore and transmembrane domain bundles adopt a five-fold pseudo-symmetry (Fig. 5.6b). The γ2 subunit in this sample was deemed to be stable enough for a large-scale data collection.

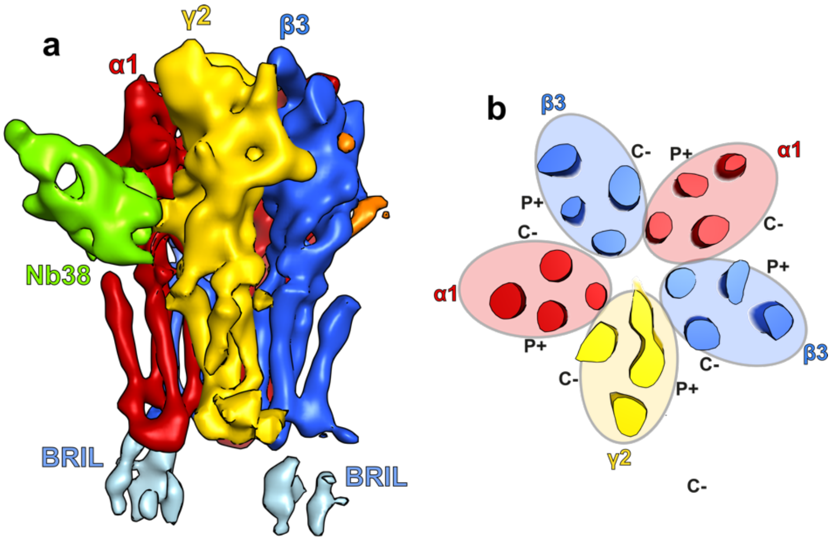

Figure 6.6 7.83 Å Cryo-EM map of a stabilised GABA$_A$R-α1β3γ2$_{EM}$ heteromer.

a, Side view of a α1β3γ2 heteromer stabilised by solubilisation in DDTM, porcine brain lipids and picrotoxin. **b,** Cross section of the stabilised state α1β3γ2 heteromer transmembrane domains.

6.6. Data collection and 3D reconstruction

A dataset of 8,548 micrographs was acquired using TF30 Polara 300 kV microscope (FEI) equipped with the K2 (Gatan) direct electron detector. Initial movie frame alignment was performed using MotionCorr. 2D classes from previous test datasets were used as autopicking templates in Relion (Scheres, 2012a). The quality of autopicked particles was manually inspected using EMAN2 (Tang et al., 2007). Particles in large aggregates or particles picked on carbon substrate were discarded. CTF parameters for whole images were first estimated using CTFFIND4 (Rohou and Grigorieff, 2015), whereas Gctf (Zhang, 2016) was used to calculate the CTF parameters for individual particles before performing the final refinement. Relion was used for 2D/3D classifications and for the final 3D volume refinement. The resulting workflow is described in detail in figure 5.7.

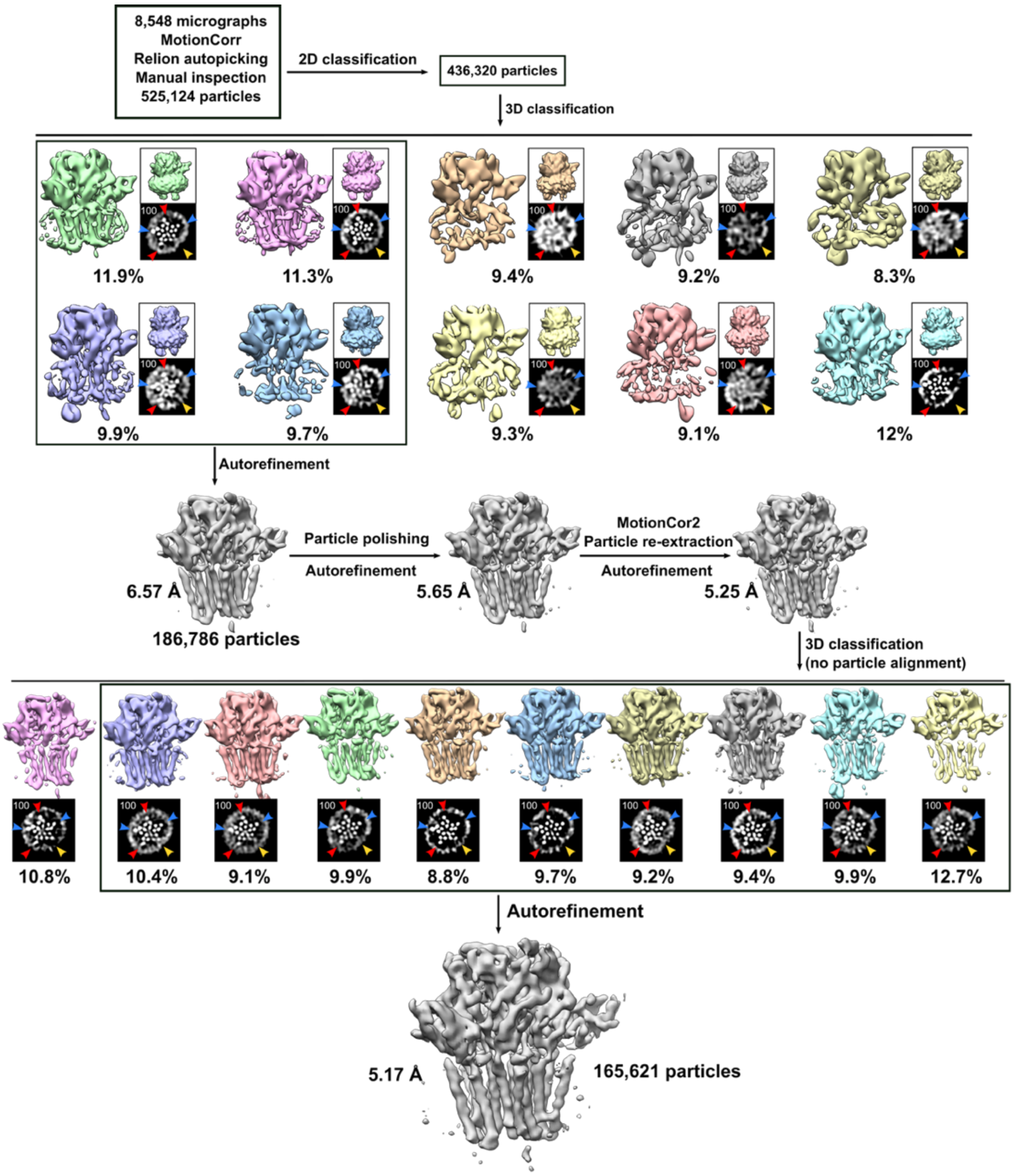

Figure 6.7 Cryo-EM data processing pipeline for GABA$_A$R-α1β3γ2$_{EM}$ sample.

A dataset of 525,124 particles were 2D classified. The best 2D classes contained 436,320 particles, which were then 3D classified into 10 classes. Four best volumes with 186,786 particles were combined and refined to 6.57 Å. "Particle polishing" protocol was applied within Relion to increase the signal-to-noise ratio of the particles used in the refinement. The refinement with the polished particles improved the resolution to 5.65 Å. When MotionCor2 became available, movies were re-aligned and dose-weighted. Refinement with particles extracted from these micrographs resulted in a cryoEM map of 5.25 Å resolution. This dataset was further 3D classified into 10 classes in Relion where particles were simply sorted into best aligning structures without changing their previous alignments. Using this method, it is possible to sort out different conformational states adopted by this receptor. Nine classes with 165,621 particles were combined and refined to 5.17 Å. Each 3D class and a corresponding slice through its TMD are shown. Colour coded (α1 – red, β3 – blue, γ2 – yellow) arrows indicate the subunit identity in the TMD slices. C1 symmetry was applied throughout the 3D classification.

This dataset still contained a lot of particles, which had structural heterogeneity associated with the γ2 subunit motion. Careful Relion classification and selection of the best classes helped to limit of such badly aligning particles in the final 3D reconstruction. This data was also re-processed with cryo-SPARC (Punjani et al., 2017) from scratch using a similar pipeline as for the GABA$_A$R-β3 homomer structure bound to Nb25 (Chapter 4), however, it yielded similar results, and in this case, the final map produced by Relion was of better quality.

The final Relion map for GABA$_A$R-α1β3γ2$_{EM}$ sample was refined to 5.17 Å based on the gold standard FSC=0.143 (Fig. 5.8a). α-α-helices in this map started to show some indication of α-helical turns and densities for several large hydrophobic amino acids were visible (Fig. 5.8b). β-sheet layers were not yet fully separated into β-strands at this resolution. The N-linked glycan shape was relatively well-defined and a typical Y-shape pattern caused by mannoses branching could be easily seen. Local resolution of this map was estimated using ResMap (Kucukelbir et al., 2014). The detergent belt, BRILS and nanobody edges were the most flexible regions in the map (Fig. 5.8c). Unsurprisingly, the γ2 subunit TMD and area around it also were also more disordered due to its residual motion. The rest of the molecule was structurally stable and local resolution estimation was even throughout.

Although amino acid side chains were not visible at this resolution, the 5.17 Å map was still of sufficient quality to dock atomic models derived from higher resolution crystal structures and refine them into the cryo-EM density. The resulting model should allow us to describe the relative positions of the ECDs and TMDs within the subunits, to trace the α-α-helices and to determine the state of the pore. It should also make it possible to describe molecular surface properties between different subunits at least with partial accuracy. Such model however, is not suitable for inferring details about individual amino acid side chain interactions, like hydrogen bonding or salt bridging.

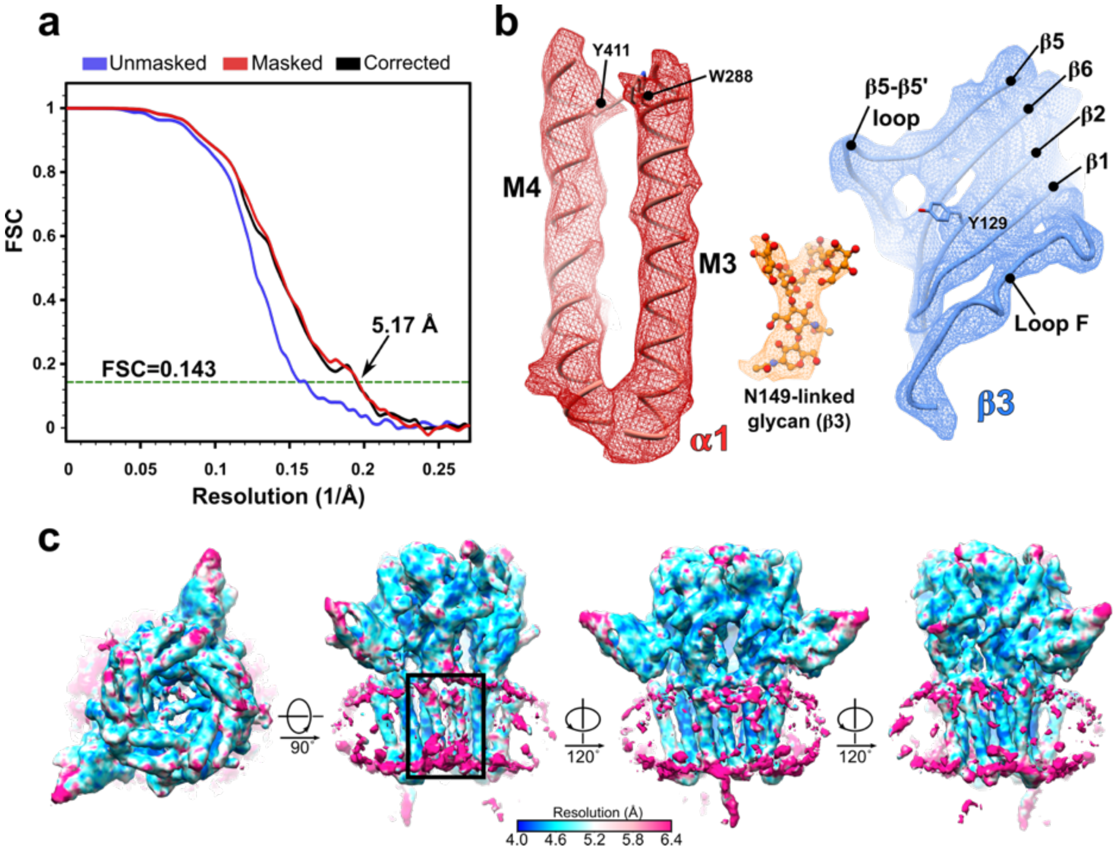

Figure 6.8 5.17 Å cryo-EM map of GABA$_A$R-α1β3γ2.

a, Resolution estimation for unmasked, masked and corrected-masked cryo-EM maps using Fourier shell correlation (FSC) at 0.143. **b,** 5.17 Å EM density (mesh) examples for α-helices, N-linked glycans and β-sheets. **c,** Unfiltered cryo-EM map coloured by local resolution estimation using ResMap. The area around the γ2 subunit is marked with a black box.

6.7. Model building

To build an atomic model using the 5.17 Å GABA$_A$R-α1β3γ2$_{EM}$ map, I first docked α1 and γ2 TMD and ECD models into the cryo-EM density. These models were generated by Paul Miller using the MODELLER package, where β3$_{cryst}$ structure (PDB 4COF) (Miller and Aricescu, 2014) was used as a reference. For heteromer β3 subunit model, I docked the β3$_{cryst}$ structure into the EM map. Since α1 and γ2 models did not have a good stereochemistry, I minimised the heteromer structure in PHENIX (Adams et al., 2010). To improve the structure fitting I used Rosetta Relax protocol (DiMaio et al., 2009) using the starting model as a reference. Then, by using COOT (Emsley and Cowtan, 2004), I manually corrected the amino acid rotamers and loop conformations so that they match the higher resolution X-ray crystal structures. The reference structures were: the 3 Å β3$_{cryst}$ (PDB 4COF), 3.15 Å β3$_{ECD}$α5$_{TMD}$ chimera (PDB 5O8F) and 2.9 Å α5 homomer (Paul Miller, personal communication). Therefore, the resulting α1 and β3 subunit atomic models were deemed to be quite accurate as they were based on higher resolution data. However, there was no such structural data available for the γ2 subunit. For this reason, γ2 amino acid side chain rotamers were based on the homologous residues between the β3 and α5 subunits. In positions where amino acids were not homologous, the most common form of rotamers was chosen. Structurally, α1, β3 and γ2 subunits are very similar (see the next section), however, the loop-F in the γ2 subunit is longer than in α5 or β3 structures, therefore it was not possible to accurately built it into the EM density. The final model was refined in the cryo-EM map using *phenix_real_space_refine.* Since the cryo-EM map had a relatively low resolution, a great care was taken to make sure that the resulting atomic model had the correct stereochemistry. Bonds and angles were restrained by using higher resolution structures as reference models, and by applying secondary structure and conformation-dependent library (cdl) restraints. N-linked glycan sugar moieties were restrained using cif files generated with the Grade Web Server. The stereochemistry quality of the model was monitored using MolProbity (Davis et al., 2007). Finally, to avoid overfitting, the model was validated using procedures described in the previous chapter (Amunts et al., 2014; Brown et al., 2015). Final refinement statistics are shown in table 9.

Table 9 Statistics of cryo-EM data collection and 3D model refinement

	$\alpha1\beta3\gamma2_{EM}$
Data collection	
Microscope	FEI TF30 Polara
Voltage (kV)	300
Particles total	525,124
Particles final	165,621
Defocus range (µm)	-3.5 to -2.5
Exposure time (s)	14.1
Dose rate (e-pix^{-1} s^{-1})	4.91
Resolution (unmasked, Å)	6.25
Resolution (sharpened, Å)	5.17
Map Sharpening B-factor (Å^{2})	-277
Refinement	
Cross-correlation (volume)	0.79
Protein atoms	18,303
R.m.s deviations	
Bond length (Å)	0.01
Bond angles (°)	1.2
Clashscore, all atoms (percentile)	8.78 (78th*)
Rotamer Outliers (%)	0.0
Ramachandran statistics	
Favoured (%)	97.61
Allowed (%)	2.39
Outliers (%)	0.0
MolProbity score (percentile)	1.55 (94th*)

*Across all resolution structures (N=1784)

6.8. GABA$_{\mathrm{A}}$-$\alpha1\beta3\gamma2_{\mathrm{EM}}$ receptor structure

6.8.1. An overview

I determined a 5.17 Å cryo-EM map of the GABA$_{\mathrm{A}}$R-$\alpha1\beta3\gamma2_{\mathrm{EM}}$ sample and built an atomic model into the density (Fig. 5.9). This structure revealed that the $\alpha1\beta3\gamma2_{\mathrm{EM}}$ heteromer has the generic pLGIC architecture defined by a characteristic barrel-like shape. Each subunit has a bundle of four α-α-helices constituting their transmembrane domains (TMD), whereas the extracellular domains (ECD) are predominantly made up of β-sheets. ECDs are also highly glycosylated (Appendix section 10.3) and interestingly two N-linked glycans, attached to the Asn111 residue of α subunits, are also present in the vestibule of the channel. Nanobody Nb38 binds specifically to the ECD of an α1 subunit and clear BRIL densities are seen in between β3 subunit M3-M4 α-helices.

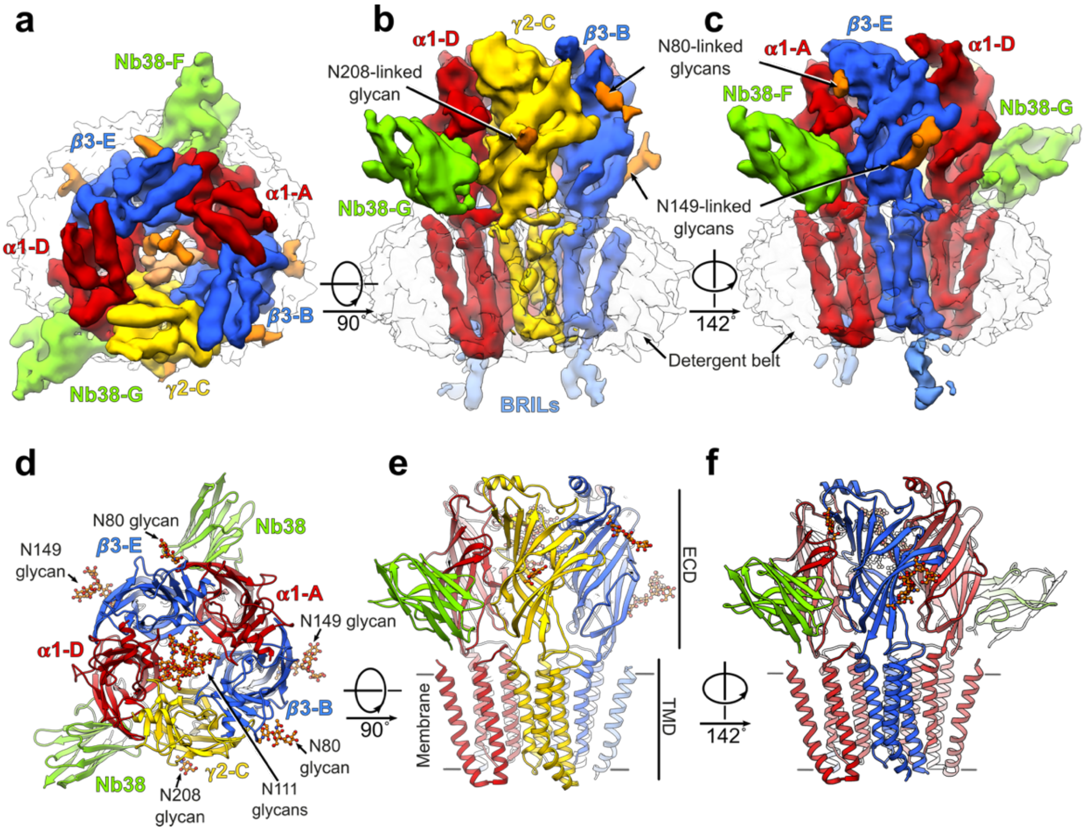

Figure 6.9 GABA$_{\mathrm{A}}$R-$\alpha1\beta3\gamma2_{\mathrm{EM}}$ architecture.

a-c, $\alpha1\beta3\gamma2_{\mathrm{EM}}$ heteromer cryo-EM map viewed from the extracellular space **(a)**, parallel to the membrane **(b-c)**. α1 subunit is coloured in red, β3 in blue, γ2 in yellow, nanobodies in green, BRILs in light blue. **d-f,** Equivalent views of the $\alpha1\beta3\gamma2_{\mathrm{EM}}$ model.

A closer look into the EM map reveals that there are some notable differences among the subunits in the heteromer (Fig. 5.10). For example, α1 N-linked glycans, which are present in the vestibule, adopt two distinct conformations. The glycan linked to Asn111 of the α1-A subunit is in an almost horizontal position, whereas the Asn111-linked glycan in the α1-D subunit is pointing towards the extracellular space. It can also be noticed that β3 subunits have a different loop-F conformation when compared to α1 or γ2 subunits. β3 loops-F are smaller and there is a gap seen between the loop-F and β1 strand. Finally, α1 subunit M2 α-helices are sloping diagonally relative to the channel axis. In contrast, β3 subunits have straighter M2 pore-lining α-helices. It should be stressed that exactly the same M2 α-helical conformation is observed in both pairs of α1 and β3 subunits, indicating that this is not a γ2 TMD induced artefact affecting its neighbouring subunits. This is likely to be a conformation which occurs in response to the agonist GABA and nanobody binding. These differences between subunits will be addressed in the sections below.

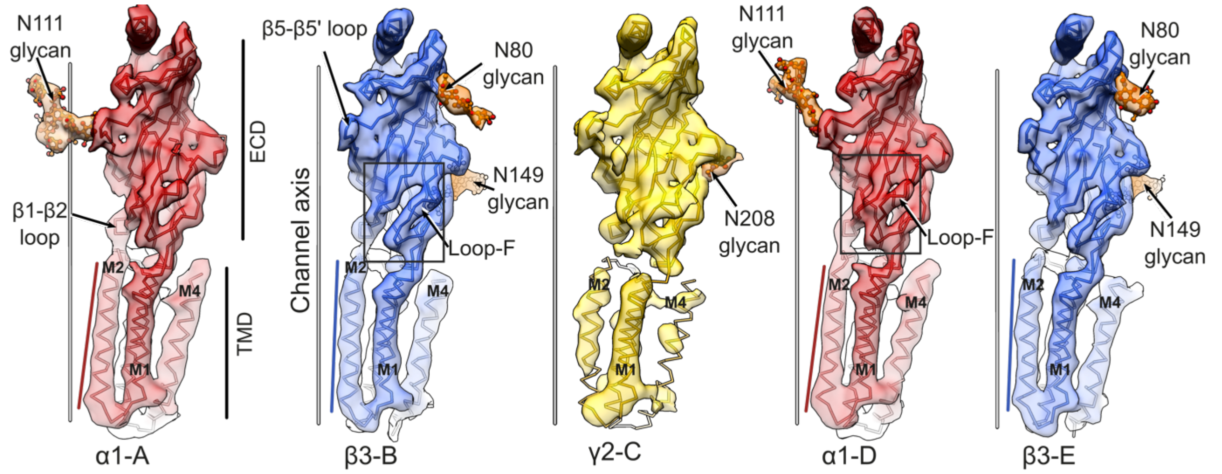

Figure 6.10 Differences between GABA$_A$R-α1β3γ2$_{EM}$ subunits.

Cryo-EM maps are shown for each α1β3γ2$_{EM}$ heteromer subunit. Subunits are displayed relative to the channel axis. Black boxes highlight the area close to the loop-F, where differences are seen across subunits. Red and blue lines drawn next to the pore-lining M2 α-helices of the α1 and β3 subunits, respectively, highlight the different M2 trajectories relative to the channel axis.

6.8.2.N-linked glycosylation of α1 subunits

For the first time in pLGIC research, this GABA$_A$R-α1β3γ2$_{EM}$ heteromer structure revealed glycosylation features inside the vestibule of a channel (Fig. 5.11a). These non-protein EM densities stem out of the GABA$_A$R-α1 subunit β5-β5′ loops (Fig. 5.11bc). Indeed, all GABA$_A$R α subunits have predicted N-linked glycosylation sites in this loop, whereas β and γ subunits do not (Fig. 5.11d). Interestingly, the densities for glycans are very well ordered and adopt non-random orientations. The Asn111-linked glycan in the α1-D subunit projects upwards to face the extracellular space (Fig. 5.11b) whereas the glycan in the α1-A subunit lies horizontally and projects towards the γ2 subunit (Fig. 5.11c). This glycan is very likely to interact with the γ2 subunit through CH-π interactions between its mannose and the Trp123 side chain in the γ2 β5-β5′ loop (~4.0 Å distance) (Fig. 5.11c). Interestingly, γ2 Trp123 is in the equivalent β5-β5′ loop position as the α1 Asn111. This residue is conserved across all γ, but not β subunits (Fig. 5.11d). In the other types of GABA$_A$ subunits, the equivalent position is occupied by Asp or Glu residues, likely to form hydrogen bonds with an α1-A mannose.

Such a conservation pattern strongly suggests that in the heteromeric context, the putative interaction between the γ2 subunit Trp123 and the opposing α1 Asn111-linked glycans could be functionally important. For example, this interaction might have a structural role in determining subunit stoichiometry and assembly rules. In addition, such N-linked glycosylation pattern in α subunits might act as a general mechanism to control the heteromeric GABA$_A$R stoichiometry by steric hindrance. If all sites are occupied by glycans, homopentamer formation from α subunits should be non-permissible due to steric clashes. Experiments in our lab performed by Paul Miller revealed that N111G mutation allows α5 subunits to form a homomer, which was not possible for wild-type subunits (data not shown). In a heteromeric context, only two α subunits can be accommodated, as their N-linked glycans occupy all the space available in the vestibule. Finally, it is unclear to whether the N-linked glycans in the vestibule might have an impact on ion conductance through the pore. To answer this, molecular dynamics simulations could be performed to estimate if chloride ions can pass through the vestibule glycans.

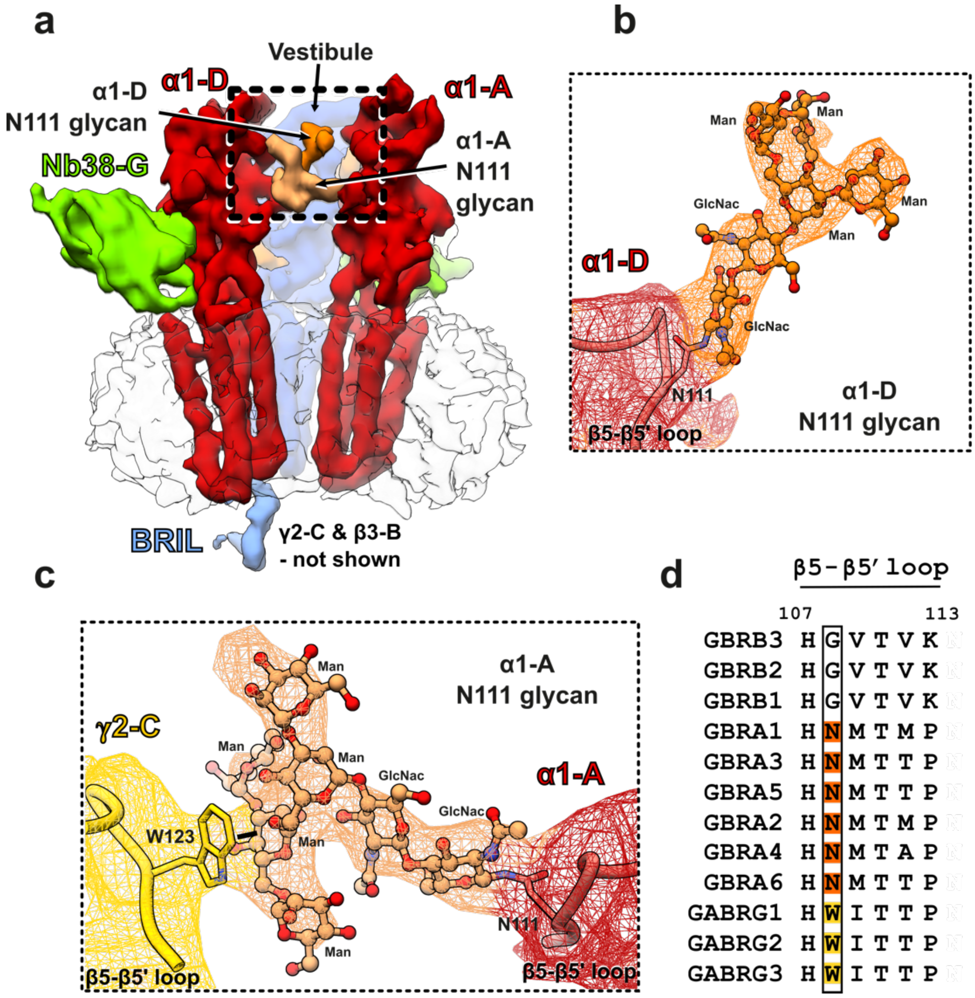

Figure 6.11 N-linked glycosylation of α subunits in GABA$_A$R-α1β3γ2$_{EM}$.

a, Side view of α1β3γ2$_{EM}$ map showing α1 N-linked glycans filling the channel vestibule. β3-B and γ2-C subunits were hidden to visualise the vestibule. **b-c,** Close-ups of α1-D **(b)** and α1-A **(c)** Asn111-linked glycans. Models and electron density maps are shown. Black line in **(c)** marks the interaction between the Trp 123 and mannose from the Asn11-linked glycan. **d,** Multiple sequence alignment of β5-β5' loop which harbours the α1 Asn111-linked glycan site. Sequence numbering above the alignment is based on β3 subunit (mature isoform 1).

6.8.3. Extracellular domains

To examine the conformational differences between heteromer subunit ECDs in more detail, a series of structural alignments was carried out. Superposition of the heteromer and β3$_{cryst}$ ECDs revealed that the overall structural organisation is highly conserved (α1: β3 RMSD is 1.09 Å; α1:g2 RMSD is 1.11 Å; α1:β3$_{cryst}$ RMSD is 1.17 Å, over 207 equivalent Cα positions) (Fig. 5.12a). This was largely expected as the amino acid conservation between the ECDs is considerable: α1 shares 36 % and γ2 shares 38 %

with β3; α1 and γ2 share 51 % with each other. However, the most notable differences were observed for the loop-F, which is longer in both α1 and γ2 subunits. Inspection of the cryo-EM map reveals that β(P+)-α(C-) interfaces will be much more closely linked together due to the large α1 loop-F (Fig. 5.12b). In contrast, the EM map suggests that interfaces with the β(C-) face should have have less contact points at the ECD level. It is very likely that loop-F might be involved in conformational change transfer between subunits when the agonist GABA is bound.

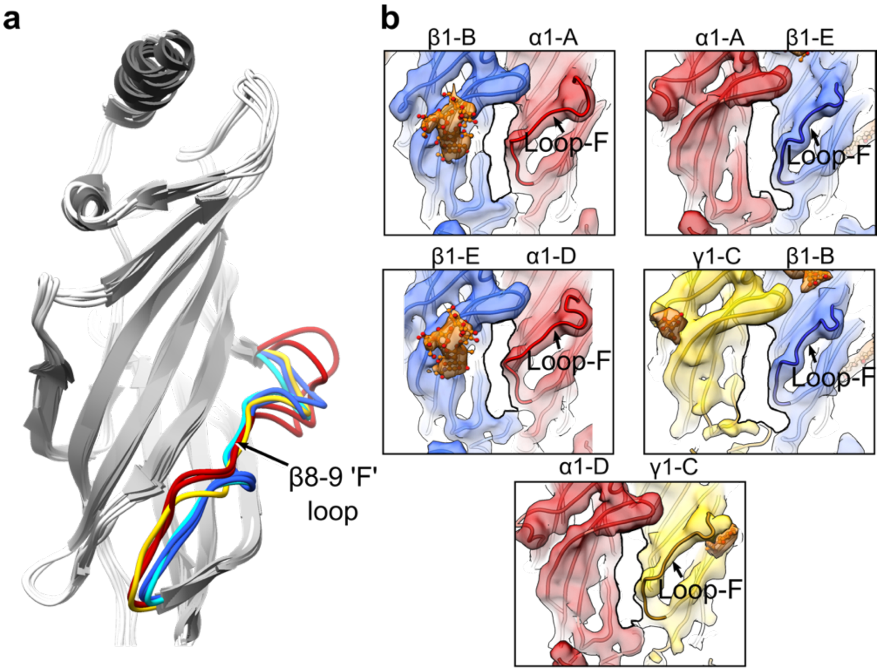

Figure 6.12 Loop-F of GABA$_A$R-α1β3γ2 subunits.

a, Superposition of ECDs from the β3$_{cryst}$ and GABA$_A$R-α1β3γ2$_{EM}$ structures. Loops-F are coloured according to the subunit. β3cryst loop-F is coloured in cyan, heteromer colouring scheme is as in previous figures in this chapter. **b,** Close-up of ECD interfaces between different subunits showing model in ribbon and the EM density as a transparent surface. Loops-F are marked by an arrow.

In addition, it is possible that loop-Fs are linked to the lateral side tunnel formation as seen in the β3 homopentamer structure (Miller and Aricescu, 2014). However, since the exact amino acid side chain positions are not known it is not possible to correctly estimate the size of these tunnels, therefore no assumptions were made whether chloride ions can pass through. A higher resolution cryo-EM, or X-ray, structure is needed to address this question.

6.8.4. Transmembrane domains

In contrast to the ECDs, α1β3γ2_{EM} TMDs share higher sequence identity. α1 and γ2 share 63% sequence identity with each other, and 53 % and 57 %, respectively, with β3. Structural alignment showed that overall organisations of the TMDs in the heteromer model are similar overall (α1: β3 RMSD is 1.1 Å; α1:γ2 RMSD is 1.2 Å; α1:$β3_{cryst}$ RMSD is 1.2 Å, over 122 equivalent Cα positions) (Fig. 5.13a). Nevertheless, comparison of $β3_{cryst}$ TMD with the heteromeric β3 TMD revealed that their M2 α-helices have different conformations. Heteromeric β3 M2 helix adopted a conformation where its "top" part is flexed towards the pore axis, similar to one observed in the $β3_{K279T}$-$Nb25_{ETM}$ structure (Fig. 5.13b).

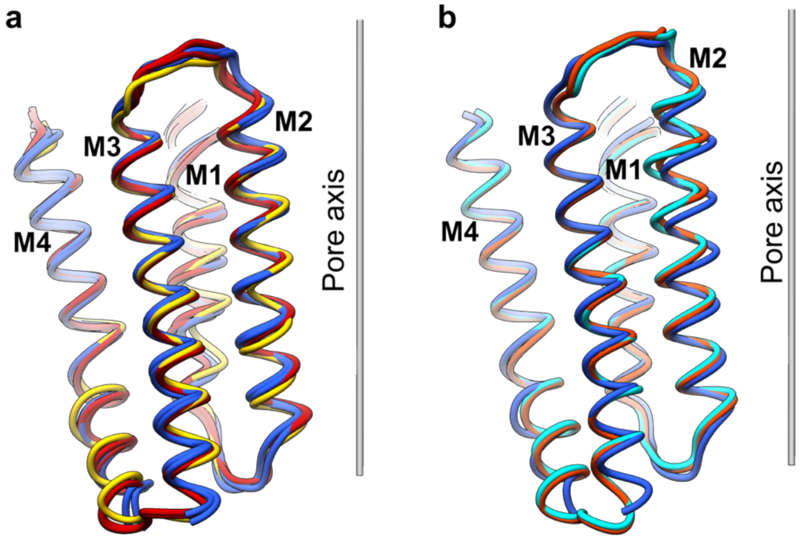

Figure 6.13 GABA$_A$R-α1β3γ2_{EM} transmembrane domain architecture.

a, Superposition of the TMD structures from α1β3γ2_{EM} heteromer. **b,** Superposition $β3_{cryst}$ (cyan), $β3_{ETM}$ (orange), and β3 from α1β3γ2_{EM} structure (blue) TMD structures. Pore axis is displayed for reference.

In Chapter 3 it was described how etomidate elicits its potentiation effects by forming a wedge in between the β3Met286 and β3Asn265 residues (Fig. 5.14a). Such binding caused the pore-lining M2 helix to bend and it was hypothesised that this particular conformational change is necessary for the receptor to achieve an open state. When the general anaesthetic pocket was visualised in the heteromeric β3 subunit, it became apparent that β3Met286 and β3Asn265 residues were apart from each other as in the etomidate bound structure (Fig. 5.14b). Since 1 mM GABA was present, together with a potentiating nanobody Nb38, it very likely that the α1β3γ2_{EM} heteromer was captured in an open state which explains the M2 flexure. Similar changes in the pore-lining M2 helix flexure associated with different conformational states were previously observed in the nAChR resting closed versus open states (Unwin, 2005; Unwin and Fujiyoshi, 2012).

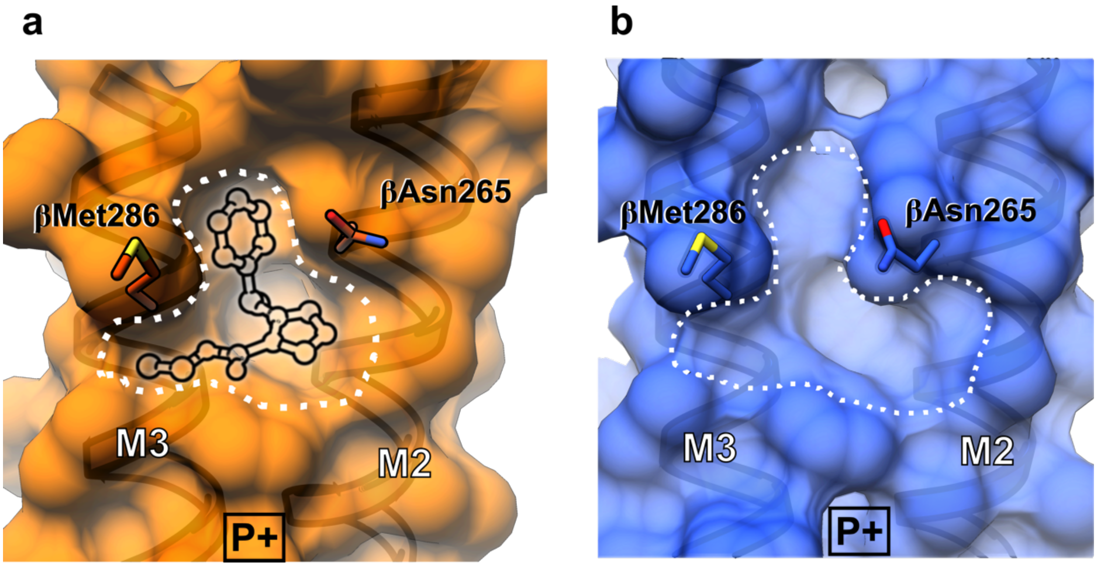

Figure 6.14 Heteromeric β3 TMD adopts an "open" state configuration.

a,b, Anaesthetic binding pocket in β3 subunit viewed from the complementary subunit perspective in the etomidate-bound state **(a)** and in the β3 subunit from the GABA$_A$R-α1β3γ2$_{EM}$ heteromer **(b)**. Pocket shape is demarcated in a white dotted line.

6.8.5. Global ECD-TMD relative orientations

To examine the relative orientations between ECD-TMDs of the α1β3γ2$_{EM}$ subunits, they were aligned by rotating each subunit along the pore axis by 72°. In addition, the β3$_{cryst}$ homomer (Miller and Aricescu, 2014) and the GlyR open and closed structures (Du et al., 2015) were superimposed onto GABA$_A$R subunits by rotation around the aligned pore axes until the match is maximised. Overall, α1, β3 and γ2 subunit ECDs maintain a similar orientation relative to the pore axis (Fig. 5.15a). Loop-C for all of the α1β3γ2$_{EM}$ subunits presents a "closed" conformation which is reminiscent of the agonist-bound β3$_{cryst}$ loop-C configuration (Miller and Aricescu, 2014) and contrasts to the closed state GlyR loop-C (Du et al., 2015) (Fig. 5.15b). This "activated" ECD conformation is consistent with the α1β3γ2$_{EM}$ receptor being bound by its neurotransmitter agonist, GABA, and reinforced by the positive allosteric modulator Nb38. Despite the general similarity of the ECD poses, a notable difference is present within the ECD-TMD interface for the β3 subunit. β1-β2 and β6-β7 loops of the β3 subunit push the M2-M3 loop at the top of the α-helical bundle, which is then translated towards the pore. This introduces a notable flexure at the top of the M2 helix and also translates the bottom of the helix away from the desensitisation gate, when compared to the α1 subunit TMD (Fig. 5.15c). The α1 subunit itself adopts a more tilted and open-like M2 configuration contrasting to the desensitised state $\beta3_{cryst}$ M2 helix trajectory (Fig. 5.15d). In addition, the α1 M2 trajectory is very similar to the open state GlyR and markedly contrasts to the closed state GlyR M2 trajectories (Fig. 5.15d).

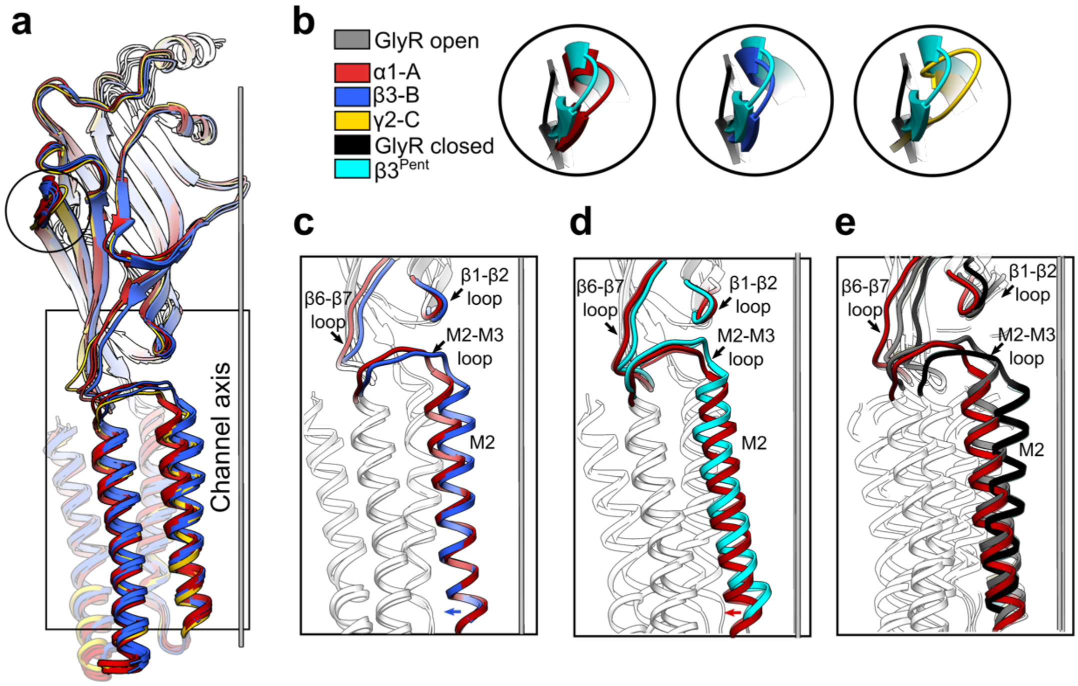

Figure 6.15 ABA_A-$\alpha1\beta3\gamma2_{EM}$ receptor global conformational changes.

a, Side view of globally aligned subunits from the $\alpha1\beta3\gamma2_{EM}$ heteromer relative to the channel axis. **b,** Comparison of $GABA_AR$ α1, β3 and γ2 subunit loops-C to closed GlyR (PDB 3JAD, black) and agonist-bound β3cryst (PDB 4COF, cyan) loops-C. **c-e,** Comparison of ECD-TMD signal transduction loops and the M2 helix between heteromer α1 an β3 subunits **(c)**, between heteromer α1 and $\beta3_{cryst}$ subunits **(d)**, and between heteromer α1, GlyR open state and GlyR closed state subunits **(e)**.

6.8.6. Channel pore

Pore diameter profile was calculated using HOLE (Smart et al., 1993). The $\alpha1\beta3\gamma2_{EM}$ pore presents a funnel narrowing from 7-10 Å diameter at the top to 6 Å at the 2′ ring (α1Val257, β3Ala252, γ2Ser267) (Fig 5.16ab), which is close to hydrated Cl$^-$ ion diameter (6.1-6.2 Å) (R. Mancinelli et al., 2007; Zhang and Gai, 2015). Molecular dynamics simulations (Trick et al., 2016) were used to estimate water behaviour within the pore domain. The simulation results indicated that water molecules can occupy the pore across its full length, which suggests that the pore should be capable of conducting hydrated Cl$^-$ ions as there is no hydrophobic barrier (Fig. 5.16c). In addition, the presence of polar γ2Ser267 residue in the hydrophobic 2′ ring is likely to facilitate the flow of charged Cl$^-$ ions through the pore. In contrast to the diagonal pore outline of the desensitised state $\beta3_{cryst}$ structure, the $\alpha1\beta3\gamma2_{EM}$ pore possesses an outline with a more vertical projection. The desensitization gate is not shut anymore and it is big enough for Cl- ion conductance (Fig. 5.16a). Interestingly, etomidate binding to β3 subunits seems to induce a similar configuration at the top of the pore, however such M2 straightening was not sufficient to open the bottom gate (Fig. 5.16a). It is possible that the $\alpha1\beta3\gamma2_{EM}$ open pore represents the outcome of what would have happened if such α-helical straightening resulted in the opening of the desensitisation gate of the β3 homomer. The general $\alpha1\beta3\gamma2_{EM}$ pore outline is similar to the open GlyR (Fig 5.16a). However, GlyR M2 α-helices translate radially outwards much further, which makes the pore wider with 8.8 Å diameter at the narrowest point. This correlates with higher GlyR conductance in cell membranes, 60-90 pS, versus 25-28 pS for the GABA$_A$ receptor (Beato et al., 2002; Mortensen and Smart, 2006). Therefore, it might be that heteromeric GABA$_A$Rs require only a small flexure and tilt in their α-helices to be able to open the pore just enough to conduct chloride ions, similar to what was suggested to happen in nAChR heteromers (Unwin and Fujiyoshi, 2012).

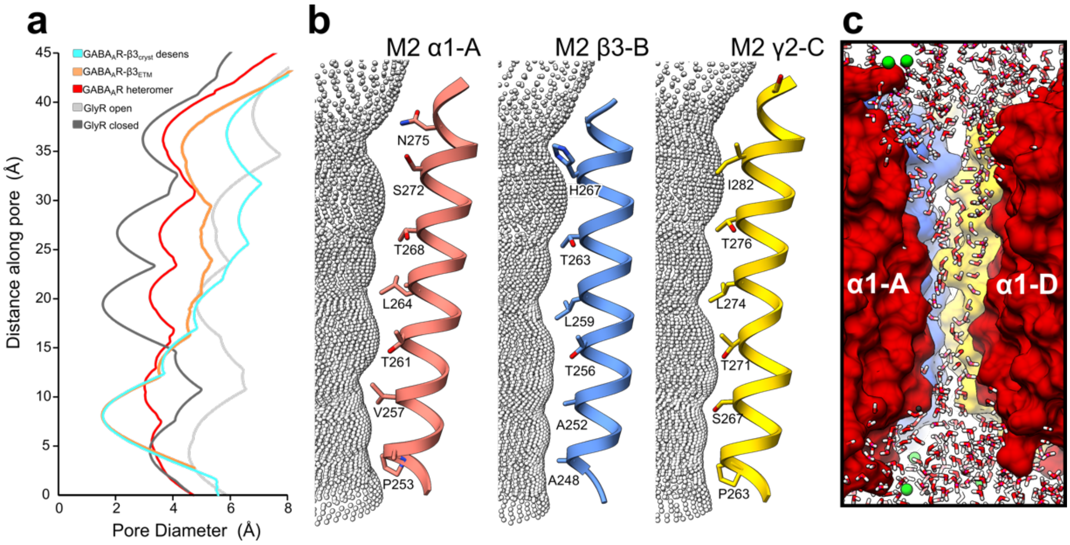

Figure 6.16 GABA$_A$R-α1β3γ2$_{EM}$ pore analysis.

a, Pore radius analysis of β3$_{cryst}$ (PDB 4COF), β3$_{ETM}$, α1β3γ2$_{EM}$, GlyR open (PDB 3JAE) and closed (PDB 3JAD) structures. **b,** Pore outline shown together with α1-A, β3-B and γ2-C M2 α-helices. Amino acid residues facing the pore are labelled. **c,** Molecular dynamics simulation of the hydration state in the pore. β3-E subunit removed to visualise the water-permeable pore of the α1β3γ2$_{EM}$ heteromer.

6.8.7. Nanobody Nb38 binding interface

Nanobody Nb38 acts a positive allosteric modulator for GABA$_A$-α1β3γ2 receptors. Nanobody binding analysis reveals that all three CDR loops interact with the α1 subunit around the loop-C. The vast majority of these interactions are mediated by the CDR2 and CDR3 loops (Fig. 5.17a). CDR3 interacts with the β9 and β10 loops at the α1 ECD, whereas the CDR2 inserts into the cavity under the loop-C (Fig. 5.17b). CDR3 also binds to complementary faces of β3/γ2 subunits to some extent, although it seems that such interactions are probably non-specific. Finally, the CDR2 loop mostly interacts with the β6-β7 loop (Cys-loop) of the α1 subunit (Fig. 5.17a). It is likely that Nb38, by tightly latching onto the surfaces around the loop-C, pushes it inwards and stabilises its closed state. This in turn leads to the transduction of the conformational change across the ECD to the TMD, which triggers the open state conformation of the channel. However, different conformational states should be obtained to understand better how this conformational change is transmitted to the pore.

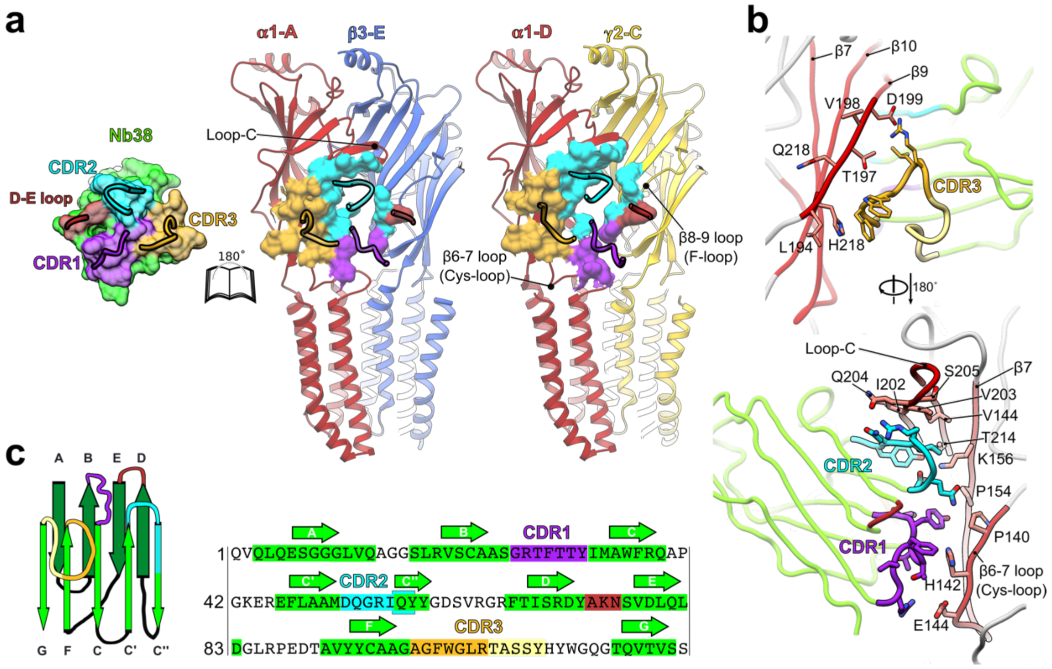

Figure 6.17 Nanobody Nb38 binding mode to GABA$_A$R-α1β3γ2 heteromer.

a, 'Open book' view of the Nb38 interaction surface with α1β3γ2 heteromer (nanobody was rotated 180º outwards around the GABA$_A$R longitudinal axis). Nanobody loops were coloured as follows: CDR1 is coloured in purple, CDR2 – in cyan and CDR3 – in orange, D-E loop in brown. Surface on the α1β3γ2 heteromer involved in interactions with the Nb38 is coloured based on the CDR loops. **b,** Detailed view of nanobody Nb38 binding to the α1 subunit of the heteromer. CDR3 loop binding to β9 and β10 strands is shown first, followed by 180° degree rotation along the GABA$_A$R longitudinal axis to reveal CDR1 and CDR2 interactions with the Cys-loop, loop-C, and β7 strand. **c,** Schematic representation of Nb38 and its sequence.

6.8.8. GABA$_A$R-α1β3γ2$_{EM}$ interface analysis

The analysis of subunit interfaces in the α1β3γ2$_{EM}$ model indicated that they are not equivalent. For example, the strongest interface, both in total buried surface and solvation free energy, was calculated between β3(P+) and α1(C-) subunit faces (Fig. 5.18a). The second strongest interactions were observed between γ2(P+)-β3(C-) and α1(P+)-β3(C-) interfaces. Finally, the α1(P+)-γ2(C-) interface had the lowest stability. The relative interface strength agrees well with the observed "collapsed" α1β2γ2$_{EM}$ structure when it was solubilised in DMNG. In this cryo-EM structure, all three weakest TMD interfaces were disrupted by the detergent, whereas only β3(P+)-α1(C-) interface maintained its integrity. In the model for the β3 homomer determined by cryo-EM, β3-β3 interfaces also have almost the same total buried surface and solvation free energy values as calculated for the heteromeric β3(P+)-α1(C-) interface and channel is not collapsed (Fig. 5.18b).

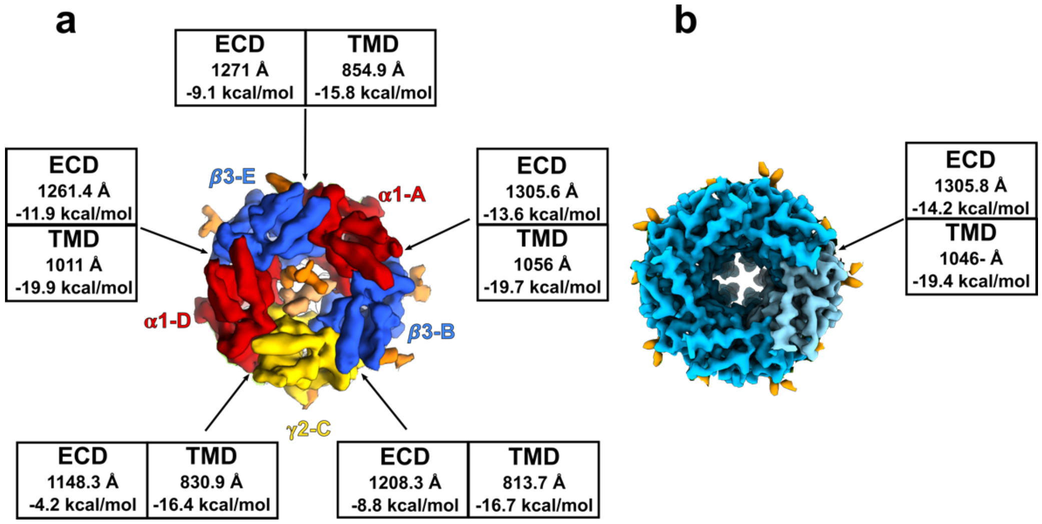

Figure 6.18 $\alpha1\beta3\gamma2_{EM}$ interface analysis.

Total surface and solvation free energy gain ($\Delta^{i}G$) for interfaces between the ECDs and the TMDs for $\alpha1\beta3\gamma2_{EM}$ **(a)** and β3-$Nb25_{EM}$ **(b)** as calculated by using the online PISA server (Krissinel and Henrick, 2007). $\Delta^{i}G$ is the gain in free energy when the interface is formed. Negative $\Delta^{i}G$ values mean that interfaces are hydrophobic and protein affinities are positive. Hydrogen bonding patterns or salt bridges are not included in $\Delta^{i}G$ calculation by PISA.

It is possible that disruption of β3(P+)-α1(C-) interface interactions by the neurotransmitter GABA, general anaesthetic or neurosteroid binding will cause conformational changes in both α and β subunits and this might form the basis for gating the channel. In addition, the relative strengths between these interfaces might explain the order in which the $GABA_AR$ heteromer assembles in the endoplasmic reticulum and why the α1Asn111-linked glycans achieve such well-defined conformations. After the nascent polypeptide sequence is released into the ER, $GABA_AR$ α1 and β3 subunits might form dimers first since the β3(P+)-α1(C-) interface complementarity is the strongest (Fig 5.19a). Then it is very likely that the next step of $GABA_AR$ subunit assembly involves the αβ dimer association with the γ subunit through the γ2(P+)-β3(C-) interface, which has a lower complementarity (Fig 5.19b). In addition, such association would allow the α1 Asn111-linked glycan to form the CH-π interaction across the vestibule with the γ2Trp123 residue and would stabilise the horizontal glycan conformer. Such αβγ trimer then could be joined by another αβ dimer to form a heteropentamer (Fig. 5.19c). Given the steric constraints in the receptor vestibule, the Asn111-linked glycan from this αβ dimer has to adopt a "vertical" position, protruding towards the extracellular space (Fig. 5.19d)

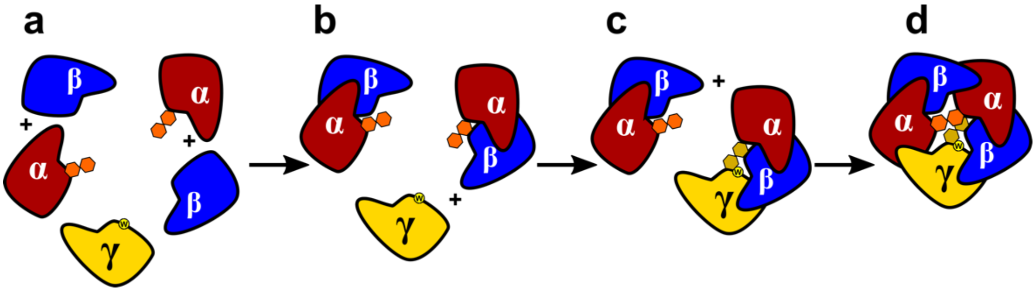

Figure 6.19 Heteromeric GABA$_A$α1β3γ2 receptor assembly model.

a, α1 and β3 subunits produced in the ER first form dimers through the β3(P+)-α1(C-) interface. **b,** α1β3 dimer binds to the γ2 subunit through the γ2(P+)-β3(C-) interface. Asn111-linked glycan on the α1 subunit interacts with γ2Trp123 and stabilises the horizontal glycan conformer. **c-d,** α1β3γ2 trimer binds to α1β3 dimer through the β3(P+)-α1(C-) and α1(P+)-γ2(C-) interfaces **(c)** to form the α1β3γ2 heteropentamer **(d)**. The Asn111-linked glycan on the joining α1β3 dimer is forced to tilt upwards, towards the extracellular milieu.

6.9. Conclusions

In this chapter, I present the first structure of a heteromeric GABA$_A$ receptor to date. Due to structural heterogeneity such receptors were difficult to crystallise and only the single particle cryo-EM approach made its structural analysis possible. I also describe a llama nanobody, which, was originally intended as a subunit tag for cryo-EM analysis, was found to be a potent positive allosteric modulator of the heteromeric α1β3γ2 GABA$_A$ receptor. Therefore, it was expected that this nanobody would help to stabilise the receptor in the open state. Cryo-EM was successfully used to solve the α1β3γ2$_{EM}$-Nb38 complex structure to medium resolution (~5 Å). The interpretation of the model built into this map taken with caution (especially the pore diameter) since it would have an approximate co-ordinate error of 0.5 Å at this resolution. It is possible to obtain a higher resolution structure, however it would require a more robust sample and better quality imaging which can be achieved with Titan Krios (FEI) microscope with a parallel beam illumination. However, this cryo-EM map provides the first glimpse of the architecture and organisation of the heteromeric $GABA_A$ receptors. It confirmed the β-a-β-a-γ (counter clock-wise, looking from the extracellular space) subunit stoichiometry determined by indirect methods. It also has revealed an unexpected N-linked glycosylation pattern in the vestibule of the channel, which constitutes a subunit stoichiometry control mechanism for α subunits. The exact physiological role of such glycosylation is not yet understood and must be investigated in more detail. Since higher resolution X-ray crystal structures of α5 and β3 subunits were available in our laboratory, an atomic model could be built into this map. This structure was shown to be in an activated state, with a pore just big enough to allow the Cl- ions to pass through. In the activated state, the β3 subunit seems to adopt a flexed M2 conformation and a slight TMD tilt, which in combination with other subunits, renders the bottom gate of the channel open. This, together with the etomidate-bound β3 homopentamer structure, suggests a mechanism by which β subunits might mediate channel opening.

In addition to this, the protein was solubilised in detergent. The initial cryo-EM data from the $\alpha1\beta3\gamma2_{EM}$ demonstrated the serious negative impact detergent can have on the structural integrity of heteromeric $GABA_A$Rs. Application of a milder detergent and a "re-lipidation" strategy did not fully resolve it. Recent work by Nigel Unwin demonstrates that cholesterol might have a mechanical role restricting the mobility of the nAChR δ subunit (Unwin, 2017). Therefore, it is not surprising that loss of lipids with structural roles for heteromeric $GABA_A$ receptors causes protein stability problems. In addition, the $\alpha1\beta3\gamma2_{EM}$ construct used in this work did not have the intracellular domains. In mouse serotonin receptor, the ICDs were shown to interact at the "bottom" of the channel (Hassaine et al., 2014). If similar ICD structures exist in $GABA_A$Rs, then they would have provided extra stability for the γ2 subunit and the completely "collapsed" state of the γ2 TMD would have not been possible. Therefore, to better understand heteromeric $GABA_A$R gating mechanism, full-length receptors should be studied in an environment which closely resembles the native lipid bilayers. Multiple conformations need to be captured of the same heteromeric receptor to understand clearly the conformational changes involved in its gating cycle.

7. Alternative GABA$_A$R solubilisation methods

7.1. Introduction

Based on the results in the previous chapters where GABA$_A$R structures were analysed in various detergents, it is clear that these channels are sensitive to the chemical environment surrounding their transmembrane domain. The intrinsically dynamic nature of a detergent belt does not recapitulate the physicochemical conditions which are present in a lipid bilayer. In the case of GABA$_A$ receptors, solubilisation in detergent tends to promote the desensitised state in homopentameric GABA$_A$Rs and leads to potentially non-physiological protein conformations in heteromeric GABA$_A$Rs. This hinders the appreciation of structural changes which could be happening during the receptor gating cycle in a lipid bilayer. In order to study GABA$_A$ receptors in an environment closely resembling native lipid bilayers, a different solubilisation strategy must be pursued. There are several alternatives which can provide a more stable environment for membrane proteins and allow single particle cryo-EM imaging, namely amphiphilic polymers (amphipols) and various lipid-bilayer nano-scale disc systems. In addition, intracellular GABA$_A$R loops, although not necessary for functional receptors (Jansen et al., 2008), might be structurally important in the context of heteromeric receptors and need to be investigated. In this chapter I will review my efforts to move away from the use of detergents as a solubilisation platform and the advances made in work with full-length heteromeric GABA$_A$Rs.

7.2. Amphipols

Amphipols are polymeric surfactants composed of hydrophilic and hydrophobic moieties which can render membrane proteins soluble in aqueous solutions (Tribet et al., 1996). One of the best characterised and the most commonly used amphipols to date is A8-35 (Popot et al., 2011) (Fig. 6.1a). Since amphipols are gentle surfactants and cannot dissolve membranes, membrane proteins are first extracted from lipid bilayer using detergents. After extraction, amphipols are added to mix with the detergents. Then detergent is removed following sample dilution or adsorption to BioBeads (Zoonens et al., 2014). Since amphipols are large polymers, they wrap around membrane protein transmembrane domains via multiple random hydrophobic interactions (Fig. 6.1b). Their dissociation is very slow since the whole polymer cannot readily detach in a single step. Therefore, in contrast to detergents, no excess of amphipols is required in the solution to keep proteins soluble. Free amphipol molecules can be removed using size exclusion chromatography, leaving only amphipol-solubilised membrane protein particles. Membrane protein solubilisation in amphipols does not lead to the "hydrophobic sink" problem where lipids or hydrophobic drug molecules become trapped in the detergent micelles. Lipid molecules can easily rebind to amphipol-solubilised proteins, therefore lipids can be supplemented back to amphipol-solubilised proteins after purification to support their structural integrity (Dahmane et al., 2013) (Fig. 6.1c). In addition, amphipols tend to increase membrane protein stability and maintain their functionality better than detergents (Etzkorn et al., 2013; Tifrea et al., 2011). For example, fluorescent agonist binding studies revealed that amphipol-solubilised nicotinic acetylcholine receptors retain conformations similar to those in lipid bilayer, whereas in detergent-solubilised protein is estimated to be largely in a desensitised state (Martinez et al., 2002). Nevertheless, amphipols still do not replicate exactly the same environment as lipid bilayers. Large conformational changes in membrane proteins were shown to be restricted by amphipols (Picard et al., 2006). This phenomenon was termed "Gulliver effect" since it is likely that amphipol polymer dampens down overall allowed protein transmembrane domain (TMD) motion through multiple unspecific interactions. High resolution structures of proteins solubilised in amphipols can be obtained by cryo-EM as exemplified by TRPV1 structures (Cao et al., 2013; Liao et al., 2013). To conclude, amphipols, even though come short of natural lipid bilayers, should be more advantageous than the detergents, especially if lipids were to be reconstituted to the protein after solubilisation.

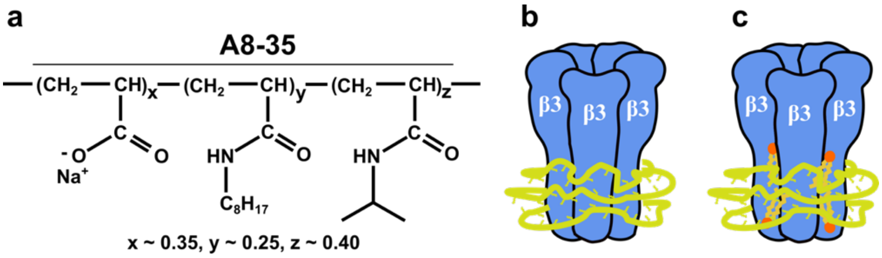

Figure 7.1 Amphipol structure and binding mode to membrane proteins.

a, Chemical structure of amphipol A8-35. **b,c,** Schematic representation of A8-35 (light green) binding to the TM region of a GABA$_A$R-β3 homopentamer (blue). **c,** Membrane protein solubilisation by A8-35 also permits lipid interaction with protein.

7.2.1. GABA$_A$R-β3 in amphipols

To test whether amphipol-solubilised GABA$_A$Rs can be imaged by cryo-EM, I reconstituted GABA$_A$R-β3 into amphipols (in detail description in Materials and Methods). Amphipol-solubilised GABA$_A$R-β3 eluted as a monodisperse peak in 150 mM NaCl, 10 mM Hepes pH 7.5 buffer in size-exclusion chromatography (Fig. 6.2a). Five-fold molar excess of Nb25 was added to the collected eluate and cryo-EM grids were prepared using protein sample concentrations at 0.1 mg/mL. Cryo-EM grids were imaged using TF30 Polara (FEI) 300 kV microscope fitted with a K2 direct electron detector (Gatan). Since there was no residual surfactant, the surface tension of protein sample was not affected and ice thickness was even throughout the holes. GABA$_A$R-β3 particles were evenly distributed across the ice and there were very few aggregates (Fig. 6.2b). This allowed to take images from the middle of the holes using automated data collection. However, all amphipol-solubilised GABA$_A$R-β3-Nb25 particles were adsorbed to water-air interface and only "top" views were observed. No side views were detected after performing the 2D classification (Fig. 6.2c). Lack of random particle orientations prevents 3D reconstruction of the protein due to the missing angular projections.

A similar particle adsorption to water-air interface problem was observed for ryanodine receptor, when this protein was reconstituted into amphipols (Baker et al., 2015) and nanodiscs (Efremov et al., 2015). In both cases random particle view distribution was partly achieved by adding octyl β-D-glucopyranoside (βOG) in concentrations ten times below its critical micelle concentration (CMC). This was only done to maintain free detergent molecules in the solution without allowing them to form micelles or solubilise protein. Detergents form a layer at the water-air interface, preventing proteins from interacting with it. Since βOG has a high CMC value, a lot of detergent was still present in the solution (0.1-0.07 % (w/v)). Unfortunately, this strategy could not be replicated with amphipol-solubilised GABA$_A$R-β3-Nb25 as it resulted in particle aggregation. It appears that βOG is a harsh detergent, which is not compatible with GABA$_A$R-β3 solubility. This highlights a general point that even in residual concentrations, detergent molecules may still bind to membrane proteins solubilised in amphipols or nanodiscs, interfering with their structural integrity or possibly causing aggregation. To avoid the uncertainties regarding detergent impact on the protein, the cryo-EM sample should be kept detergent-free while tackling particle orientation problem.

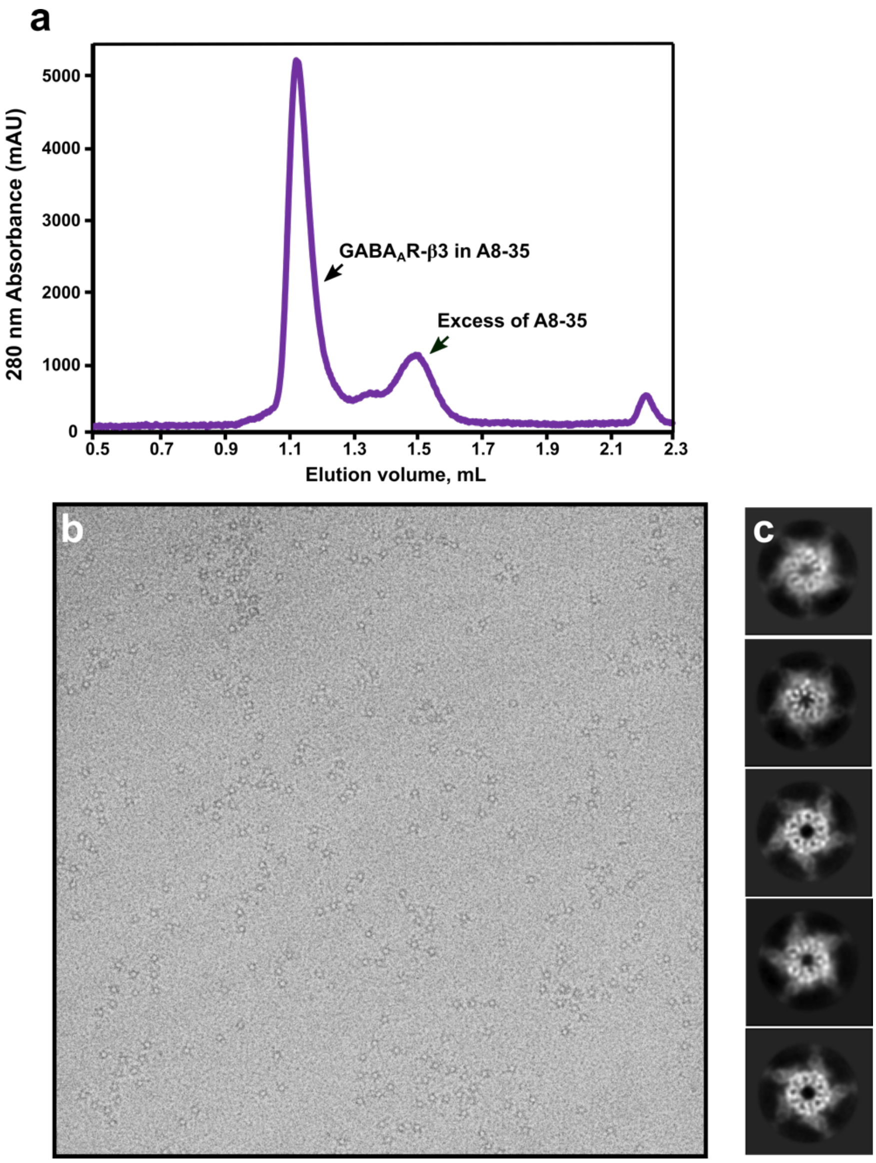

Figure 7.2 GABA$_A$R-β3 reconstitution to amphipols and imaging with cryo-EM.

a, Size exclusion chromatogram (Superdex 200 3.2/300) of a GABA$_A$R-β3 sample solubilised in amphipols. **b,** Representative cryo-EM micrograph for GABA$_A$R-β3-Nb25 sample in amphipols at 0.1 mg/mL concentration. **c,** Representative 2D classes of GABA$_A$R-β3-Nb25-amphipol particles. Only top/bottom views are visible with five nanobodies extending radially outwards.

To summarise, this experiment demonstrated that amphipol-solubilised GABA$_A$R particles would enable more high-throughput data collection of protein particles solubilised in a more benign environment compared to the detergent samples used before. However, it was not clear which GABA$_A$R-β3 surface (TMD or ECD) was responsible for adsorption to water-air-interface. It also was not known whether different subunits have the same propensity to adhere to this interface. To learn more, different GABA$_A$R samples were reconstituted into amphipols and were analysed by cryo-EM.

7.2.2. Full-length GABAAR-α1β3γ2 in amphipols

In our laboratory, full-length GABA$_A$Rs were difficult targets to pursue owing to low expression yields in transiently transfected cells and poor solubilisation results in detergent. In contrast, GABA$_A$R intracellular loop truncation constructs always could be produced in much higher yields, the resulting channels were functional and, finally, these proteins were more likely to crystallise due to the absence of large flexible regions. However, advances in cryo-EM single particle analysis make it possible to structurally study full-length GABA$_A$Rs as it does not require crystallisation. Nonetheless, significant amounts of protein are needed for biochemical characterisation and cryo-EM sample optimisation. Higher protein yields can be achieved by producing full-length heteromeric GABA$_A$Rs in stable cell lines. As part of the collaboration with Prof. Keith W. Miller's laboratory (Massachusetts General Hospital, US) we obtained a HEK293S GnTI$^-$ stable cell line expressing full-length GABA$_A$-α1β3γ2 receptors. For purification purposes, this cell line contains α1 subunits tagged with an N-terminal FLAG tag (Munro and Pelham, 1984) and γ2L subunits tagged with a C-terminal 1D4 tag (Molday and MacKenzie, 1983). These receptors were shown to be activated by GABA in the same fashion as the wild-type receptors, they were resistant to inhibition by zinc and were shown to be modulated by diazepam and etomidate (Dostalova et al., 2014a). This cell line allowed us to obtain enough material to perform full-length GABA$_A$-α1β3γ2 (FL-α1β3γ2, for short) structural studies by cryo-EM.

First, FL-α1β3γ2 purification was attempted using detergent. Stable cells were induced for 18-28 h period, collected and lysed with DDTM as described in Materials and Methods. FL-α1β3γ2 was isolated by affinity purification using the 1D4 tag at the C-terminus of the γ2 subunit. FL-α1β3γ2 purification using 1D4 beads normally results in smaller yields than purification through α1 FLAG tag, but it guarantees that FL-α1β3 heteromers, still present in the cell line in small amounts, will not be co-purified (Dostalova et al., 2014b). The detergent-solubilised sample was run on a size exclusion column, however most of the protein eluted as a large aggregate peak and only a small fraction eluted at an approximate elution volume for a pentameric receptor (Fig 6.3a). It was assumed that size exclusion column adsorbed the detergent causing the FL-α1β3γ2 to aggregate. More tests were performed where size exclusion column was equilibrated with higher detergent concentrations and for longer time. However, this made no difference on protein aggregation, therefore it is unlikely that loss of detergent on the column is the cause. To check whether sample aggregation occurred preceding the size exclusion chromatography, negative stain electron microscopy was carried out. Surprisingly, the negative stain micrographs of the input sample revealed that the 1D4 bead eluate contains just a small amount of aggregates with most particles being single pentamers (Fig. 6.3b). This means FL-α1β3γ2 forms large aggregates during the contact with the column during size exclusion chromatography. It also shows that intact FL-α1β3γ2 molecules can be extracted from membranes in detergent, meaning that subsequent exchange to amphipols or nanodiscs is possible.

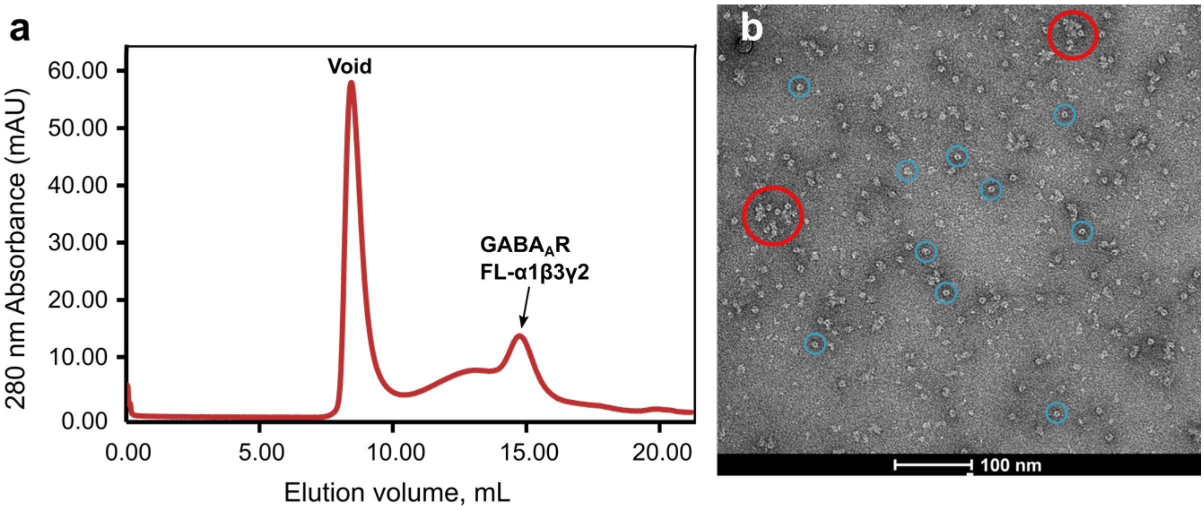

Figure 7.3 FL-α1β3γ2 purification in detergent.

a, Size exclusion chromatogram of a FL-α1β3γ2 sample run on a Superose 6 3.2/300 Increase^{TM} size exclusion column. FL-α1β3γ2 peak at around 14.8 mL is much smaller when compared to the void volume at 8 mL elution volume. **b,** Negative stain micrograph of the FL-α1β3γ2 input sample for the size exclusion experiment reveals that sample is not completely aggregated before being loaded onto the column. Blue circles mark the intact heteromers, whereas red circles highlight large aggregates.

FL-α1β3γ2 was extracted using DDTM and the eluate from 1D4 beads was used for protein transfer into A8-35 as described in Material and Methods section. The protein was run on a Superose 6 size exclusion column which showed that there was much less aggregation than before and much more protein eluted in the pentamer peak (Fig. 6.4a). The pentamer peak fraction was analysed using negative stain and homogenous well-separated particles were revealed (Fig 6.4b).

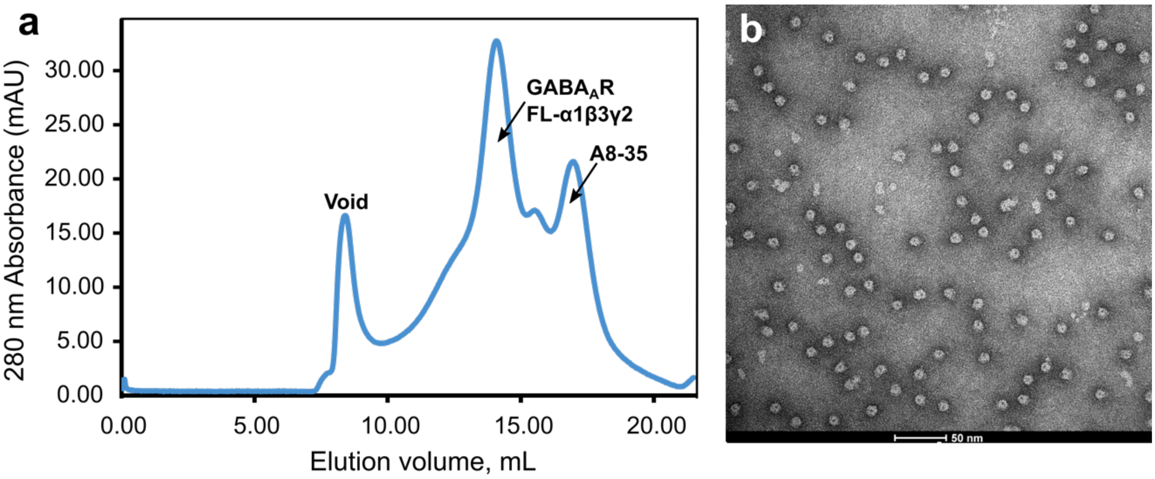

Figure 7.4 FL-α1β3γ2 purification in amphipol A8-35.

a, Size exclusion chromatogram of an amphipol-solubilised FL-α1β3γ2 sample run on a Superose 6 3.2/300 Increase^{TM} column. The void volume peak (8 mL) significantly lower than the GABA$_{A}$R pentamer peak (14 mL). An excess amphipol peak was also observed at 17 mL of the elution volume. **b,** Negative stain micrograph of the gel filtrated FL-α1β3γ2 in A8-35 reveals a monodisperse particle population.

In order to check whether FL-α1β3γ2 particles have the right subunit stoichiometry, α subunits of FL-α1β3γ2 were tagged with nanobody Nb30. Nb30 is an α1 subunit-specific nanobody. FSEC experiments indicated that Nb30 and Nb38 can bind to an α1β3 heteromer at the same time, suggesting that Nb30 targets a different epitope compared to Nb38 (Paul Miller, personal communication). Electrophysiology experiments performed by Dr. Paul Miller and Suzanne Scott have also shown that Nb30 acts as a GABA$_{A}$R agonist (Paul Miller, Suzanne Scott, personal communication). We considered the possibility that this nanobody could target a site at the top of the channel so that, if the ECD was responsible for particle adsorption to the water-air interface, it might help with the particle orientation problem. For this reason, the Nb30 binding mode was analysed by electron microscopy. This nanobody was incubated with A8-35-solubilised FL-α1β3γ2 and size exclusion chromatography was performed. Negative stain images were taken of the protein in the elution peak fraction. Particles were picked with EMAN2 and subjected to 2D classification with Relion. The 2D classification showed that FL-α1β3γ2 particles tend to be positioned on the carbon substrate in an upright fashion with a varying degree of tilt (Fig. 6.5a). There were some side views, however their respective 2D classes showed no presence of intracellular loops (Fig. 6.5a). It was not clear whether the disordered loops of the intracellular domains (ICD) did not stain well with uranyl formate or whether they have been truncated by proteolytic cleavage during the purification. In addition, the 2D classes with particle top views revealed that two Nb30 molecules were bound to this receptor (Fig. 6.5a). Since the protein was captured through the 1D4 tag on the γ2 subunit, this means that the receptor has the right subunit composition, as the other two untagged subunits can only be β3s. The exact order of subunits arrangement could not be discerned from these images, but is likely to be the same as in the α1β3γ2$_{EM}$ structure. This sample was also used to prepare the cryo-EM grids which revealed that FL-α1β3γ2 particles were still interacting with the water-air interface in the same manner as GABA$_{A}$R-β3 homopentamer (Fig. 6.5b). 2D classification of the cryo-EM FL-α1β3γ2-Nb30 particles showed a major class of top views with two Nb30 molecules arranged in the same fashion as in the negative stain micrograph (Fig. 6.5c).

Overall, these results show that heteromeric GABA$_{A}$Rs are also prone to adsorption to the water-air interface and that it must be common problem for any GABA$_{A}$Rs when detergent is removed. Therefore, a strategy to solve this problem must be developed to allow their imaging with cryo-EM.

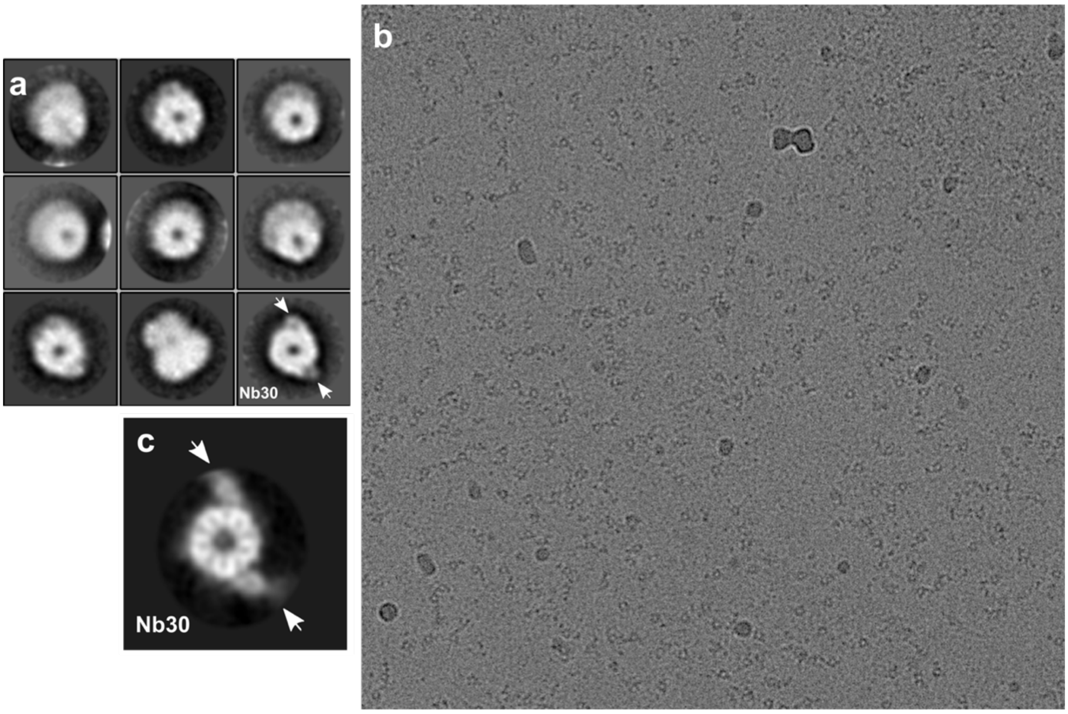

Figure 7.5 Electron microscopy of FL-α1β3γ2-Nb30 sample.

a, Negative stain 2D classification results for FL-α1β3γ2-Nb30 sample. Nb30 is highlighted with white arrows. **b,** Cryo-EM micrograph of a FL-α1β3γ2-Nb30 sample (~0.1 mg/mL) reveals an even distribution of particles across the ice, however all particles are aligned in single orientation making the 3D reconstruction of this sample impossible. **c,** The major 2D class observed for FL-α1β3γ2-Nb30 cryo-EM sample. Nb30 is marked with white arrows.

7.3. Tackling preferential particle orientation in amphipol-solubilised FL-α1β3γ2

7.3.1. N-linked glycan binding lectins

Several GABA$_A$R samples in amphipols were tested for adherence to water-air interface. GABA$_A$R-β3 homopentamer, FL-α1β3γ2 and α1β3γ2$_{EM}$ heteromers all adsorbed to water-air interface when solubilised in amphipols. FL-α1β3γ2 and α1β3γ2$_{EM}$ should have either intracellular loops or soluble BRIL fragments extending away from TMD. Therefore, it is very unlikely that GABA$_A$Rs associate with the water-air interface through their TMDs. The ECDs, however, in all three cases, provide a flat and contiguous surface for adherence. Generally, it is thought that protein and water-air interface interactions occur through exposed hydrophobic patches of protein (de Jongh et al., 2004). However, the exact mechanism of adherence in case of GABA$_A$Rs is not clear as their ECDs tend to have an overall positive charge due to a high number of lysine and arginine residues (Fig 6.6a). In addition, multiple GABA$_A$R subunits possess glycosylation sites at their N-termini (Fig 6.6b), where glycans are poised to be pointing upwards as seen in the GABA$_A$R-β3 structure (Fig. 6.6c) (Miller and Aricescu, 2014). It is therefore expected that GABA$_A$R FL-α1β3γ2 heteromer should have its ECD covered with N-linked glycans at equivalent positions (Fig 6.6d).

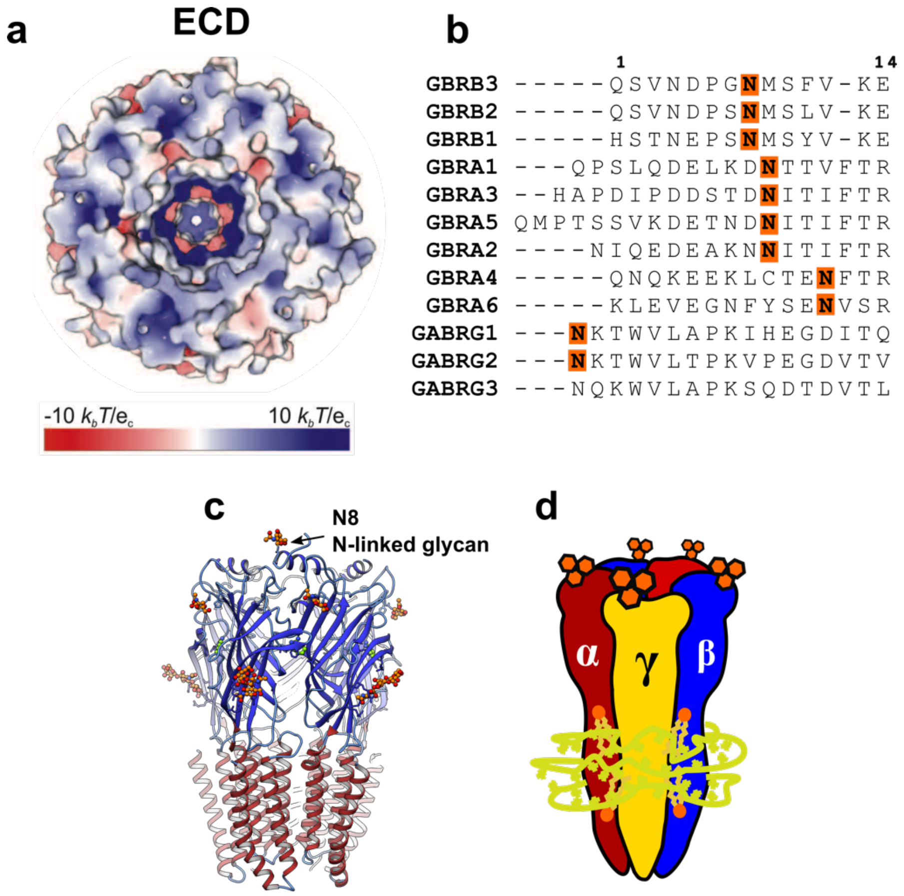

Figure 7.6 Electrostatic properties and N-linked glycosylation at the top of the GABA$_A$R ECD

a, Electrostatic potential distribution for solvent accessible surface of the GABA$_A$R-β3 ECD as seen from the extracellular environment. Panel **(a)** was adapted from Miller and Aricescu, 2014. **b,** Multiple sequence alignment of GABA$_A$R α, β and γ subunits at the N-termini. The shown sequence numbering is for the β3 subunit. N-linked glycan sites at the N-terminus of subunits are highlighted in bold and orange. **c,** Side view of a GABA$_A$R-β3 receptor. N-linked glycan at Asn8 at the N-terminus of the receptor was resolved in one of the chains and is highlighted by an arrow. **d,** Schematic representation of FL-α1β3γ2 receptor showing putative N-linked glycans at the top of the ECD.

One way of tackling the preferential particle orientation problem is to physically block the interaction site between the protein and the water-air interface. If this interaction occurs at the top of the ECD, then proteins specifically targeting this site could prevent its adsorption. It seems that N-linked glycans present a naturally occurring motive which can be exploited for specific binding of proteins without re-engineering of the available GABA_AR constructs. N-linked glycans could be coated with lectins, which are carbohydrate-binding proteins with variety of folds and specificities (Gabius et al., 2011). Since FL-α1β3γ2 receptors are produced in HEK293S GnTI$^-$ cells, the final N-linked glycosylation products are mannose rich (Chang et al., 2007) and this could be exploited by using mannose-specific lectins. In the antiviral therapy field, there were various mannose-binding lectins described (Balzarini, 2007; Singh et al., 2014), however they are all multimers where binding affinity depends on the oligomerisation state. Oligomeric lectins would aggregate FL-α1β3γ2, therefore it was necessary to produce a monomeric form of mannose-binding lectin. Griffithsin, an algae-derived lectin, was described to bind to mannose 9 (Man9) carbohydrate moieties with high affinity as a monomer (Moulaei et al., 2010) (Fig. 6.7a) and was used for this study. This 13 kDa protein can be easily produced in bacteria with high yields and purity (Fig. 6.7b). For further details, see Materials and Methods section. It was hypothesised that a monomeric griffithsin (mGRFT) binding to N-linked glycans on FL-α1β3γ2 receptor N-terminus would help to prevent particle adsorption to the water-air interface and solve the particle orientation problem for this sample (Fig. 6.7c). In addition, it was expected that mGRFT will bind to other N-linked glycans present on the β3 (Asn80, Asn149) and γ2 subunits (Asn90, Asn208) and increase the overall particle size. In addition, since mGRFT is unlikely to modulate GABA_AR function through glycan binding, it could be used as a functionally-neutral subunit tag for single particle alignment without the need of nanobodies.

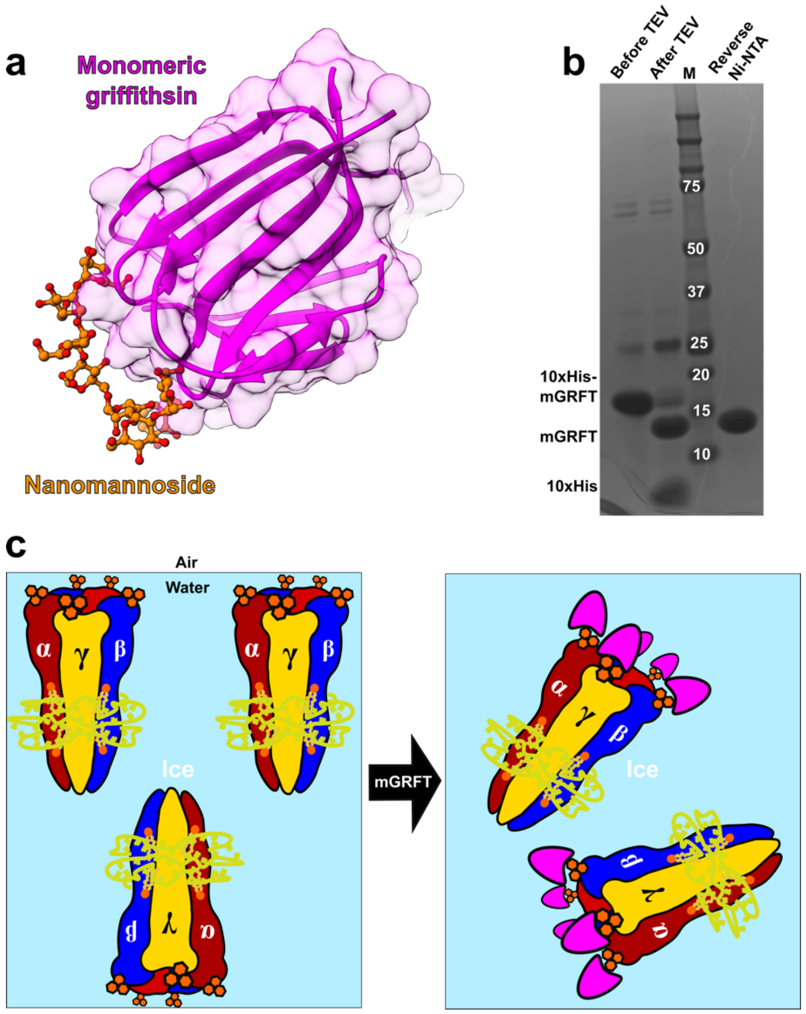

Figure 7.7 Targeting GABA$_A$R N-linked glycosylation using monomeric lectins.

a, Monomeric griffithsin (magenta) binding mode to a nanomannoside (orange) (PDB 3LL2). **b,** SDS-PAGE gel analysis of samples from monomeric griffithsin (mGRFT) purification. Cleavage with TEV and reverse Ni-NTA yields a highly pure mGRFT sample. **c,** Model of griffithsin-mediated disruption of the interaction between water-air interface and FL-α1β3γ2 ECD. mGRFT binding to other N-linked glycans present on the GABA$_A$R subunits is not shown in this schematic model.

During the FL-α1β3γ2 expression, kifunensine was supplemented to the suspension cell medium to inhibit the mannosidase I-mediated trimming of Man9 glycan precursor (Elbein et al., 1990). This was done since mGRFT has higher affinity for Man9 carbohydrate moieties (Moulaei et al., 2010). Since mGRFT tends to interact with carbohydrate-based size exclusion columns in an unspecific manner, 5-fold molar excess of mGRFT was added into an already gel-filtrated FL-α1β3γ2-Nb30 sample in amphipols. After incubation for 30 min, cryo-EM grids were prepared and imaged with a 300 kV microscope. Unfortunately, the micrographs revealed that FL-α1β3γ2-Nb30-mGRFT particles still adhere to water-air interface (Fig. 6.8a). A closer examination of particles with 2D classification revealed that mGRFT is bound to N-linked glycans found at the sides of FL-α1β3γ2 ECD, but not at the top (Fig. 6.8b). mGRFT can be seen as the diffuse densities at the edges of the receptor, which were not visible in the FL-α1β3γ2-Nb30 sample. mGRFT density pattern matches well with the N-linked glycan positions on the β3 and γ2 receptors revealing the stoichiometry of FL-α1β3γ2 (Fig. 6.8c). From this 2D class it is clear that FL-α1β3γ2 has the same stoichiometry as $\alpha1\beta3\gamma2_{EM}$. In addition, it is possible to see glycan densities in the FL-α1β3γ2 vestibule, which are not visible in the 2D classes of β3 hompentamer in amphipols (Fig. 6.2c).

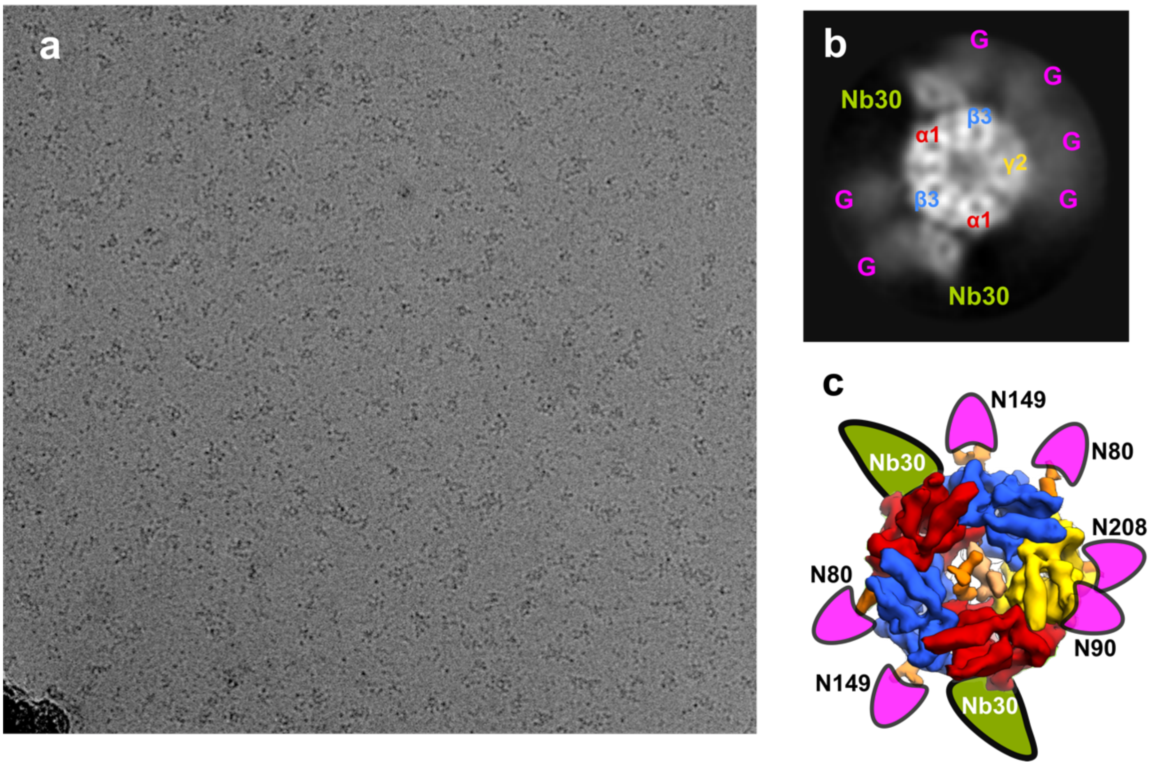

Figure 7.8 Cryo-electron microscopy of FL-α1β3γ2-Nb30-mGRFT sample.

a, Representative cryo-EM micrograph of a FL-α1β3γ2-Nb30-mGRFT sample shows particles covered in mGRFT which are still oriented in a single orientation. **b,** Major 2D class for FL-α1β3γ2-Nb30-mGRFT particles in cryo-EM images. GABA$_A$R subunits are marked based on the N-linked glycosylation pattern revealed by mGRFT and nanobody positions. **c,** Model of FL-α1β3γ2-Nb30-mGRFT particles describing the 2D classification results. Note, that Nb30 recognises the complementary side of α1 subunit, in contrast to Nb38, which binds to the principal side of α1.

It is not clear why griffithsin is not binding to the N-linked glycans located at the N-termini of $GABA_ARs$. N-linked glycan presence at this site was confirmed structurally in the β3 homopentamer. It is possible that FL-α1β3γ2 particles in amphipols are already adsorbed to water-air interface and monomeric griffithsin cannot access the N-linked glycans anymore. If this was the case, griffithsin should be supplemented to the sample before detergent removal. Finally, the role of the N-linked glycans in $GABA_AR$ particle adherence to the water-air interface should be investigated in more detail by glycosylation site mutations or simply by treatment with protein N-glycanase F (PNGase F). PNGase F cleaves the bond between the innermost N-acetylglucosamine and asparagine residues (Freeze and Kranz, 2010) and should remove fully the N-linked glycans from the $GABA_AR$ N-termini.

7.3.2. Graphene oxide grid tilting

A recent study has described a method where preferred particle orientation problem was mitigated by collecting single particle cryo-EM data from tilted grids (Tan et al., 2017). This study found that data collection at single high tilt (40°) were effective for influenza haemaglutinnin (HA) particle 3D reconstruction to 4.2 Å even though these particles adopt a highly preferred specimen orientation. The same strategy was applied for FL-α1β3γ2 receptors deposited on graphene oxide grids. Graphene oxide (GO) is a hydrophilic derivative of graphene (~1 nm thickness) which allows protein sample adsorption better than graphene, but still retains high electron conductivity and is more transparent than amorphous carbon supports (Pantelic et al., 2014). As judged by negative stain microscopy, FL-α1β3γ2 particles distribute well on carbon substrates and have a certain degree of tilt, which could be also true for sample deposited on the GO grids (Fig 6.9). By tilting the GO grids coated with FL-α1β3γ2, it could be possible to recover a higher proportion of missing angles than from samples in suspended ice grids. Therefore, I explored whether GO grids are suitable for FL-α1β3γ2 particle imaging and whether tilting of such grids would allow the 3D reconstruction of the protein.

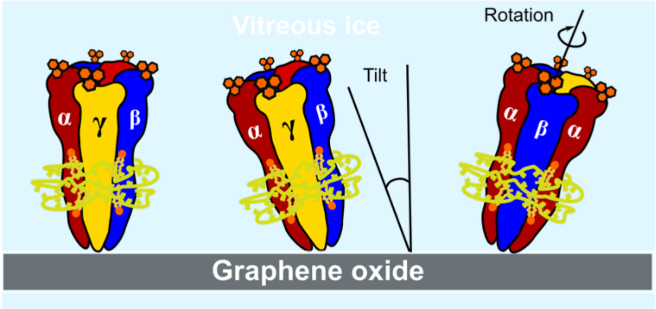

Figure 7.9 FL-α1β3γ2 deposition mode on carbon substrate cryoEM grids.

FL-α1β3γ2 sample deposited on the carbon substrate can adopt a tilt and rotate freely.

Graphene oxide grids were prepared in-house based on the protocol described in Bokori-Brown et al., 2016. This method involves graphene flake exfoliation and deposition on glow discharged Quantifoil (R1.2/1.3, 300 mesh, gold). GO deposition efficiency was estimated by imaging the grids with T12 100 kV electron microscope (FEI Company) at low magnification (LM 400x). Freshly prepared grids were air-dried and used immediately for sample adsorption. GO cryo-EM grids were then imaged with the TF30 Polara microscope (FEI company) at 300 kV. Overall, GO grids were not ideal for automated data collection as GO film coverage was not homogenous across grids (Fig. 6.10a). In addition, the graphene oxide film easily breaks (Fig. 6.10b) and folds over (Fig. 6.10c). Therefore, data collection was carried out manually and it is time consuming and inefficient.

Nevertheless, a large number of (200-300) FL-α1β3γ2-Nb30 particles could be imaged in a single micrograph providing the GO layer was even and well-hydrated (Fig. 6.11a). As anticipated from the negative stain images, the 2D classification revealed that FL-α1β3γ2-Nb30 particles sit on the GO substrate in a preferential orientation with a varying degree of tilt and there was a small number of side views (Fig. 6.11b). GO grids also caused some loss of high resolution information and 2D classes were noisier than what is expected from a similar number of particles suspended in ice. Due to missing view angles, a 3D reconstruction could not be performed from these particles. To increase the view angle distribution, a FL-α1β3γ2-Nb30 dataset was collected from GO grids tilted by 40°. Particles were picked with Gautomatch (Kai Zhang, LMB-MRC) and local particle CTF information was estimated using Gctf (Zhang, 2016). The estimated local particle CTF parameters seemed to correlate well with the tilt direction in the micrographs (Fig. 6.11c). Nevertheless, 2D classification of tilted particles revealed noisy classes with few features. It is likely, that tilting of a GO made the sample cross-section thicker and more background noise was introduced.

Overall, GO grid tilting by 40° seemed to increase the angular distribution of particles, but at a loss of the high resolution information. Since $GABA_A$Rs are relatively small proteins any increase in background noise is detrimental to particle alignment. As a consequence, a very large number of particles would be needed to produce a 3D reconstruction with sufficient resolution for biological interpretation. Slow manual data collection on GO grids would make it a very difficult task, therefore GO grid tilting does not provide an effective solution for fixing particle orientation problem.

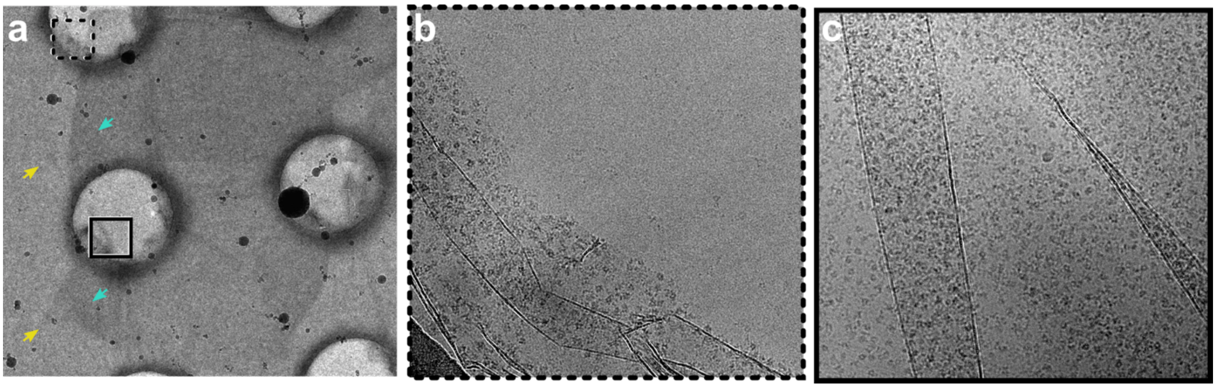

Figure 7.10 Graphene oxide grids for FL-α1β3γ2 imaging.

a, Low magnification cryo-EM image showing a graphene oxide flake (cyan arrows) deposited on the amorphous carbon support (yellow arrows). Note, this particular area is dry and graphene oxide is easy to see. Normally, the contrast is much worse and during manual collection at low magnification and it is difficult to judge whether the GO support film is covering a hole or not. **b,** Cryo-EM image of a broken GO support coated with FL-α1β3γ2 particles. **c,** Cryo-EM image of the GO layer folded over itself. Both **(b)** and **(c)** images are sub-optimal for data processing as a considerable amount of time would be required to manually inspect these micrographs and to pick the correct particles.

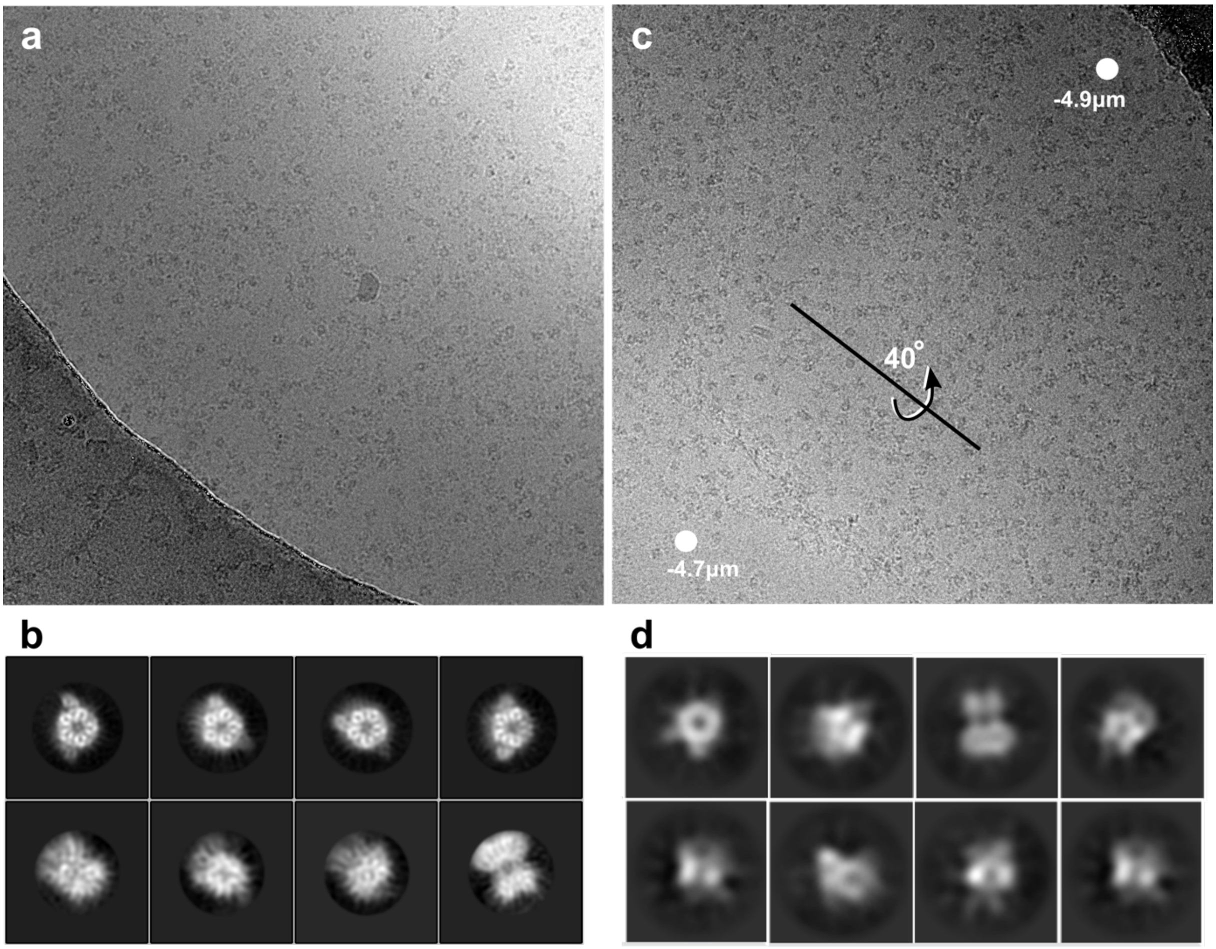

Figure 7.11 FL-α1β3γ2 sample imaged on GO grids tilted by 0° and 40°.

a,b, Representative cryo-EM micrograph **(a)** and 2D classes **(b)** for FL-α1β3γ2-Nb30 sample on the GO grids with 0° tilt. **c,d,** Representative cryo-EM micrograph **(c)** and 2D classes **(d)** for the same sample on the GO grids but with 40° tilt. Note, particles are seen well on this micrograph because it is highly defocused. Grid tilt axis and tilt direction is shown. Defocus values are given for two corners at the extreme ends of tilt.

7.4. FL-α1β3γ2 heteromer preferred orientation question

It was observed that FL-α1β3γ2 sample behaviour on the negative stain grids is inconsistent between different batches of samples. During the most of the experiments performed, “top views” were the dominant class and there was only a small fraction of side views, which displayed no signs of intracellular domains (Fig. 6.5a). However, several FL-α1β3γ2 sample preparations had a completely different particle distribution on the continuous carbon grids used for negative staining (Fig 6.12a). In these micrographs, most of the FL-α1β3γ2 particles adopted “side view” orientations and, for the first time, intracellular domains were observed in the 2D classes (Fig. 6.12b). A balanced view distribution like this allowed me to reconstruct a 3D map from negative stain particles. This map possesses a density attributable to the ICDs (Fig. 6.12c). It appears to me that the presence of the ICDs did not allow FL-α1β3γ2 receptors to be positioned fully upright on the carbon substrate like before. Therefore, I hypothesised that ICDs could have been lost through some sort of proteolytic cleavage during the previous purifications.

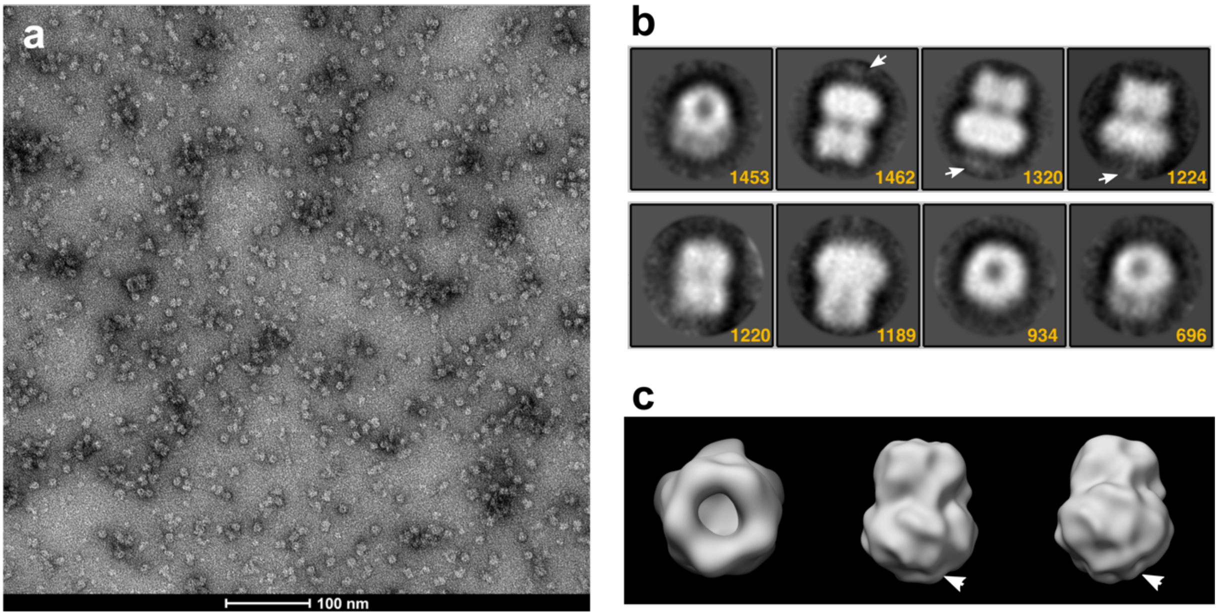

Figure 7.12 Negative stain analysis of FL-α1β3γ2 sample where ICD was retained.

a, Negative stain micrographs of FL-α1β3γ2 samples purified in Hepes pH 7.6 using a standard purification protocol. **b,** 2D classes for this FL-α1β3γ2 show multiple views and there is a signal for the ICDs (marked with white arrows). **c,** *Ab initio* 3D reconstruction from negative stain particles using cryo-SPARC (Punjani et al., 2017). White arrows mark the ICDs.

In order to establish what could cause the possible ICDs cleavage, I performed small scale purification experiments where I increased the mammalian protease inhibitor concentration to 2.5% during all purification steps and screened buffers with pH values of 7.2 and 8.0 (all previous purifications were carried out in pH 7.6). Mostly "top" particle views were observed for protein eluates at pH 7.2 and 8.0 (Fig. 6.13), indicating that buffer pH and cleavage by cellular proteases are unlikely to cause the ICD loss. Alternatively, these changes in particle orientation could be explained by differences in glow discharging or some other properties of the grids used. Further experiments need to be performed in order to understand when and how such preferential orientation of particles occurs on continuous carbon substrates.

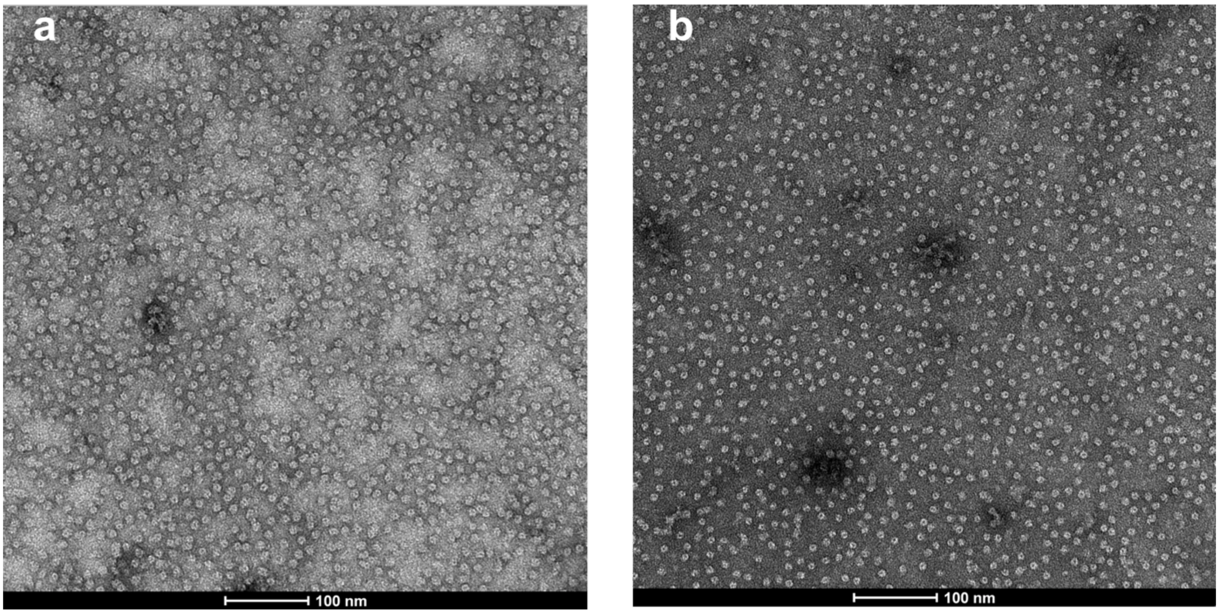

Figure 7.13 FL-α1β3γ2 purification in different pH buffers.

a,b, Negative stain micrographs of FL-α1β3γ2 samples purified in Hepes pH 7.2 **(a)** and Tris pH 8.0 **(b)** buffers. "Top views" are the majority in both samples.

7.5. Styrene-maleic acid copolymer for GABA$_A$R solubilisation

Styrene-maleic acid (SMA) copolymers (also known as Lipodisqs®) are novel amphipathic molecules (Fig. 6.14a), which are able to solubilise membrane proteins by wrapping around a patch of native lipid bilayer surrounding a protein (Fig. 6.14b) (Lee et al., 2016). This reagent allows direct protein extraction from membranes in form of SMA-lipid particles (SMALPs) for biophysical and structural studies (Pollock et al., 2017). For example, SMA extraction was successfully applied for microbial rhodopsin crystallisation in lipid-cubic phase (LCP) without exposing the protein to detergent (Broecker et al., 2017) and to image *E. coli* ArcB in SMALPs with negative stain (Postis et al., 2015). Such solubilisation technique would be invaluable for GABA$_A$R research as it enables protein structural analysis directly in its native environment without the detergent extraction step.

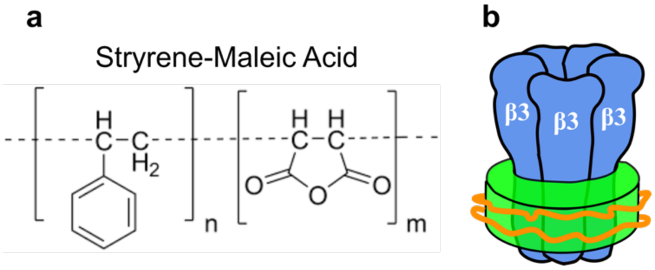

Figure 7.14 Styrene-maleic acid copolymer structure and its solubilisation mode of membrane proteins.

a, Chemical structure of SMA copolymer comprising of styrene (n) and maleic acid (m) monomers. **b,** Schematic representation of a GABA$_A$R-β3 homopentamer (blue) in a lipid nanodisc (green) stabilised by a SMA copolymer (orange).

To test whether SMA copolymers can be used to produce GABA$_A$R SMALPs, I carried out small scale GABA$_A$R-β3 solubilisation experiments as described in Materials and Methods. In short, 6% Lipodisq® 3:1 (Sigma) solution was added to HEK293S cells expressing GABA$_A$R-β3 in order to lyse the membrane and form GABA$_A$R-β3 SMALPs. Cells were readily lysed and GABA$_A$R-β3 lipid nanodiscs were captured through the C-terminal 1D4 tag using affinity purification. Sample was eluted with 1D4 peptide and analysed by small scale size exclusion chromatography, negative stain and cryo-electron microscopy (Fig. 6.15). The eluate was ran first on a size exclusion column, however, GABA$_A$R-β3 SMALPs eluted in the void volume and its tailing peak (Fig. 6.15a). We observed similar results for all tested membrane protein SMALPs in our laboratory. It seems that SEC might not be a generally suitable technique for SMALP separation by size. Negative stain electron microscopy was used in order to confirm whether the 1D4 eluate is indeed aggregated. Negative stain images revealed a large number of single GABA$_A$R-β3 SMALPs were intermixed with some aggregates (Fig. 6.15b). Negative stain confirms that molecules were successfully excised from the membrane and formed well-defined pentamers. The eluate was also used to prepare cryo-EM grids to check whether GABA$_A$R-β3 SMALPs tumble freely in ice. Unfortunately, the majority of particles were adsorbed to water-air interface in the same way as amphipol-solubilised protein, with only a few potential side views observed (Fig. 6.15c).

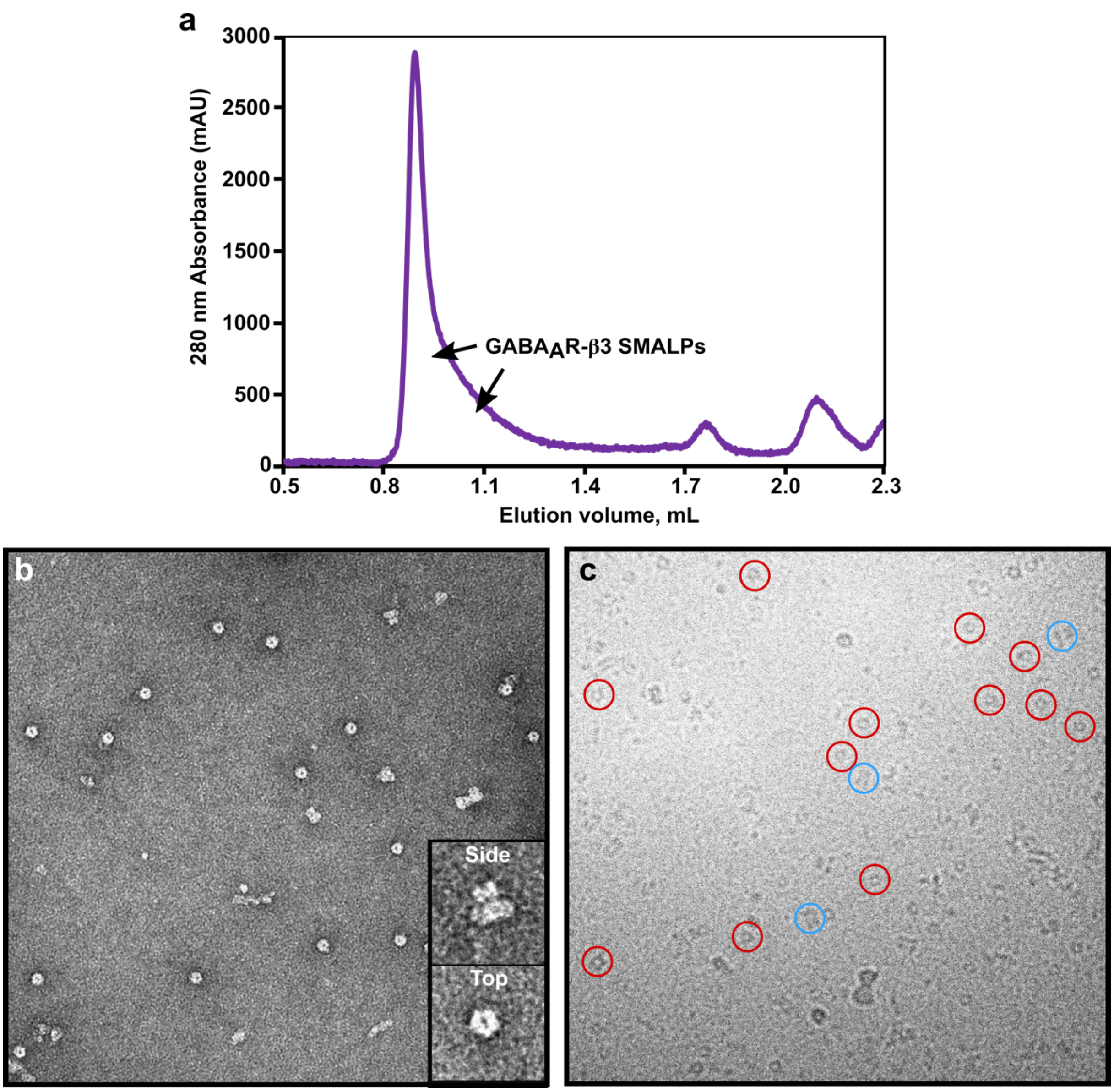

Figure 7.15 Electron microscopy of GABA$_A$R-β3 in SMA copolymer and lipid nanodiscs.

a, Size exclusion chromatogram (Superdex 200 3.2/300) of a GABA$_A$R-β3 extracted from membrane using SMA copolymer. **b,c,** GABA$_A$R-β3 SMALPs analysed by electron microscopy. Representative micrographs of GABA$_A$R-β3 SMALPs sample imaged with negative stain **(b)** and cryo-EM **(c)**. In the cryo-EM micrograph blue red circles mark particle top views, whereas the blue circles highlight side views.

Initial FL-α1β3γ2 solubilisation experiments were also carried out using Lipodisq® SMA copolymer 3:1, however the heteromeric receptor SMALPs tend to aggregate more than the β3 homopentamer. Different available SMA copolymers need to be tested for the heteromer sample to optimise its quality. However, the most important result from these experiments is that the particle orientation issue also affects SMALPs and thus it must be resolved before any data can be collected.

7.6. Conclusions

To be able to draw the correct conclusions about the gating mechanism of $GABA_A$Rs, these proteins should be studied in an environment which closely resembles native lipid bilayers. In addition, they should be studied without ICD truncations in order to fully appreciate their function and structural dynamics. I have shown that full-length heteromeric $GABA_A$ receptors can be purified in amphipols supplemented with lipids, and that there is a potential in using styrene-maleic acid for $GABA_A$R-lipid nanodisc production. In addition, since heteromeric full-length $GABA_A$ receptors can be extracted in detergent, it means that they can also be reconstituted into more traditional membrane scaffold protein (MSP)-based nanodiscs (Bayburt and Sligar, 2010) or saposin-lipoprotein nanoparticle systems (Frauenfeld et al., 2016). All these solubilisation techniques should help to yield more informative structures than samples solubilised in detergent. In addition, detergent removal from the sample should increase particle numbers collected per image and should allow more reproducible cryo-EM grid preparation. Overall, these improvements should enable the collection of data that is of much better quality than was possible before with detergent-solubilised samples.

Single particle cryo-EM of $GABA_A$R samples in amphipols or nanodiscs is hampered by the specimen preferred orientation problem. $GABA_A$R adsorption to the water-air interface is very likely to occur during sample thinning when a cryo-EM grids are prepared. Since the liquid layer which is left after the grid blotting has a huge surface-to-volume ratio, molecules can easily diffuse and hit the water-air interface multiple times even if the grid plunging into liquid ethane happens very fast. For example, it was estimated that protein particles can collide with water-air interface >1000 times per second in aqueous films which are <100 nm thick (Taylor and Glaeser, 2008). Therefore, if a protein has a hydrophobic patch or any other surface properties causing it to interact with the water-air interface, it will acquire preferential orientations under normal grid making conditions.

There are several possible ways to overcome preferential orientation problem. One solution would be to freeze the thinned cryo-EM sample so rapidly that proteins do not have enough time to diffuse and interact with the water-air interface. However, at the moment there are no such devices available and their development will be difficult since protein diffusion happens very quickly. The most common solution which is likely to work, is the application of surfactants like detergents which cover the water-air interface and act as a protective layer against protein adsorption (Baker et al., 2015; Efremov et al., 2015). However, detergents can have a harmful impact on proteins as it was the case for the GABA$_A$R-β3 receptor in amphipols. There are more benign surfactant molecules which should be tested using this approach. It would be interesting to see whether the same protective effect is achieved using lipids or amphipols instead of detergents. For example, lipids dissolved in organic solvents like dimethyl sulfoxide (DMSO) or ethanol could be applied onto the sample in small amounts just before blotting the cryo-EM grids, producing lipid coating similar to Langmuir monolayers (Stefaniu et al., 2014). Alternatively, cryo-EM grids or blotting paper could be soaked with lipids dissolved in organic solvent and air-dried. Upon sample application, it is possible that the deposited lipids could adhere and spread across the water-air interface forming a protective layer. Similarly, a small excess of amphipols in the solution might shield GABA$_A$R surfaces responsible for the adsorption to the water-air interface. However, surfactant molecules will affect sample surface tension properties. This can cause grid reproducibility problems, uneven ice thickness in grid holes, potential particle clustering at the hole edges and much higher protein concentrations might be needed as for detergent-solubilised samples.

Another approach would be to immobilise GABA$_A$R particles so that they cannot diffuse and interact with the water-air interface. One form of such method was tried, where GABA$_A$R FL-α1β3γ2 heteromer was deposited onto the GO film. However, GABA$_A$R FL-α1β3γ2 particles showed preferential orientation while interacting with the GO substrate. If I establish what conditions are necessa the GO grids might present a feasible approach for cryo-EM data collection. Nevertheless, the mechanism of protein particle adsorption to the GO film is unclear, as well as what structural implications it might have to a membrane protein. In addition, automated data collection would be difficult and collected images would have higher background noise. Overall, GABA$_A$R particle deposition on a substrate should be avoided, if possible.

Grid tilting experiments have many limitations. First, if particles are suspended in ice and interact with the water-air interface, they are likely to be structurally damaged by the denaturing nature of this interface (Yano et al., 2013). Grid tilting cannot fully recover all missing angles and the resulting EM maps cannot be as good as when views are distributed isotropically. In addition, tilting of grids increases the background noise, making it difficult to align small particles. Due to these complications, it is unlikely that this particular technique will help to determine GABA$_A$R structures by cryo-EM.

Finally, the preferred orientation problems can be solved by blocking or modifying the protein surface which causes adsorption to the water-air interface. Although the lectin approach did not work for GABA$_A$ FL-α1β3γ2 receptor as expected, different strategies can be used. For example, GABA$_A$R subunits can be engineered to possess large soluble globular domains at their N-termini to interfere with adsorption to the water-air interface through the ECD. Antibodies or nanobodies binding at the top of the GABA$_A$R ECDs could perform the same function. The aim of this strategy is to maintain GABA$_A$ receptor behaviour in amphipols/nanodiscs as closely as possible to those of soluble proteins. This would allow me to make reproducible cryo-EM grids with minimal complications and with maximum collectible particle numbers per micrograph.

8. Concluding remarks and future work

8.1. Llama nanobodies alleviate GABA$_A$R structural characterisation

During this DPhil study I have successfully applied llama nanobodies in GABA$_A$R structural work. I initially showed that llama nanobodies bind to GABA$_A$Rs with high affinities in a subunit-specific manner which meant they were suitable for crystallisation studies as they form a robust complex. The application of nanobodies as crystallisation chaperones allowed me to obtain GABA$_A$R-β3 homomer crystals more reproducibly. Nanobodies enhanced the lateral packing of GABA$_A$R-β3 homomers by providing a hydrophilic surface compatible with crystal contact formation. GABA$_A$R-β3-Nb25 crystals routinely diffracted to 3.2-4.0 Å resolution, which later enabled me to perform small drug molecule soaking experiments. In addition to using nanobodies as crystallisation chaperones, I found that they can be applied in GABA$_A$R structural determination by cryo-EM. Nanobody binding makes GABA$_A$R particles larger, which improves their contrast in noisy cryo-EM images and facilitates the 3D reconstruction. In particular, rigid, subunit-specific tags were crucial for heteromeric GABA$_A$R structure determination by cryo-EM. This is because the differences between the various GABA$_A$R subunits are only apparent at high resolutions (<4 Å). During the initial 3D reconstruction steps, the resolution of the receptor structure is low and hence different subunits in the heteromer appear identical and cannot be aligned correctly. In this thesis, I demonstrated that the α1-specific nanobody Nb38 provided the extra features needed to superimpose heteromeric GABA$_A$R particles accurately. Apart from making the 3D reconstruction possible, Nb38 allowed me to sort GABA$_A$R particles *in silico* to select receptors with the correct subunit stoichiometry. Nb38 also acted as a positive allosteric modulator and helped the $\alpha1\beta3\gamma2_{EM}$ receptor to adopt an open-like conformation.

In general, nanobodies can target unique sites between different subunits, cause conformational changes and modulate the function of the channel. Due to time limitations during this project, an extensive functional screening of the available nanobodies was not performed and will therefore need to be carried out in future. It is possible that more nanobodies from this library will act as GABA$_A$R agonists or antagonists. Structural characterisation of such nanobody binding mode and mechanism might propel novel drug design efforts. In addition to this, nanobodies could be adapted to further facilitate GABA$_A$R structural biology. For example, nanobodies could be used as a scaffold for grafting more potent crystallisation chaperones, which might facilitate the process of generating reproducible well-diffracting crystals. Grafting of large proteins onto the nanobody might also physically prevent GABA$_A$R particles from sticking to the water-air interface, which should be useful for cryo-EM analysis of GABA$_A$Rs. To summarise, this work demonstrates that llama nanobodies are powerful tools assisting GABA$_A$R functional and structural characterisation.

8.2. Mechanism of action of the general anaesthetic etomidate

During the course of this work, I have been able to describe how the general anaesthetic etomidate binds and induces conformational changes in the GABA$_A$R-β3$_{K279T}$ homomer. Etomidate targets a pocket in the transmembrane domain between the two neighbouring β3 subunits. This structure helped me to reconcile various photolabeling, mutagenesis and functional experiments performed to date. It also offered insights into how etomidate might modulate GABA$_A$R function. First, I found that the binding pocket is primarily formed by residues from the principal face of the β3 subunit, whereas the complementary face subunit did not contribute much to etomidate binding. This observation explains why etomidate can bind both to β(P+)β(C-) and β(P+)α(C-) interfaces in αβγ GABA$_A$R heteromers. Therefore, etomidate is likely to convey its function primarily by altering the conformational state of β subunits. Since the β subunit ECDs also contribute to the GABA pocket, it is likely that conformational changes induced by etomidate help to coordinate the communication between β ECDs and TMDs upon agonist binding. Analysis of the apo and etomidate-bound GABA$_A$R-β3$_{K279T}$ structures revealed that etomidate binding deformed the C-terminus of the M2 helix. This conformational change was caused by insertion of the etomidate phenyl ring between residues Met286 (M3 helix) and Asn265 (M2 helix). In particular, Asn265 (M2-15′) is the key residue which links the M2 helix to the etomidate binding pocket and accordingly, mutations of this residue render etomidate ineffective. After etomidate binding, the C-terminus of the M2 helix moves closer to the channel pore axis, narrowing the diameter of the pore. Overall, the channel maintains a desensitised configuration. In the context of GABA$_A$R-β3$_{K279T}$ homomers, it is still not immediately clear how etomidate would promote channel opening.

The GABA$_A$R-β3$_{K279T}$ crystal structures offer some further clues on how etomidate binding could lead to a more efficient signal transmission from ECDs to TMDs. The GABA$_A$R-β3$_{K279T}$ apo structure shows that a thermostabilising K279T (M2-M3 loop) mutation allows the highly conserved β3Arg269 (M2 helix) to form extensive contacts with the M2-M3 loop. These interactions stabilise the M2-M3 loop and the neighbouring portions of the M2 and M3 helices. It is possible that this extra hydrogen bonding makes the M2-M3 loop region more rigid, allowing the ECDs to communicate more efficiently to the transmembrane region. It was shown recently that GABA$_A$R homomers containing α5 subunit TMDs (threonine residues equivalent to β3Lys279 are conserved in all α and γ subunits,) tend to open spontaneously, whereas when a lysine residue is introduced at this site, the channel activity is significantly reduced (Miller et al., 2017). In addition, if the β3Lys279 residue in a α1β3γ2L receptor is mutated to a threonine, this mutation increases the receptor's sensitivity to GABA (Fisher, 2002). In turn, this means that the βLys279 in the M2/M3 loop decreases the efficiency of signal transduction by allowing the M2-M3 loop to be more flexible. Based on these observations, I propose that etomidate binding between the M2/M3 helices and in close proximity to the M2-M3 loop, has a similar stabilising effect as the K279T mutation. Etomidate might lock the M2/M3 helices together and make this fragment more rigid, thus increasing the sensitivity to ECD conformational changes and GABA binding. Another potential etomidate mechanism of action might be related to decreasing the probability of GABA$_A$Rs entering the desensitised state. β3 subunit TMDs in the desensitised state do not have a large enough cavity to accommodate etomidate, whereas it expands significantly when the drug is present. The β3 TMDs from the open-like state model (5.17 Å α1β3γ2$_{EM}$ map) adopt a similar conformation as in the etomidate bound state. It is possible therefore that etomidate binding to this pocket reduces the rate at which the β3 TMD transitions to a desensitised conformation and prolongs the amount of time the channel is open. However, it is not yet clear whether desensitised β3 subunits look the same when they are in the context of a homomer and a heteromer. Electrophysiology studies have divergent findings regarding modulation of the desensitisation rate by etomidate. Studies of etomidate action on rat spinal dorsal horn neurons (Zhang et al., 2002) and on α1β3δ expressed in HEK cells (Liu et al., 2015a) showed that etomidate reduced the desensitisation of GABA$_A$Rs. However, electrophysiology experiments using etomidate and its derivatives on α1β2γ2 receptors expressed in *Xenopus* oocytes indicated there was very little effect on the desensitisation rate (Liu et al., 2015b). Propofol, another general anaesthetic which is believed to act through the same pocket, was shown to decrease the desensitisation rates in GABA_ARs from hippocampal neuron slices (Bai et al., 1999). To summarise, solving crystal structures of the homomeric complex bound to etomidate was an important step forward towards understanding how general anaesthetics, like etomidate, work. In the future, high resolution cryo-EM structures of heteromeric GABA_ARs in different conformations will help to advance this knowledge further.

8.3. The first glance at a human GAB_AAR-α1β3γ2 heteromer

The most challenging part of this DPhil project was the determination of the first 3D structure of a heteromeric human GABA_AR. In order to produce this structure, major problems in cryo-EM sample preparation, data collection and data processing had to be overcome. The most significant setback was caused by the non-physiological TMD conformations introduced by the detergent belt. Numerous rounds of sample optimisation had to be performed until we found that reconstitution of lipids to the detergent belt minimises the TMD motion of the γ2 subunit. Acquisition of preferential orientations in vitreous ice of the GABA_AR particles prevented me from collecting data using samples free from detergent. Detergent solubilised GABA_AR particles tend to aggregate on cryo-EM grids, which translated to a low number of usable particles per image. However, these particles adopted different views and hence a 3D reconstruction was possible. After a large amount of data was collected, a cryo-EM map of human GABA_AR-α1β3γ2 bound to a positively modulating nanobody, Nb38, was obtained to 5.17 Å resolution. Overall, this map was almost complete with well-ordered ECDs and TMDs, except for the M2, M3 and M4 helices of the γ2 subunit, which were not well defined. This map allowed me to build an atomic model using components from higher resolution structures. However, a high degree of caution needs to be exercised when interpreting this model as EM densities could not be seen for individual amino acid side chains at this resolution. Therefore, their coordinates in the model should not be over-interpreted, especially at the interfaces between different subunits, where rotamers and loop conformations could be very different from what is observed in high resolution homomeric structures.

Nevertheless, this structure offered us a first and informative glimpse at the architecture of a synaptic heteromeric GABA receptor.

Initially, $GABA_AR$-α1β3γ2 was shown to adopt a β-α-β-α-γ (counter clock-wise, viewing from the extracellular space) configuration, which was predicted based on electrophysiology, mutagenesis and drug binding experiments. Then, an α1 subunit N-linked glycosylation present inside the channel was identified unexpectedly. These glycans were remarkably well ordered with two distinct configurations, where one carbohydrate chain stretched horizontally across the channel vestibule while the other one was poised towards the extracellular milieu. The vestibule N-linked glycans are likely to regulate $GABA_AR$ stoichiometry by limiting the number of α subunits and could reflect the way αβγ heteromers are assembled in the endoplasmic reticulum. The $\alpha1\beta3\gamma2_{EM}$ structure also revealed that β3(P+)α1(C-) interfaces form the most extensive contacts in the heteromer. Since it is the same interface where neurotransmitter GABA binds, it is likely that close interaction between these subunits is involved in conformational change transfer during agonist binding. This structure also allowed me to compare the relative angles between ECDs and TMDs among α1, β3 and γ2 subunits. ECD/TMD configuration of α1 and γ2 subunits resembled the desensitised β3 homomer (Miller and Aricescu, 2014), whereas the heteromer β3 subunit configuration was more closely related to the glycine receptor open-desensitised state (Du et al., 2015). Different relative angles between M2 pore lining helices caused the channel pore to become asymmetric. The diameter at the narrowest point of the pore (desensitisation gate) was ~6 Å. Molecular dynamics simulations suggested that this diameter is wide enough for chloride to pass through the pore and we concluded that this conformation should represent an open-like state.

Overall, this structure represents a breakthrough in the field as it is the first heteromeric $GABA_AR$ receptor structure determined to date. It delineates the pseudosymmetric organisation of a prototypic synaptic $GABA_AR$ heteromer in an open-like conformation. In the future, it would be interesting to obtain a structure showing the closed state of the channel. Orthosteric site antagonists like gabazine or bicuculline could be used to induce the closure of the channel in the presence of the potentiating nanobody Nb38. This would allow measurement of the rotation of the ECD/TMD of each subunit and help to understand the gating cycle of a heteromeric $GABA_AR$.

8.4. Future directions in $GABA_AR$ heteromer research

The most important and physiologically relevant targets in $GABA_AR$ research are the heteromeric receptors. Use of single particle cryo-EM and llama nanobodies offers a viable approach to study such heteromeric $GABA_ARs$. The resolution of 3D reconstructions attainable with this method will be further improved by the arrival of better software, detectors or new technologies to improve particle contrast, like phase plates. In the future, it is very likely that the full gating cycle and the rich pharmacology of heteromeric $GABA_ARs$ will be explored in resolutions nearing 3 Å or better. Cryo-EM could also replace X-ray crystallography for solving structures of homomeric $GABA_ARs$ bound to small drug molecules, essentially removing the need to produce crystals of these membrane proteins. However, the cryo-EM approach still needs to overcome some major roadblocks along the way to these goals. As it was shown in this work, all detergent-solubilised homomeric $GABA_ARs$ adopt a desensitised state configuration, whereas the heteromeric $GABA_ARs$ display a significant conformational heterogeneity in the transmembrane region. Such TMD motions might not have a physiological relevance and could be merely an artefact introduced by the detergent belt. In the future, to avoid these pitfalls, one should aim to solubilise these proteins using lipid nanodiscs. The reconstitution of protein into the lipid bilayer should reduce the chances of $GABA_AR$ adopting non-native conformations. The use of nanodiscs could also help to learn more about the lipid interactions with $GABA_ARs$. In addition, full-length $GABA_AR$ heteromers should be studied, in order to understand the function of the intracellular domains and whether they are linked to channel structural integrity. In order to achieve these objectives using cryo-EM, the propensity of $GABA_AR$ to adhere to the water-air interface must be minimised without reintroducing the use of detergent. More experiments are needed to establish the best strategy to achieve this. Some likely methods might include nanobodies or other antibody fragments blocking the surface with which $GABA_ARs$ are interacting with the water-air interface. After the particle orientation problem is addressed, it will be possible to obtain cryo-EM structures of full-length heteromeric $GABA_ARs$ in lipid nanodiscs, fully unlocking its pharmacology and mechanisms of action.

9. References

Van den Abbeele, A., De Clercq, S., De Ganck, A., De Corte, V., Van Loo, B., Soror, S.H., Srinivasan, V., Steyaert, J., Vandekerckhove, J., and Gettemans, J. (2010). A llama-derived gelsolin single-domain antibody blocks gelsolin–G-actin interaction. Cell. Mol. Life Sci. *67*, 1519–1535.

Abulrob, A., Zhang, J., Tanha, J., MacKenzie, R., and Stanimirovic, D. (2005). Single domain antibodies as blood-brain barrier delivery vectors. Int. Congr. Ser. *1277*, 212–223.

Adams, P.D., Afonine, P. V, Bunkóczi, G., Chen, V.B., Davis, I.W., Echols, N., Headd, J.J., Hung, L.-W., Kapral, G.J., Grosse-Kunstleve, R.W., et al. (2010). PHENIX: a comprehensive Python-based system for macromolecular structure solution. Acta Crystallogr. D. Biol. Crystallogr. *66*, 213–221.

Althoff, T., Hibbs, R.E., Banerjee, S., and Gouaux, E. (2014). X-ray structures of GluCl in apo states reveal a gating mechanism of Cys-loop receptors. Nature *512*, 333–337.

Amunts, A., Brown, A., Bai, X., Llácer, J.L., Hussain, T., Emsley, P., Long, F., Murshudov, G., Scheres, S.H.W., and Ramakrishnan, V. (2014). Structure of the yeast mitochondrial large ribosomal subunit. Science (80-.). *343*, 1485–1489.

Anandan, A., and Vrielink, A. (2016). Detergents in Membrane Protein Purification and Crystallisation. In Advances in Experimental Medicine and Biology, pp. 13–28.

Aricescu, A.R., and Owens, R.J. (2013). Expression of recombinant glycoproteins in mammalian cells: towards an integrative approach to structural biology. Curr. Opin. Struct. Biol. *23*, 345–356.

Aricescu, A.R., Lu, W., and Jones, E.Y. (2006). A time- and cost-efficient system for high-level protein production in mammalian cells. Acta Crystallogr. D. Biol. Crystallogr. *62*, 1243–1250.

Bai, D., Pennefather, P.S., MacDonald, J.F., and Orser, B.A. (1999). The general anesthetic propofol slows deactivation and desensitization of GABA(A) receptors. J. Neurosci. *19*, 10635–10646.

Bai, X.-C., Yan, C., Yang, G., Lu, P., Ma, D., Sun, L., Zhou, R., Scheres, S.H.W., and Shi, Y. (2015a). An atomic structure of human γ-secretase. Nature *525*, 212–217.

Bai, X., McMullan, G., and Scheres, S.H.W. (2015b). How cryo-EM is revolutionizing structural biology. Trends Biochem. Sci. *40*, 49–57.

Bai, X., Rajendra, E., Yang, G., Shi, Y., and Scheres, S.H. (2015c). Sampling the conformational space of the catalytic subunit of human γ-secretase. Elife *4*.

Baker, M.R., Fan, G., and Serysheva, I.I. (2015). Single-particle cryo-EM of the ryanodine receptor channel. Eur. J. Transl. Myol. *25*, 35.

Bali, M., and Akabas, M.H. (2004). Defining the propofol binding site location on the GABAA receptor. Mol. Pharmacol. *65*, 68–76.

Balzarini, J. (2007). Carbohydrate-Binding Agents: A Potential Future Cornerstone for the Chemotherapy of Enveloped Viruses? Antivir. Chem. Chemother. *18*, 1–11.

Barrantes, F.J. (2015). Phylogenetic conservation of protein–lipid motifs in pentameric ligand-gated ion channels. Biochim. Biophys. Acta - Biomembr. *1848*, 1796–1805.

Bayburt, T.H., and Sligar, S.G. (2010). Membrane protein assembly into Nanodiscs. FEBS Lett. *584*, 1721–1727.

Beato, M., Groot-Kormelink, P.J., Colquhoun, D., and Sivilotti, L.G. (2002). Openings of the rat recombinant alpha 1 homomeric glycine receptor as a function of the number of agonist molecules bound. J. Gen. Physiol. *119*, 443–466.

Belelli, D., and Lambert, J.J. (2005). Neurosteroids: endogenous regulators of the GABAA receptor. Nat. Rev. Neurosci. *6*, 565–575.

Benke, D., Fakitsas, P., Roggenmoser, C., Michel, C., Rudolph, U., and Mohler, H. (2004). Analysis of the Presence and Abundance of GABA $_A$ Receptors Containing Two Different Types of α Subunits in Murine Brain Using Point-mutated α Subunits. J. Biol. Chem. *279*, 43654–43660.

Berman, H., Henrick, K., and Nakamura, H. (2003). Announcing the worldwide Protein Data Bank. Nat. Struct. Biol. *10*, 980–980.

Berriman, J., and Unwin, N. (1994). Analysis of transient structures by cryo-microscopy combined with rapid mixing of spray droplets. Ultramicroscopy *56*, 241–252.

Van Bockstaele, F., Holz, J.-B., and Revets, H. (2009). The development of nanobodies for therapeutic applications. Curr. Opin. Investig. Drugs *10*, 1212–1224.

Bocquet, N., Prado de Carvalho, L., Cartaud, J., Neyton, J., Le Poupon, C., Taly, A., Grutter, T., Changeux, J.-P., and Corringer, P.-J. (2007). A prokaryotic proton-gated ion channel from the nicotinic acetylcholine receptor family. Nature *445*, 116–119.

Bocquet, N., Nury, H., Baaden, M., Le Poupon, C., Changeux, J.-P., Delarue, M., and Corringer, P.-J.

(2009). X-ray structure of a pentameric ligand-gated ion channel in an apparently open conformation. Nature *457*, 111–114.

Bokori-Brown, M., Martin, T.G., Naylor, C.E., Basak, A.K., Titball, R.W., and Savva, C.G. (2016). Cryo-EM structure of lysenin pore elucidates membrane insertion by an aerolysin family protein. Nat. Commun. 2016 7null *7*, ncomms11293.

Boom, R., Sol, C.J., Salimans, M.M., Jansen, C.L., Wertheim-van Dillen, P.M., and van der Noordaa, J. (1990). Rapid and simple method for purification of nucleic acids. J. Clin. Microbiol. *28*, 495–503.

Bordag, N., and Keller, S. (2010). α-Helical transmembrane peptides: A "Divide and Conquer" approach to membrane proteins. Chem. Phys. Lipids *163*, 1–26.

Boué-Grabot, E., Barajas-López, C., Chakfe, Y., Blais, D., Bélanger, D., Emerit, M.B., and Séguéla, P. (2003). Intracellular cross talk and physical interaction between two classes of neurotransmitter-gated channels. J. Neurosci. *23*, 1246–1253.

Brickley, S.G., and Mody, I. (2012). Extrasynaptic GABA(A) receptors: their function in the CNS and implications for disease. Neuron *73*, 23–34.

Broecker, J., Eger, B.T., and Ernst, O.P. (2017). Crystallogenesis of Membrane Proteins Mediated by Polymer-Bounded Lipid Nanodiscs. Structure *25*, 384–392.

Brown, A., Long, F., Nicholls, R.A., Toots, J., Emsley, P., and Murshudov, G. (2015). Tools for macromolecular model building and refinement into electron cryo-microscopy reconstructions. Acta Crystallogr. D. Biol. Crystallogr. *71*, 136–153.

Callaway, E. (2015). The revolution will not be crystallized: a new method sweeps through structural biology. Nature *525*, 172–174.

Cao, E., Liao, M., Cheng, Y., and Julius, D. (2013). TRPV1 structures in distinct conformations reveal activation mechanisms. Nature *504*, 113–118.

Cestari, I.N., Min, K.T., Kulli, J.C., and Yang, J. (2000). Identification of an amino acid defining the distinct properties of murine beta1 and beta3 subunit-containing GABA(A) receptors. J. Neurochem. *74*, 827–838.

Chang, V.T., Crispin, M., Aricescu, A.R., Harvey, D.J., Nettleship, J.E., Fennelly, J.A., Yu, C., Boles, K.S., Evans, E.J., Stuart, D.I., et al. (2007). Glycoprotein structural genomics: solving the glycosylation problem. Structure *15*, 267–273.

Chen, S., McMullan, G., Faruqi, A.R., Murshudov, G.N., Short, J.M., Scheres, S.H.W., and Henderson, R. (2013). High-resolution noise substitution to measure overfitting and validate resolution in 3D structure determination by single particle electron cryomicroscopy. Ultramicroscopy *135*, 24–35.

Chen, V.B., Arendall, W.B., Headd, J.J., Keedy, D.A., Immormino, R.M., Kapral, G.J., Murray, L.W., Richardson, J.S., and Richardson, D.C. (2010). *MolProbity*: all-atom structure validation for macromolecular crystallography. Acta Crystallogr. Sect. D Biol. Crystallogr. *66*, 12–21.

Cheng, Y., Grigorieff, N., Penczek, P.A., and Walz, T. (2015). A primer to single-particle cryo-electron microscopy. Cell *161*, 438–449.

Chiara, D.C., Dostalova, Z., Jayakar, S.S., Zhou, X., Miller, K.W., and Cohen, J.B. (2012). Mapping General Anesthetic Binding Site(s) in Human α1β3 γ-Aminobutyric Acid Type A Receptors with [^{3} H]TDBzl-Etomidate, a Photoreactive Etomidate Analogue. Biochemistry *51*, 836–847.

Cho, H.-J., Hyun, J.-K., Kim, J.-G., Jeong, H.S., Park, H.N., You, D.-J., and Jung, H.S. (2013). Measurement of ice thickness on vitreous ice embedded cryo-EM grids: investigation of optimizing condition for visualizing macromolecules. J. Anal. Sci. Technol. *4*, 7.

Chun, E., Thompson, A.A., Liu, W., Roth, C.B., Griffith, M.T., Katritch, V., Kunken, J., Xu, F., Cherezov, V., Hanson, M.A., et al. (2012). Fusion partner toolchest for the stabilization and crystallization of G protein-coupled receptors. Structure *20*, 967–976.

Cope, D.W., Hughes, S.W., and Crunelli, V. (2005). GABAA receptor-mediated tonic inhibition in thalamic neurons. J. Neurosci. *25*, 11553–11563.

Corringer, P.-J., Baaden, M., Bocquet, N., Delarue, M., Dufresne, V., Nury, H., Prevost, M., and Van Renterghem, C. (2010). Atomic structure and dynamics of pentameric ligand-gated ion channels: new insight from bacterial homologues. J. Physiol. *588*, 565–572.

Curtis, D.R., and Crawford, J.M. (1969). Central Synaptic Transmission-Microelectrophoretic Studies. Annu. Rev. Pharmacol. *9*, 209–240.

daCosta, C.J.B., Dey, L., Therien, J.P.D., and Baenziger, J.E. (2013). A distinct mechanism for activating uncoupled nicotinic acetylcholine receptors. Nat. Chem. Biol. *9*, 701–707.

Dahmane, T., Rappaport, F., and Popot, J.-L. (2013). Amphipol-assisted folding of bacteriorhodopsin in the presence or absence of lipids: functional consequences. Eur. Biophys. J. *42*, 85–101.

Dani, J.A. (2015). Neuronal Nicotinic Acetylcholine Receptor Structure and Function and Response to Nicotine. Int. Rev. Neurobiol. *124*, 3–19.

Davies, P.A., Wang, W., Hales, T.G., and Kirkness, E.F. (2003). A Novel Class of Ligand-gated Ion Channel Is Activated by Zn $^{2+}$. J. Biol. Chem. *278*, 712–717.

Davis, I.W., Leaver-Fay, A., Chen, V.B., Block, J.N., Kapral, G.J., Wang, X., Murray, L.W., Arendall, W.B., Snoeyink, J., Richardson, J.S., et al. (2007). MolProbity: all-atom contacts and structure validation for proteins and nucleic acids. Nucleic Acids Res. *35*, W375-83.

Delmar, J.A., Bolla, J.R., Su, C.-C., and Yu, E.W. (2015). Crystallization of Membrane Proteins by Vapor Diffusion. In Methods in Enzymology, pp. 363–392.

Deniaud, A., Moiseeva, E., Gordeliy, V., and Pebay-Peyroula, E. (2010). Crystallography of membrane proteins: from crystallization to structure. Methods Mol. Biol. *654*, 79–103.

Denisov, I.G., and Sligar, S.G. (2017). Nanodiscs in Membrane Biochemistry and Biophysics. Chem. Rev. *117*, 4669–4713.

Desai, R., Ruesch, D., and Forman, S.A. (2009). Gamma-amino butyric acid type A receptor mutations at beta2N265 alter etomidate efficacy while preserving basal and agonist-dependent activity. Anesthesiology *111*, 774–784.

Detalle, L., Stohr, T., Palomo, C., Piedra, P.A., Gilbert, B.E., Mas, V., Millar, A., Power, U.F., Stortelers, C., Allosery, K., et al. (2015). Generation and Characterization of ALX-0171, a Potent Novel Therapeutic Nanobody for the Treatment of Respiratory Syncytial Virus Infection. Antimicrob. Agents Chemother. *60*, 6–13.

DiMaio, F., Tyka, M.D., Baker, M.L., Chiu, W., and Baker, D. (2009). Refinement of Protein Structures into Low-Resolution Density Maps Using Rosetta. J. Mol. Biol. *392*, 181–190.

Dostalova, Z., Zhou, X., Liu, A., Zhang, X., Zhang, Y., Desai, R., Forman, S.A., and Miller, K.W. (2014a). Human α1β3γ2L gamma-aminobutyric acid type A receptors: High-level production and purification in a functional state. Protein Sci. *23*, 157–166.

Dostalova, Z., Zhou, X., Liu, A., Zhang, X., Zhang, Y., Desai, R., Forman, S.A., and Miller, K.W. (2014b). Human α1β3γ2L gamma-aminobutyric acid type A receptors: High-level production and purification in a functional state. Protein Sci. *23*, 157–166.

Du, J., Lü, W., Wu, S., Cheng, Y., and Gouaux, E. (2015). Glycine receptor mechanism elucidated by electron cryo-microscopy. Nature *advance on*.

Dumoulin, A., Lévi, S., Riveau, B., Gasnier, B., and Triller, A. (2000). Formation of mixed glycine and GABAergic synapses in cultured spinal cord neurons. Eur. J. Neurosci. *12*, 3883–3892.

Efremov, R.G., Leitner, A., Aebersold, R., and Raunser, S. (2015). Architecture and conformational switch mechanism of the ryanodine receptor. Nature *517*, 39–43.

Elbein, A.D., Tropea, J.E., Mitchell, M., and Kaushal, G.P. (1990). Kifunensine, a potent inhibitor of the glycoprotein processing mannosidase I. J. Biol. Chem. *265*, 15599–15605.

Emsley, P., and Cowtan, K. (2004). Coot: model-building tools for molecular graphics. Acta Crystallogr. D. Biol. Crystallogr. *60*, 2126–2132.

Essrich, C., Lorez, M., Benson, J.A., Fritschy, J.-M., and Lüscher, B. (1998). Postsynaptic clustering of major GABAA receptor subtypes requires the γ2 subunit and gephyrin. Nat. Neurosci. *1*, 563–571.

Eswar, N., Webb, B., Marti-Renom, M.A., Madhusudhan, M.S., Eramian, D., Shen, M.-Y., Pieper, U., and Sali, A. (2006). Comparative protein structure modeling using Modeller. Curr. Protoc. Bioinforma. *Chapter 5*, Unit 5.6.

Etzkorn, M., Raschle, T., Hagn, F., Gelev, V., Rice, A.J., Walz, T., and Wagner, G. (2013). Cell-free Expressed Bacteriorhodopsin in Different Soluble Membrane Mimetics: Biophysical Properties and NMR Accessibility. Structure *21*, 394–401.

Evans, P.R., and Murshudov, G.N. (2013). How good are my data and what is the resolution? Acta Crystallogr. Sect. D Biol. Crystallogr. *69*, 1204–1214.

Fisher, J.L. (2002). A lysine residue in the beta3 subunit contributes to the regulation of GABA(A) receptor activity by voltage. Mol. Cell. Neurosci. *20*, 683–694.

Flajnik, M.F., Deschacht, N., and Muyldermans, S. (2011). A Case Of Convergence: Why Did a Simple Alternative to Canonical Antibodies Arise in Sharks and Camels? PLoS Biol. *9*, e1001120.

Forman, S.A. (2011). Clinical and molecular pharmacology of etomidate. Anesthesiology *114*, 695–707.

Forman, S.A., and Miller, K.W. (2011). Anesthetic sites and allosteric mechanisms of action on Cys-loop ligand-gated ion channels. Can. J. Anaesth. *58*, 191–205.

Franks, N.P. (2008). General anaesthesia: from molecular targets to neuronal pathways of sleep and arousal. Nat. Rev. Neurosci. *9*, 370–386.

Franks, N.P. (2015). Structural comparisons of ligand-gated ion channels in open, closed, and desensitized states identify a novel propofol-binding site on mammalian γ-aminobutyric acid type A receptors. Anesthesiology *122*, 787–794.

Frauenfeld, J., Löving, R., Armache, J.-P., Sonnen, A.F.-P., Guettou, F., Moberg, P., Zhu, L., Jegerschöld, C., Flayhan, A., Briggs, J.A.G., et al. (2016). A saposin-lipoprotein nanoparticle system for membrane proteins. Nat. Methods *13*, 345–351.

Freeze, H.H., and Kranz, C. (2010). Endoglycosidase and glycoamidase release of N-linked glycans. Curr. Protoc. Mol. Biol. *Chapter 17*, Unit 17.13A.

Gabius, H.-J., André, S., Jiménez-Barbero, J., Romero, A., and Solís, D. (2011). From lectin structure to functional glycomics: principles of the sugar code. Trends Biochem. Sci. *36*, 298–313.

Gao, Y., Cao, E., Julius, D., and Cheng, Y. (2016). TRPV1 structures in nanodiscs reveal mechanisms of ligand and lipid action. Nature *534*, 347–351.

Hassaine, G., Deluz, C., Grasso, L., Wyss, R., Tol, M.B., Hovius, R., Graff, A., Stahlberg, H., Tomizaki, T., Desmyter, A., et al. (2014). X-ray structure of the mouse serotonin 5-HT3 receptor. Nature.

Hassanzadeh-Ghassabeh, G., Devoogdt, N., De Pauw, P., Vincke, C., and Muyldermans, S. (2013). Nanobodies and their potential applications. Nanomedicine (Lond). *8*, 1013–1026.

Hattori, M., Hibbs, R.E., and Gouaux, E. (2012). A fluorescence-detection size-exclusion chromatography-based thermostability assay for membrane protein precrystallization screening. Structure *20*, 1293–1299.

Hebb, C. (1970). CNS at the Cellular Level: Identity of Transmitter Agents. Annu. Rev. Physiol. *32*, 165–192.

Hibbs, R.E., and Gouaux, E. (2011). Principles of activation and permeation in an anion-selective Cys-loop receptor. Nature *474*, 54–60.

Hilf, R.J.C., and Dutzler, R. (2008). X-ray structure of a prokaryotic pentameric ligand-gated ion channel. Nature *452*, 375–379.

Hill-Venning, C., Belelli, D., Peters, J.A., and Lambert, J.J. (1997). Subunit-dependent interaction of the general anaesthetic etomidate with the gamma-aminobutyric acid type A receptor. Br. J. Pharmacol. *120*, 749–756.

Hosie, A.M., Wilkins, M.E., da Silva, H.M.A., and Smart, T.G. (2006). Endogenous neurosteroids regulate GABAA receptors through two discrete transmembrane sites. Nature *444*, 486–489.

Hosie, A.M., Clarke, L., da Silva, H., and Smart, T.G. (2009). Conserved site for neurosteroid modulation of GABAA receptors. Neuropharmacology *56*, 149–154.

Huang, X., Chen, H., Michelsen, K., Schneider, S., and Shaffer, P.L. (2015). Crystal structure of human glycine receptor-α3 bound to antagonist strychnine. Nature *526*, 277–280.

Husain, S.S., Stewart, D., Desai, R., Hamouda, A.K., Li, S.G.-D., Kelly, E., Dostalova, Z., Zhou, X., Cotten, J.F., Raines, D.E., et al. (2010). *p* -Trifluoromethyldiazirinyl-etomidate: A Potent Photoreactive General Anesthetic Derivative of Etomidate That Is Selective for Ligand-Gated Cationic Ion Channels. J. Med. Chem. *53*, 6432–6444.

Jansen, M., Bali, M., and Akabas, M.H. (2008). Modular Design of Cys-loop Ligand-gated Ion Channels: Functional 5-HT3 and GABA 1 Receptors Lacking the Large Cytoplasmic M3M4 Loop. J. Gen. Physiol. *131*, 137–146.

Jenkins, A., Greenblatt, E.P., Faulkner, H.J., Bertaccini, E., Light, A., Lin, A., Andreasen, A., Viner, A., Trudell, J.R., and Harrison, N.L. (2001). Evidence for a common binding cavity for three general anesthetics within the GABAA receptor. J. Neurosci. *21*, RC136.

de Jongh, H.H.J., Kosters, H.A., Kudryashova, E., Meinders, M.B.J., Trofimova, D., and Wierenga, P.A. (2004). Protein adsorption at air-water interfaces: A combination of details. Biopolymers *74*, 131–135.

Jurd, R., Arras, M., Lambert, S., Drexler, B., Siegwart, R., Crestani, F., Zaugg, M., Vogt, K.E., Ledermann, B., Antkowiak, B., et al. (2002). General anesthetic actions in vivo strongly attenuated by a point mutation in the GABAA receptor &beta;3 subunit. FASEB J. *17*, 250–252.

Kaila, K., Rivera, C., Voipio, J., Payne, J.A., Ruusuvuori, E., Lahtinen, H., Lamsa, K., Pirvola, U., and Saarma, M. (1999). The K+/Cl- co-transporter KCC2 renders GABA hyperpolarizing during neuronal maturation. Nature *397*, 251–255.

Karlin, A., and Akabas, M.H. (1995). Toward a structural basis for the function of nicotinic acetylcholine receptors and their cousins. Neuron *15*, 1231–1244.

Khoshouei, M., Radjainia, M., Baumeister, W., and Danev, R. (2017). Cryo-EM structure of haemoglobin at 3.2 Å determined with the Volta phase plate. Nat. Commun. *8*, 16099.

Kimanius, D., Forsberg, B.O., Scheres, S.H., and Lindahl, E. (2016). Accelerated cryo-EM structure determination with parallelisation using GPUs in RELION-2. Elife *5*.

Kirmse, K., Hübner, C.A., Isbrandt, D., Witte, O.W., and Holthoff, K. (2017). GABAergic Transmission during Brain Development: Multiple Effects at Multiple Stages. Neurosci. 107385841770138.

Kopp Lugli, A., Yost, C.S., and Kindler, C.H. (2009). Anaesthetic mechanisms: update on the challenge of unravelling the mystery of anaesthesia. Eur. J. Anaesthesiol. *26*, 807–820.

Krasowski, M.D., Nishikawa, K., Nikolaeva, N., Lin, A., and Harrison, N.L. (2001). Methionine 286 in transmembrane domain 3 of the GABAA receptor beta subunit controls a binding cavity for propofol and other alkylphenol general anesthetics. Neuropharmacology *41*, 952–964.

Krissinel, E., and Henrick, K. (2007). Inference of Macromolecular Assemblies from Crystalline State. J. Mol. Biol. *372*, 774–797.

Kucukelbir, A., Sigworth, F.J., and Tagare, H.D. (2014). Quantifying the local resolution of cryo-EM density maps. Nat. Methods *11*, 63–65.

Kühlbrandt, W. (2014). Cryo-EM enters a new era. Elife *3*, e03678.

Laverty, D., Thomas, P., Field, M., Andersen, O.J., Gold, M.G., Biggin, P.C., Gielen, M., and Smart, T.G. (2017). Crystal structures of a GABAA-receptor chimera reveal new endogenous neurosteroid-binding sites. Nat. Struct. Mol. Biol.

Lee, S.C., Knowles, T.J., Postis, V.L.G., Jamshad, M., Parslow, R.A., Lin, Y.-P., Goldman, A., Sridhar, P., Overduin, M., Muench, S.P., et al. (2016). A method for detergent-free isolation of membrane proteins in their local lipid environment. Nat. Protoc. *11*, 1149–1162.

Li, G.-D., Chiara, D.C., Sawyer, G.W., Husain, S.S., Olsen, R.W., and Cohen, J.B. (2006). Identification of a GABAA receptor anesthetic binding site at subunit interfaces by photolabeling with an etomidate analog. J. Neurosci. *26*, 11599–11605.

Li, G.-D., Chiara, D.C., Cohen, J.B., and Olsen, R.W. (2010). Numerous classes of general anesthetics inhibit etomidate binding to gamma-aminobutyric acid type A (GABAA) receptors. J. Biol. Chem. *285*, 8615–8620.

Li, T., Bourgeois, J.-P., Celli, S., Glacial, F., Le Sourd, A.-M., Mecheri, S., Weksler, B., Romero, I., Couraud, P.-O., Rougeon, F., et al. (2012). Cell-penetrating anti-GFAP VHH and corresponding fluorescent fusion protein VHH-GFP spontaneously cross the blood-brain barrier and specifically recognize astrocytes: application to brain imaging. FASEB J. *26*, 3969–3979.

Li, X., Mooney, P., Zheng, S., Booth, C.R., Braunfeld, M.B., Gubbens, S., Agard, D.A., and Cheng, Y. (2013). Electron counting and beam-induced motion correction enable near-atomic-resolution single-particle cryo-EM. Nat. Methods *10*, 584–590.

Liao, M., Cao, E., Julius, D., and Cheng, Y. (2013). Structure of the TRPV1 ion channel determined by electron cryo-microscopy. Nature *504*, 107–112.

Liu, K., Jounaidi, Y., Forman, S.A., and Feng, H.-J. (2015a). Etomidate uniquely modulates the desensitization of recombinant α1β3δ GABAA receptors. Neuroscience *300*, 307–313.

Liu, K., Jounaidi, Y., Forman, S.A., and Feng, H.-J. (2015b). Etomidate uniquely modulates the desensitization of recombinant α1β3δ GABA(A) receptors. Neuroscience *300*, 307–313.

Lo, W., Lagrange, A.H., Hernandez, C.C., Harrison, R., Dell, A., Haslam, S.M., Sheehan, J.H., and Macdonald, R.L. (2010). Glycosylation of β2 Subunits Regulates GABA $_A$ Receptor Biogenesis and Channel Gating. J. Biol. Chem. *285*, 31348–31361.

Löw, K., Crestani, F., Keist, R., Benke, D., Brünig, I., Benson, J.A., Fritschy, J.M., Rülicke, T., Bluethmann, H., Möhler, H., et al. (2000). Molecular and neuronal substrate for the selective attenuation of anxiety. Science *290*, 131–134.

Lummis, S.C.R. (2012). 5-HT(3) receptors. J. Biol. Chem. *287*, 40239–40245.

Luscher, B., Fuchs, T., and Kilpatrick, C.L. (2011). GABAA receptor trafficking-mediated plasticity of inhibitory synapses. Neuron *70*, 385–409.

Lynch, J.W. (2004). Molecular Structure and Function of the Glycine Receptor Chloride Channel. Physiol. Rev. *84*, 1051–1095.

Maguire, J.L., Stell, B.M., Rafizadeh, M., and Mody, I. (2005). Ovarian cycle-linked changes in GABA(A) receptors mediating tonic inhibition alter seizure susceptibility and anxiety. Nat. Neurosci. *8*, 797–804.

Martinez, K.L., Gohon, Y., Corringer, P.-J., Tribet, C., Mérola, F., Changeux, J.-P., and Popot, J.-L.

(2002). Allosteric transitions of Torpedo acetylcholine receptor in lipids, detergent and amphipols: molecular interactions vs. physical constraints. FEBS Lett. *528*, 251–256.

McCann, C.M., Bracamontes, J., Steinbach, J.H., and Sanes, J.R. (2006). The cholinergic antagonist alpha-bungarotoxin also binds and blocks a subset of GABA receptors. Proc. Natl. Acad. Sci. U. S. A. *103*, 5149–5154.

McCoy, A.J., Grosse-Kunstleve, R.W., Adams, P.D., Winn, M.D., Storoni, L.C., and Read, R.J. (2007a). Phaser crystallographic software. J. Appl. Crystallogr. *40*, 658–674.

McCoy, A.J., Grosse-Kunstleve, R.W., Adams, P.D., Winn, M.D., Storoni, L.C., and Read, R.J. (2007b). Phaser crystallographic software. J. Appl. Crystallogr. *40*, 658–674.

McKeage, K., and Perry, C.M. (2003). Propofol: a review of its use in intensive care sedation of adults. CNS Drugs *17*, 235–272.

McPherson, A., and Gavira, J.A. (2014). Introduction to protein crystallization. Acta Crystallogr. Sect. F, Struct. Biol. Commun. *70*, 2–20.

Merk, A., Bartesaghi, A., Banerjee, S., Falconieri, V., Rao, P., Davis, M.I., Pragani, R., Boxer, M.B., Earl, L.A., Milne, J.L.S., et al. (2016). Breaking Cryo-EM Resolution Barriers to Facilitate Drug Discovery. Cell *165*.

Mesa, P., Deniaud, A., Montoya, G., and Schaffitzel, C. (2013). Directly from the source: endogenous preparations of molecular machines. Curr. Opin. Struct. Biol. *null*.

Mihic, S.J., Ye, Q., Wick, M.J., Koltchine, V. V., Krasowski, M.D., Finn, S.E., Mascia, M.P., Valenzuela, C.F., Hanson, K.K., Greenblatt, E.P., et al. (1997). Sites of alcohol and volatile anaesthetic action on GABA(A) and glycine receptors. Nature *389*, 385–389.

Miller, P.S., and Aricescu, A.R. (2014). Crystal structure of a human GABAA receptor. Nature *512*, 270–275.

Miller, P.S., and Smart, T.G. (2010). Binding, activation and modulation of Cys-loop receptors. Trends Pharmacol. Sci. *31*, 161–174.

Miller, P.S., Scott, S., Masiulis, S., Colibus, L. De, Pardon, E., Steyaert, J., and Aricescu, A.R. (2017). Structural basis for GABA A receptor potentiation by neurosteroids. Nat. Struct. Mol. Biol.

Minier, F., and Sigel, E. (2004). Positioning of the alpha-subunit isoforms confers a functional signature to gamma-aminobutyric acid type A receptors. Proc. Natl. Acad. Sci. U. S. A. *101*, 7769–7774.

Möhler, H. (2006). GABA(A) receptor diversity and pharmacology. Cell Tissue Res. *326*, 505–516.

Möhler, H., Fritschy, J.M., and Rudolph, U. (2002). A new benzodiazepine pharmacology. J. Pharmacol. Exp. Ther. *300*, 2–8.

Molday, R.S., and MacKenzie, D. (1983). Monoclonal antibodies to rhodopsin: characterization, cross-reactivity, and application as structural probes. Biochemistry *22*, 653–660.

Mortensen, M., and Smart, T.G. (2006). Extrasynaptic αβ subunit GABA $_A$ receptors on rat hippocampal pyramidal neurons. J. Physiol. *577*, 841–856.

Moulaei, T., Shenoy, S.R., Giomarelli, B., Thomas, C., McMahon, J.B., Dauter, Z., O'Keefe, B.R., and Wlodawer, A. (2010). Monomerization of viral entry inhibitor griffithsin elucidates the relationship between multivalent binding to carbohydrates and anti-HIV activity. Structure *18*, 1104–1115.

Munro, S., and Pelham, H.R. (1984). Use of peptide tagging to detect proteins expressed from cloned genes: deletion mapping functional domains of Drosophila hsp 70. EMBO J. *3*, 3087–3093.

Murshudov, G.N., Skubák, P., Lebedev, A.A., Pannu, N.S., Steiner, R.A., Nicholls, R.A., Winn, M.D., Long, F., and Vagin, A.A. (2011). REFMAC5 for the refinement of macromolecular crystal structures. Acta Crystallogr. D. Biol. Crystallogr. *67*, 355–367.

Muyldermans, S. (2013). Nanobodies: natural single-domain antibodies. Annu. Rev. Biochem. *82*, 775–797.

Nagai, T., Ibata, K., Park, E.S., Kubota, M., Mikoshiba, K., and Miyawaki, A. (2002). A variant of yellow fluorescent protein with fast and efficient maturation for cell-biological applications. Nat. Biotechnol. *20*, 87–90.

Neale, C., Ghanei, H., Holyoake, J., Bishop, R.E., Privé, G.G., and Pomès, R. (2013). Detergent-mediated protein aggregation. Chem. Phys. Lipids *169*, 72–84.

Newstead, S., Ferrandon, S., and Iwata, S. (2008). Rationalizing α-helical membrane protein crystallization. Protein Sci. *17*, 466–472.

Nishikawa, K., Jenkins, A., Paraskevakis, I., and Harrison, N.L. (2002). Volatile anesthetic actions on the GABAA receptors: contrasting effects of alpha 1(S270) and beta 2(N265) point mutations. Neuropharmacology *42*, 337–345.

Nothdurfter, C., Tanasic, S., Di Benedetto, B., Uhr, M., Wagner, E.-M., Gilling, K.E., Parsons, C.G., Rein, T., Holsboer, F., Rupprecht, R., et al. (2013). Lipid raft integrity affects GABAA receptor, but not NMDA receptor modulation by psychopharmacological compounds. Int. J. Neuropsychopharmacol. *16*, 1361–1371.

Nusser, Z., and Mody, I. (2002). Selective modulation of tonic and phasic inhibitions in dentate gyrus granule cells. J. Neurophysiol. *87*, 2624–2628.

Olsen, R.W., and Sieghart, W. (2008). International Union of Pharmacology. LXX. Subtypes of gamma-aminobutyric acid(A) receptors: classification on the basis of subunit composition, pharmacology, and function. Update. Pharmacol. Rev. *60*, 243–260.

Otwinowski, Z., and Minor, W. (1997a). Macromolecular Crystallography Part A (Elsevier).

Otwinowski, Z., and Minor, W. (1997b). Processing of X-ray diffraction data collected in oscillation mode. Methods Enzymol. *276*, 307–326.

Pantelic, R.S., Fu, W., Schoenenberger, C., and Stahlberg, H. (2014). Rendering graphene supports hydrophilic with non-covalent aromatic functionalization for transmission electron microscopy. Appl. Phys. Lett. *104*, 134103.

Pardon, E., Laeremans, T., Triest, S., Rasmussen, S.G.F., Wohlkönig, A., Ruf, A., Muyldermans, S., Hol, W.G.J., Kobilka, B.K., and Steyaert, J. (2014). A general protocol for the generation of Nanobodies for structural biology. Nat. Protoc. *9*, 674–693.

Parker, J.L., and Newstead, S. (2012a). Current trends in α-helical membrane protein crystallization: an update. Protein Sci. *21*, 1358–1365.

Parker, J.L., and Newstead, S. (2012b). Current trends in α-helical membrane protein crystallization: An update. Protein Sci. *21*, 1358–1365.

Parker, J.L., and Newstead, S. (2016). Membrane Protein Crystallisation: Current Trends and Future Perspectives. Adv. Exp. Med. Biol. *922*, 61–72.

Petroff, O.A.C. (2002). Book Review: GABA and Glutamate in the Human Brain. Neurosci. *8*, 562–573.

Pettersen, E.F., Goddard, T.D., Huang, C.C., Couch, G.S., Greenblatt, D.M., Meng, E.C., and Ferrin, T.E. (2004). UCSF Chimera--a visualization system for exploratory research and analysis. J. Comput. Chem. *25*, 1605–1612.

Picard, M., Dahmane, T., Garrigos, M., Gauron, C., Giusti, F., le Maire, M., Popot, J.-L., and Champeil,

P. (2006). Protective and Inhibitory Effects of Various Types of Amphipols on the Ca $^{2+}$ -ATPase from Sarcoplasmic Reticulum: A Comparative Study [†]. Biochemistry *45*, 1861–1869.

Pollock, N.L., Lee, S.C., Patel, J.H., Gulamhussein, A.A., and Rothnie, A.J. (2017). Structure and function of membrane proteins encapsulated in a polymer-bound lipid bilayer. Biochim. Biophys. Acta - Biomembr.

Popot, J.-L., Althoff, T., Bagnard, D., Banères, J.-L., Bazzacco, P., Billon-Denis, E., Catoire, L.J., Champeil, P., Charvolin, D., Cocco, M.J., et al. (2011). Amphipols from A to Z. Annu. Rev. Biophys. *40*, 379–408.

Postis, V., Rawson, S., Mitchell, J.K., Lee, S.C., Parslow, R.A., Dafforn, T.R., Baldwin, S.A., and Muench, S.P. (2015). The use of SMALPs as a novel membrane protein scaffold for structure study by negative stain electron microscopy. Biochim. Biophys. Acta *1848*, 496–501.

Punjani, A., Rubinstein, J.L., Fleet, D.J., and Brubaker, M.A. (2017). cryoSPARC: algorithms for rapid unsupervised cryo-EM structure determination. Nat. Methods *14*, 290–296.

R. Mancinelli, A. Botti, F. Bruni, and, Ricci*, M.A., and Soper†, A.K. (2007). Hydration of Sodium, Potassium, and Chloride Ions in Solution and the Concept of Structure Maker/Breaker.

Rasmussen, S.G.F., Choi, H.-J., Fung, J.J., Pardon, E., Casarosa, P., Chae, P.S., Devree, B.T., Rosenbaum, D.M., Thian, F.S., Kobilka, T.S., et al. (2011). Structure of a nanobody-stabilized active state of the β(2) adrenoceptor. Nature *469*, 175–180.

Reddy, D.S., and Estes, W.A. (2016). Clinical Potential of Neurosteroids for CNS Disorders. Trends Pharmacol. Sci. *37*, 543–561.

Reddy, D.S., and Rogawski, M.A. (2009). Neurosteroid replacement therapy for catamenial epilepsy. Neurotherapeutics *6*, 392–401.

Richter, L., de Graaf, C., Sieghart, W., Varagic, Z., Mörzinger, M., de Esch, I.J.P., Ecker, G.F., and Ernst, M. (2012). Diazepam-bound GABAA receptor models identify new benzodiazepine binding-site ligands. Nat. Chem. Biol. *8*, 455–464.

Ring, A.M., Manglik, A., Kruse, A.C., Enos, M.D., Weis, W.I., Garcia, K.C., and Kobilka, B.K. (2013). Adrenaline-activated structure of β2-adrenoceptor stabilized by an engineered nanobody. Nature *502*, 575–579.

Rissiek, B., Koch-Nolte, F., and Magnus, T. (2014). Nanobodies as modulators of inflammation:

potential applications for acute brain injury. Front. Cell. Neurosci. *8*, 344.

Rohou, A., and Grigorieff, N. (2015). CTFFIND4: Fast and accurate defocus estimation from electron micrographs. J. Struct. Biol. *192*, 216–221.

Rosenthal, P.B., and Henderson, R. (2003). Optimal Determination of Particle Orientation, Absolute Hand, and Contrast Loss in Single-particle Electron Cryomicroscopy. J. Mol. Biol. *333*, 721–745.

Rudolph, U., and Knoflach, F. (2011). Beyond classical benzodiazepines: novel therapeutic potential of GABAA receptor subtypes. Nat. Rev. Drug Discov. *10*, 685–697.

Rüsch, D., Zhong, H., and Forman, S.A. (2004). Gating allosterism at a single class of etomidate sites on alpha1beta2gamma2L GABA A receptors accounts for both direct activation and agonist modulation. J. Biol. Chem. *279*, 20982–20992.

Russo, C.J., and Passmore, L.A. (2014). Ultrastable gold substrates for electron cryomicroscopy. Science (80-.). *346*, 1377–1380.

Sanchez-Weatherby, J., Bowler, M.W., Huet, J., Gobbo, A., Felisaz, F., Lavault, B., Moya, R., Kadlec, J., Ravelli, R.B.G., and Cipriani, F. (2009). Improving diffraction by humidity control: a novel device compatible with X-ray beamlines. Acta Crystallogr. D. Biol. Crystallogr. *65*, 1237–1246.

Saras, A., Gisselmann, G., Vogt-Eisele, A.K., Erlkamp, K.S., Kletke, O., Pusch, H., and Hatt, H. (2008). Histamine action on vertebrate GABAA receptors: direct channel gating and potentiation of GABA responses. J. Biol. Chem. *283*, 10470–10475.

Scheres, S.H.W. (2012a). RELION: implementation of a Bayesian approach to cryo-EM structure determination. J. Struct. Biol. *180*, 519–530.

Scheres, S.H.W. (2012b). RELION: implementation of a Bayesian approach to cryo-EM structure determination. J. Struct. Biol. *180*, 519–530.

Scheres, S.H.W., and Chen, S. (2012). Prevention of overfitting in cryo-EM structure determination. Nat. Methods *9*, 853–854.

Schroeder, H.W., Cavacini, L., and Cavacini, L. (2010). Structure and function of immunoglobulins. J. Allergy Clin. Immunol. *125*, S41-52.

Schüttelkopf, A.W., and van Aalten, D.M.F. (2004). *PRODRG*: a tool for high-throughput crystallography of protein–ligand complexes. Acta Crystallogr. Sect. D Biol. Crystallogr. *60*, 1355–

1363.

Seddon, A.M., Curnow, P., and Booth, P.J. (2004). Membrane proteins, lipids and detergents: not just a soap opera. Biochim. Biophys. Acta *1666*, 105–117.

Shen, H., Gong, Q.H., Aoki, C., Yuan, M., Ruderman, Y., Dattilo, M., Williams, K., and Smith, S.S. (2007). Reversal of neurosteroid effects at alpha4beta2delta GABAA receptors triggers anxiety at puberty. Nat. Neurosci. *10*, 469–477.

Siegwart, R., Krähenbühl, K., Lambert, S., and Rudolph, U. (2003). Mutational analysis of molecular requirements for the actions of general anaesthetics at the gamma-aminobutyric acidA receptor subtype, alpha1beta2gamma2. BMC Pharmacol. *3*, 13.

Sigel, E., and Steinmann, M.E. (2012). Structure, function, and modulation of GABA(A) receptors. J. Biol. Chem. *287*, 40224–40231.

Singh, S., Devi, S., and Ng, T. (2014). Banana Lectin: A Brief Review. Molecules *19*, 18817–18827.

Skarina, T., Xu, X., Evdokimova, E., and Savchenko, A. (2014). High-Throughput Crystallization Screening. In Methods in Molecular Biology (Clifton, N.J.), pp. 159–168.

Smart, T.G., and Paoletti, P. (2012). Synaptic neurotransmitter-gated receptors. Cold Spring Harb. Perspect. Biol. *4*.

Smart, O.S., Goodfellow, J.M., and Wallace, B.A. (1993). The pore dimensions of gramicidin A. Biophys. J. *65*, 2455–2460.

Smart, O.S., Womack, T.O., Flensburg, C., Keller, P., Paciorek, W., Sharff, A., Vonrhein, C., and Bricogne, G. (2012). Exploiting structure similarity in refinement: automated NCS and target-structure restraints in BUSTER. Acta Crystallogr. D. Biol. Crystallogr. *68*, 368–380.

Stefaniu, C., Brezesinski, G., and Möhwald, H. (2014). Langmuir monolayers as models to study processes at membrane surfaces. Adv. Colloid Interface Sci. *208*, 197–213.

Stern, A.T., and Forman, S.A. (2016). A Cysteine Substitution Probes β3H267 Interactions with Propofol and Other Potent Anesthetics in α1β3γ2L γ-Aminobutyric Acid Type A Receptors. Anesthesiology *124*, 89–100.

Stewart, D., Desai, R., Cheng, Q., Liu, A., and Forman, S.A. (2008). Tryptophan Mutations at Azi-Etomidate Photo-Incorporation Sites on 1 or 2 Subunits Enhance GABAA Receptor Gating and

Reduce Etomidate Modulation. Mol. Pharmacol. *74*, 1687–1695.

Stewart, D.S., Savechenkov, P.Y., Dostalova, Z., Chiara, D.C., Ge, R., Raines, D.E., Cohen, J.B., Forman, S.A., Bruzik, K.S., and Miller, K.W. (2011). p -(4-Azipentyl)propofol: A Potent Photoreactive General Anesthetic Derivative of Propofol. J. Med. Chem. *54*, 8124–8135.

Stewart, D.S., Hotta, M., Li, G.-D., Desai, R., Chiara, D.C., Olsen, R.W., and Forman, S.A. (2013a). Cysteine substitutions define etomidate binding and gating linkages in the α-M1 domain of γ-aminobutyric acid type A (GABAA) receptors. J. Biol. Chem. *288*, 30373–30386.

Stewart, D.S., Hotta, M., Desai, R., and Forman, S.A. (2013b). State-dependent etomidate occupancy of its allosteric agonist sites measured in a cysteine-substituted GABAA receptor. Mol. Pharmacol. *83*, 1200–1208.

Stewart, D.S., Pierce, D.W., Hotta, M., Stern, A.T., and Forman, S.A. (2014). Mutations at Beta N265 in γ-Aminobutyric Acid Type A Receptors Alter Both Binding Affinity and Efficacy of Potent Anesthetics. PLoS One *9*, e111470.

Stuart, D.I., Levine, M., Muirhead, H., and Stammers, D.K. (1979). Crystal structure of cat muscle pyruvate kinase at a resolution of 2.6 Å. J. Mol. Biol. *134*, 109–142.

Tan, Y.Z., Baldwin, P.R., Davis, J.H., Williamson, J.R., Potter, C.S., Carragher, B., and Lyumkis, D. (2017). Addressing preferred specimen orientation in single-particle cryo-EM through tilting. Nat. Methods *14*, 793–796.

Tang, G., Peng, L., Baldwin, P.R., Mann, D.S., Jiang, W., Rees, I., and Ludtke, S.J. (2007). EMAN2: an extensible image processing suite for electron microscopy. J. Struct. Biol. *157*, 38–46.

Tasneem, A., Iyer, L.M., Jakobsson, E., and Aravind, L. (2005). Identification of the prokaryotic ligand-gated ion channels and their implications for the mechanisms and origins of animal Cys-loop ion channels. Genome Biol. *6*, R4.

Taylor, K.A., and Glaeser, R.M. (2008). Retrospective on the early development of cryoelectron microscopy of macromolecules and a prospective on opportunities for the future. J. Struct. Biol. *163*, 214–223.

Tifrea, D.F., Sun, G., Pal, S., Zardeneta, G., Cocco, M.J., Popot, J.-L., and de la Maza, L.M. (2011). Amphipols stabilize the Chlamydia major outer membrane protein and enhance its protective ability as a vaccine. Vaccine *29*, 4623–4631.

Topf, N., Jenkins, A., Baron, N., and Harrison, N.L. (2003). Effects of isoflurane on gamma-aminobutyric acid type A receptors activated by full and partial agonists. Anesthesiology *98*, 306–311.

Traenkle, B., Kaiser, P.D., Rothbauer, U., Traenkle, B., Kaiser, P.D., and Rothbauer, U. (2016). Nanobody Platform for Determination of Protein Structure, Application of. In Encyclopedia of Analytical Chemistry, (Chichester, UK: John Wiley & Sons, Ltd), pp. 1–14.

Tribet, C., Audebert, R., and Popot, J.L. (1996). Amphipols: polymers that keep membrane proteins soluble in aqueous solutions. Proc. Natl. Acad. Sci. U. S. A. *93*, 15047–15050.

Trick, J.L., Chelvaniththilan, S., Klesse, G., Aryal, P., Wallace, E.J., Tucker, S.J., and Sansom, M.S.P. (2016). Functional Annotation of Ion Channel Structures by Molecular Simulation. Structure *24*, 2207–2216.

Ulens, C., Spurny, R., Thompson, A.J., Alqazzaz, M., Debaveye, S., Han, L., Price, K., Villalgordo, J.M., Tresadern, G., Lynch, J.W., et al. (2014). The Prokaryote Ligand-Gated Ion Channel ELIC Captured in a Pore Blocker-Bound Conformation by the Alzheimer's Disease Drug Memantine. Structure *22*, 1399–1407.

Unwin, N. (2005). Refined structure of the nicotinic acetylcholine receptor at 4A resolution. J. Mol. Biol. *346*, 967–989.

Unwin, N. (2017). Segregation of lipids near acetylcholine-receptor channels imaged by cryo-EM. IUCrJ *4*, 393–399.

Unwin, N., and Fujiyoshi, Y. (2012). Gating movement of acetylcholine receptor caught by plunge-freezing. J. Mol. Biol. *422*, 617–634.

Uzun, S., Kozumplik, O., Jakovljević, M., and Sedić, B. (2010). Side effects of treatment with benzodiazepines. Psychiatr. Danub. *22*, 90–93.

Vlassakov, K. V., and Kissin, I. (2016). Decline in the Development of New Anesthetics. Trends Pharmacol. Sci. *37*, 344–352.

Vu, K.B., Ghahroudi, M.A., Wyns, L., and Muyldermans, S. (1997). Comparison of llama VH sequences from conventional and heavy chain antibodies. Mol. Immunol. *34*, 1121–1131.

Walter, T.S., Diprose, J.M., Mayo, C.J., Siebold, C., Pickford, M.G., Carter, L., Sutton, G.C., Berrow, N.S., Brown, J., Berry, I.M., et al. (2005). A procedure for setting up high-throughput nanolitre crystallization experiments. Crystallization workflow for initial screening, automated storage, imaging and optimization. Acta Crystallogr. D. Biol. Crystallogr. *61*, 651–657.

Whiting, P., McKernan, R.M., and Iversen, L.L. (1990). Another mechanism for creating diversity in gamma-aminobutyrate type A receptors: RNA splicing directs expression of two forms of gamma 2 phosphorylation site. Proc. Natl. Acad. Sci. U. S. A. *87*, 9966–9970.

Winter, G., Lobley, C.M.C., and Prince, S.M. (2013). Decision making in xia2. Acta Crystallogr. D. Biol. Crystallogr. *69*, 1260–1273.

Yano, Y.F., Arakawa, E., Voegeli, W., and Matsushita, T. (2013). Real-time investigation of protein unfolding at an air-water interface at the 1 s time scale. J. Synchrotron Radiat. *20*, 980–983.

Yip, G.M.S., Chen, Z.-W., Edge, C.J., Smith, E.H., Dickinson, R., Hohenester, E., Townsend, R.R., Fuchs, K., Sieghart, W., Evers, A.S., et al. (2013). A propofol binding site on mammalian GABAA receptors identified by photolabeling. Nat. Chem. Biol. *9*, 715–720.

Zhang, K. (2016). Gctf: Real-time CTF determination and correction. J. Struct. Biol. *193*.

Zhang, X., and Gai, J.-G. (2015). Single-layer graphyne membranes for super-excellent brine separation in forward osmosis. RSC Adv. *5*, 68109–68116.

Zhang, Z.-X., Lü, H., Dong, X.-P., Liu, J., and Xu, T.-L. (2002). Kinetics of etomidate actions on GABAA receptors in the rat spinal dorsal horn neurons. Brain Res. *953*, 93–100.

Zheng, S., Palovcak, E., Armache, J.-P., Cheng, Y., and Agard, D. (2016). Anisotropic Correction of Beam-induced Motion for Improved Single-particle Electron Cryo-microscopy. BioRxiv.

Zheng, S.Q., Palovcak, E., Armache, J.-P., Verba, K.A., Cheng, Y., and Agard, D.A. (2017). MotionCor2: anisotropic correction of beam-induced motion for improved cryo-electron microscopy. Nat. Methods *14*, 331–332.

Zoonens, M., Zito, F., Martinez, K.L., and Popot, J.-L. (2014). Amphipols: A General Introduction and Some Protocols. In Membrane Proteins Production for Structural Analysis, (New York, NY: Springer New York), pp. 173–203.

Zouridakis, M., Giastas, P., Zarkadas, E., Chroni-Tzartou, D., Bregestovski, P., and Tzartos, S.J. (2014). Crystal structures of free and antagonist-bound states of human α9 nicotinic receptor extracellular domain. Nat. Struct. Mol. Biol.

10. Appendix

10.1. Nanobody sequences

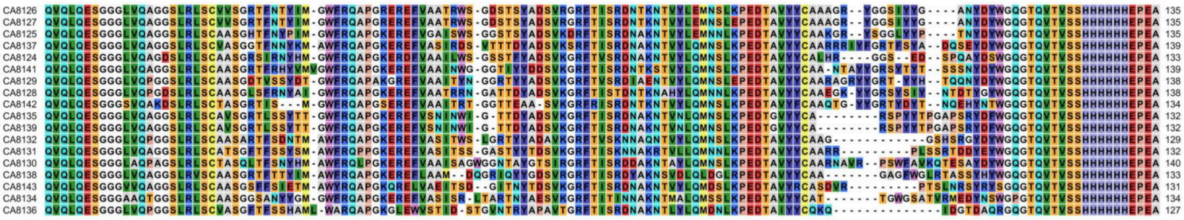

```
  CA8126 QVQLQESGGGLVQAGGSLRLSCVVSGRTFNTYIM-GWFRQAPGREREFVAATRWS-GDSTSYADSVRGRFTISRDNTKNTVYLEMNSLKPEDTAVYYCAAAGR--YGGSIYYG----ANYDYWGQGTQVTVSSHHHHHHEPEA 135
  CA8127 QVQLQESGGGLVQAGGSLRLSCVVSGRTFNTYIM-GWFRQAPGREREFVAATRWS-GDSTSYADSVRGRFTISRDNTKNTVYLEMNSLEPEDTAVYYCAAAGR--YGGSIYYG----ANYDYWGQGTQVTVSSHHHHHHEPEA 135
  CA8125 QVQLQESGGGLVQAGGSLRLSCAASGHTFNYPIM-GWFRQAPGKEREFVGAISWS-GGSTSYADSVKDRFTISRDNAKNTVYLEMNNLKPEDTAVYYCAAKGR--YSGGLYYP----TNYDYWGQGTQVTVSSHHHHHHEPEA 135
  CA8137 QVQLQESGGGLVQAGGSLRLSCVASGGTFNNYKM-AWFRQAPGKEREFVASIRDS-VTTTDYADSVKSRFTISRDNAKNTVYLQMNSLKPEDTAVYYCAARRRIYFGRTFSYA--DQSEYDYWGQGTQVTVSSHHHHHHEPEA 139
* CA8124 QVQLQESGGGLVQAGDSLRLSCAASGRSIRNYHM-GWFRQAPGKERDFVAAILWS-GSSTFYADSVKGRFTVSRDNAKNTVYLQMNSLKPEDTAVYYCALHR----GGS--ED--SPQAYDSWGQGTQVTVSSHHHHHHEPEA 133
  CA8141 QVQLQESGGGLVQAGGSLRLSCAASGRTFRHYVMVGWFRQAPGKEREFVAAINWG-GGTIYYDDSVKGRFTISRDNTKSTVYLQMNSLKPEDTAVYYCAA-NTAYYGRSYTYT--SSSNYDYWGQGTQVTVSSHHHHHHEPEA 139
  CA8129 QVQLQESGGGLVQPGGSLRLSCAASGDTVSSYDT-GWFRQAPAKGREFVAAITYN-GGRTYYADSVKGRFTVSRDIAENTVYLQMNSLEPEDTAVYYCAARAGRYYGRT-YYH--TQQNYDYWGQGTQVTVSSHHHHHHEPEA 138
  CA8128 QVQLQESGGGLVQPGDSLRLSCAASGLSFRNYAI-GWFRQAPGKEREFVAATRRN-GATTDYADSVKGRFTISTDNTKNAHYLQMNNLKPEDTAVYYCAAEGK-YYGRSYSIY--NTDTYGYWGQGTQVTVSSHHHHHHEPEA 138
  CA8142 QVQLQESGGGSVQAKDSLRLSCTASGRTIS---M-GWFRQAPGSEREFVAAITRT-GGTTEAA-SVKGRFRISRDNTKNTVYLQMNSLKPEDTAVYFCAAQTG-YYGRTYDYT--NQEHYNTWGQGTQVTVSSHHHHHHEPEA 134
  CA8135 QVQLQESGGGLVQAGGSLRLSCAVSGRTLSSYTT-GWFRQAPGKEREFVSNINWI-G-TTDYADSVKGRFTISRDNAKNTVNLQMNSLKPEDTGVYYCA--------RSPYYTPGAPSRYDFWGQGTQVTVSSHHHHHHEPEA 132
* CA8139 QVQLQESGGGLVQAGGSLRLSCAVSGRTLSSYTT-GWFRQAPGKEREFVSNINWI-G-TTDYADSVKGRFTISRDNAKNTVNLQMNSLKPEDTGVYYCA--------RSPYYTPGAPSRYDFWGQGTQVTVSSHHHHHHEPEA 132
  CA8132 QVQLQESGGGLVQPGGSLRLSCAASARTFSDNTM-AWFRQAPGKEREFVASITWS-LGRTYYADAVKGRFTVSKNNAQNTVYLQMNSLKPEDTAVYYCAAG------------GSHSRGYDYWGQGTQVTVSSHHHHHHEPEA 129
  CA8131 QVQLQESGGGLVQAGGSLRLSCATSGFTFSSYSM-AWFRQPPGKEREFVASITSS-GASTYYTDSVKGRFTISKNNAKRTVLLQMNNLKPEDTAVYYCAARR---------PLSSRTDDYEYWGQGTQVTVSSHHHHHHEPEA 132
  CA8130 QVQLQESGGGLAQPAGSLRLSCTASQLTFSNYHM-AWFRQLPGKEREFVAAISAGWGGNTAYGTSIRGRFTISRDDAKNTAYLQMNSLKPEDTAVYYCAARNAVR--PSWFAVKQTESAYDYWGQGTQVTVSSHHHHHHEPEA 140
  CA8138 QVQLQESGGGLVQAGGSLRVSCAASGRTFTTYIM-AWFRQAPGKEREFLAAM--DQGRIQYYGDSVRGRFTISRDYAKNSVDLQLDGLRPEDTAVYYCAA-------GAGFWGLRTASSYHYWGQGTQVTVSSHHHHHHEPEA 133
  CA8143 QVQLQESGGGVVQAGGSLRLSCAASGSFFSIETM-AWYRQAPGKQRELVAEITSD--GITNYTDSVKGRFTISRDNAKNTVYLQMDSLKPEDTAVYRCASDVR---------PTSLNRSYRYSGQGTQVTVSSHHHHHHEPEA 131
  CA8134 QVQLQESGGGAAQTGGSLRLSCAASGGSANYYGM-GWFRQAPGKEREFVASISR-LTARTNYAESVKGRFTITINNAKNTMALQMSSLKPEDTAVYYCAT-------TGWGSATVRMEDYNSWGPGTQVTVSSHHHHHHEPEA 134
  CA8136 QVQLQESGGGLVQPGGSLRLSCVASGFTFSSHAML-WARQAPGKGLEWVSTID-STGVNTRYAPAVTGRFTISRDNAKNTLYLQMDNLKPEDTAIYYCQKQ--------------IDGTDAQRGQGTQVTVSSHHHHHHEPEA 127
```

10.2. Nanobody families

Reference No.	Conc. (ng/µl)	Antigen Selection and Screening	Family	Vector	Antibiotic Resistance	Clone ID	Occurance
CA8125	435,47	GABRa1b3 solid phase coated and captured with 1D4 monoclonal	1	pMESy4	Ampicillin	MP534D7#a	11x
CA8126	494,03			pMESy4	Ampicillin	MP534F4#a	
CA8127	394,58			pMESy4	Ampicillin	MP534B10#a	
CA8137	449,03		2	pMESy4	Ampicillin	MP534F10#a	5x
CA8143	307,73		3	pMESy4	Ampicillin	MP534E12#a	4x
CA8129	278,59	GABRa1b3 solid phase coated	4	pMESy4	Ampicillin	MP534D2#a	1x
CA8130	422,42		5	pMESy4	Ampicillin	MP534E7#a	1x
CA8134	385,23		6	pMESy4	Ampicillin	MP534B7#a	1x
CA8135	401,55		7	pMESy4	Ampicillin	MP534H7#a	2x
*CA8139	503,8		8	pMESy4	Ampicillin	MP534C7#a	2x
*CA8124	474,32	GABRa1b3 captured with 1D4 monoclonal	9	pMESy4	Ampicillin	MP534C2#a	1x
CA8131	462,53		10	pMESy4	Ampicillin	MP534H4#b	1x
CA8132	345,45		11	pMESy4	Ampicillin	MP534E10#a	1x
CA8136	424,57		12	pMESy4	Ampicillin	MP534G5#a	1x
CA8138	400,07		13	pMESy4	Ampicillin	MP534H11#a	1x
CA8141	367,97		14	pMESy4	Ampicillin	MP534B6#a	1x
CA8142	430,64		15	pMESy4	Ampicillin	MP534A11#a	1x
CA8128	347,71		16	pMESy4	Ampicillin	MP534E11#a	1x

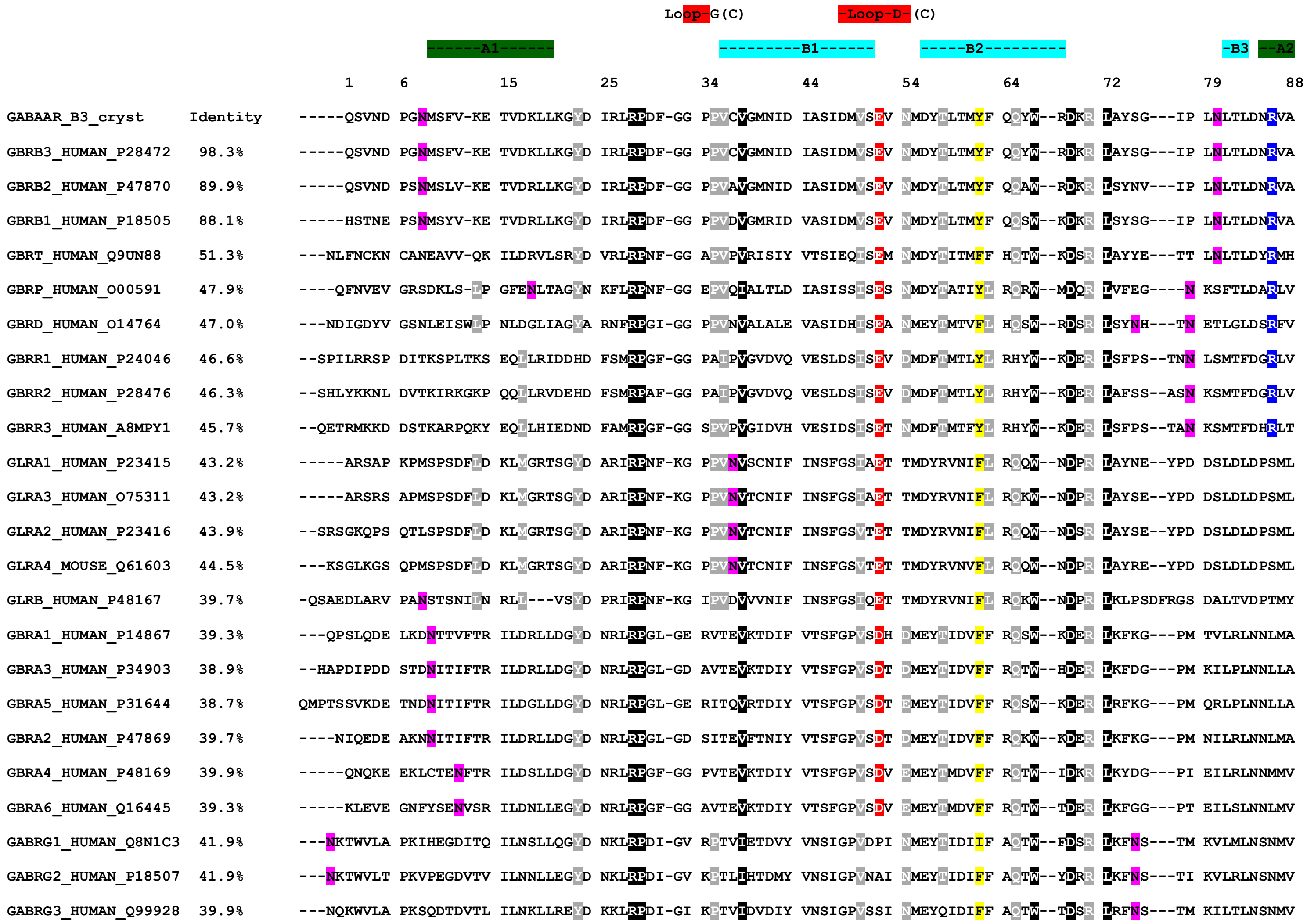

```
                                                                        Loop-G(C)          -Loop-D-(C)
                                              ------A1------                  ---------B1------     -----B2---------                 -B3 --A2
                                     1     6          15         25         34         44         54         64         72         79       88
GABAAR_B3_cryst     Identity    -----QSVND PGNMSFV-KE TVDKLLKGYD IRLRPDF-GG PPVCVGMNID IASIDMVSEV NMDYTLTMYF QQYW--RDKR LAYSG---IP LNLTLDNRVA
GBRB3_HUMAN_P28472   98.3%      -----QSVND PGNMSFV-KE TVDKLLKGYD IRLRPDF-GG PPVCVGMNID IASIDMVSEV NMDYTLTMYF QQYW--RDKR LAYSG---IP LNLTLDNRVA
GBRB2_HUMAN_P47870   89.9%      -----QSVND PSNMSLV-KE TVDRLLKGYD IRLRPDF-GG PPVAVGMNID IASIDMVSEV NMDYTLTMYF QQAW--RDKR LSYNV---IP LNLTLDNRVA
GBRB1_HUMAN_P18505   88.1%      -----HSTNE PSNMSYV-KE TVDRLLKGYD IRLRPDF-GG PPVDVGMRID VASIDMVSEV NMDYTLTMYF QQSW--KDKR LSYSG---IP LNLTLDNRVA
GBRT_HUMAN_Q9UN88    51.3%      ---NLFNCKN CANEAVV-QK ILDRVLSRYD VRLRPNF-GG APVPVRISIY VTSIEQISEM NMDYTITMFF HQTW--KDSR LAYYE---TT LNLTLDYRMH
GBRP_HUMAN_O00591    47.9%      ----QFNVEV GRSDKLS-LP GFENLTAGYN KFLRPNF-GG EPVQIALTLD IASISSISES NMDYTATIYL RQRW--MDQR LVFEG----N KSFTLDARLV
GBRD_HUMAN_O14764    47.0%      ---NDIGDYV GSNLEISWLP NLDGLIAGYA RNFRPGI-GG PPVNVALALE VASIDHISEA NMEYTMTVFL HQSW--RDSR LSYNH---TN ETLGLDSRFV
GBRR1_HUMAN_P24046   46.6%      --SPILRRSP DITKSPLTKS EQLLRIDDHD FSMRPGF-GG PAIPVGVDVQ VESLDSISEV DMDFTMTLYL RHYW--KDER LSFPS--TNN LSMTFDGRLV
GBRR2_HUMAN_P28476   46.3%      --SHLYKKNL DVTKIRKGKP QQLLRVDEHD FSMRPAF-GG PAIPVGVDVQ VESLDSISEV DMDFTMTLYL RHYW--KDER LAFSS--ASN KSMTFDGRLV
GBRR3_HUMAN_A8MPY1   45.7%      --QETRMKKD DSTKARPQKY EQLLHIEDND FAMRPGF-GG SPVPVGIDVH VESIDSISET NMDFTMTFYL RHYW--KDER LSFPS--TAN KSMTFDHRLT
GLRA1_HUMAN_P23415   43.2%      -----ARSAP KPMSPSDFLD KLMGRTSGYD ARIRPNF-KG PPVNVSCNIF INSFGSIAET TMDYRVNIFL RQQW--NDPR LAYNE--YPD DSLDLDPSML
GLRA3_HUMAN_O75311   43.2%      -----ARSRS APMSPSDFLD KLMGRTSGYD ARIRPNF-KG PPVNVTCNIF INSFGSIAET TMDYRVNIFL RQKW--NDPR LAYSE--YPD DSLDLDPSML
GLRA2_HUMAN_P23416   43.9%      --SRSGKQPS QTLSPSDFLD KLMGRTSGYD ARIRPNF-KG PPVNVTCNIF INSFGSVTET TMDYRVNIFL RQQW--NDSR LAYSE--YPD DSLDLDPSML
GLRA4_MOUSE_Q61603   44.5%      ---KSGLKGS QPMSPSDFLD KLMGRTSGYD ARIRPNF-KG PPVNVTCNIF INSFGSVTET TMDYRVNVFL RQQW--NDPR LAYRE--YPD DSLDLDPSML
GLRB_HUMAN_P48167    39.7%      -QSAEDLARV PANSTSNILN RLL---VSYD PRIRPNF-KG IPVDVVVNIF INSFGSIQET TMDYRVNIFL RQKW--NDPR LKLPSDFRGS DALTVDPTMY
GBRA1_HUMAN_P14867   39.3%      ---QPSLQDE LKDNTTVFTR ILDRLLDGYD NRLRPGL-GE RVTEVKTDIF VTSFGPVSDH DMEYTIDVFF RQSW--KDER LKFKG---PM TVLRLNNLMA
GBRA3_HUMAN_P34903   38.9%      --HAPDIPDD STDNITIFTR ILDRLLDGYD NRLRPGL-GD AVTEVKTDIY VTSFGPVSDT DMEYTIDVFF RQTW--HDER LKFDG---PM KILPLNNLLA
GBRA5_HUMAN_P31644   38.7%      QMPTSSVKDE TNDNITIFTR ILDGLLDGYD NRLRPGL-GE RITQVRTDIY VTSFGPVSDT EMEYTIDVFF RQSW--KDER LRFKG---PM QRLPLNNLLA
GBRA2_HUMAN_P47869   39.7%      ----NIQEDE AKNNITIFTR ILDRLLDGYD NRLRPGL-GD SITEVFTNIY VTSFGPVSDT DMEYTIDVFF RQKW--KDER LKFKG---PM NILRLNNLMA
GBRA4_HUMAN_P48169   39.9%      -----QNQKE EKLCTENFTR ILDSLLDGYD NRLRPGF-GG PVTEVKTDIY VTSFGPVSDV EMEYTMDVFF RQTW--IDKR LKYDG---PI EILRLNNMMV
GBRA6_HUMAN_Q16445   39.3%      -----KLEVE GNFYSENVSR ILDNLLEGYD NRLRPGF-GG AVTEVKTDIY VTSFGPVSDV EMEYTMDVFF RQTW--TDER LKFGG---PT EILSLNNLMV
GABRG1_HUMAN_Q8N1C3  41.9%      ---NKTWVLA PKIHEGDITQ ILNSLLQGYD NKLRPDI-GV RPTVIETDVY VNSIGPVDPI NMEYTIDIIF AQTW--FDSR LKFNS---TM KVLMLNSNMV
GABRG2_HUMAN_P18507  41.9%      ---NKTWVLT PKVPEGDVTV ILNNLLEGYD NKLRPDI-GV KPTLIHTDMY VNSIGPVNAI NMEYTIDIFF AQTW--YDRR LKFNS---TI KVLRLNSNMV
GABRG3_HUMAN_Q99928  39.9%      ---NQKWVLA PKSQDTDVTL ILNKLLREYD KKLRPDI-GI KPTVIDVDIY VNSIGPVSSI NMEYQIDIFF AQTW--TDSR LRFNS---TM KILTLNSNMV
```

```
GBRE_HUMAN_P78334    35.0%  --STETETGS RVGKLPEASR ILNTILSNYD HKLRPGI-GE KPTVVTVEIS VNSLGPLSIL DMEYTIDIIF SQTW--YDER LCYND---TF ESLVLNGNVV
ACHA1_HUMAN_P02708-2 18.4%  -------------SEHETRLV AKLFKD--YS SVVRPVEDHR QVVEVTVGLQ LIQLINVDEV NQIVTTNVRL KQQW--VDYN LKWNP--DDY GGVKKIHIPS
ACHA2_HUMAN_Q15822   20.5%  ------SHTE T----EDRLF KHLFRG--YN RWARPVPNTS DVVIVRFGLS IAQLIDVDEK NQMMTTNVWL KQEW--SDYK LRWNP--TDF GNITSLRVPS
ACHA4_HUMAN_P43681   20.2%  -----SSHVE TRAHAEERLL KKLFSG--YN KWSRPVANIS DVVLVRFGLS IAQLIDVDEK NQMMTTNVWV KQEW--HDYK LRWDP--ADY ENVTSIRIPS
ACHA3_HUMAN_P32297   20.2%  -------------SEAEHRLF ERLFED--YN EIIRPVANVS DPVIIHFEVS MSQLVKVDEV NQIMETNLWL KQIW--NDYK LKWNP--SDY GGAEFMRVPA
ACHA6_HUMAN_Q15825   21.0%  -------KGC VGCATEERLF HKLFSH--YN QFIRPVENVS DPVTVHFEVA ITQLANVDEV NQIMETNLWL RHIW--NDYK LRWDP--MEY DGIETLRVPA
ACHA5_HUMAN_P30532   18.8%  ------SEPS SIAKHEDSLL KDLFQD--YE RWVRPVEHLN DKIKIKFGLA ISQLVDVDEK NQLMTTNVWL KQEW--IDVK LRWNP--DDY GGIKVIRVPS
ACHB3_HUMAN_Q05901   18.2%  --------------ENEDALL RHLFQG--YQ KWVRPVLHSN DTIKVYFGLK ISQLVDVDEK NQLMTTNVWL KQEW--TDHK LRWNP--DDY GGIHSIKVPS
ACHB2_HUMAN_P17787   19.8%  -------------TDTEERLV EHLLDPSRYN KLIRPATNGS ELVTVQLMVS LAQLISVHER EQIMTTNVWL TQEW--EDYR LTWKP--EEF DNMKKVRLPS
ACHB4_HUMAN_P30926   20.9%  --------------NAEEKLM DDLLNKTRYN NLIRPATSSS QLISIKLQLS LAQLISVNER EQIMTTNVWL KQEW--TDYR LTWNS--SRY EGVNILRIPA
ACHB1_HUMAN_P11230   20.4%  -------------SEAEGRLR EKLFSG--YD SSVRPAREVG DRVRVSVGLI LAQLISLNEK DEEMSTKVYL DLEW--TDYR LSWDP--AEH DGIDSLRITA
ACHD_HUMAN_Q07001    17.4%  ---------------EEERLI RHLFQEKGYN KELRPVAHKE ESVDVALALT LSNLISLKEV EETLTTNVWI EHGW--TDNR LKWNA--EEF GNISVLRLPP
ACHE_HUMAN_Q04844    17.3%  ---------------EELRLY HHLFNN--YD PGSRPVREPE DTVTISLKVT LTNLISLNEK EETLTTSVWI GIDW--QDYR LNYSK--DDF GGIETLRVPS
ACHG_HUMAN_P07510    16.2%  ---------------QEERLL ADLMQN--YD PNLRPAERDS DVVNVSLKLT LTNLISLNER EEALTTNVWI EMQW--CDYR LRWDP--RDY EGLWVLRVPS
ACHA7_HUMAN_P36544   19.6%  ------------QGEFQRKLY KELVKN--YN PLERPVANDS QPLTVYFSLS LLQIMDVDEK NQVLTTNIWL QMSW--TDHY LQWNV--SEY PGVKTVRFPD
ACHA9_HUMAN_Q9UGM1   20.9%  --------ET ADGKYAQKLF NDLFED--YS NALRPVEDTD KVLNVTLQIT LSQIKDMDER NQILTAYLWI RQIW--HDAY LTWDR--DQY DGLDSIRIPS
ACHA10_HUMAN_Q9GZZ6  20.5%  ------------EGRLALKLF RDLFAN--YT SALRPVADTD QTLNVTLEVT LSQIIDMDER NQVLTLYLWI RQEW--TDAY LRWDP--NAY GGLDAIRIPS
5HT3A_HUMAN_P46098   18.7%  ---EARRSRN TTRPALLRLS DYLLTNY--R KGVRPVRDWR KPTTVSIDVI VYAILNVDEK NQVLTTYIWY RQYW--TDEF LQWNP--EDF DNITKLSIPT
5HT3B_HUMAN_O95264   14.8%  -----TDTHH PQDSALYHLS KQLLQKY--H KEVRPVYNWT KATTVYLDLF VHAILDVDAE NQILKTSVWY QEVW--NDEF LSWNS--SMF DEIREISLPL
5HT3E_HUMAN_A5X5Y0   16.1%  ----VTFTIN CSGFGQHGAD PTALNSVFNR KPFRPVTNIS VPTQVNISFA MSAILDVNEQ LHLLSSFLWL EMVW--DNPF ISWNP--EEC EGITKMSMAA
5HT3C_HUMAN_Q8WXA8   16.7%  ----DAFTIN CSGFDQHGVD PAVFQAVFDR KAFRPFTNYS IPTRVNISFT LSAILGVDAQ LQLLTSFLWM DLVW--DNPF INWNP--KEC VGINKLTVLA
ELIC_ERWCH_P0C7BY7   20.7%  ----------------------------------APADNAADA RPVDVSVSIF INKIYGVNTL EQTYKVDGYI VAQWTGKPRK TPGDKP-LIV ENTQIERWIN
GLIC_GLOVI_Q7NDN8    21.0%  --------------------W FSPPVWGQDM VSPPPPIAD- EPLTVNTGIY LIECYSLDDK AETFKVNAFL SLSW--KDRR LAFDP---VR SGVRVKTYEP
GluCl_cryst          35.7%  ----------------SDSKI LAHLFTSGYD FRVRPPTDNG GPVVVSVNML LRTISKIDVV NMEYSAQLTL RESW--IDKR LSYGVKGDGQ PDFVI-LTVG
                                            ----A1------                  --------b1-------   ---------b2-------                 -B3-
```

```
                                     Loop-A(P)               --Loop-E----(C)      ----Cys-loop-----    -Loop-B-(P)            -Loop-F-(C)
                              --     -B4   --B5--        -B5′-     ------B6------            -----B7----        -B8--        B8′         --
                              89         99         109        119        129        139        149        159        169        178      187
GABAAR_B3_cryst               DQLWVPDTYF LNDKKSFVHG VTVKNRMIRL HPDGTVLYGL RITTTAACMM DLRRYPLDEQ NCTLEIESYG YTTDDIEFYW RGGDK-AVTG VERIELPQFS
GBRB3_HUMAN_P28472            DQLWVPDTYF LNDKKSFVHG VTVKNRMIRL HPDGTVLYGL RITTTAACMM DLRRYPLDEQ NCTLEIESYG YTTDDIEFYW RGGDK-AVTG VERIELPQFS
GBRB2_HUMAN_P47870            DQLWVPDTYF LNDKKSFVHG VTVKNRMIRL HPDGTVLYGL RITTTAACMM DLRRYPLDEQ NCTLEIESYG YTTDDIEFYW RGDDN-AVTG VTKIELPQFS
GBRB1_HUMAN_P18505            DQLWVPDTYF LNDKKSFVHG VTVKNRMIRL HPDGTVLYGL RITTTAACMM DLRRYPLDEQ NCTLEIESYG YTTDDIEFYW NGGEG-AVTG VNKIELPQFS
GBRT_HUMAN_Q9UN88             EKLWVPDCYF LNSKDAFVHD VTVENRVFQL HPDGTVRYGI RLTTTAACSL DLHKFPMDKQ ACNLVVESYG YTVEDIILFW DDNGN-AIHM TEELHIPQFT
GBRP_HUMAN_O00591             EFLWVPDTYI VESKKSFLHE VTVGNRLIRL FSNGTVLYAL RITTTVACNM DLSKYPMDTQ TCKLQLESWG YDGNDVEFTW LRGND-SVRG LEHLRLAQYT
GBRD_HUMAN_O14764             DKLWLPDTFI VNAKSAWFHD VTVENKLIRL QPDGVILYSI RITSTVACDM DLAKYPMDEQ ECMLDLESYG YSSEDIVYYW SESQE-HIHG LDKLQLAQFT
GBRR1_HUMAN_P24046            KKIWVPDMFF VHSKRSFIHD TTTDNVMLRV QPDGKVLYSL RVTVTAMCNM DFSRFPLDTQ TCSLEIESYA YTEDDLMLYW KKGND-SLKT DERISLSQFL
GBRR2_HUMAN_P28476            KKIWVPDVFF VHSKRSFTHD TTTDNIMLRV FPDGHVLYSM RITVTAMCNM DFSHFPLDSQ TCSLELESYA YTDEDLMLYW KNGDE-SLKT DEKISLSQFL
GBRR3_HUMAN_A8MPY1            RKIWVPDIFF VHSKRSFIHD TTMENIMLRV HPDGNVLLSL RITVSAMCFM DFSRFPLDTQ NCSLELESYA YNEDDLMLYW KHGNK-SLNT EEHMSLSQFF
GLRA1_HUMAN_P23415            DSIWKPDLFF ANEKGAHFHE ITTDNKLLRI SRNGNVLYSI RITLTLACPM DLKNFPMDVQ TCIMQLESFG YTMNDLIFEW QEQGA--VQV ADGLTLPQF-
GLRA3_HUMAN_O75311            DSIWKPDLFF ANEKGANFHE VTTDNKLLRI FKNGNVLYSI RLTLTLSCPM DLKNFPMDVQ TCIMQLESFG YTMNDLIFEW QDEAP--VQV AEGLTLPQF-
GLRA2_HUMAN_P23416            DSIWKPDLFF ANEKGANFHD VTTDNKLLRI SKNGKVLYSI RLTLTLSCPM DLKNFPMDVQ TCTMQLESFG YTMNDLIFEW LSDGP--VQV AEGLTLPQF-
GLRA4_MOUSE_Q61603            DSIWKPDLFF ANEKGANFHE VTTDNKLLRI FKNGNVLYSI RLTLILSCPM DLKNFPMDIQ TCTMQLESFG YTMNDLMFEW LEDAP-AVQV AEGLTLPQF-
GLRB_HUMAN_P48167             KCLWKPDLFF ANEKSANFHD VTQENILLFI FRDGDVLVSM RLSITLSCPL DLTLFPMDTQ RCKMQLESFG YTTDDLRFIW QSGDP--VQL -EKIALPQFD
GBRA1_HUMAN_P14867            SKIWTPDTFF HNGKKSVAHN MTMPNKLLRI TEDGTLLYTM RLTVRAECPM HLEDFPMDAH ACPLKFGSYA YTRAEVVYEW TREPA-RSVV VAEDGSRLNQ
GBRA3_HUMAN_P34903            SKIWTPDTFF HNGKKSVAHN MTTPNKLLRL VDNGTLLYTM RLTIHAECPM HLEDFPMDVH ACPLKFGSYA YTTAEVVYSW TLGKN-KSVE VAQDGSRLNQ
GBRA5_HUMAN_P31644            SKIWTPDTFF HNGKKSIAHN MTTPNKLLRL EDDGTLLYTM RLTISAECPM QLEDFPMDAH ACPLKFGSYA YPNSEVVYVW TNGST-KSVV VAEDGSRLNQ
GBRA2_HUMAN_P47869            SKIWTPDTFF HNGKKSVAHN MTMPNKLLRI QDDGTLLYTM RLTVQAECPM HLEDFPMDAH SCPLKFGSYA YTTSEVTYIW TYNAS-DSVQ VAPDGSRLNQ
GBRA4_HUMAN_P48169            TKVWTPDTFF RNGKKSVSHN MTAPNKLFRI MRNGTILYTM RLTISAECPM RLVDFPMDGH ACPLKFGSYA YPKSEMIYTW TKGPE-KSVE VPKESSSLVQ
GBRA6_HUMAN_Q16445            SKIWTPDTFF RNGKKSIAHN MTTPNKLFRI MQ GTILYTM RLTINADCPM RLVNFPMDGH ACPLKFGSYA YPKSEIIYTW KKGPL-YSVE VPEESSSLLQ
GABRG1_HUMAN_Q8N1C3           GKIWIPDTFF RNSRKSDAHW ITTPNRLLRI WNDGRVLYTL RLTINAECYL QLHNFPMDEH SCPLEFSSYG YPKNEIEYKW KKPSV-EVAD --PKYWRLYQ
GABRG2_HUMAN_P18507           GKIWIPDTFF RNSKKADAHW ITTPNRMLRI WNDGRVLYTL RLTIDAECQL QLHNFPMDEH SCPLEFSSYG YPREEIVYQW KRSSV-EVGD --TRSWRLYQ
GABRG3_HUMAN_Q99928           GLIWIPDTIF RNSKTAEAHW ITTPNQLLRI WNDGKILYTL RLTINAECQL QLHNFPMDEH SCPLIFSSYG YPKEEMIYRW RKNSV-EAAD --QKSWRLYQ
GBRE_HUMAN_P78334             SQLWIPDTFF RNSKRTHEHE ITMPNQMVRI YKDGKVLYTI RMTIDAGCSL HMLRFPMDSH SCPLSFSSFS YPENEMIYKW ENFKL-EINE --KNSWKLFQ
ACHA1_HUMAN_P02708-2          EKIWRPDLVL YNNADGDFAI VKFTKVLLQ- -YTGHITWTP PAIFKSYCEI IVTHFPFDEQ NCSMKLGTWT YDGSVVAINP ESD-----QP DLSNFMESGE
```

```
ACHA2_HUMAN_Q15822  EMIWIPDIVL YNNADGEFAV THMTKAHLF- -STGTVHWVP PAIYKSSCSI DVTFFPFDQQ NCKMKFGSWT YDKAKIDLEQ MEQ-----TV DLKDYWESGE
ACHA4_HUMAN_P43681  ELIWRPDIVL YNNADGDFAV THLTKAHLF- -HDGRVQWTP PAIYKSSCSI DVTFFPFDQQ NCTMKFGSWT YDKAKIDLVN MHS-----RV DQLDFWESGE
ACHA3_HUMAN_P32297  QKIWKPDIVL YNNAVGDFQV DDKTKALLK- -YTGEVTWIP PAIFKSSCKI DVTYFPFDYQ NCTMKFGSWS YDKAKIDLVL IGS-----SM NLKDYWESGE
ACHA6_HUMAN_Q15825  DKIWKPDIVL YNNAVGDFQV EGKTKALLK- -YNGMITWTP PAIFKSSCPM DITFFPFDHQ NCSLKFGSWT YDKAEIDLLI IGS-----KV DMNDFWENSE
ACHA5_HUMAN_P30532  DSVWTPDIVL FDNADGRFEG T-STKTVIR- -YNGTVTWTP PANYKSSCTI DVTFFPFDLQ NCSMKFGSWT YDGSQVDIIL EDQ-----DV DKRDFFDNGE
ACHB3_HUMAN_Q05901  ESLWLPDIVL FENADGRFEG SLMTKVIVK- -SNGTVVWTP PASYKSSCTM DVTFFPFDRQ NCSMKFGSWT YDGTMVDLIL INE-----NV DRKDFFDNGE
ACHB2_HUMAN_P17787  KHIWLPDVVL YNNADGMYEV SFYSNAVVS- -YDGSIFWLP PAIYKSACKI EVKHFPFDQQ NCTMKFRSWT YDRTEIDLVL KSE-----VA SLDDFTPSGE
ACHB4_HUMAN_P30926  KRIWLPDIVL YNNADGTYEV SVYTNLIVR- -SNGSVLWLP PAIYKSACKI EVKYFPFDQQ NCTLKFRSWT YDHTEIDMVL MTP-----TA SMDDFTPSGE
ACHB1_HUMAN_P11230  ESVWLPDVVL LNNNDGNFDV ALDISVVVS- -SDGSVRWQP PGIYRSSCSI QVTYFPFDWQ NCTMVFSSYS YDSSEVSLQT QEI-----HI HEGTFIENGQ
ACHD_HUMAN_Q07001   DMVWLPEIVL ENNNDGSFQI SYSCNVLVY- -HYGFVYWLP PAIFRSSCPI SVTYFPFDWQ NCSLKFSSLK YTAKEITLSL KQD-----AI DPEGFTENGE
ACHE_HUMAN_Q04844   ELVWLPEIVL ENNIDGQFGV AYDANVLVY- -EGGSVTWLP PAIYRSVCAV EVTYFPFDWQ NCSLIFRSQT YNAEEVEFTF AVD-----NI DTEAYTENGE
ACHG_HUMAN_P07510   TMVWRPDIVL ENNVDGVFEV ALYCNVLVS- -PDGCIYWLP PAIFRSACSI SVTYFPFDWQ NCSLIFQSQT YSTNEIDLQL SQE-----DI DPEAFTENGE
ACHA7_HUMAN_P36544  GQIWKPDILL YNSADERFDA TFHTNVLVN- -SSGHCQYLP PGIFKSSCYI DVRWFPFDVQ HCKLKFGSWS YGGWSLDL-- QMQ-----EA DISGYIPNGE
ACHA9_HUMAN_Q9UGM1  DLVWRPDIVL YNKADDESSE PVNTNVVLR- -YDGLITWDA PAITKSSCVV DVTYFPFDNQ QCNLTFGSWT YNGNQVDIFN ALD-----SG DLSDFIEDVE
ACHA10_HUMAN_Q9GZZ6 SLVWRPDIVL YNKADAQPPG SASTNVVLR- -HDGAVRWDA PAITRSSCRV DVAAFPFDAQ HCGLTFGSWT HGGHQLDVRP RGA-----AA SLADFVENVE
5HT3A_HUMAN_P46098  DSIWVPDILI NEFVDVG-KS PNIPYVYIR- -HQGEVQNYK PLQVVTACSL DIYNFPFDVQ NCSLTFTSWL HTIQDINISL WRLPEKV-KS DRSVFMNQGE
5HT3B_HUMAN_O95264  SAIWAPDIII NEFVDIE-RY PDLPYVYVN- -SSGTIENYK PIQVVSACSL ETYAFPFDVQ NCSLTFKSIL HTVEDVDLAF LRSPEDI-QH DKKAFLNDSE
5HT3E_HUMAN_A5X5Y0  KNLWLPDIFI IELMDVD-KT PKGLTAYVS- -NEGRIRYKK PMKVDSICNL DIFYFPFDQQ NCTLTFSSFL YTVDSMLLDM EKEVWEITDA SRNILQTHGE
5HT3C_HUMAN_Q8WXA8  ENLWLPDIFI VESMDVD-QT PSGLTAYIS- -SEGRIKYDK PMRVTSICNL DIFYFPFDQQ NCTFTFSSFL YTVDSMLLGM DKEVWEITDT SRKVIQTQGE
ELIC_ERWCH_P0C7BY7  NGLWVPALEF INVVGS---- PDTGNKRLML FPDGRVIYNA RFLGSFSNDM DFRLFPFDRQ QFVLELEPFS YNNQQLRFSD IQVYT--ENI DNEEIDEWWI
GLIC_GLOVI_Q7NDN8   EAIWIPEIRF VNVENA---- RDADVVDISV SPDGTVQYLE RFSARVLSPL DFRRYPFDSQ TLHIYLIVRS VDTRNIVLAV DLEKV--GKN DDVFLTGWDI
GluCl_cryst         HQIWMPDTFF PNEKQAYKHT IDKPNVLIRI HNDGTVLYSV RISLVLSCPM YLQYYPMDVQ QCSIDLASYA YTTKDIEYLW KEHSPLQLKV GLSSSLPSFQ
                                 --B4-         --B5--- -------B6-------          -----B7-----         -B8--      B8         --B9-
```

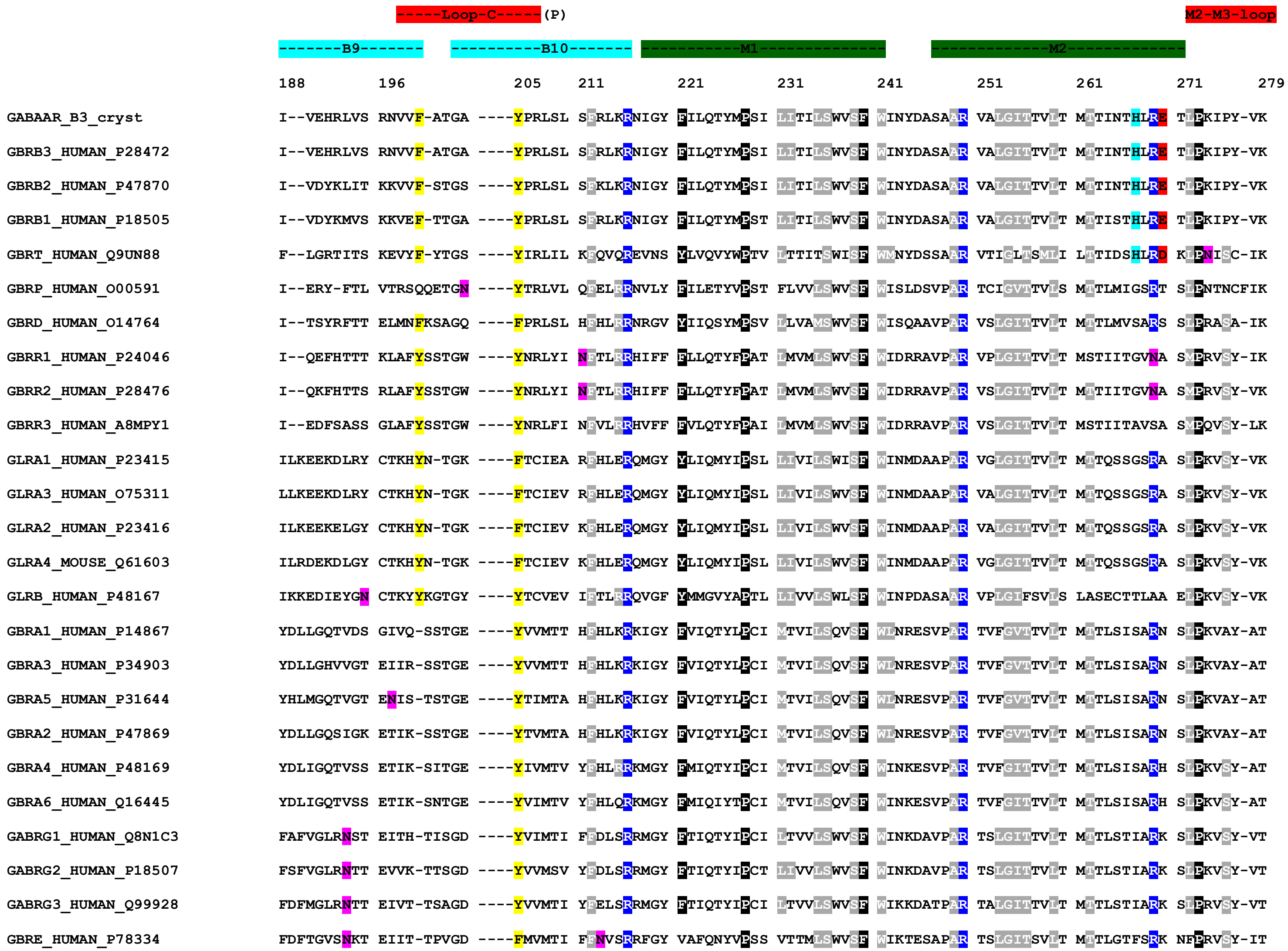

```
                                    -----Loop-C-----(P)                                                                                M2-M3-loop
                           -------B9-------  ----------B10------- -----------M1-------------     ------------M2------------
                           188        196            205    211        221        231        241        251        261        271     279
GABAAR_B3_cryst            I--VEHRLVS RNVVF-ATGA ----YPRLSL SFRLKRNIGY FILQTYMPSI LITILSWVSF WINYDASAAR VALGITTVLT MTTINTHLRE TLPKIPY-VK
GBRB3_HUMAN_P28472         I--VEHRLVS RNVVF-ATGA ----YPRLSL SFRLKRNIGY FILQTYMPSI LITILSWVSF WINYDASAAR VALGITTVLT MTTINTHLRE TLPKIPY-VK
GBRB2_HUMAN_P47870         I--VDYKLIT KKVVF-STGS ----YPRLSL SFKLKRNIGY FILQTYMPSI LITILSWVSF WINYDASAAR VALGITTVLT MTTINTHLRE TLPKIPY-VK
GBRB1_HUMAN_P18505         I--VDYKMVS KKVEF-TTGA ----YPRLSL SFRLKRNIGY FILQTYMPST LITILSWVSF WINYDASAAR VALGITTVLT MTTISTHLRE TLPKIPY-VK
GBRT_HUMAN_Q9UN88          F--LGRTITS KEVYF-YTGS ----YIRLIL KFQVQREVNS YLVQVYWPTV LTTITSWISF WMNYDSSAAR VTIGLTSMLI LTTIDSHLRD KLPNISC-IK
GBRP_HUMAN_O00591          I--ERY-FTL VTRSQQETGN ----YTRLVL QFELRRNVLY FILETYVPST FLVVLSWVSF WISLDSVPAR TCIGVTTVLS MTTLMIGSRT SLPNTNCFIK
GBRD_HUMAN_O14764          I--TSYRFTT ELMNFKSAGQ ----FPRLSL HFHLRRNRGV YIIQSYMPSV LLVAMSWVSF WISQAAVPAR VSLGITTVLT MTTLMVSARS SLPRASA-IK
GBRR1_HUMAN_P24046         I--QEFHTTT KLAFYSSTGW ----YNRLYI NFTLRRHIFF FLLQTYFPAT LMVMLSWVSF WIDRRAVPAR VPLGITTVLT MSTIITGVNA SMPRVSY-IK
GBRR2_HUMAN_P28476         I--QKFHTTS RLAFYSSTGW ----YNRLYI NFTLRRHIFF FLLQTYFPAT LMVMLSWVSF WIDRRAVPAR VSLGITTVLT MTTIITGVNA SMPRVSY-VK
GBRR3_HUMAN_A8MPY1         I--EDFSASS GLAFYSSTGW ----YNRLFI NFVLRRHVFF FVLQTYFPAI LMVMLSWVSF WIDRRAVPAR VSLGITTVLT MSTIITAVSA SMPQVSY-LK
GLRA1_HUMAN_P23415         ILKEEKDLRY CTKHYN-TGK ----FTCIEA RFHLERQMGY YLIQMYIPSL LIVILSWISF WINMDAAPAR VGLGITTVLT MTTQSSGSRA SLPKVSY-VK
GLRA3_HUMAN_O75311         LLKEEKDLRY CTKHYN-TGK ----FTCIEV RFHLERQMGY YLIQMYIPSL LIVILSWVSF WINMDAAPAR VALGITTVLT MTTQSSGSRA SLPKVSY-VK
GLRA2_HUMAN_P23416         ILKEEKELGY CTKHYN-TGK ----FTCIEV KFHLERQMGY YLIQMYIPSL LIVILSWVSF WINMDAAPAR VALGITTVLT MTTQSSGSRA SLPKVSY-VK
GLRA4_MOUSE_Q61603         ILRDEKDLGY CTKHYN-TGK ----FTCIEV KFHLERQMGY YLIQMYIPSL LIVILSWVSF WINMDAAPAR VGLGITTVLT MTTQSSGSRA SLPKVSY-VK
GLRB_HUMAN_P48167          IKKEDIEYGN CTKYYKGTGY ----YTCVEV IFTLRRQVGF YMMGVYAPTL LIVVLSWLSF WINPDASAAR VPLGIFSVLS LASECTTLAA ELPKVSY-VK
GBRA1_HUMAN_P14867         YDLLGQTVDS GIVQ-SSTGE ----YVVMTT HFHLKRKIGY FVIQTYLPCI MTVILSQVSF WLNRESVPAR TVFGVTTVLT MTTLSISARN SLPKVAY-AT
GBRA3_HUMAN_P34903         YDLLGHVVGT EIIR-SSTGE ----YVVMTT HFHLKRKIGY FVIQTYLPCI MTVILSQVSF WLNRESVPAR TVFGVTTVLT MTTLSISARN SLPKVAY-AT
GBRA5_HUMAN_P31644         YHLMGQTVGT ENIS-TSTGE ----YTIMTA HFHLKRKIGY FVIQTYLPCI MTVILSQVSF WLNRESVPAR TVFGVTTVLT MTTLSISARN SLPKVAY-AT
GBRA2_HUMAN_P47869         YDLLGQSIGK ETIK-SSTGE ----YTVMTA HFHLKRKIGY FVIQTYLPCI MTVILSQVSF WLNRESVPAR TVFGVTTVLT MTTLSISARN SLPKVAY-AT
GBRA4_HUMAN_P48169         YDLIGQTVSS ETIK-SITGE ----YIVMTV YFHLRRKMGY FMIQTYIPCI MTVILSQVSF WINKESVPAR TVFGITTVLT MTTLSISARH SLPKVSY-AT
GBRA6_HUMAN_Q16445         YDLIGQTVSS ETIK-SNTGE ----YVIMTV YFHLQRKMGY FMIQIYTPCI MTVILSQVSF WINKESVPAR TVFGITTVLT MTTLSISARH SLPKVSY-AT
GABRG1_HUMAN_Q8N1C3        FAFVGLRNST EITH-TISGD ----YVIMTI FFDLSRRMGY FTIQTYIPCI LTVVLSWVSF WINKDAVPAR TSLGITTVLT MTTLSTIARK SLPKVSY-VT
GABRG2_HUMAN_P18507        FSFVGLRNTT EVVK-TTSGD ----YVVMSV YFDLSRRMGY FTIQTYIPCT LIVVLSWVSF WINKDAVPAR TSLGITTVLT MTTLSTIARK SLPKVSY-VT
GABRG3_HUMAN_Q99928        FDFMGLRNTT EIVT-TSAGD ----YVVMTI YFELSRRMGY FTIQTYIPCI LTVVLSWVSF WIKKDATPAR TALGITTVLT MTTLSTIARK SLPRVSY-VT
GBRE_HUMAN_P78334          FDFTGVSNKT EIIT-TPVGD ----FMVMTI FFNVSRRFGY VAFQNYVPSS VTTMLSWVSF WIKTESAPAR TSLGITSVLT MTTLGTFSRK NFPRVSY-IT
```

```
ACHA1_HUMAN_P02708-2  WVIKESRGWK HSVTYSCCPD --TPYLDITY HFVMQRLPLY FIVNVIIPCL LFSFLTGLVF YLPTDSG-EK MTLSISVLLS LTVFLLVIVE LIPSTSSAVP
ACHA2_HUMAN_Q15822    WAIVNATGTY NSKKYDCCAE ---IYPDVTY AFVIRRLPLF YTINLIIPCL LISCLTVLVF YLPSDCG-EK ITLCISVLLS LTVFLLLITE IIPSTSLVIP
ACHA4_HUMAN_P43681    WVIVDAVGTY NTRKYECCAE ---IYPDITY AFVIRRLPLF YTINLIIPCL LISCLTVLVF YLPSECG-EK ITLCISVLLS LTVFLLLITE IIPSTSLVIP
ACHA3_HUMAN_P32297    WAIIKAPGYK HDIKYNCCEE ---IYPDITY SLYIRRLPLF YTINLIIPCL LISFLTVLVF YLPSDCG-EK VTLCISVLLS LTVFLLVITE TIPSTSLVIP
ACHA6_HUMAN_Q15825    WEIIDASGYK HDIKYNCCEE ---IYTDITY SFYIRRLPMF YTINLIIPCL FISFLTVLVF YLPSDCG-EK VTLCISVLLS LTVFLLVITE TIPSTSLVVP
ACHA5_HUMAN_P30532    WEIVSATGSK GNRTDSCCW- ----YPYVTY SFVIKRLPLF YTLFLIIPCI GLSFLTVLVF YLPSNEG-EK ICLCTSVLVS LTVFLLVIEE IIPSSSKVIP
ACHB3_HUMAN_Q05901    WEILNAKGMK GNRRDGVYS- ----YPFITY SFVLRRLPLF YTLFLIIPCL GLSFLTVLVF YLPSDEG-EK LSLSTSVLVS LTVFLLVIEE IIPSSSKVIP
ACHB2_HUMAN_P17787    WDIVALPGRR NENPDDST-- ----YVDITY DFIIRRKPLF YTINLIIPCV LITSLAILVF YLPSDCG-EK MTLCISVLLA LTVFLLLISK IVPPTSLDVP
ACHB4_HUMAN_P30926    WDIVALPGRR TVNPQDPS-- ----YVDVTY DFIIKRKPLF YTINLIIPCV LTTLLAILVF YLPSDCG-EK MTLCISVLLA LTFFLLLISK IVPPTSLDVP
ACHB1_HUMAN_P11230    WEIIHKPSRL IQPPGDPRGG REGQRQEVIF YLIIRRKPLF YLVNVIAPCI LITLLAIFVF YLPPDAG-EK MGLSIFALLT LTVFLLLLAD KVPETSLSVP
ACHD_HUMAN_Q07001     WEIVHRPARV NVDPRAPLDS --PSRQDITF YLIIRRKPLF YIINILVPCV LISFMVNLVF YLPADSG-EK TSVAISVLLA QSVFLLLISK RLPATSMAIP
ACHE_HUMAN_Q04844     WAIDFCPGVI RRHHGGATDG --PGETDVIY SLIIRRKPLF YVINIIVPCV LISGLVLLAY FLPAQAGGQK CTVSINVLLA QTVFLFLIAQ KIPETSLSVP
ACHG_HUMAN_P07510     WAIQHRPAKM LLDPAAPAQE --AGHQKVVF YLLIQRKPLF YVINIIAPCV LISSVAILIH FLPAKAGGQK CTVAINVLLA QTVFLFLVAK KVPETSQAVP
ACHA7_HUMAN_P36544    WDLVGIPGKR SERFYECCKE ---PYPDVTF TVTMRRRTLY YGLNLLIPCV LISALALLVF LLPADSG-EK ISLGITVLLS LTVFMLLVAE IMPATSDSVP
ACHA9_HUMAN_Q9UGM1    WEVHGMPAVK NVISYGCCSE ---PYPDVTF TLLLKRRSSF YIVNLLIPCV LISFLAPLSF YLPAASG-EK VSLGVTILLA MTVFQLMVAE IMPA-SENVP
ACHA10_HUMAN_Q9GZZ6   WRVLGMPARR RVLTYGCCSE ---PYPDVTF TLLLRRRAAA YVCNLLLPCV LISLLAPLAF HLPADSG-EK VSLGVTVLLA LTVFQLLLAE SMPP-AESVP
5HT3A_HUMAN_P46098    WELLGVLPYF REFSMESSNY ----YAEMKF YVVIRRRPLF YVVSLLLPSI FLMVMDIVGF YLPPNSG-ER VSFKITLLLG YSVFLIIVSD TLPATAIGTP
5HT3B_HUMAN_O95264    WELLSVSSTY -SILQSSAGG ----FAQIQF NVVMRRHPLV YVVSLLIPSI FLMLVDLGSF YLPPNCR-AR IVFKTSVLVG YTVFRVNMSN QVPRSVGSTP
5HT3E_HUMAN_A5X5Y0    WELLGLSKAT AKLSR-GGNL ----YDQIVF YVAIRRRPSL YVINLLVPSG FLVAIDALSF YLPVKSG-NR VPFKITLLLG YNVFLLMMSD LLPTS--GTP
5HT3C_HUMAN_Q8WXA8    WELLGINKAT PKMSM-GNNL ----YDQIMF YVAIRRRPSL YIINLLVPSS FLVAIDALSF YLPAESE-NR APFKITLLLG YNVFLLMMND LLPAS--GTP
ELIC_ERWCH_P0C7BY7    RKASTHISDI RYDHLSSVQP NQNEFSRITV RIDAVRNPSY YLWSFILPLG LIIAASWSVF WLESFS--ER LQTSFTLMLT VVAYAFYTSN ILPRLPY-TT
GLIC_GLOVI_Q7NDN8     ESFTAVVKPA NFALEDRLE- -----SKLDY QLRISRQYFS YIPNIILPML FILFISWTAF WSTSYE--AN VTLVVSTLIA HIAFNILVET NLPKTPY-MT
GluCl_cryst           L---TNTSTT YCTSVTNTGI ----YSCLRT TIQLKREFSF YLLQLYIPSC MLVIVSWVSF WFDRTAIPAR VTLGVTTLLT MTAQSAGINS QLPPVSY-IK
                      ----B9------  -B9  --B10--- ----B10---- -------------M1-------------     --------------M2-----------       --
```

```
                              ----------------M3----------         ------------------M4--------------
                              280        290        300                    423        433        443        453
GABAAR_B3_cryst               AIDMYLMGCF VFVFLALLEY AFVNYIFF-- --SQPARAAA IDRWSRIVFP FTFSLFNLVY WLYYVNGATE TSQVAPA
GBRB3_HUMAN_P28472            AIDMYLMGCF VFVFLALLEY AFVNYIFFG- ----LTDVNA IDRWSRIVFP FTFSLFNLVY WLYYVN
GBRB2_HUMAN_P47870            AIDMYLMGCF VFVFMALLEY ALVNYIFFG- ----LTDVNA IDRWSRIFFP VVFSFFNIVY WLYYVN
GBRB1_HUMAN_P18505            AIDIYLMGCF VFVFLALLEY AFVNYIFFG- ----LTDVNS IDKWSRMFFP ITFSLFNVVY WLYYVH
GBRT_HUMAN_Q9UN88             AIDIYILVCL FFVFLSLLEY VYINYLFYS- ----PDYVPK VDKWSRFLFP LAFGLFNIVY WVYHMY
GBRP_HUMAN_O00591             AIDVYLGICF SFVFGALLEY AVAHYSSLQ- ----IQNPSN VDHYSKLLFP LIFMLANVFY WAYYMYF
GBRD_HUMAN_O14764             ALDVYFWICY VFVFAALVEY AFAHFNADY- ----PIDADT IDIYARAVFP AAFAAVNVIY WAAYAM
GBRR1_HUMAN_P24046            AVDIYLWVSF VFVFLSVLEY AAVNYLTTV- ----RIDTHA IDKYSRIIFP AAYILFNLIY WSIFS
GBRR2_HUMAN_P28476            AVDIYLWVSF VFVFLSVLEY AAVNYLTTV- ----FQNTHA IDKYSRLIFP ASYIFFNLIY WSVFS
GBRR3_HUMAN_A8MPY1            AVDVYLWVSS LFVFLSVIEY AAVNYLTTV- ----LENNHV IDTYSRILFP IVYILFNLFY WGVYV
GLRA1_HUMAN_P23415            AIDIWMAVCL LFVFSALLEY AAVNFVSRQ- ----IQRAKK IDKISRIGFP MAFLIFNMFY WIIYKIVRRE DVHNQ
GLRA3_HUMAN_O75311            AIDIWMAVCL LFVFSALLEY AAVNFVSRQ- ----IDRAKK IDTISRACFP LAFLIFNIFY WVIYKILRHE DIHQQQD
GLRA2_HUMAN_P23416            AIDIWMAVCL LFVFAALLEY AAVNFVSRQ- ----VDRAKR IDTISRAAFP LAFLIFNIFY WITYKIIRHE DVHKK
GLRA4_MOUSE_Q61603            AIDIWMAVCL LFVFAALLEY AAVNFVSRQ- ----VDRAKR IDTISRAVFP FTFLVFNIFY WVVYKVLRSE DIHQAL
GLRB_HUMAN_P48167             ALDVWLIACL LFGFASLVEY AVVQVMLNN- ----PTAAKR IDLYARALFP FCFLFFNVIY WSIYL
GBRA1_HUMAN_P14867            AMDWFIAVCY AFVFSALIEF ATVNYFTKR- ----FNSVSK IDRLSRIAFP LLFGIFNLVY WATYLNREPQ LKAPTPHQ
GBRA3_HUMAN_P34903            AMDWFIAVCY AFVFSALIEF ATVNYFTKR- ----YNSVSK VDKISRIIFP VLFAIFNLVY WATYVNRESA IKGMIRKQ
GBRA5_HUMAN_P31644            AMDWFIAVCY AFVFSALIEF ATVNYFTKR- ----YNSISK IDKMSRIVFP VLFGTFNLVY WATYLNREPV IKGAASPK
GBRA2_HUMAN_P47869            AMDWFIAVCY AFVFSALIEF ATVNYFTKR- ----FNSVSK IDRMSRIVFP VLFGTFNLVY WATYLNREPV LGVSP
GBRA4_HUMAN_P48169            AMDWFIAVCF AFVFSALIEF AAVNYFTNI- ----GSGTSK IDKYARILFP VTFGAFNMVY WVVYLSKDTM EKSESLM
GBRA6_HUMAN_Q16445            AMDWFIAVCF AFVFSALIEF AAVNYFTNL- ----FGGTSK IDQYSRILFP VAFAGFNLVY WVVYLSKDTM EVSSSVE
GABRG1_HUMAN_Q8N1C3           AMDLFVSVCF IFVFAALMEY GTLHYFTSN- ----HIRIAK IDSYSRIFFP TAFALFNLVY WVGYLYL
GABRG2_HUMAN_P18507           AMDLFVSVCF IFVFSALVEY GTLHYFVSN- ----HIRIAK MDSYARIFFP TAFCLFNLVY WVSYLYL
GABRG3_HUMAN_Q99928           AMDLFVTVCF LFVFAALMEY ATLNYYSSC- ----HIDILE LDSYSRVFFP TSFLLFNLVY WVGYLYL
GBRE_HUMAN_P78334             ALDFYIAICF VFCFCALLEF AVLNFLIYN- ----CIHVYR LDNYSRVVFP VTFFFFNVLY WLVCLNL
ACHA1_HUMAN_P02708-2          LIGKYMLFTM VFVIASIIIT VIVINTHHR- ----KYVAMV MDHILLGVFM LVCIIGTLAV FAGRLIELNQ QG
ACHA2_HUMAN_Q15822            LIGEYLLFTM IFVTLSIVIT VFVLNVHHR- ----KYVAMV IDRIFLWLFI IVCFLGTIGL FLPPFLAGMI
ACHA4_HUMAN_P43681            LIGEYLLFTM IFVTLSIVIT VFVLNVHHR- ----KYVAMV IDRIFLWMFI IVCLLGTVGL FLPPWLAGMI
ACHA3_HUMAN_P32297            LIGEYLLFTM IFVTLSIVIT VFVLNVHYR- ----KYVAMV IDRIFLWVFT LVCILGTAGL FLQPLMARED A
```

```
ACHA6_HUMAN_Q15825            LVGEYLLFTM IFVTLSIVVT VFVLNIHYR- ----KYVAMV VDRVFLWVFI IVCVFGTAGL FLQPLLGNTG KS
ACHA5_HUMAN_P30532            LIGEYLVFTM IFVTLSIMVT VFAINIHHR- ----KFIAQV LDRMFLWTFL FVSIVGSLGL FVPVIYKWAN ILIPVHIGNA NK
ACHB3_HUMAN_Q05901            LIGEYLLFIM IFVTLSIIVT VFVINVHHR- ----KFVAQV LDRIFLWLFL IVSVTGSVLI FTPALKMWLH SYH
ACHB2_HUMAN_P17787            LVGKYLMFTM VLVTFSIVTS VCVLNVHHR- ----KYVAMV IDRLFLWIFV FVCVFGTIGM FLQPLFQNYT TTTFLHSDHS APSSK
ACHB4_HUMAN_P30926            LIGKYLMFTM VLVTFSIVTS VCVLNVHHR- ----KYVAMV VDRLFLWVFM FVCVLGTVGL FLPPLFQTHA ASEGPYAAQR D
ACHB1_HUMAN_P11230            IIIKYLMFTM VLVTFSVILS VVVLNLHHR- ----QFVAMV VDRLFLWTFI IFTSVGTLVI FLDATYHLPP PDPFP
ACHD_HUMAN_Q07001             LIGKFLLFGM VLVTMVVVIC VIVLNIHFR- ----NRVART VDRLCLFVVT PVMVVGTAWI FLQGVYNQPP PQPFPGDPYS YNVQDKRFI
ACHE_HUMAN_Q04844             LLGRFLIFVM VVATLIVMNC VIVLNVSQR- ----VRMGNA LDNICFWAAL VLFSVGSSLI FLGAYFNRVP DLPYAPCIQP
ACHG_HUMAN_P07510             LISKYLTFLL VVTILIVVNA VVVLNVSLR- ----FLVGRV LDRVCFLAML SLFICGTAGI FLMAHYNRVP ALPFPGDPRP YLPSPD
ACHA7_HUMAN_P36544            LIAQYFASTM IIVGLSVVVT VIVLQYHHH- ----KFAACV VDRLCLMAFS VFTIICTIGI LMSAPNFVEA VSKDFA
ACHA9_HUMAN_Q9UGM1            LIGKYYIATM ALITASTALT IMVMNIHFC- ----KKVAKV IDRFFMWIFF IMVFVMTILI IARAD
ACHA10_HUMAN_Q9GZZ6           LIGKYYMATM TMVTFSTALT ILIMNLHYC- ----KRLARV MDRFFLAIFF SMALVMSLLV LVQAL
5HT3A_HUMAN_P46098            LIGVYFVVCM ALLVISLAET IFIVRLVHK- ----LRVGSV LDKLLFHIYL LAVLAYSITL VMLWSIWQYA
5HT3B_HUMAN_O95264            LIGHFFTICM AFLVLSLAKS IVLVKFLHD- ----LVLLSR FDRLLFQSYL FMLGIYTITL CSLWALWGGV
5HT3E_HUMAN_A5X5Y0            LIGVYFALCL SLMVGSLLET IFITHLLHV- ----LQFSHA MDAMLFRLYL LFMASSIITV ICLWNT
5HT3C_HUMAN_Q8WXA8            LISVYFALCL SLMVVSLLET VFITYLLHV- ----VQFSHA MDTLLFRLYL LFMASSILTV IVLWNT
ELIC_ERWCH_P0C7BY7            VIDQMIIAGY GSIFAAILLI IFAHHRQAM- ----GVEDDL LIQRCRLAFP LGFLAIGCVL VIRGITL
GLIC_GLOVI_Q7NDN8             YTGAIIFMIY LFYFVAVIEV TVQHYLKVE- --SQPARAAS ITRASRIAFP VVFLLANIIL AFLFFGF
GluCl_cryst                   AIDVWIGACM TFIFCALLEF ALVNHIANAG TTEWNDISKR VDLISRALFP VLFFVFNILY WSRFGHHHHH H
                              -----M3-----------------------    -------------M4---------------------
```